DOCTORAL THESIS

Magnesium incorporation dynamics in amorphous and crystalline calcium carbonate affected by sulfate

by

Katja Elisabeth Goetschl

to

achieve the university degree of Natural Sciences
–Doctor rerum naturalium–
(Dr. rer. nat.)

submitted to

Graz University of Technology

Supervisors

Martin Dietzel and Vasileios Mavromatis

Reviewers

Martin Dietzel and Harald Strauss

Graz, July 2021

"Don't let anyone rob you of your imagination, your creativity, or your curiosity."

- Mae Jemison -

STATUTORY DECLARATION

I declare that I have authored this thesis independently, that I have not used other than the declared sources/resources, and that I have explicitly indicated all material which has been quoted either literally or by content from the sources used. The text document uploaded to TUGRAZonline is identical to the present doctoral thesis

…….…………….………….……….   ….….…………….………….………….……….….

Date   Signature

ACKNOWLEDGEMENTS

ABSTRACT

The replacement of Ca^{2+} by Mg^{2+} in sedimentary carbonates is one of the most studied ion substitutions enforced by the geoscientific community. Magnesium is a main component of seawater and is readily incorporated into the thermodynamically stable $CaCO_3$ polymorph calcite during its precipitation. Hence, the Mg content of calcite is used to reconstruct environmental conditions that occurred at the time of mineral formation. Biogenic calcite with Mg contents up to 45 mol% has been found in many marine organisms such as bivalves, brachiopods, echinoderms, calcareous plankton and coralline algae. Contradictory, inorganic precipitation of Mg calcite in the laboratory exceeding 20 mol% is hardly ever observed at ambient conditions. Besides biogenic control, the Mg content of calcite is determined by prevailing solution composition, temperature, growth kinetic, etc., and Mg is known to significantly modify mineral nucleation/growth, crystal shape, lattice parameters and the solubility of calcite. Thus, it is of high relevance for geoscientific issues to understand incorporation mechanisms and formation pathways to quantitively assess the Mg content of calcite. The present contribution comprises experimental designs under precisely defined physicochemical conditions that allow to mechanistically describe and value the parameters controlling the elemental composition of a forming mineral. Mineralogical characterizations together with chemical analyses of the solution and geochemical modeling are powerful tools to unravel the complex interplay between solid and solution at the time of precipitation and/or transformation during ongoing mineral-water interactions. In the course of this thesis, the role of SO_4 – the dominant divalent anion in seawater – was examined experimentally during the formation of low- and high-Mg calcite (LMC, HMC). Results show LMC grown in the presence of aqueous SO_4 exhibiting a systematic reduction in its Mg content compared to LMC formed in the absence of SO_4. The incorporation of the tetrahedral SO_4 ion in calcite results in a significant crystal lattice expansion which induces Mg incorporation into calcite to be unfavorable. HMC that is formed via an amorphous precursor occurs as nanocrystalline aggregates which are highly reactive solids that exhibit continuous exchange of Mg and SO_4 between calcite and an interacting solution throughout reaction time. This thesis also quantifies solubilities of amorphous calcium magnesium carbonate (ACMC) solids. ACMC transformation experiments at near-dolomite stoichiometry level reveal the Mg content of forming HMC not to be pre-determined by the Mg content of the amorphous precursor, but to be strongly controlled by dynamic ion exchange reactions between the amorphous solid and the reactive solution during the transformation. The results of this thesis improve our current understanding on $CaCO_3$ mineral formation mechanisms and offer new guides for the interpretation of chemical signatures of carbonates in natural and technical settings.

X

KURZFASSUNG

Der Austausch von Ca^{2+} durch Mg^{2+} in sedimentären Karbonaten ist eine der am besten untersuchten Ionensubstitutionen angespornt durch die geowissenschaftliche Community. Magnesium ist ein Hauptbestandteil des Meerwassers und wird in die thermodynamisch stabile $CaCO_3$ Modifikation, das Mineral Kalzit, bei seiner Abscheidung eingebaut. Der Mg-Gehalt von Kalzit wird verwendet, um die Umweltbedingungen, die zu der Zeit seiner Bildung herrschten, zu rekonstruieren. Biogener Kalzit mit Mg-Gehalten bis zu 45 Mol-% kommt in vielen Meeresorganismen, wie Muscheln, Brachiopoden, Stachelhäutern, kalkhaltigem Plankton und Kalkalgen, vor. Im Gegensatz dazu wird im Labor anorganisch ausgefällter Kalzit mit Mg-Gehalten höher als 20 Mol-% nur selten erhalten. Neben biogen kontrollierten Mechanismen wird der Mg-Gehalt von Kalzit durch Lösungszusammensetzung, Temperatur, Wachstumskinetik usw. bestimmt. Magnesium kann zudem die Keimbildung, das Mineralwachstum, die Kristallform, die Gitterparameter und die Löslichkeit von Kalzit signifikant verändern. Daher ist es für geowissenschaftliche Fragestellungen von großem Interesse, die Substitutionsmechanismen und Mineralbildungspfade zu verstehen, um den Mg-Gehalt von Kalzit quantitativ bewerten zu können. Der vorliegende wissenschaftliche Beitrag umfasst hierzu experimentelle Ansätze unter gut definierten physikalisch-chemischen Bedingungen, die es ermöglichen die kontrollierenden Parameter während der Mineralbildung mechanistisch zu dechiffrieren und zu bewerten. Mineralogische Charakterisierungen gekoppelt mit chemischer Lösungsanalytik und geochemischen Modellierungen sind leistungsstarke Werkzeuge, um das komplexe Wechselspiel zwischen Feststoff und Lösung zum Zeitpunkt der Mineralbildung und/oder -umwandlung während fortlaufender Mineral-Wasser-Wechselwirkungen zu entschlüsseln. Im Rahmen dieser Dissertation wurde die Rolle von SO_4 - dem dominierenden zweiwertigen Anion im Meerwasser - während der Bildung von Kalzit mit niedrigem und hohem Mg-Gehalt (LMC, HMC) experimentell untersucht. Die Ergebnisse zeigen, dass LMC - gebildet in Gegenwart von gelöstem SO_4 - eine systematische Verringerung des Mg-Gehalts im Vergleich zu LMC aufweist, der in Abwesenheit von SO_4 gebildet wird. Der Einbau des tetraedrischen SO_4-Ions im Kalzit führt zu einer erheblichen Ausdehnung des Kristallgitters, was den Einbau von Mg in Kalzit beeinträchtigt. HMC, der über eine amorphe Vorläuferphase gebildet wurde, tritt in Form von nanokristallinen Aggregaten auf, bei denen es sich um hochreaktive Feststoffe handelt, die während der Versuchszeit einen kontinuierlichen Austausch von Mg und SO_4 Ionen zwischen Kalzit und reaktiver Lösung ermöglichen. In dieser Dissertation werden ferner die Löslichkeiten von amorphen Kalzium-Magnesium-Karbonat-Feststoffen (ACMC) quantifiziert. Umwandlungsexperimente von ACMC mit Dolomit-ähnlicher Zusammensetzung zeigen, dass der Mg-Gehalt des sich bildenden HMC nicht durch den Mg-Gehalt der amorphen Vorläuferphase vorbestimmt ist, sondern wesentlich durch das dynamische Austauschverhalten zwischen dem amorphen Feststoff und der reaktiven Lösung während der Umwandlung gesteuert wird. Die Ergebnisse dieser Dissertation verbessern unser aktuelles Verständnis der Bildungsmechanismen von $CaCO_3$ Mineralen und bieten neue Ansatzpunkte für die Interpretation chemischer Signaturen von Karbonaten in natürlichen und technischen Systemen.

TABLE OF CONTENT

Chapter 1 - **INTRODUCTION**

1.1 CHARON II – Marine **C**arbonate arc**H**ives: Controls on c**AR**bonate precipitation and pathways of diagenetic alterati**ON** (Phase II)

CHARON II is a continued collaborative research initiative funded by the DFG (Deutsche Forschungsgemeinschaft) and FWF (Fonds zur Förderung der wissenschaftlichen Forschung) which involves geoscientists from a broad field of expertise including sedimentologists, microbiologists, geochemists, mineralogists, crystallographers and material scientists from universities located in Germany and Austria. The main research goals include (i) improved knowledge of physicochemical and micro-biological parameters that are controlling the geochemical signature of inorganic and biogenic carbonates at the time of their formation, and (ii) in-depth and quantitative understanding of post-depositional/post-mortem diagenetic processes that are affecting the geochemical and mineralogical composition of marine carbonate archives (e.g. skeletal hard parts). To reach these goals, the collaborative research initiative CHARON applies a series of multidisciplinary and innovative approaches, involving laboratory and field studies, high-resolution geochemical analyses and computational concepts. The focus is given on a combined archive and proxy research including the investigation of the chemical and isotopic signals (e.g. Mg/Ca, Sr/Ca, Ba/Ca, SO_4/CO_3, $\delta^{13}C$, $\delta^{18}O$, $\delta^{44/40}Ca$, $\delta^{26}Mg$, $\delta^{34}S$, $\delta^{88/86}Sr$) in carbonates in order to reconstruct past environmental conditions occurring during mineral formation. Systematic investigations of structural, elemental and isotopic changes during individual pathways of mineral formation and diagenetic alteration provide fundamental prerequisites for the interpretation of environmental conditions recorded in carbonate archives.

1.2 Formation of calcium carbonate in aqueous environments

Calcium carbonate ($CaCO_3$) minerals occur with a tremendous diversity in natural and technical environments on the Earth's surface. Inorganic and bio-induced precipitation of $CaCO_3$ occurs in terrestrial and marine environments from supersaturated solutions to form speleothems, lake deposits, sinter/scale deposits, ooids, microbialites, evaporites, etc.. However, the vast majority of $CaCO_3$ in nature is formed in the context of biogenic activity, whereas less carbonates derive from a strict inorganic origin. Marine organisms such as corals, echinoderms, bivalves, foraminifera and brachiopods precipitate actively carbonate hard parts for their protective shells, skeletons, spicules or sensory organs. However, the high degree in diversity of $CaCO_3$ becomes visible by the different crystal structures, morphologies, physical properties, hydration states ($0 \leq H_2O \leq 6$) and trace element compositions. Up to now, 7 different forms of $CaCO_3$ are known: the 3 anhydrous crystalline polymorphs calcite, aragonite and vaterite, the 3 hydrous crystalline forms calcium carbonate hemihydrate, monohydrocalcite, and ikaite, and amorphous calcium carbonate (ACC). Calcite is the thermodynamically stable polymorph under ambient conditions and is expected to form predominantly (Kawano et al., 2009). Aragonite - as stable polymorph at high pressure - occurs with a denser structure compared to calcite and is the primary polymorph inorganically formed from seawater, in particular at elevated temperature and Mg/Ca ratio (Balthasar and Cusack, 2015). Vaterite is generally considered to be metastable and transforms easily and irreversibly into the more stable polymorphs. However, vaterite is found e.g. in fish otoliths (Gauldie, 1986) or gastropod egg-shells (Hall and Taylor, 1971) and is often found during synthetic precipitation which takes place at high supersaturation (Rodriguez-Blanco et al., 2017) and/or in the presence of organic compounds e.g. polyaspartic acid (Niedermayr et al., 2013; Wedenig et al., 2021). Calcium carbonate hemihydrate (CCHH; $CaCO_3 \cdot \frac{1}{2}H_2O$) was just recently discovered during experimental investigations where it was formed from ACC in solution in the presence of Mg^{2+} ions (Zou et al., 2019). Monohydrocalcite ($CaCO_3 \cdot H_2O$) is rarely observed in geological settings but usually forms from Mg-rich solutions at high pH (Nishiyama et al., 2013; Purgstaller et al., 2017a). Ikaite ($CaCO_3 \cdot 6H_2O$) usually forms from supersaturated solutions in cold or near-freezing environments (Suess et al., 1982) and exhibits retrograde solubility as a function of temperature (Bischoff et al., 1993). Besides the crystalline forms, $CaCO_3$ exists as an amorphous phase which has been identified to play a crucial role in the formation of

calcareous biominerals (Addadi et al., 2003), and is also the most soluble form (Brečević and Nielsen, 1989). Many calcifying biomineralization strategies include ACC as a transient precursor phase which can act as a temporary storage of Ca^{2+} ions or can be transported to the desired location before its transformation into crystalline forms of $CaCO_3$. This crystallization pathway offers the advantage to create unique shapes and well-defined orientations of the crystals (Gower, 2008; Weiner and Addadi, 2011). During the last two decades, a tremendous number of studies was assigned to investigate the formation of crystalline carbonate minerals via amorphous precursors (e.g. Koga et al., 1998; Sethmann et al., 2005; Xu et al., 2006; Jiang et al., 2011; Rodriguez-Blanco et al., 2011; Bots et al., 2012; De Yoreo, 2013; Ihli et al., 2014; Giuffre et al., 2015; Ma and Feng, 2015; Rodriguez-Navarro et al., 2015; Zou et al., 2015; Blue et al., 2017; Albéric et al., 2018; Qiao et al., 2020).

1.3 Carbonate archives and paleoenvironmental reconstructions

Performing geochemical analyses of sedimentary rocks enables us to reconstruct environmental conditions of the geological past. Carbonate precipitates and deposits in natural and technical environments represent important environmental archives. The chemical and isotopic signature of carbonate minerals are strongly controlled by physicochemical parameters, like e.g. temperature (e.g. Dietzel et al., 2004; Tang et al., 2008), pH (e.g. Füger et al, 2019; Mavromatis et al., 2019), precipitation rate (e.g. Lorens, 1981; Tesoriero and Pankow, 1996), mineral structure (e.g. Mavromatis et al., 2015) and mineral-forming solution chemistry (e.g. Schott et al., 2016). This dependence one can utilize to reconstruct the environmental conditions that occurred at the time of mineral formation, transformation or diagenesis (Swart et al., 2015; Immenhauser et al., 2016). Understanding the physicochemical parameters controlling the distribution of elemental and isotopic signals in carbonates is a fundamental requirement for the interpretation of paleo-temperatures (e.g. Elderfield and Ganssen, 2000), weathering regimes (e.g. Annovi et al., 1980), global changes in element cycles (e.g. Pogge von Strandmann et al., 2014), redox conditions (e.g. Frei et al., 2011) or the past seawater composition (e.g. Turchyn and DePaolo, 2019). Not only physicochemical parameters prevailing during $CaCO_3$ formation can control its composition but also the mineral formation pathway. Here we distinguish between direct mineral precipitation from a supersaturated solution and mineral formation via the transformation of a precursor phase. In the latter case

3

ACC can act as precursor phase for all anhydrous and hydrous crystalline forms of $CaCO_3$ (Purgstaller et al., 2016, 2017a, 2017b; Konrad et al., 2016; 2018; Zou et al., 2019). Despite intensive research, the transformation mechanism of ACC into the different crystalline forms is still under debate but of great relevance for biogenic and abiogenic carbonate precipitation (De Yoreo et al., 2015). Detailed understanding of the distribution of trace elements and isotopes during the transformation of ACC is largely lacking but required in order to rely on geochemical proxies to reconstruct past environmental conditions (Mavromatis et al., 2017). Systematic experimental studies under controlled physical-chemical conditions that mechanistically describe elemental and isotopic distribution during mineral formation are crucial prerequisites for accurate interpretations.

1.4 Mg calcite

Magnesium (Mg) is the most common impurity in calcite and beyond that the solid-solution behavior between calcite and magnesite is one of the most well-examined systems in mineralogy (Lippmann 1982; Allan et al., 2019). Low-Mg calcite (LMC) refers to calcite containing <4 mol% Mg whereas calcite containing >4 mol% is classified as high-Mg calcite (HMC; Tucker and Wright, 1990). The solubility of Mg calcite varies as a function of $MgCO_3$ content exhibiting the lowest solubility at 3-4 mol% $MgCO_3$ and enhanced solubility in particular towards higher Mg contents (Mackenzie et al., 1983). Aragonite and HMC that form predominantly in shallow-marine, tropical waters are less stable than calcite, LMC and dolomite and tend to transform to the more stable phase during diagenesis (Morse and Mackenzie, 1990). The most stable phase within the $CaCO_3$-$MgCO_3$ solid-solution system is dolomite ($CaMg(CO_3)_2$) which forms diagenetically by secondary replacement of limestone but is rarely found in modern marine sediments (Gregg et al., 2015). Dolomite consists of an ordered alternation of Ca^{2+} and Mg^{2+} layers separated by layers of CO_3^{2-}, whereas in Mg calcite Ca^{2+} and Mg^{2+} ions are randomly distributed among the cation sites. However, the inorganic precipitation of HMC under ambient conditions exceeding Mg contents of 20 mol% remains an enigma despite intensive research since several decades (Kitano and Kanamori, 1966; Berner, 1975; Mucci and Morse, 1983; Busenberg and Plummer, 1989; Fernández-Díaz et al., 1996; Morse et al., 1997; 2006; 2007; Pokrovsky, 1998; Long et al., 2014) although HMC with Mg contents up to 45 mol% exists in the skeletal components of marine organisms (Ma et al., 2009). One of the main reasons for the failure of synthesizing Mg calcites with high Mg contents lies in the adsorption of hydrated Mg^{2+} on the surface of the growing calcite

which acts as an inhibitor of calcite growth and thus favors the precipitation of aragonite (Lippmann, 1973). Compared to calcite, aragonite is not affected by the adsorption of hydrated Mg^{2+}, nor is Mg^{2+} readily incorporated into the aragonite crystal lattice (Berner, 1975). Dissolved Mg^{2+} ions are more extensively hydrated compared to Ca^{2+} ions because of their smaller ionic radii and higher ionic potential. Thus, the high energy required for the dehydration of the hydrophilic Mg^{2+} priorits incorporation in the crystal lattice is the rate-limiting step to form HMC (Mucci and Morse, 1983). More recently it was suggested that the formation of HMC via an amorphous precursor may overcome rate-limiting steps observed during direct mineral nucleation and/or growth from a supersaturated solution (Raz et al., 2000; Loste et al., 2003). Elevated Mg content of HMC is frequently attributed to the transformation of Mg-bearing ACC, so-called amorphous calcium magnesium carbonate (ACMC).

1.5 SO_4 in the scope of marine carbonates

Sulfate (SO_4) is the most concentrated divalent anion in seawater (~28 mM) and thus always present during marine $CaCO_3$ formation. The main influx of SO_4 to the oceans occurs via continental weathering and riverine run-off (Jørgensen and Kasten, 2006). In evaporating modern seawater brines the SO_4 concentration can be high as 100 mM before gypsum starts to precipitate (Bąbel and Schreiber, 2014). SO_4 is known to play a crucial role in the oscillation between calcite and aragonite seas throughout the Phanerozoic (Bots et al., 2011). Moreover, a few studies have addressed its potential role on controlling the $CaCO_3$ polymorphism and its effect on calcite growth (Fernández-Díaz et al., 2010; Arroyo-de Dompablo et al., 2015; Nielsen et al., 2016). Other studies investigated the sulfate incorporation in natural and synthetic calcites and aragonites (Kitano et al., 1975; Takano et al., 1980; Takano, 1985; Busenberg and Plummer, 1985; Kontrec et al., 2004; Wynn et al., 2018; Okumura et al., 2018). This fraction of sulfate is commonly referred to carbonate-associated sulfate (CAS) and it is presumed that the tetrahedral SO_4 ion substitutes the trigonal-planar CO_3 ion in the respective crystal lattice. The sulfur isotopic composition of CAS ($\delta^{34}S_{CAS}$) is a useful paleoenvironmental proxy as it reflects the sulfur isotope composition of seawater and is commonly used to reconstruct the evolution of the marine sulfur cycle of past oceans (Burdett et al., 1989; Kampschulte and Strauss, 2004; Paris et al., 2014; Barkan et al., 2020). However, the exact position of SO_4 within the calcium carbonate crystal lattice and the pathway of

incorporation during mineral growth and biomineralization is poorly understood (e.g. Pingitore et al., 1995; Perrin et al., 2017). In the scope of calcium carbonate mineral formation, the correlation between Mg^{2+} and SO_4^{2-} ions has been of relevant interest due to their natural high abundance in seawater (Takano 1985; Tracy et al., 1998; Vielzeuf et al., 2013; Nielsen et al., 2016; van Dijk et al., 2019). Mucci and coworkers (Mucci et al., 1989) observed that the $MgCO_3$ incorporation in calcite is significantly influenced by the presence or absence of SO_4 ions in seawater but the responsible mechanisms are still poorly understood.

1.6 Outline of the DOCTORAL THESIS

The occurrence and formation of calcium carbonate minerals is in most cases related to precipitation from aqueous solutions where mineral formation proceeds along different pathways (Chapter 1). In this thesis, the effect of SO_4 during the formation of Mg calcite via seeded mineral growth and via transformation of an amorphous precursor was experimentally investigated. Another main focus was given on investigating the solubility of ACC as a function of its Mg content by synthesizing amorphous calcium magnesium carbonates (ACMCs) with distinct Mg contents ranging from 0 to 100 mol%. Subsequent transformation of ACMC with near-dolomite stoichiometry has been systematically examined from 10 to 80 °C in order to assess the effect of temperature on the Mg content of the final HMC. The obtained results are presented and discussed in detail in Chapter 2 to 5 which are based on four publications in *Geochimica et Cosmochimica Acta* and *CrystEngComm*. Finally, Chapter 6 summarizes some future perspectives.

Chapter 2 describes the effect of SO_4 on the Mg partitioning between calcite and reactive solution during seeded mineral overgrowth experiments. The results indicated that LMC formed in the presence of aqueous SO_4 exhibits a systematic reduction in its magnesium content compared to calcite formed in the absence of SO_4. The experimental findings suggest that the presence of SO_4 inhibits calcite growth and promotes the formation of aragonite. Chapter 2 has been published in *Geochimica et Cosmochimica Acta* (2019) Volume 265, Pages 505-519 (K.E. Goetschl, B. Purgstaller, M. Dietzel, V. Mavromatis).

Chapter 3 provides new insights on the role of Mg and SO_4 during the transformation of pure ACC to HMC. In the presence of SO_4, the subsequent formation of $MgSO_4^0(aq)$ causes the ACC transformation to occur earlier, proportionally to the concentration of $Mg^{2+}(aq)$. Aqueous complexation is controlling the metastability of ACC, the amorphous-to-crystalline transformation kinetics, and the Mg content of the resulting HMC. Moreover, a continuous exchange of Mg and SO_4 between nanocrystalline HMC and experimental solution is observed up to 1 year of reaction time. Chapter 3 has been published in *Geochimica et Cosmochimica Acta* (2021) in press (K.E. Goetschl, M. Dietzel, B. Purgstaller, C. Grengg, V. Mavromatis).

Chapter 4 provides new insights on the solubility of ACMC in the aqueous system and the factors controlling its transformation into distinct crystalline calcium magnesium carbonate minerals. The results reveal a fast exchange of ions between the synthesized ACMC solids and aqueous solutions, which is stimulated by the large surface area of the nanoporous ACMCs. The calculated ion activity products reveal that the solubility of ACMC increases as a function of the Mg content. Chapter 4 has been published in *CrystEngComm* (2019) Volume 21, Pages 155-164 (B. Purgstaller, K.E. Goetschl, V. Mavromatis, M. Dietzel).

Chapter 5 deals with the transformation of ACMC (containing initially 48 mol% Mg) into HMC at temperatures ranging from 10 to 80 °C. The results reveal that at higher temperatures the Mg incorporation into HMC is enhanced due to the reduced solvation energy barrier of $Mg^{2+}(aq)$ and the high prevailing Mg^{2+}/Ca^{2+} ratio of the experimental solution which is controlled by the temperature-dependent solubility of ACMC. The Mg content of the forming HMC is not pre-determined by the Mg content of the amorphous precursor, but strongly influenced by the reaction temperature and physicochemical conditions of the prevailing solution during ACMC transformation. Chapter 5 has been published in *CrystEngComm* (2021) Volume 23, Pages 1969-1981 (B. Purgstaller, V. Mavromatis, K.E. Goetschl, F.R. Steindl, M. Dietzel).

References

Addadi L., Raz S. and Weiner S. (2003) Taking advantage of disorder: Amorphous calcium carbonate and its roles in biomineralization. *Adv. Mater.* **15**, 959–970.

Albéric M., Bertinetti L., Zou Z., Fratzl P., Habraken W. and Politi Y. (2018) The Crystallization of Amorphous Calcium Carbonate is Kinetically Governed by Ion Impurities and Water. *Adv. Sci.* **5**.

Allan N. L., Thomas L., Hart J. N., Freeman C. L. and Mohn C. E. (2019) Calcite –magnesite solid solutions: using genetic algorithms to understand non-ideality. *Phys. Chem. Miner.* **46**, 193–202.

Annovi A., Fontana D., Gelmini R., Gorgoni C. and Sighinolfi G. (1980) Geochemistry of carbonate rocks and ferruginous horizons in the verrucano in southern Tuscany - paleoenvironmental and paleogeographic implications. *Palaeogeogr. Palaeoclimatol. Palaeoecol.* **30**, 1–16.

Arroyo-De Dompablo M. E., Fernández-González M. A. and Fernández-Díaz L. (2015) Computational investigation of the influence of tetrahedral oxoanions (sulphate, selenate and chromate) on the stability of calcium carbonate polymorphs. *RSC Adv.* **5**, 59845–59852.

Bąbel M. and Schreiber B. C. (2014) Geochemistry of Evaporites and Evolution of Seawater. In *Treatise on Geochemistry (Second Edition)* **9**, 483-560.

Balthasar U. and Cusack M. (2015) Aragonite-calcite seas-Quantifying the gray area. *Geology* **43**, 99–102.

Barkan Y., Paris G., Webb S. M., Adkins J. F. and Halevy I. (2020) Sulfur isotope fractionation between aqueous and carbonate-associated sulfate in abiotic calcite and aragonite. *Geochim. Cosmochim. Acta* **280**, 317–339.

Berner R. A. (1975) The role of magnesium in the crystal growth of calcite and aragonite from sea water. *Geochim. Cosmochim. Acta* **39**, 489–504.

Bischoff J. L., Fitzpatrick J. A. and Rosenbauer R. J. (1993) The solubility and stabilization of ikaite ($CaCO_3 \cdot 6H_2O$) from $0°$ to $25°C$: Environmental and paleoclimatic implications for thinolite tufa. *J. Geol.* **101**, 21–33.

Blue C. R., Giuffre A., Mergelsberg S., Han N., De Yoreo J. J. and Dove P. M. (2017) Chemical and physical controls on the transformation of amorphous calcium carbonate into crystalline $CaCO_3$ polymorphs. *Geochim. Cosmochim. Acta* **196**, 179–196.

Bots P., Benning L. G., Rickaby R. E. M. and Shaw S. (2011) The role of SO_4 in the switch from calcite to aragonite seas. *Geology* **39**, 331–334.

Bots P., Benning L. G., Rodriguez-Blanco J. D., Roncal-Herrero T. and Shaw S. (2012) Mechanistic insights into the crystallization of amorphous calcium carbonate (ACC). *Cryst. Growth Des.* **12**, 3806–3814.

Brečević L. and Nielsen A. E. (1989) Solubility of amorphous calcium carbonate. *J. Cryst. Growth* **98**, 504–510.

Burdett J. W., Arthur M. A. and Richardson M. (1989) A Neogene seawater sulfur isotope age curve from calcareous pelagic microfossils. *Earth Planet. Sci. Lett.* **94**, 189–198.

Busenberg E. and Plummer L. N. (1985) Kinetic and thermodynamic factors controlling the distribution of SO_4^{2-} and Na^+ in calcites and selected aragonites. *Geochim. Cosmochim. Acta* **49**, 713–725.

Busenberg E. and Plummer N. L. (1989) Thermodynamics of magnesian calcite solid-solutions at 25°C and 1 atm total pressure. *Geochim. Cosmochim. Acta* **53**, 1189–1208.

Dietzel M., Gussone N. and Eisenhauer A. (2004) Co-precipitation of Sr^{2+} and Ba^{2+} with aragonite by membrane diffusion of CO_2 between 10 and 50 °C. *Chem. Geol.* **203**, 139–151.

van Dijk I., Barras C., De Nooijer L. J., Mouret A., Geerken E., Oron S. and Reichart G. J. (2019) Coupled calcium and inorganic carbon uptake suggested by magnesium and sulfur incorporation in foraminiferal calcite. *Biogeosciences* **16**, 2115–2130.

Elderfield H. and Ganssen G. (2000) Past temperature and d18O of surface ocean waters inferred from foraminiferal Mg/Ca ratios. *Nature* **405**, 442–445.

Fernández-Díaz L., Fernández-González Á. and Prieto M. (2010) The role of sulfate groups in controlling $CaCO_3$ polymorphism. *Geochim. Cosmochim. Acta* **74**, 6064–6076.

Fernández-Díaz L., Putnis A., Prieto M. and Putnis C. V (1996) The role of magnesium in the crystallization of calcite and aragonite in a porous medium. *J. Sediment. Res.* **66**, 482–491.

Frei R., Gaucher C., Døssing L. N. and Sial A. N. (2011) Chromium isotopes in carbonates - A tracer for climate change and for reconstructing the redox state of ancient seawater. *Earth Planet. Sci. Lett.* **312**, 114–125.

Füger A., Konrad F., Leis A., Dietzel M. and Mavromatis V. (2019) Effect of growth rate and pH on lithium incorporation in calcite. *Geochim. Cosmochim. Acta* **248**, 14–24.

Gauldie R. W. (1986) Vaterite otoliths from chinook salmon (Oncorhynchus tshawytscha). *New Zeal. J. Mar. Freshw. Res.* **20**, 209–217.

Giuffre A. J., Gagnon A. C., De Yoreo J. J. and Dove P. M. (2015) Isotopic tracer evidence for the amorphous calcium carbonate to calcite transformation by dissolution–reprecipitation. *Geochim. Cosmochim. Acta* **165**, 407–417.

Gower L. B. (2008) Biomimetic model systems for investigating the amorphous precursor pathway and its role in biomineralization. *Chem. Rev.* **108**, 4551–4627.

Gregg J. M., Bish D. L., Kaczmarek S. E. and Machel H. G. (2015) Mineralogy, nucleation and growth of dolomite in the laboratory and sedimentary environment: A review. *Sedimentology* **62**, 1749–1769.

Hall A. and Taylor J. D. (1971) The occurrence of vaterite in gastropod egg-shells. *Mineral. Mag.* **38**, 521–522.

Ihli J., Wong W. C., Noel E. H., Kim Y. Y., Kulak A. N., Christenson H. K., Duer M. J. and Meldrum F. C. (2014) Dehydration and crystallization of amorphous calcium carbonate in solution and in air. *Nat. Commun.* **5**, 1–10.

Immenhauser A., Schöne B. R., Hoffmann R. and Niedermayr A. (2016) Mollusc and brachiopod skeletal hard parts: Intricate archives of their marine environment. *Sedimentology* **63**, 1–59.

Jiang J., Gao M. R., Qiu Y. H., Wang G. S., Liu L., Cai G. Bin and Yu S. H. (2011) Confined crystallization of polycrystalline high-magnesium calcite from compact Mg-ACC precursor tablets and its biological implications. *CrystEngComm* **13**, 952–956.

Jørgensen B. B. and Kasten S. (2006) Sulfur Cycling and Methane Oxidation. In *Marine Geochemistry* pp. 271–310.

Kampschulte A. and Strauss H. (2004) The sulfur isotopic evolution of Phanerozoic seawater based on the analysis of structurally substituted sulfate in carbonates. *Chem. Geol.* **204**, 255–286.

Kawano J., Shimobayashi N., Miyake A. and Kitamura M. (2009) Precipitation diagram of calcium carbonate polymorphs: Its construction and significance. *J. Phys. Condens. Matter* **21**.

Kitano Y. and Kanamori N. (1966) Synthesis of magnesian calcite at low temperatures and pressures. *Geochem. J.* **1**, 1–10.

Kitano Y., Okumura M. and Idogaki M. (1975) Incorporation of sodium, chloride and sulfate with calcium carbonate. *Geochem. J.* **9**, 75–84.

Koga N., Nakagoe Y. and Tanaka H. (1998) Crystallization of amorphous calcium carbonate. *Thermochim. Acta* **318**, 239–244.

Konrad F., Gallien F., Gerard D. E. and Dietzel M. (2016) Transformation of Amorphous Calcium Carbonate in Air. *Cryst. Growth Des.* **16**, 6310–6317.

Konrad F., Purgstaller B., Gallien F., Mavromatis V., Gane P. and Dietzel M. (2018) Influence of aqueous Mg concentration on the transformation of amorphous calcium carbonate. *J. Cryst. Growth* **498**, 381–390.

Kontrec J., Kralj D., Brečević L., Falini G., Fermani S., Noethig-Laslo V. and Mirosavljević K. (2004) Incorporation of inorganic anions in calcite. *Eur. J. Inorg. Chem.*, 4579–4585.

Lippmann F. (1973) *Sedimentary Carbonate Minerals.*, Springer, Berlin.

Lippman F. (1982) Stable and metastable solubility diagrams for the system $CaCO_3$-$MgCO_3$-H_2O at ordinary temperature. *Bull. Mineral.* **105**, 273–279.

Long X., Ma Y. and Qi L. (2014) Biogenic and synthetic high magnesium calcite - A review. *J. Struct. Biol.* **185**, 1–14.

Lorens R. B. (1981) Sr, Cd, Mn and Co distribution coefficients in calcite as a function of calcite precipitation rate. *Geochim. Cosmochim. Acta* **45**, 553–561.

Loste E., Wilson R. M., Seshadri R. and Meldrum F. C. (2003) The role of magnesium in stabilising amorphous calcium carbonate and controlling calcite morphologies. *J. Cryst. Growth* **254**, 206–218.

Ma Y., Aichmayer B., Paris O., Fratzl P., Meibom A., Metzler R. A., Politi Y., Addadi L., Gilbert P. U. P. A. and Weiner S. (2009) The grinding tip of the sea urchin tooth exhibits exquisite control over calcite crystal orientation and Mg distribution. *Proc. Natl. Acad. Sci. U. S. A.* **106**, 6048–6053.

Ma Y. and Feng Q. (2015) A crucial process: Organic matrix and magnesium ion control of amorphous calcium carbonate crystallization on β-chitin film. *CrystEngComm* **17**, 32–39.

Mackenzie F. T., Bischoff W. D., Bishop F. C., Loijens M., Schoonmaker J. and Wollast R. (1983) Magnesian calcites: low-temperature occurrence, solubility and solid-solution behavior. *Carbonates Mineral. Chem.*, 97–144.

Mavromatis V., González A. G., Dietzel M. and Schott J. (2019) Zinc isotope fractionation during the inorganic precipitation of calcite – Towards a new pH proxy. *Geochim. Cosmochim. Acta* **244**, 99–112.

Mavromatis V., Montouillout V., Noireaux J., Gaillardet J. and Schott J. (2015) Characterization of boron incorporation and speciation in calcite and aragonite from co-precipitation experiments under controlled pH, temperature and precipitation rate. *Geochim. Cosmochim. Acta* **150**, 299–313.

Mavromatis V., Purgstaller B., Dietzel M., Buhl D., Immenhauser A. and Schott J. (2017) Impact of amorphous precursor phases on magnesium isotope signatures of Mg-calcite. *Earth Planet. Sci. Lett.* **464**, 227–236.

Morse J. W., Andersson A. J. and Mackenzie F. T. (2006) Initial responses of carbonate-rich shelf sediments to rising atmospheric pCO_2 and "ocean acidification": Role of high Mg-calcites. *Geochim. Cosmochim. Acta* **70**, 5814–5830.

Morse J. W., Arvidson R. S. and Lüttge A. (2007) Calcium carbonate formation and dissolution. *Chem. Rev.* **107**, 342–381.

Morse J. W. and Mackenzie F. T. (1990) *Geochemistry of sedimentary carbonates.*, Elsevier, Amsterdam, Oxford, New York, Tokyo.

Morse J. W., Wang Q. and Tsio M. Y. (1997) Influences of temperature and Mg:Ca ratio on $CaCO_3$ precipitates from seawater. *Geology* **25**, 85–87.

Mucci A., Canuel R. and Zhong S. (1989) The solubility of calcite and aragonite in sulfate-free seawater and the seeded growth kinetics and composition of the precipitates at 25°C. *Chem. Geol.* **74**, 309–320.

Mucci A. and Morse J. W. (1983) The incorporation of Mg^{2+} and Sr^{2+} into calcite overgrowths: influences of growth rate and solution composition. *Geochim. Cosmochim. Acta* **47**, 217–233.

Niedermayr A., Köhler S. J. and Dietzel M. (2013) Impacts of aqueous carbonate accumulation rate, magnesium and polyaspartic acid on calcium carbonate formation (6-40 °C). *Chem. Geol.* **340**, 105–120.

Nielsen M. R., Sand K. K., Rodriguez-Blanco J. D., Bovet N., Generosi J., Dalby K. N. and Stipp S. L. S. (2016) Inhibition of Calcite Growth: Combined Effects of Mg^{2+} and SO_4^{2-}. *Cryst. Growth Des.* **16**, 6199–6207.

Nishiyama R., Munemoto T. and Fukushi K. (2013) Formation condition of monohydrocalcite from $CaCl_2$-$MgCl_2$-Na_2CO_3 solutions. *Geochim. Cosmochim. Acta* **100**, 217–231.

Okumura T., Kim H., Kim J. and Kogure T. (2018) Sulfate-containing calcite: crystallographic characterization of natural and synthetic materials. *Eur. J. Mineral.* **30**, 929–937.

Paris G., Fehrenbacher J. S., Sessions A. L., Spero H. J. and Adkins J. F. (2014) Experimental determination of carbonate-associated sulfate $\delta^{34}S$ in planktonic foraminifera shells. *Geochemistry, Geophys. Geosystems* **15**, 1452–1461.

Perrin J., Rivard C., Vielzeuf D., Laporte D., Fonquernie C., Ricolleau A., Cotte M. and Floquet N. (2017) The coordination of sulfur in synthetic and biogenic Mg calcites: The red coral case. *Geochim. Cosmochim. Acta* **197**, 226–244.

Pingitore N. E., Meitzner G. and Love K. M. (1995) Identification of sulfate in natural carbonates by X-ray absorption spectroscopy. *Geochim. Cosmochim. Acta* **59**, 2477–2483.

Pogge von Strandmann P. A. E., Forshaw J. and Schmidt D. N. (2014) Modern and Cenozoic records of seawater magnesium from foraminiferal Mg isotopes. *Biogeosciences* **11**, 5155–5168.

Pokrovsky O. S. (1998) Precipitation of calcium and magnesium carbonates from homogeneous supersaturated solutions. *J. Cryst. Growth* **186**, 233–239.

Purgstaller B., Mavromatis V., Immenhauser A. and Dietzel M. (2016) Transformation of Mg-bearing amorphous calcium carbonate to Mg-calcite - In situ monitoring. *Geochim. Cosmochim. Acta* **174**, 180–195.

Purgstaller Bettina, Konrad F., Dietzel M., Immenhauser A. and Mavromatis V. (2017a) Control of Mg^{2+}/Ca^{2+} Activity Ratio on the Formation of Crystalline Carbonate Minerals via an Amorphous Precursor. *Cryst. Growth Des.* **17**, 1069–1078.

Purgstaller B., Dietzel M., Baldermann A. and Mavromatis V. (2017b) Control of temperature and aqueous Mg^{2+}/Ca^{2+} ratio on the (trans-)formation of ikaite. *Geochim. Cosmochim. Acta* **217**, 128–143.

Qiao L., Zizak I., Zaslansky P. and Ma Y. (2020) The crystallization process of vaterite microdisc mesocrystals via proto-vaterite amorphous calcium carbonate characterized by cryo-x-ray absorption spectroscopy. *Crystals* **10**, 1–12.

Raz S., Weiner S. and Addadi L. (2000) Formation of high-magnesian calcites via an amorphous precursor phase: Possible biological implications. *Adv. Mater.* **12**, 38–42.

Rodriguez-Blanco J. D., Sand K. K. and Benning L. G. (2017) ACC and Vaterite as Intermediates in the Solution-Based Crystallization of CaCO3. In *New Perspectives on Mineral Nucleation and Growth* pp. 93–111.

Rodriguez-Blanco J. D., Shaw S. and Benning L. G. (2011) The kinetics and mechanisms of amorphous calcium carbonate (ACC) crystallization to calcite, via vaterite. *Nanoscale* **3**, 265–271.

Rodriguez-Navarro C., Kudłacz K., Cizer Ö. and Ruiz-Agudo E. (2015) Formation of amorphous calcium carbonate and its transformation into mesostructured calcite. *CrystEngComm* **17**, 58–72.

Schott J., Mavromatis V., Fujii T., Pearce C. R. and Oelkers E. H. (2016) The control of carbonate mineral Mg isotope composition by aqueous speciation: Theoretical and experimental modeling. *Chem. Geol.* **445**, 120–134.

Sethmann I., Putnis A., Grassmann O. and Löbmann P. (2005) Observation of nano-clustered calcite growth via a transient phase mediated by organic polyanions: A close match for biomineralization. *Am. Mineral.* **90**, 1213–1217.

Suess E., Balzer W., Hesse K. F., Müller P. J., Ungerer C. A. and Wefer G. (1982) Calcium carbonate hexahydrate from organic-rich sediments of the antarctic shelf: Precursors of glendonites. *Science (80-.).* **216**, 1128–1131.

Swart P. K. (2015) The geochemistry of carbonate diagenesis: The past, present and future. *Sedimentology* **62**, 1233–1304.

Takano B. (1985) Geochemical implications of sulfate in sedimentary carbonates. *Chem. Geol.* **49**, 393–403.

Takano B., Asano Y. and Watanuki K. (1980) Characterization of sulfate ion in travertine. *Contrib. to Mineral. Petrol.* **72**, 197–203.

Tang J., Köhler S. J. and Dietzel M. (2008) Sr^{2+}/Ca^{2+} and $^{44}Ca/^{40}Ca$ fractionation during inorganic calcite formation: I. Sr incorporation. *Geochim. Cosmochim. Acta* **72**, 3718–3732.

Tesoriero A. J. and Pankow J. F. (1996) Solid solution partitioning of Sr^{2+}, Ba^{2+}, and Cd^{2+} to calcite. *Geochim. Cosmochim. Acta* **60**, 1053–1063.

Tracy S. ., François C. J. P. and Jennings H. . (1998) The growth of calcite spherulites from solution I. Experimental design techniques. *J. Cryst. Growth* **193**, 374–381.

Tucker M. E. and Wright V. P. (1990) *Carbonate Sedimentology.*, Blackwell Science Ltd.

Turchyn A. V. and DePaolo D. J. (2019) Seawater chemistry through phanerozoic time. *Annu. Rev. Earth Planet. Sci.* **47**, 197–224.

Vielzeuf D., Garrabou J., Gagnon A., Ricolleau A., Adkins J., Günther D., Hametner K., Devidal J. L., Reusser E., Perrin J. and Floquet N. (2013) Distribution of sulphur and magnesium in the red coral. *Chem. Geol.* **355**, 13–27.

Wedenig M., Boch R., Leis A., Wagner H. and Dietzel M. (2021) Green Inhibitor Performance against $CaCO_3$ Scaling: Rate-Modeling Aided Test Procedure. *Cryst. Growth Des.* **21**, 1959–1971.

Weiner S. and Addadi L. (2011) Crystallization Pathways in Biomineralization. *Annu. Rev. Mater. Res.* **41**, 21–40.

Wynn P. M., Fairchild I. J., Borsato A., Spötl C., Hartland A., Baker A., Frisia S. and Baldini J. U. L. (2018) Sulphate partitioning into calcite: Experimental verification of pH control and application to seasonality in speleothems. *Geochim. Cosmochim. Acta* **226**, 69–83.

Xu X., Han J. T., Kim D. H. and Cho K. (2006) Two modes of transformation of amorphous calcium carbonate films in air. *J. Phys. Chem. B* **110**, 2764–2770.

De Yoreo J. (2013) Crystal nucleation: More than one pathway. *Nat. Mater.* **12**, 284–285.

De Yoreo J. J., Gilbert P. U. P. A., Sommerdijk N. A. J. M., Penn R. L., Whitelam S., Joester D., Zhang H., Rimer J. D., Navrotsky A., Banfield J. F., Wallace A. F., Michel F. M., Meldrum F. C., Colfen H. and Dove P. M. (2015) Crystallization by particle attachment in synthetic, biogenic, and geologic environments. *Science* **349**, aaa6760.

Zou Z., Bertinetti L., Politi Y., Jensen A. C. S., Weiner S., Addadi L., Fratzl P. and Habraken W. J. E. M. (2015) Opposite Particle Size Effect on Amorphous Calcium Carbonate Crystallization in Water and during Heating in Air. *Chem. Mater.* **27**, 4237–4246.

Zou Z., Habraken W. J. E. M., Matveeva G., Jensen A. C. S., Bertinetti L., Hood M. A., Sun C.-Y., Gilbert P. U. P. A., Polishchuk I., Pokroy B., Mahamid J., Politi Y., Weiner S., Werner P., Bette S., Dinnebier R., Kolb U., Zolotoyabko E. and Fratzl P. (2019) A hydrated crystalline calcium carbonate phase: Calcium carbonate hemihydrate. *Science* **363**, 396–400.

Chapter 2

Effect of sulfate on magnesium incorporation in low–magnesium calcite

Katja E. Goetschl[1], Bettina Purgstaller[1], Martin Dietzel[1], Vasileios Mavromatis[1,2]

[1]Institute of Applied Geosciences, Graz University of Technology, Rechbauerstrasse 12, 8010 Graz, Austria
[2]Géosciences Environment Toulouse (GET), CNRS, UMR 5563, Observatoire Midi-Pyrénées, 14 Av. E. Belin, 31400 Toulouse, France

ABSTRACT: The incorporation of magnesium and sulfate in calcite is frequently used to characterize and trace the environmental conditions occurring during carbonate mineral formation. Although both ions are simultaneously incorporated in the growing calcite, the effect of sulfate on magnesium incorporation in calcite is still under-explored. In this study, we examine the Mg incorporation in low-Mg calcite as a function of growth rate at 25 °C and 1 bar pCO_2 in the presence and absence of aqueous sulfate. The obtained results suggest that high calcite growth rates induce a significant increase in the partitioning coefficient of Mg between the precipitated low-Mg calcite and aqueous solution (i.e. $D_{Mg} = \frac{(n_{Mg}/n_{Ca})_{calcite}}{([Mg^{2+}]/[Ca^{2+}])_{solution}}$). Obtained D_{Mg} values exhibit similar dependence to mineral growth rate for experiments performed in the presence and absence of sulfate, however a systematic shift to lower D_{Mg} values is observed for calcites formed in the presence of sulfate. The lower D_{Mg} values of calcites formed in sulfate-bearing solutions are attributed to the incorporated SO_4 ions which provoke expansion in the unit cell along the c-axis of the newly formed calcite. A larger unit cell is unfavorable for the substitution of Ca by smaller Mg ions in calcite. The coupled effect of (i) sulfate uptake during calcite growth and (ii) precipitation rate on D_{Mg} can be expressed by the equation $D_{Mg} = 0.03726 - 0.02345 \times \left[-log\left(r_p\right) - 7 \right] - X_{SO4} \times \left\{ 0.004607 + 0.002109 \times \left[-log\left(r_p\right) - 7 \right] \right\}$; ($-8 \leq log(r_p) \leq -7$; $0 \leq X_{SO_4} \leq 2.6$; T = 25 °C) and is valid for $0.01 \leq D_{Mg} \leq 0.04$. In analogy to Mg also SO_4 ions are inhibiting calcite growth, thus promoting the formation of aragonite due to adsorption phenomena and blocking of calcite surface sites. These results improve our understanding on physicochemical parameters controlling $CaCO_3$ composition and mineral polymorphism and are discussed in their relevance for the use of magnesium and sulfate environmental proxies in natural surroundings.

2.1 Introduction

Calcium carbonate minerals ($CaCO_3$) are readily forming in natural aquatic environments and they comprise geological archives that have been extensively studied for their chemical, structural and isotopic composition (e.g. Morse and Mackenzie, 1990; Tucker and Wright, 1990; Schlager, 2005; Morse et al., 2007; Böttcher and Dietzel, 2010; Dietzel, 2011). The two most common polymorphs of calcium carbonate in sedimentary environments are calcite and aragonite. Their trace-to-major cation ratios (e.g. Mg/Ca, Sr/Ca and Ba/Ca) as well as their isotopic compositions (e.g. $\delta^{26}Mg$, $\delta^{44/40}Ca$ and $\delta^{18}O$) are routinely used to reconstruct the physicochemical conditions occurred during mineral formation (e.g. Elderfield and Ganssen, 2000; Hall and Chan, 2004; Gussone et al., 2005; Hippler et al., 2006, 2009; Immenhauser et al., 2010; Onuk et al., 2014). Unravelling, however, the information that is recorded in the chemical and isotopic composition of traces/impurities in carbonates requires insights on the reaction mechanisms controlling their incorporation during mineral growth. This is because the distribution behavior of traces during mineral formation depends on many parameters such as mineral structure, temperature, pH, precipitation rate, composition of parental solution, etc. (Morse and Bender, 1990; Tang et al., 2008; Mavromatis et al., 2013; Füger et al., 2019). In order to unravel the physicochemical parameters controlling the chemical composition of the solid phase, rigorous experimental work is of great necessity. For example, the trace metal concentration in the precipitating mineral is controlled by the isomorphic substitution of a host ion by a foreign ion in the given crystal structure (e.g. McIntire, 1963). Isomorphic substitution is the replacement of the main cation by a trace cation which can form a pure carbonate phase with the same coordination. The substitution of divalent cations in carbonate minerals depends on the cation radius and its coordination of metal ion to oxygen ion yielding in specific crystal structure. Trigonal carbonates (calcite type) have a 6-fold coordination of metal ions to oxygen ions and host preferentially smaller cations compared to Ca^{2+} whereas orthorhombic carbonates (aragonite type) have a 9-fold coordination where Ca is substituted readily by bigger cations compared to Ca^{2+} (Dietzel, 2011). Ideal divalent cation substitution (e.g. Mg^{2+}, Sr^{2+}, Ba^{2+}) is not the only case for foreign element incorporation into $CaCO_3$ as for example trivalent rare earth elements (REE^{3+}: Zhong and Mucci, 1995; Voigt et al., 2017) and monovalent cations, e.g. Na^+ and Li^+ (Busenberg and Plummer, 1985; Marriott et al., 2004; Füger et al., 2019), are also present in carbonates. In analogy the incorporation of anions

in carbonates is in the focus of intense research with the most well explored substitution to be that of (i) boron/borate in calcite and aragonite (Gabitov et al., 2014; Mavromatis et al., 2015; Uchikawa et al., 2015; 2017; Noireaux et al., 2015; Balan et al., 2016; 2018; Saldi et al., 2018), owing to its wide application as a pH-proxy tool and (ii) sulfate which in $CaCO_3$ minerals records sulfur isotope composition of oceanic waters that is used as a proxy signal for reconstructing redox conditions, biological activity and the evolution of the marine sulfur cycle in former oceans (Kampschulte and Strauss, 2004; Fichtner et al., 2017). This fraction of sulfur in the carbonate minerals is commonly referred to as carbonate-associated sulfate (CAS: Burdett et al., 1989; Wotte et al., 2012).

To date a large body of studies has been devoted to characterize the impact of different physical and chemical parameters on the incorporation of Mg in synthetic carbonates (Mucci and Morse, 1983; Oomori et al., 1987; Busenberg and Plummer, 1989; Burton and Walter, 1991; Morse et al., 1997; Lin and Singer, 2009; Mavromatis et al., 2013; Purgstaller et al., 2016; 2017). This interest stems from the fact that Mg is the most concentrated divalent cation in seawater and the most common impurity in calcite. To the best of our knowledge only one study (Mucci et al., 1989) has focused on investigating systematically the effect of dissolved sulfate on Mg partitioning during its incorporation in calcite, although sulfate is the second most concentrated anion in seawater (~28 mM). In contrast, a few studies have addressed the incorporation behavior of sulfate in calcium carbonate (Kitano et al., 1975; Takano 1985; Busenberg and Plummer, 1985; Pingitore et al., 1995; Balan et al., 2014; Kartnaller et al., 2018) and its potential role in controlling $CaCO_3$ polymorphism and calcite growth (Reddy and Nancollas, 1976; Fernández-Díaz et al., 2010; Bots et al., 2011; Arroyo-de Dompablo et al., 2015; Nielsen et al., 2016; Han et al., 2017).

In this study we explore experimentally the effect of dissolved sulfate on the Mg partitioning during its incorporation in calcite in an abiotic system as a function of mineral growth rate and sulfate concentration. The obtained results allow for a critical evaluation of the role of sulfate on the incorporation of Mg in calcite both as a dissolved anion and as a component of the calcite crystal lattice. The obtained results are discussed in the context of Mg content of natural low-Mg calcite as an environmental proxy.

2.2 Methods

2.2.1 Experimental set-up

Low-Mg calcite precipitation experiments were carried out on synthetic pure calcite seeds at 25 °C and 1 bar pCO_2 using a mixed-flow reactor experimental set-up similar as previously described in Mavromatis et al. (2019). The experimental set-up used in the present study is illustrated in Fig. 1 and consists of two separate inlet solutions A and B, and a reaction vessel placed on a stirring plate in a constant temperature room. This design was adapted because it allows to control pH and chemical steady-state during mineral growth. The initial solution in the reactor of 0.5 L contained ~10 mM of $CaCl_2$ and $MgCl_2$ as well as different concentrations of Na_2SO_4 (Table 1). Note here that a single Mg source was used for all experiments by diluting a concentrated $MgCl_2$ stock solution in order to precisely constrain the Mg concentration. The inlet solution A contained $CaCl_2$ and $MgCl_2$, in which the Mg concentration was in all experiments the same and equal to 20 mM. This concentration was equal to the double of that present initially in the reactor in order to avoid its dilution by the addition of inlet solution B. The inlet solution B contained Na_2CO_3 and Na_2SO_4. The concentration of Na_2CO_3 was equal to the concentration of $CaCl_2$ in the corresponding inlet solution A in each experiment, whereas the concentration of sulfate was also adjusted to the double of its concentration present in the initial reactor solution. In the experiments conducted in this study the aqueous SO_4 concentration ranged between 10 and 30 mM (see Table 1). Background electrolyte concentration of all solutions maintained constant during each experimental run and was set to 400 mM adjusted by the addition of NaCl when necessary. The initial amount of ~1 g synthetic calcite with a BET specific surface area of 0.29 m^2/g (see methods below) was used in all reactors as seed material.

To induce overgrowth, both inlet solutions were pumped via a peristaltic pump (Ismatec IPC) in the reaction vessel at an equal flow rate of ~10 mL/day each. The precipitation rate for $CaCO_3$ was modified by changing the molalities of $CaCl_2$ and Na_2CO_3 in the inlet solutions (50-400 mM). During the whole experimental run the solution pH was kept constant at 6.3 ±0.1 via continuous bubbling of CO_2 gas in the reaction vessel. The reactor solution was continuously stirred at a constant rate of 300 rpm using a floating magnetic stir bar. All reacting solutions were prepared with analytical grade chemicals ($CaCl_2 \cdot 2H_2O$, $MgCl_2 \cdot 6H_2O$, Na_2CO_3, Na_2SO_4 and NaCl from Roth) dissolved in ultrapure deionized water (Millipore Integral 3: 18.2 $M\Omega\,cm^{-1}$).
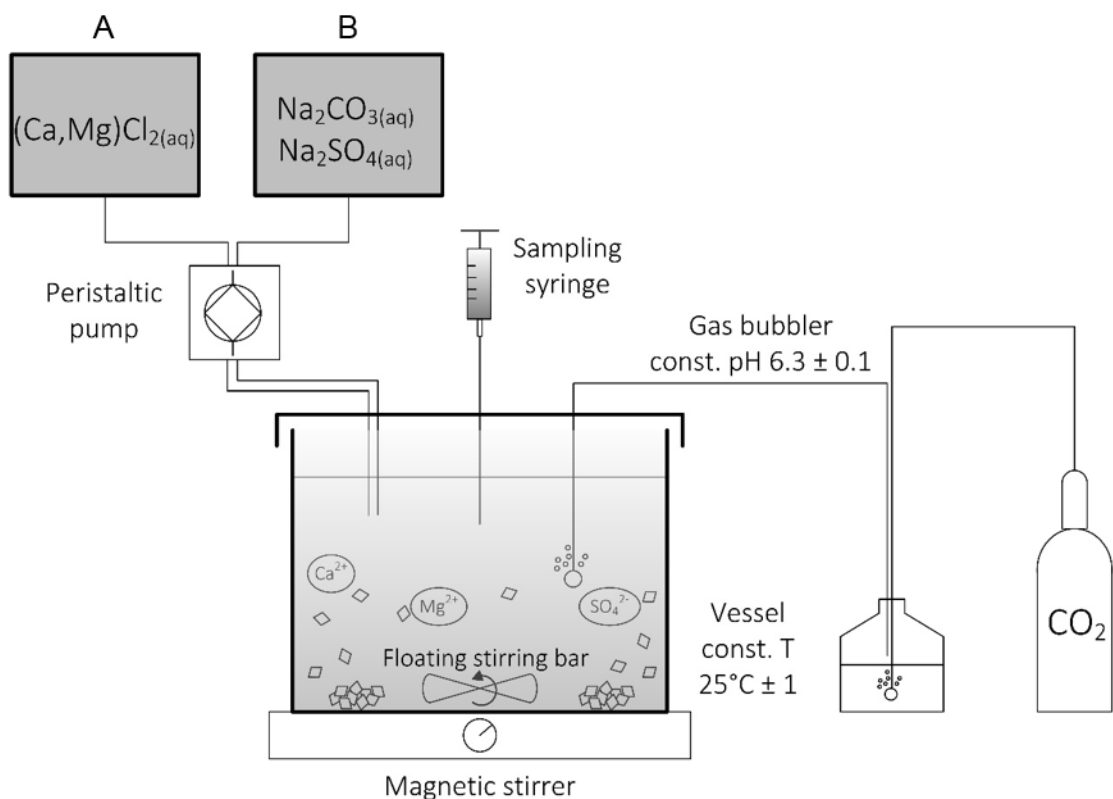
Fig. 1: Experimental set-up for low-Mg calcite precipitation experiments using a mixed-flow reactor and two inlet solutions.

Every 24 h a volume of the reactive solution – equal to the volume of the sum of the inlet solutions added in 24 hours (~20 mL) – was collected with a syringe for chemical analyses of Ca, Mg, S, SO_4 and alkalinity. In this way the volume of the reactor solution maintained almost constant within ±4 % and variations in growth rate were minimized. Shortly prior to sampling the magnetic stirrers were stopped to allow the solid material to settle and to minimize its removal by sampling. In this way the solid/solution ratio was kept almost constant during the course of an experiment. Directly after sampling, the collected solution was filtered through a 0.2 μm membrane cellulose acetate syringe filter and pH was measured *in situ*. An adequate amount of the sample was taken to measure the solution carbonate alkalinity and selected samples were directly diluted for further SO_4 analyses by ion chromatography (IC), whereas the rest of the reactive solution was acidified for further Ca, Mg and S analyses by inductive coupled plasma optical emmision spectrometry (ICP-OES). At the end of each experimental run the entire reactive solution was filtered through a 0.2 μm membrane using suction filtration. The solid material was

rinsed extensively with ultrapure deionized water and dried at 40 °C. In total, 27 experiments were performed at varying growth rates but constant concentrations with respect to Mg (10 mM) and SO_4 (30 mM; i.e. MgS2-MgS8, MgS19, MgS20, MgS23, MgS25 and MgS27 in Table 1). In order to investigate the effect of varying sulfate concentration on Mg incorporation in calcite in the absence of growth rate effects, selected experiments were performed in duplicates, where the Mg concentration was kept constant (10 mM), but the SO_4 concentration was adjusted to 10, 15, 20, 25 and 30 mM, respectively. Duplicate experiments were performed at low and high growth rate respectively (i.e. MgS11-MgS20, MgS29 and MgS30 in Table 1). Finally, the effect of growth rate on Mg incorporation in calcite in the absence of dissolved sulfate was examined in six experiments (i.e. MgS9, MgS10, MgS22, MgS24, MgS26 and MgS28 in Table 1).

2.2.2 Mineralogical and chemical analyses

2.2.2.1 Solids

The specific surface area of solid materials was determined by multi-point krypton adsorption using the Brunauer-Emmett-Teller (BET) method. Measurements were performed using a Quantachrome Autosorb-1 MP with an analytical uncertainty of ±10 %. Powder X-ray diffraction (XRD) patterns of the solids collected at the end of the experimental run were recorded by a PANalytical X'Pert PRO diffractometer using Co-Kα-radiation (40 mA, 40 kV) at a 2θ range from 15° to 60° and a scan speed of $0.03° s^{-1}$. For qualitative characterization of crystalline products the PANalytical HighScore Plus software with the ICSD database was used and the mineral phases were quantified by Rietveld refinement. Analytical uncertainty of the quantification lies within 1 wt. %. The precipitates were gold-coated and imaged using a ZEISS DSM 982 Gemini scanning electron microscope (SEM) equipped with a field emission gun operating at 2 kV accelerating voltage. Ca, Mg and SO_4 content of the solids were measured by Ion Chromatography (IC) using a Dionex IC S 3000 with IonPac® AS19 and CS16 column with an analytical precision of ±3 %. In order to precisely determine the chemical composition of the collected solids by IC, a new protocol for sample digestion and dilution was developed. About 10 mg of solid was dissolved in 10 mL of 0.024 M HCl and treated in the ultrasonic bath and shaker over night to ensure complete dissolution. Subsequently a second dilution step with ultrapure deionized water was performed to achieve concentrations within the calibration range from 1 to 300 mg L^{-1}.

2.2.2.2 Solutions

Measurements of pH were performed with a WTW SenTix® 945 gel electrode coupled to a pH-meter (WTW Multi 3420) and calibrated on the activity scale with NIST standard buffer solutions at pH 4.01, 7.00 and 10.00 with an uncertainty of ±0.03 units. The total alkalinity of the solutions was determined by a Schott TitroLine alpha plus titrator using a 0.01 M HCl solution and an analytical precision of ±2 %. Ca, Mg and S (in this case referring to SO_4) concentrations were measured by Inductive Coupled Plasma Optical Emission Spectrometry (ICP-OES) using a PerkinElmer Optima ICP-OES 8300 DV with an analytical uncertainty of ±3 %. The calibration ranges of concentrations for Ca 1-500 mg L^{-1}, Mg 0.2-100 mg L^{-1} and for S 10-100 mg L^{-1} have been used and the samples were diluted accordingly. The quantitative control of the measured S concentrations was performed by IC measurements. Selected samples were diluted immediately after sampling without acidification and measured S and SO_4 data were identical within ±5 %.

The molalities of aqueous species in the reactive solutions, ion activities and saturation indices were calculated using the PHREEQC software in combination with its minteq.v4 database. The ion activity coefficients of free aqueous ions and charged complexes in this model are calculated using the Davis equation. Saturation index (SI) with respect to calcite or aragonite is referred to the activities of the free ions and is expressed as

$$SI_{CaCO_3} = log \frac{(Ca^{2+})(CO_3^{2-})}{K_{sp}} \tag{1}$$

where $K_{sp} = 10^{-8.48}$ for calcite and $K_{sp} = 10^{-8.34}$ for aragonite at 25 °C respectively (Plummer and Busenberg, 1982). Note here that owing to the low concentration of Mg in the synthetic precipitates of this work, that does not exceed 1.6 mol% $MgCO_3$ as it can be seen in Table 1, the forming mineral has been considered to be calcite and no further modifications in eq. 1 due to variations in solubility of Mg-rich calcite were considered similar to Mavromatis et al. (2013; 2017).

2.3 Results

2.3.1 Mineralogy and chemical composition of the precipitated phases

Quantitative results of XRD analyses suggest that the solid material collected after the experimental runs consists of calcite, except for 8 samples that additionally contain aragonite (i.e. MgS4, MgS5, MgS6, MgS8, MgS16, MgS18, MgS20 and MgS27). The proportions of the two mineral phases have been corrected for the amount of calcite seed and are reported in Table 1. The amount of precipitated aragonite varied from 0.8 to 40.9 wt. % and has been detected in experiments conducted at 20 mM, 25 mM and 30 mM sulfate concentration in the reactive solution, respectively. The calcite XRD patterns of the solids which were precipitated in the presence of sulfate do not exhibit major differences compared to the calcite seed material and no significant shift of the characteristic $d_{(104)}$ calcite peak (d = 3.035 Å) to lower d-values due to Mg incorporation in the crystal lattice (corresponding to calcite containing $MgCO_3$; Goldsmith and Graf, 1958) or to higher d-values due to SO_4 incorporation (Busenberg and Plummer, 1985) was observed. Only the calcite patterns of samples with Mg content > 1 mol% that were conducted in the absence of sulfate show a minor shift to lower d-values for the $d_{(104)}$ peak (max $d_{(104)}$ shift = -0.008 Å) compared to calcite seed material. Notably, according to Rietveld refinement of the XRD patterns, the dimensions of the calcite unit cell parameters (i.e. a and c) of the collected precipitates exhibit significant changes in the dimension of the c-axis, whereas the refinement of the calcite seed material pattern is in excellent agreement with the parameters for reference calcite (a = 4.989 Å, c = 17.062 Å; Swanson and Fuyat, 1953; Markgraf and Reeder, 1985). More precisely the length of the calcite c-axis of precipitates formed in the presence of sulfate increased and varies in the range of 17.062-17.106 Å, exhibiting an increase up to +0.25 %. Note here, however, that no changes in the unit cell parameters of aragonite (a = 5.740 Å, b = 4.961 Å, c = 7.967 Å; De Villiers, 1971) were observed.

Table 1: Concentrations of inlet solutions and reactive solutions, pH(ss stands for chemical steady-state), calculated calcite precipitation rates (r_p), Mg and SO_4 content of final precipitates measured by IC and corrected for aragonite if necessary, distribution coefficients (D_{Mg}) and saturation index (SI) with respect to both calcite and aragonite. Mass and proportions of precipitated calcite and aragonite are corrected for calcite seed.

Experiment	Inlet solution Mg/Ca	SO_4 (mM)	Ca_{ss} (mM)	Mg_{ss} (mM)	pH_{ss}	$\log(r_p)$ (mol m^{-2} s^{-1})	X_{Mg} (mol%)	X_{SO4} (mol%)	$\log(D_{Mg})$	SI$_{calcite}$	SI$_{aragonite}$	Precipitate (g)	Calcite (wt.%)	Aragonite (wt.%)
MgS2	0.19	30	23.87	9.55	6.38	-7.56	0.7	1.2	-1.78	0.53	0.35	1.0	100.0	-
MgS3	0.19	30	23.76	7.93	6.37	-7.50	0.6	1.3	-1.75	0.54	0.36	1.1	100.0	-
MgS4	0.10	30	23.39	8.62	6.44	-7.22*	0.9	2.2	-1.67	0.64	0.46	2.5	91.5	8.5
MgS5	0.08	30	24.78	8.97	6.41	-7.14*	0.8	2.3	-1.69	0.63	0.45	3.2	87.9	12.1
MgS6	0.08	30	29.07	9.66	6.41	-7.15*	0.8	2.6	-1.67	0.70	0.52	3.2	84.8	15.2
MgS8	0.05	30	26.24	9.19	6.43	-7.15*	0.7	2.4	-1.76	0.65	0.47	5.3	59.1	40.9
MgS9	0.39	-	18.73	9.96	6.18	-7.99	0.8	-	-1.86	0.14	-0.04	0.3	100.0	-
MgS10	0.05	-	22.82	9.60	6.20	-6.92	1.6	-	-1.43	0.27	0.09	5.4	100.0	-
MgS11	0.20	10	22.02	9.73	6.29	-7.68	0.9	0.7	-1.74	0.43	0.25	0.7	100.0	-
MgS12	0.06	10	25.74	9.35	6.39	-6.97	1.2	1.6	-1.50	0.68	0.50	4.4	100.0	-
MgS13	0.20	15	26.84	10.13	6.28	-7.63	0.6	0.7	-1.84	0.51	0.33	0.8	100.0	-
MgS14	0.06	15	24.80	8.95	6.45	-6.97	1.1	2.1	-1.55	0.75	0.57	4.5	100.0	-
MgS15	0.19	20	24.54	9.56	6.34	-7.57	0.6	1.0	-1.82	0.57	0.39	0.9	100.0	-
MgS16	0.06	20	34.58	9.66	6.43	-7.01*	0.7	2.6	-1.61	0.85	0.67	4.2	94.7	5.3
MgS17	0.19	25	25.56	9.86	6.32	-7.60	0.6	1.2	-1.84	0.52	0.34	0.8	100.0	-
MgS18	0.06	25	25.55	9.45	6.49	-7.10*	0.8	2.4	-1.69	0.83	0.65	3.5	89.0	11.0
MgS19	0.19	30	26.66	10.16	6.31	-7.74	0.5	1.2	-1.91	0.55	0.37	0.6	100.0	-
MgS20	0.06	30	32.05	9.91	6.48	-7.16*	0.6	2.7	-1.74	0.88	0.70	3.8	73.0	27.0
MgS22	0.40	-	16.47	9.02	6.15	-8.09	0.7	-	-1.91	0.09	-0.09	0.3	100.0	-
MgS23	0.26	30	21.81	8.88	6.31	-7.97	0.4	0.4	-2.05	0.46	0.28	0.3	100.0	-
MgS24	0.26	-	18.04	9.36	6.16	-7.81	1.1	-	-1.70	0.18	0.00	0.5	100.0	-
MgS25	0.19	30	24.06	9.37	6.37	-7.78	0.6	1.0	-1.86	0.59	0.41	0.5	100.0	-
MgS26	0.19	-	19.47	9.54	6.17	-7.52	1.3	-	-1.59	0.21	0.03	1.0	100.0	-
MgS27	0.13	30	26.37	9.88	6.39	-7.35*	0.8	2.0	-1.71	0.65	0.47	1.5	99.2	0.8
MgS28	0.13	-	19.05	9.24	6.19	-7.31	1.4	-	-1.54	0.23	0.05	1.7	100.0	-
MgS29	0.13	25	26.07	9.48	6.37	-7.35	0.8	1.9	-1.70	0.64	0.46	1.5	100.0	-
MgS30	0.13	20	23.67	9.48	6.29	-7.39	0.7	1.4	-1.77	0.47	0.29	1.4	100.0	-
Seed							0.0	0.0						

*Growth rate was corrected for precipitated aragonite

In accord to the XRD patterns, the SEM microphotographs of the solid material show the occurrence of aragonite in the respective samples. Needle-like aragonite prisms with a pseudo hexagonal form were present in experiments MgS4, MgS5, MgS6, MgS8, MgS16, MgS18, MgS20 and MgS27 (see Fig. 2D) and they were growing on the calcite seed material or were distributed randomly. In Fig. 2B it can be seen that the precipitated calcite at low growth rates kept the same rhombohedral morphology as the initial calcite seed material (see Fig. 2A) whereas the shape of precipitated calcite at elevated growth rates was scalenohedral, as it can be seen in Fig. 2C. Most prominent was the observed porous surface structure of calcite grown in the presence of sulfate (see Fig. 2B).
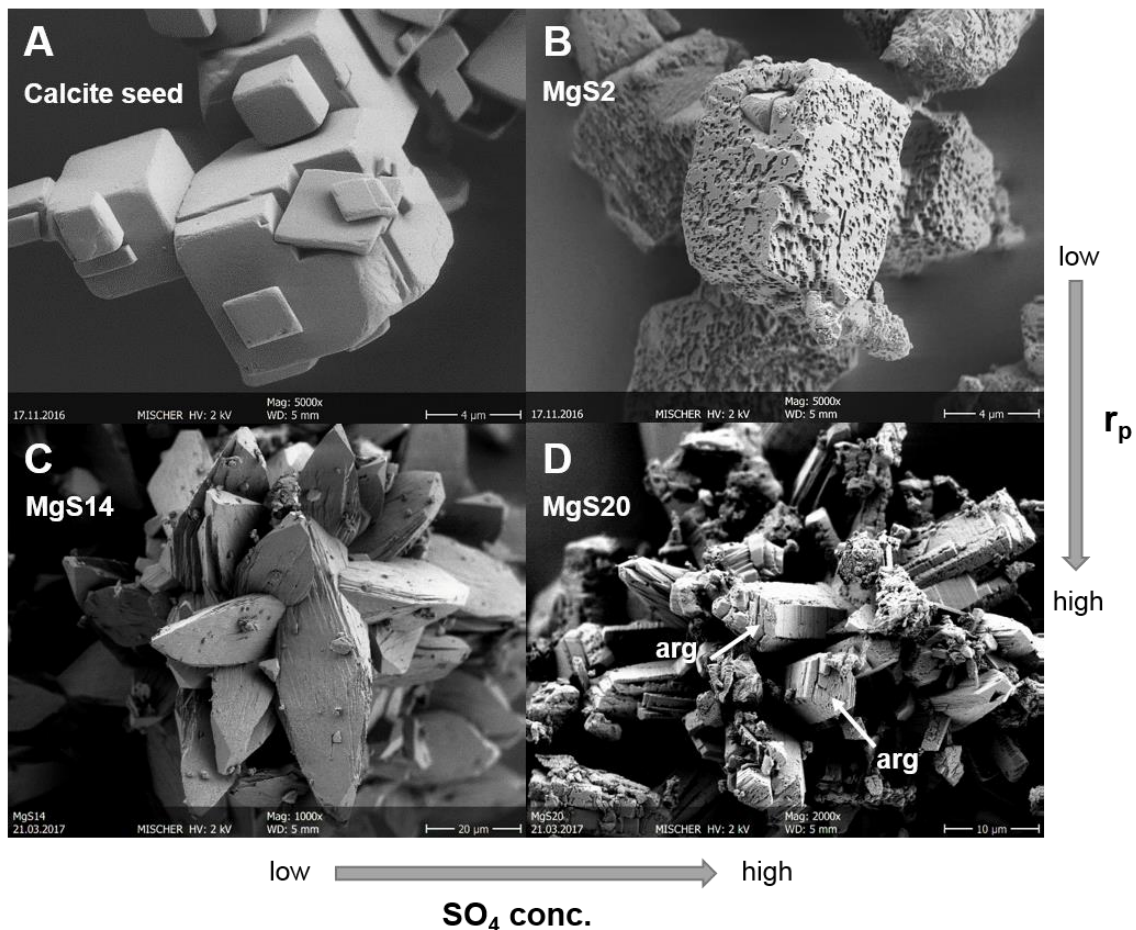
Fig. 2: SEM images of (A) calcite seed material, (B) precipitates from experiment MgS2 performed at low growth rate ($\log(r_p)$ = -7.6) in the presence of 30 mM sulfate in the reactive solution (calcite with rhombohedral shape), (C) MgS14 at high growth rate ($\log(r_p)$ = -7.0) and 15 mM sulfate (calcite with scalenohedral shape), (D) MgS20 at high growth rate ($\log(r_p)$ = -7.2) and 30 mM sulfate, where pseudo-hexagonal, elongated aragonite crystals (see white arrows) are formed besides calcite growth.

The Mg content of the precipitates (in mol%) sampled at the end of the experimental run was calculated according to the equation

$$X_{Mg} = \frac{n_{Mg}}{n_{Mg}+n_{Ca}} \times 100 \qquad (2)$$

where n_{Mg} and n_{Ca} represent the moles of Mg and Ca of the solid phase derived from IC measurements after digestion in HCl and were corrected for the amount of the seed material and precipitated aragonite as Mg^{2+} is not taken up to any extent into the bulk aragonite structure (Berner, 1975; Kawano et al., 2015). The results are listed in Table 1. In similar terms, the amount of incorporated sulfate (listed in Table 1 as mol%) into the solid was estimated according to the equation

$$X_{SO_4} = \frac{n_{SO_4}}{n_{SO_4}+n_{CO_3}} \times 100 \qquad (3)$$

where n_{SO_4} refers to the moles of SO_4 in the solid phase which was quantified using IC measurements. The number of moles of CO_3 was calculated as $n_{CO_3} = 1 - n_{SO_4}$. The molarities of SO_4 and CO_3 were corrected for the amount of the seed material as well as for the amount of precipitated aragonite. The estimated error of the reported calculation lies within ±4 %. As such the SO_4 content estimated using eq. 3 is only corresponding to the precipitating calcite as it was defined by quantitative XRD analyses. The working assumption here is that the incorporation of SO_4 in aragonite can be considered negligible (Fernándes-Díaz et al., 2010; Kartnaller et al., 2018).

2.3.2 Chemical evolution of the reactive solution and growth rate calculation
Chemical steady-state (abbrv.: ss) in terms of aqueous Ca concentration was achieved within 6000 to 8000 min (Fig. 3), which is in good agreement with Mavromatis et al. (2017). Concentrations of aqueous Mg and SO_4 remained constant at the pre-selected concentration for the whole duration of the experimental runs (Fig. 3). Carbonate alkalinity was increasing initially and achieved steady-state due to ongoing precipitation of calcium carbonate. Aqueous Mg/Ca compositions of the inlet solution and the reactive solution at chemical steady-state are reported in Table 1. The aqueous concentrations of Ca, Mg and alkalinity in the reactive solution together with the molalities of aqueous Ca and Mg species are presented in Table A1 of the supplementary material. Calcite growth

rate, r_p (mol m^{-2} s^{-1}), under steady-state conditions was calculated based on mass balance considerations using the amount of moles of Ca and Mg added in the reactor in 24 hours, corrected for the moles of Ca and Mg removed from the reactor via sampling during the same period of time, as

$$r_p = \frac{[Ca]_{(add)} + [Mg]_{(add)} - [Ca]_{(rem)} - [Mg]_{(rem)}}{86400}/S \qquad (4)$$

where $[Ca]_{(add)}$ and $[Mg]_{(add)}$ refer to the moles of Ca and Mg respectively added in the reactor within 24 hours and $[Ca]_{(rem)}$ and $[Mg]_{(rem)}$ denote the moles of Ca and Mg respectively removed from the reactor within 24 hours. The value 86400 represents the number of seconds within 24 hours and S stands for calcite total surface in m^2/g that has been corrected for the amount of precipitated material using mass balance estimations. Growth rate estimation required only corrections for the precipitated calcite mass because the specific surface area of selected samples collected from the reactors at the end of each run was similar to that of the seed material. Note here that r_p is calculated based on the average molar concentrations at steady-state conditions. Calcite growth rates (r_p) in this study range from $10^{-8.1}$ to $10^{-6.9}$ mol m^{-2} s^{-1}, where r_p of precipitates consisting of aragonite beside calcite, has been corrected for the amount of precipitated aragonite. The estimated error for the calcite growth rate calculation lies within ± 0.05 log units. For this correction it is assumed that aragonite precipitates simultaneously with calcite.
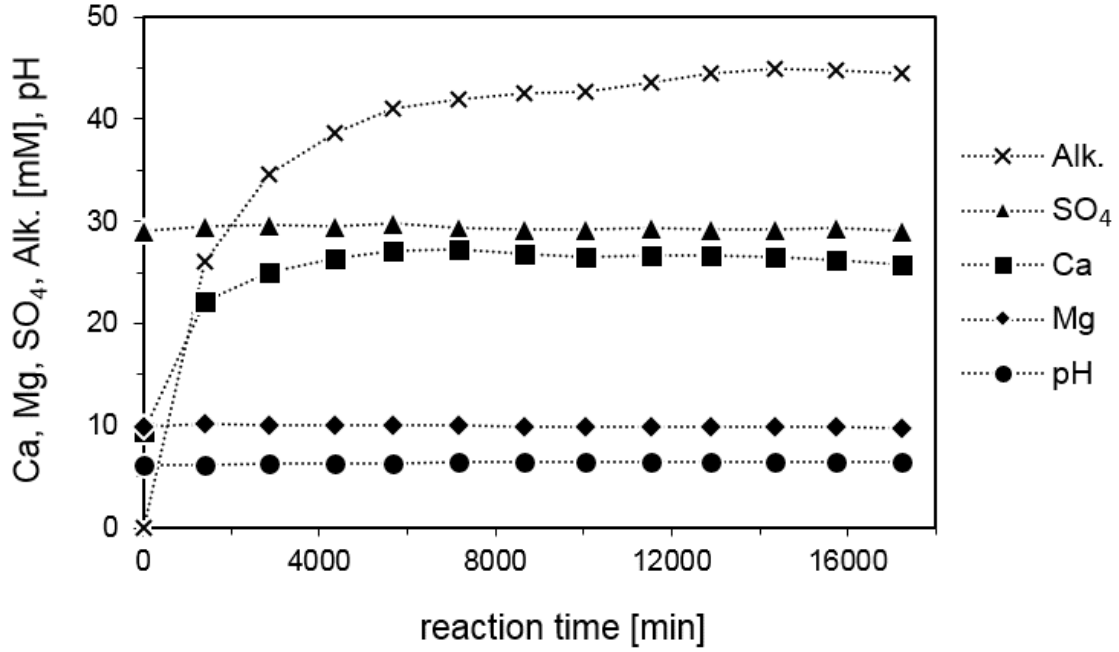
Fig. 3: Temporal evolution of Ca, Mg, SO$_4$ and alkalinity concentrations and pH value for experiment MgS27 performed in the presence of 30 mM sulfate. Analytical uncertainty is included in the symbol size.

2.3.3 Magnesium partitioning between calcite and solution

The partitioning coefficient of Mg between calcite and reactive solution, D_{Mg}, has been determined from the number of moles of Ca and Mg in the solids collected after the experimental run and the average number of moles of Ca^{2+} and Mg^{2+} in the reactive solution at chemical steady-state conditions. The results of speciation calculation indicate that only in the absence of sulfate the Ca^{2+} and Mg^{2+} free ions account for more than 94 % of total aqueous Ca and Mg present in the reactive solution, consistent with the percentages reported earlier by Mavromatis et al. (2017). In the presence of e.g. 30 mM sulfate in the reactive solution, 25 % of the total aqueous Mg and more than 30 % of the total aqueous Ca was complexed and corrections for Mg and Ca complexation were necessary in order to determine D_{Mg} value according to the expression:

$$D_{Mg} = \frac{\left(\frac{n_{Mg}}{n_{Ca}}\right)_{calcite}}{\left(\frac{[Mg^{2+}]}{[Ca^{2+}]}\right)_{solution}} \qquad (5)$$

27

The molar contents of Mg and Ca of the precipitated calcite, n_{Mg} and n_{Ca}, have been corrected for the amount of the seed material and aragonite assuming that the latter mineral phase is free of Mg. $[Mg^{2+}]$ and $[Ca^{2+}]$ denote the aqueous molar concentrations of free Mg^{2+} and Ca^{2+} ions at chemical steady-state. The calculated $\log(D_{Mg})$ values are given in Table 1 and are plotted as a function of $\log(r_p)$ in Fig. 4. The obtained results suggest that D_{Mg} increases with solution saturation state of the reactive solution with respect to calcite and consequently with calcite precipitation rate. More specific, in the absence of sulfate the increase of D_{Mg} as a function of calcite growth rate in the range $10^{-8.1} \leq r_p \leq 10^{-6.9} \, mol \, m^{-2} s^{-1}$ can be described by the expression:

$$\log(D_{Mg}) = 0.4048(\pm 0.0500) \times \log(r_p) + 1.4075(\pm 0.3809); R^2 = 0.93 \qquad (6)$$

As it can be seen in Fig. 4, all experiments performed in the presence of sulfate plot below the experiments performed in the absence of sulfate. In the presence of 30 mM sulfate which is the concentration similar to seawater and at which most of the experiments of this study were performed (n = 11) the Mg partitioning coefficient increases with calcite growth rate within the range $10^{-8.0} \leq r_p \leq 10^{-7.0} \, mol \, m^{-2} s^{-1}$ according to the expression:

$$\log(D_{Mg}) = 0.3463(\pm 0.0581) \times \log(r_p) + 0.7921(\pm 0.4316); R^2 = 0.78 \qquad (7)$$

This linear relationship is indicated by the dashed line in Fig. 4.
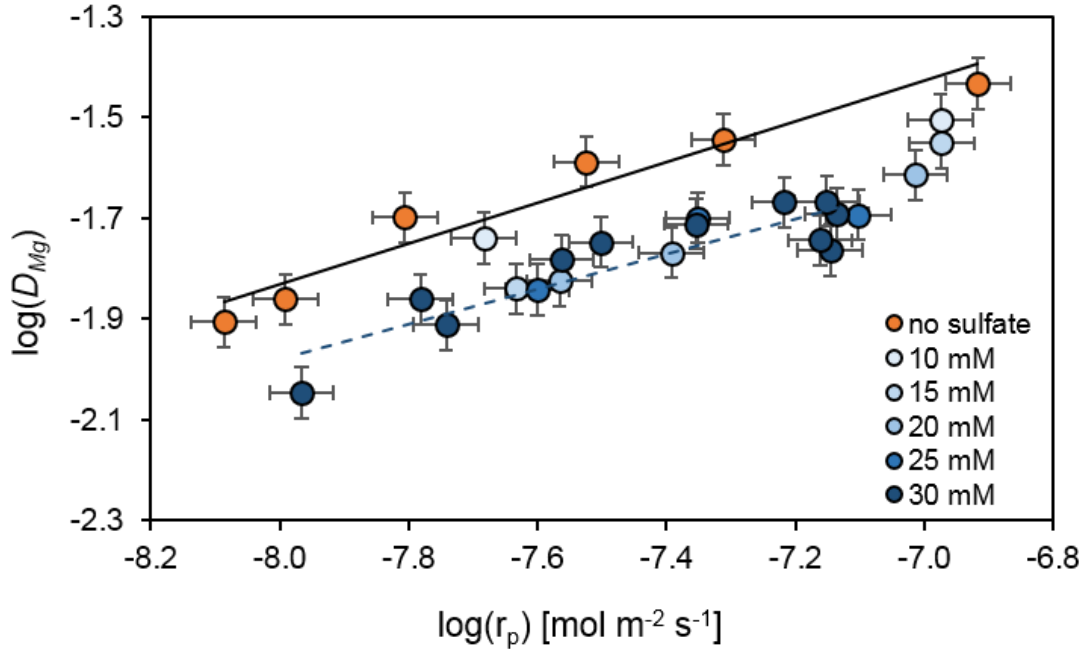
Fig. 4: Mg partitioning coefficient between low-Mg calcite and aqueous solution according to eq. 5 as a function of calcite growth rate. The linear fit of experiments in the absence of sulfate (orange circles) is given by: $\log(D_{Mg}) = 0.4048(\pm0.0500) \times \log(r_p) + 1.4075(\pm0.3809)$; $R^2 = 0.93$. All experiments conducted in the presence of sulfate (10-30 mM; blue circles) plot below. The dashed line indicates the linear fit of experiments performed at 30 mM sulfate concentration and can be expressed by: $\log(D_{Mg}) = 0.3463(\pm0.0581) \times \log(r_p) + 0.7921(\pm0.4316)$; $R^2 = 0.78$.

2.4 Discussion

2.4.1 Control on mineralogy and surface structure

The mineralogy of the final precipitates suggests that nucleation of aragonite takes place only in the presence of dissolved sulfate. The presence of calcite seed material in overgrowth experiments generally assures that the precipitating mineral phase is the same to that of the seed (Lin and Singer, 2005). According to classical terrace-ledge-kink (TLK) model of crystal growth (Burton et al., 1951; Chernov, 1984) that assumes an ion-by-ion attachment of solutes to the step edges of mineral surfaces, the molecular level of recognition of the seed surface (Stumm and Morgan, 1996) is one of the critical requirements of crystal overgrowth. Active blocking of growth sites on the growing calcite crystal results in excess of free ions in the reactive solution that augments its saturation with respect to all $CaCO_3$ polymorphs that have the potential to nucleate in the fluid phase. For example, increasing Mg/Ca ratios induce a mineralogical change in precipitates formed from seawater at 25 °C, causing aragonite to precipitate instead of

29

calcite at aqueous Mg/Ca ratios higher than ~ 1 mol/mol (Morse et al., 1997). Note here that the formation of aragonite in the present study cannot be solely attributed to calcite inhibition due to the prevailing aqueous Mg^{2+}/Ca^{2+} ratio (Lippmann, 1973; Berner, 1975; Reddy and Wang, 1980). Evidence for this comes from the fact that similar aqueous Mg^{2+}/Ca^{2+} ratios at chemical steady-state are met in all the experimental runs (0.3 < Mg^{2+}/Ca^{2+} < 0.6). Accordingly, the nucleation of aragonite can be attributed to the presence of dissolved sulfate in the reactive solution (Fig. 5). It is worth noting that aragonite was only observed at growth rates $\geq 10^{-7.4}$ mol m^{-2} s^{-1} and sulfate concentrations ≥ 20 mM as well as only above a certain degree of supersaturation of the reactive solution with respect to this mineral phase. This suggests that aragonite nucleation can occur only when $SI_{aragonite}$ overcomes a certain threshold value, here $SI_{aragonite}$ > 0.4, which reflects the energy barrier for nucleation at the prevailing conditions (De Yoreo and Vekilov, 2003). The increasing saturation state with respect to aragonite as a function of aqueous SO_4 concentration (Fig. 5) may be explained by adsorption phenomena on the calcite crystal surfaces. There is strong evidence that calcite growth is inhibited by adsorption of Mg^{2+} and SO_4^{2-} ions at calcite growth sites (Lin and Singer, 2009; Nielsen et al., 2016). Similarly, the porous calcite surface that can be seen in Fig. 2B, is indicative of the active blocking of calcite growth sites in the presence of sulfate, e.g. by either aqueous SO_4^{2-} or $CaSO_4^0$ and $MgSO_4^0$ aquo-complexes. This blocking of active surface sites for calcite growth was also observed in the presence of aqueous phosphate ions, where crystallization of calcite was retarded due to adsorption phenomena and/or $CaPO_4^0$ aquo-complex formation (Katsifaras and Spanos, 1999). As soon as growth positions at the crystal surface are occupied or disturbed, e.g. by adsorption of foreign ions, new molecules cannot adapt at the surface (Reddy and Wang, 1980; Meyer, 1984). More specifically the inhibition effect of magnesium and sulfate ions follows the order SO_4^{2-} < Mg^{2+} < $MgSO_4^0$ as it has been recently suggested by Nielsen et al. (2016).
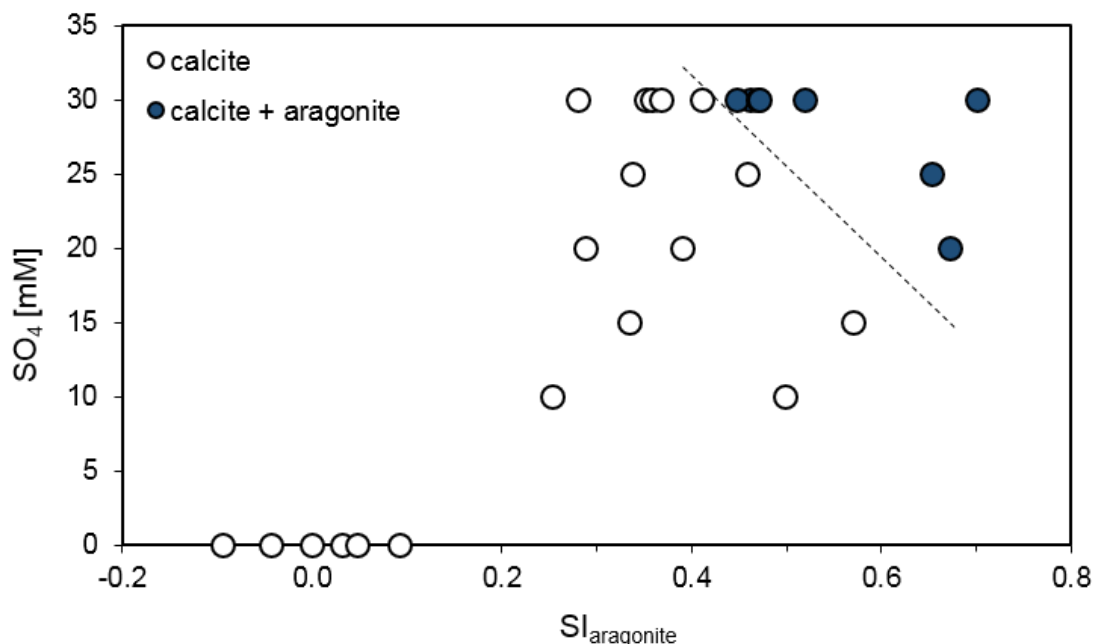
Fig. 5: Saturation index (SI) of aragonite plotted as a function of sulfate concentration in the reactive solution. Aragonite precipitation occurs only in the presence of sulfate (SO_4 conc. in solution $\geq$ 20 mM) and at elevated saturation degrees ($SI_{aragonite} > 0.4$; corresponding to $SI_{calcite} > 0.6$).

Adsorption and incorporation of impurities during mineral growth can cause a change of the calcite crystal morphology (Zhang and Dawe, 2000). Indeed, the SEM images of calcite recorded at the end of the experimental runs show a modification in the crystal surface of the overgrowths compared to the calcite seed material (Fig. 2). The highly porous surface, which was observed on calcite precipitates conducted at low growth rates and in the presence of 30 mM sulfate in the reactive solution, suggests that adsorption of foreign molecules occurs on distinct crystal growth sites. The adsorbed molecules may disturb the growth mechanism creating a porous crystal surface (see Fig. 2B). Also the incorporation of Mg in the calcite overgrowth could be responsible for a change in the morphology due to the difference in the ionic radii of Mg and Ca that are 0.72 Å and 1.0 Å, respectively, though calcite collected from experiments conducted in the absence of sulfate exhibit smooth surfaces.

Another observation was a differing calcite crystal shape in experiments conducted at high growth rates. At high growth rates, dog-tooth (scalenohedral) shapes of the calcite crystals were observed (see Fig. 2C), whereas at low growth rates the rhombohedral shape of the seed material was maintained (see Fig. 2B). Note here that, within the context of

this study, differences in the incorporation of Mg in calcite that can be attributed to preferential attachment of Mg^{2+}(aq) ions to different calcite surfaces (Paquette and Reeder, 1995) were not observed. Indeed, as can be seen in Fig. 4, D_{Mg} exhibits a continuous, linear correlation to growth rate, while an abrupt transition from rhombohedral to scalenohedral shape was observed (Fig. 2). If enhanced Mg uptake occurred by scalenohedral calcite versus rhombohedral calcite, the correlation of D_{Mg} with growth rate would not be continuous. Calcite is known to show variable habitus, where a scalenohedral habitus is obtained e.g. by adding an impurity component in the precipitating solution (Sunagawa, 2005). In our study the habitus is obviously changing with growth rates and consequently higher supersaturation in respect to calcite. There was no change observed in habitus between seed and precipitate in experiments conducted at low growth rates, but with the same concentrations of impurities (Mg and SO_4) in the reactive solution.

2.4.2 Coupled effect of sulfate and precipitation rate on Mg partitioning in calcite

As it is illustrated in Fig. 4, D_{Mg} values of calcite are affected by both mineral growth rate and the presence of dissolved sulfate in the reactive solution. In detail a ~2-fold increase of calcite $\log(r_p)$ induces a ~1-fold increase in $\log(D_{Mg})$ value. Overall the D_{Mg} values obtained in the present study (i.e. $0.01 \leq D_{Mg} \leq 0.04$) lay within the range of available experimental data for calcite at 25 °C (Oomori et al., 1987; Mucci, 1987; Howson et al., 1987; Burton and Walter, 1991; Hartley and Mucci, 1996; Huang and Fairchild, 2001). This behavior is in excellent agreement with the general behavior of divalent cation incorporation in calcium carbonate as a function of precipitation rate as it has been earlier shown in the literature (e.g. Lorens, 1981; Mucci and Morse, 1983; Tesoriero and Pankow, 1996; Huang and Fairchild, 2001; Tang et al., 2008; Mavromatis et al., 2013; 2018; Gabitov et al., 2014). This is because at higher growth rates there is less discrimination in respect to elemental uptake and the composition of the forming solid tends to become similar to that of the solution, resulting in a general increase or decrease in D values (Rimstid et al., 1998). Note here that the slope of eq. 6 that describes the dependence of D_{Mg} on growth rate is somewhat higher than that previously defined by Mavromatis et al. (2013). We attribute this small difference in variations between the experimental set-up used. Those include varying Mg concentration and background electrolyte concentrations (i.e. NaCl) in the experiments conducted by Mavromatis et al. (2013). However, both studies exhibit a positive increase of D_{Mg} as a function of growth

rate. Overall, the observed enrichment of the trace element concentration in calcite as a function of mineral growth rate can be explained by the growth entrapment model (GEM) developed by Watson and Liang (1995). According to this model the incorporation of Mg into calcite depends on the crystal growth kinetics and the ion diffusion behavior within a reactive surface layer in the vicinity of the growing crystal. As it has been suggested by Watson (1996; 2004) the incorporation of traces into calcite is dependent on the enrichment or depletion of impurities in the distorted and hydrated thin layer present at the crystal surface. The entrapment of Mg will be favored as soon as Mg^{2+} is enriched in the surface layer and precipitation takes place at rapid growth rates, which is increasing the diffusion distance.

As it is depicted in Fig. 6, however, in the absence of growth rate effects, Mg partitioning in the forming calcite is affected by the presence of dissolved sulfate. Although the growth rate dependence is similar in the presence and absence of sulfate, as it is suggested by the almost parallel slopes in Fig. 6A, the Mg/Ca ratio of calcite formed in the presence of sulfate exhibits an overall offset (32-50 % less) which lays highly above the analytical uncertainty of the measurements. The observed offset at 30 mM sulfate concentration corresponds to 45-50 % less Mg incorporation (Fig. 6B) in calcite and which reflects D_{Mg} values that are 31-35 % lower than in the absence of sulfate. This finding is in good agreement with that of Mucci et al. (1989), who examined the influence of dissolved SO_4^{2-} ions on the amount of Mg^{2+} incorporated in high-Mg calcite overgrowths in artificial seawater solutions at 25 °C. These authors reported that the Mg distribution coefficient of calcite precipitated from seawater (~ 28 mM SO_4) was 34 % lower than precipitated from sulfate-free seawater. They did not however present detailed information for the changes in the calcite crystal lattice due to incorporation of Mg^{2+} and SO_4^{2-} ions. In order to shed light on the limiting effects of sulfate on Mg incorporation in calcite we discuss in the following section the effects of (i) sulfate complex formation in aqueous solution and adsorption on active growth sites, and (ii) sulfate incorporation on calcite lattice parameters.
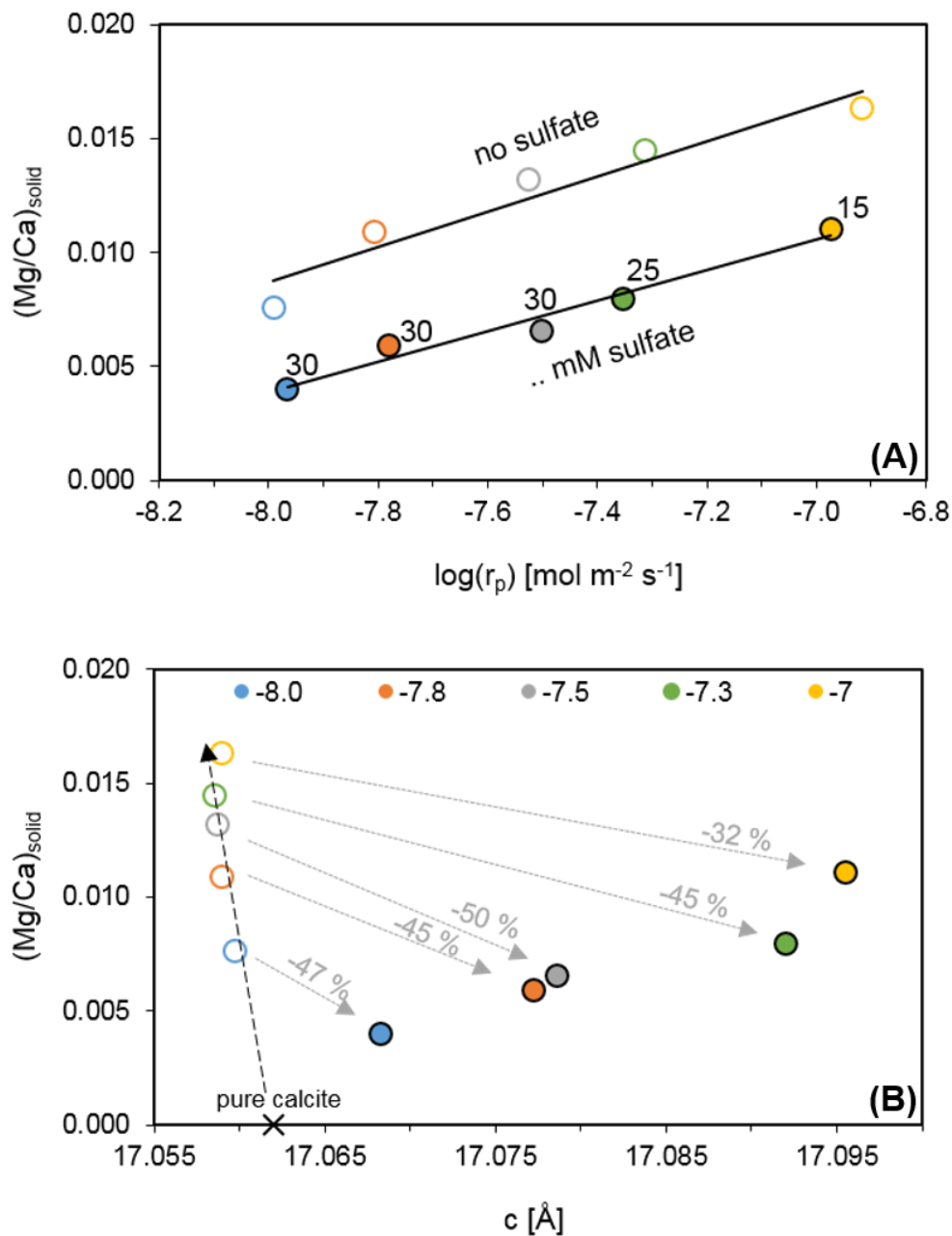
Fig. 6: Comparison of selected experiments in the presence (closed circles) and absence (open circles) of sulfate at similar growth rates. Note here that this figure includes only experiments in which calcite was the only phase formed. (A) Mg/Ca ratio of calcite as a function of growth rate. The numbers next to the closed circles represent the sulfate concentration in the reactive solution. (B) Mg/Ca ratio of calcite as a function of calcite c-axis, where the expansion of c-axis shows a positive correlation with the sulfate content in calcite. The colors denote the distinct precipitation rates $\log(r_p)$ from -8 to -7 (r_p in mol m^2 s^{-1}), where the unit cell dimension of the calcite c-axes shifts to lower values at elevated incorporation of Mg (corresponding to higher calcite precipitation rates; see dashed black arrow). Percent values are referring to the decrease of Mg vs. Ca incorporation into calcite caused by the presence of sulfate in calcite (corresponding to the expansion of c-axis; dotted gray arrows and closed circles).

34

The partitioning coefficient, D_{Mg}, is related to the molar concentrations of free ions, i.e. Ca^{2+} and Mg^{2+}, which are considered to be incorporated in the newly growing crystal. The presence of an aqueous ligand, however, can reduce the availability of free aqueous ions via the formation of metal-ligand aquo-complexes, a process that has to be taken into account during the calculation of the D value. Speciation calculations revealed that at the highest sulfate concentration of 30 mM in the reactive solution the SO_4 aquo-complexes for Ca and Mg account for up to 20 and 17 % of their total concentrations, respectively. Due to higher abundance of $CaSO_4^0(aq)$ compared to $MgSO_4^0(aq)$ complexes, the free Mg^{2+}/Ca^{2+} ratio in the aqueous solution is slightly higher compared to the ratio of the total concentrations (i.e. Mg/Ca). A comparison of the aqueous Mg^{2+}/Ca^{2+} ratios in the presence and absence of sulfate yields slightly lower Mg^{2+}/Ca^{2+} ratio in the presence of sulfate. This can be explained by two processes. First, the observed behavior can be attributed to the fact that Mg concentration is constant in all experiments but Ca concentration is variable among the experimental runs and controlled by the concentration of the inlet solution. Moreover, the presence of sulfate leads to formation of $CaSO_4^0$ complexes which provokes an overall increase of the total Ca concentration at steady-state conditions. Secondly, the adsorption of sulfate or sulfate-bearing complexes on the crystal surface reduces the amount of active growth sites and induces an increase of aqueous Ca^{2+} concentrations similar to that what was observed by Mavromatis et al. (2017) in the presence of organic ligands. These investigators suggest that the adsorption of organic ligands on the calcite surfaces is resulting in less sites for ongoing mineral growth and an excess of Ca in the solution. Nevertheless, the marginal variations in Mg^{2+}/Ca^{2+} ratio of the reactive solution cannot be considered as a parameter to explain the decreasing Mg partitioning in calcite with increased sulfate concentrations, but a different mechanism has to be the controlling factor. Thus, the lower D_{Mg} values of calcite induced in the presence of sulfate are likely caused by processes occurring on or near the surface of the growing crystal. We consider here that the adsorption of the rather big sulfate ions or sulfate-bearing complexes on calcite growth steps may disturb the Mg uptake by temporary blocking the growth sites. Indeed, the formation of a competitive surface-complex at the calcite surface, occurring as either charged or uncharged SO_4 species, might contribute to the decreased Mg incorporation during calcite growth in the presence of sulfate, found in this study.
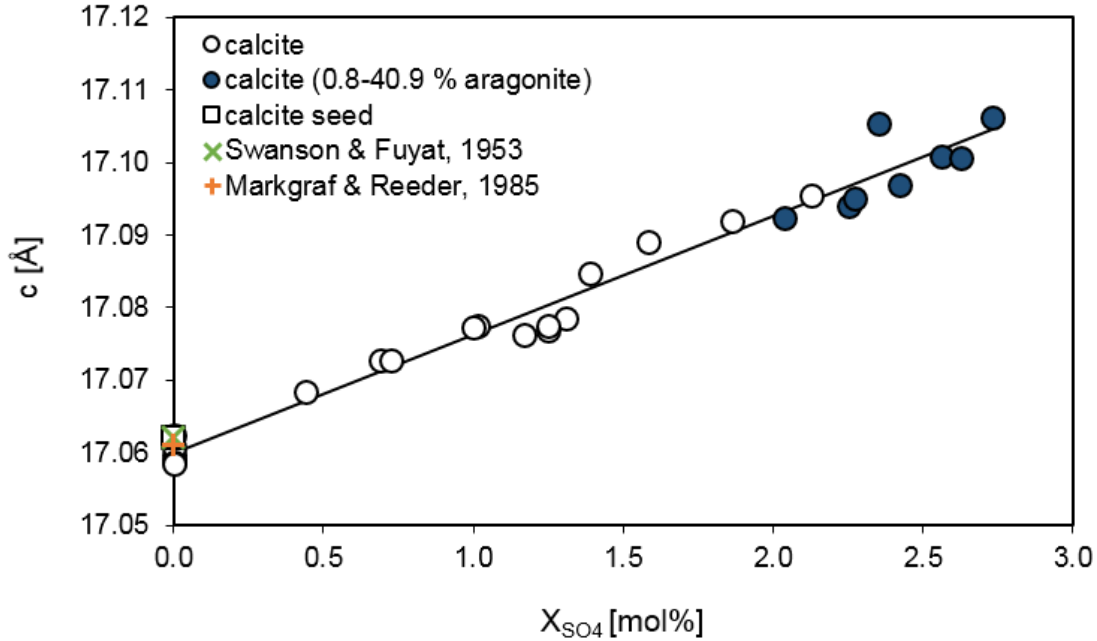
Fig. 7: Unit cell dimension of the calcite c-axes plotted as a function of sulfate content. The increase of the c-axis with increasing sulfate content in calcite can be described by the linear function $c[\text{Å}] = 0.0163 \times X_{SO4} + 17.062$; $R^2 = 0.98$.

The growth of calcite in the presence of dissolved sulfate, however, is accompanied by the incorporation of this ion in the newly forming solid. Indeed, the chemical composition of the solid material reveals that also sulfate is present in the precipitated solids (see Table 1). Precipitates, which contain sulfate, show an anisotropic change in the calcite unit cell parameters, where the largest increase along the c-axis was +0.25 % compared to the calcite seed material (c = 17.062 Å) which can be parameterized according to the equation

$$c[\text{Å}] = 0.0163 \times X_{SO4} + 17.062; \quad R^2 = 0.98 \tag{8}$$

where X_{SO_4} is the concentration of SO_4 in the precipitate expressed in mol% (see Fig. 7). A similar increase of the c-axis has been observed by Bots et al. (2011), who nucleated calcite in the presence of sulfate. The increasing length of the c-axis is the result of the replacement of the planar trigonal CO_3 ion by the tetrahedral SO_4 ion (Kontrec et al., 2004) in the crystal lattice. In contrast the low-Mg calcites precipitated in the absence of sulfate in this study show a minor decrease of the c-axis (-0.02 %) compared to the pure

36

calcite seed material (see Fig. 6B). This decrease can be well explained by the ideal substitution of the small Mg ion (i.e. 0.72 Å) in the site of the hexa-coordinated Ca ion (i.e. 1.0 Å) in calcite that is accompanied by a reduction in the mean Mg-O bond length in the crystal lattice. This observation is in good agreement with the unit cell contraction expected in calcite with increased Mg content (Paquette and Reeder, 1990). From the obtained results it can be deduced that an increase of the c-axis in the calcite lattice that is controlled by the presence of sulfate ions (Fig. 7) effectively restricts the D_{Mg} of calcite (Fig. 8). The coupled effect of (i) sulfate uptake during calcite growth and (ii) precipitation rate on D_{Mg} can be quantified by the equation

$$D_{Mg} = 0.03726 - 0.02345 \times \left[-log(r_p) - 7 \right] - X_{SO4} \times \left\{ 0.004607 + 0.002109 \times \left[-log(r_p) - 7 \right] \right\} \qquad (9)$$

where growth rate takes values in the range $-8 \leq log(r_p) \leq -7$ and sulfate content takes value in the range $0 \leq Xso_4 \leq 2.6$. In this approach the aberrations of the D_{Mg} trend on SO_4 incorporation into calcite at $r_p = 10^{-7}$ mol m^{-2} s^{-1} (as a basic value for (-log(r_p) - 7)) is caused by differences of precipitation rate. Least squares method (solver code; Excel) was used to fit the above equation on data shown in Fig. 8. In this equation the D_{Mg} values are ranging from 0.009 ±0.001 at low precipitation rate (log(r_p) = -8) and Xso_4 = 0.4 mol% up to 0.037 ±0.003 at elevated precipitation rate (log(r_p) = -7) and no sulfate. The restriction of D_{Mg} in the presence of sulfate is because sulfate - when incorporated in the crystal lattice - results in a significant expansion of calcite unit cell which requires an increase in the mean Mg-O bond length in the solid in order to allow Mg to be present. Thus, the increase in the unit cell along the c-axis and consequently in the mean Mg-O bond length likely makes the presence of Mg in calcite less favorable. Actually, a comparison of calcite formed at similar growth rates in the presence and absence of dissolved sulfate (Fig. 6), reveals that the Mg content of calcite is significantly lower in the presence of sulfate. More precisely, the Mg content of the solids decreases by as much as 50 % as it can be seen in Fig. 6B by the provoked unit cell expansion along the c-axis which is strongly correlated with sulfate content in calcite.
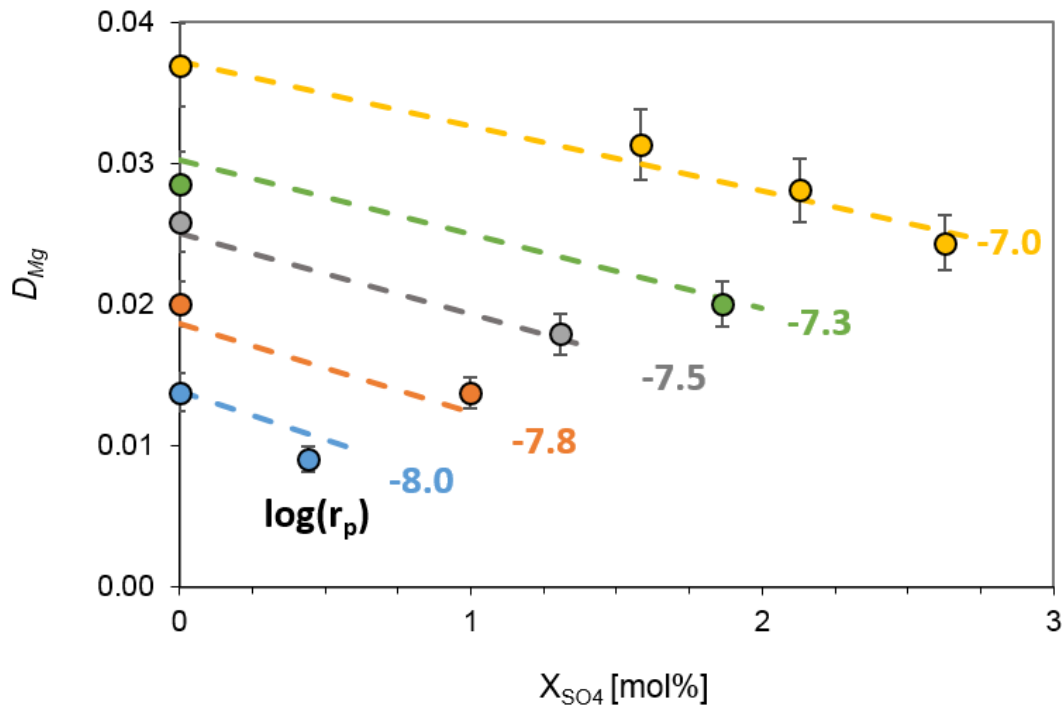
Fig. 8: The distribution coefficient of Mg^{2+} between low-Mg calcite and the precipitating solution as a function of sulfate concentration at distinct precipitation rates ($log(r_p)$) can be described by the function $D_{Mg} = 0.03726 - 0.02345 \times [-log(r_p) - 7] - X_{SO4} \times \{0.004607 + 0.002109 \times [-log(r_p) - 7]\}$, where $log(r_p)$ is given in mol m^2 s^{-1} and X_{SO4} is given in mol%. In the presence of 30 mM sulfate which is the concentration similar to seawater the D_{Mg} value decreased by 31-35%.

2.4.3 Implications for natural systems

Sulfate is the second most concentrated anion in modern seawater and commonly present in marine mineralization environments. During the Phanerozoic the sulfate concentration of seawater was fluctuating between ~5 and ~30 mM (Horita et al., 2002; Lowenstein et al., 2003). Bots et al. (2011) suggested that this change in sulfate concentration controlled the primary marine calcium carbonate polymorph. These authors claimed that an increase in dissolved sulfate decreases the Mg/Ca ratio at which calcite is destabilized and aragonite becomes the dominant $CaCO_3$ polymorph. Moreover, previous studies noted that dissolved sulfate favors aragonite precipitation by selectively inhibiting calcite precipitation (Kitano et al., 1975; Walter, 1986), and Busenberg and Plummer (1985) observed that calcite solubility increases and is the same as that of aragonite if calcite contains more than ~3 mol% SO_4. Note here that the incorporation of SO_4 into aragonite is less favored than into calcite (Fernández-Díaz et al., 2010; Kartnaller

et al., 2018). From the results of the present study it can be concluded that the destabilization of calcite induced by the incorporation of SO_4 is strongly controlled by growth rate. This is supported by the pronounced correlation of calcite unit cell expansion with sulfate content (Fig. 7). The obtained results, however, clearly show that the formation of aragonite cannot be solely attributed to the presence of sulfate. Indeed, precipitation of aragonite does not occur at low growth rates, although the sulfate concentration of the reactive solution was the same as in experiments conducted at high growth rates. As such the obtained results suggest that both the concentration of Mg and SO_4 and their inhibiting effect on calcite growth likely control the calcium carbonate polymorph formed in marine environments over the geological past.

Another finding of this study is that the D_{Mg} values of growing low-Mg calcite can be restricted significantly by the presence of sulfate, in agreement with the earlier findings by Mucci et al. (1989), who studied the effect of sulfate during the formation of high-Mg calcite. The novelty of our findings is the anticorrelation between D_{Mg} and sulfate content (X_{SO_4}) in low-Mg calcite. This effect can be explained by the anisotropic elongation of the calcite unit cell that is increasing with increasing sulfate content. This observation may shed light on our understanding of the parameters controlling biomineralisation processes as well as abiotically formed calcium carbonates. Furthermore it implies that the validity of D_{Mg} for the reconstruction of the physicochemical conditions during calcite growth in natural settings (e.g. growth rate, temperature, etc.) likely requires re-evaluation. This holds specially true for low-Mg calcites which are generally assumed to be good carbonate archives and have the potential to preserve their primary geochemistry throughout geological time (Veizer et al., 1999). For example the sulfate content of low-Mg calcites (< 2 mol% $MgCO_3$) of biogenic origin, range from 0.1 to 2.5 mol% SO_4 as it can be seen in Fig. 9 for 5 selected organisms (see Table A2) and lays within the range of sulfate content of synthetic calcites examined in this study. Actually the application of the results of the present work to natural abiotic low-Mg calcites is straightforward because the range of mineral growth rates studied herein overlap with most calcite precipitation rates measured in various natural environments. For example the net growth rates of carbonate mud banks in Florida Bay range from $10^{-9.0}$ to $10^{-6.5}$ mol m^{-2} s^{-1} (Yates and Halley, 2006). In contrast biogenic carbonates exhibit growth rates in the order of 10^{-7} mol m^{-2} s^{-1} (Gussone et al., 2005) or higher (e.g. $10^{-6.0}$-$10^{-4.0}$ mol m^{-2} s^{-1}; Peck et al., 1997; Hippler et al., 2009; Lorrain et al., 2015). As such further experimental work
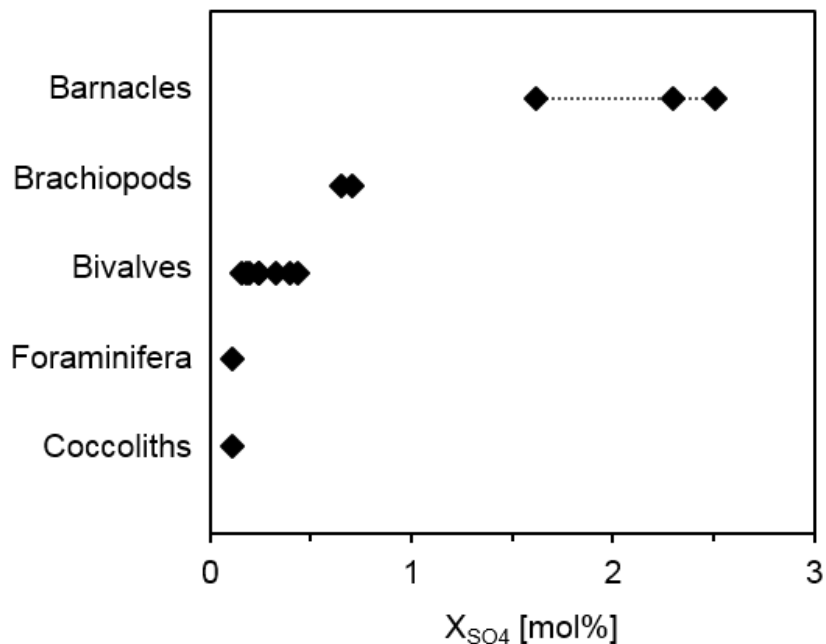
Fig. 9: Average sulfate content of biogenic low-Mg calcites (< 2 mol% MgCO$_3$: Millimann, 1974; Busenberg and Plummer, 1985; Foster and Chacko, 1995; Brand et al., 2015) of marine organisms. Data from species of Brachiopods (*Magellania fragilis, Liothyrella uva*) and Bivalves (*Mytilus edulis, Pinna fragilis, Patella vulgata*) derived from Kampschulte et al. (2001); Data from species of Barnacles (*Balanus sp., Balanus balanoidesi*), Bivalves (*Lyropecten nodasus, Crassostrea virginica*), Foraminifera (*Globigerina sp.*) and Coocoliths derived from Busenberg and Plummer (1985). The plotted values are listed in Table A2 (supplementary material).

at higher calcite growth rates is required. However, we note that in the case of biomineralization vital effects have to be taken under consideration as well. Moreover the used concentration of SO$_4$ (30 mM) in the reactive solution represents the prevailing concentration of sulfate in present seawater which is about 2700 mg L^{-1} (~ 28 mM). With increasing depth in marine sediments the concentration of SO$_4$ is commonly decreasing due to microbial respiration processes (Canfield et al., 2005). As soon as sediment is settled on the seafloor and early burial proceeds, anaerobic oxidation of methane (AOM) and bacterial sulfate reduction takes place. With ongoing sulfate reduction, alkalinity is increasing in the pore solutions and precipitation of carbonate minerals takes place (Berner et al., 1970; Raiswell and Fisher, 2004). Therefore the experiments conducted at lower sulfate concentrations (25 mM, 20 mM, 15 mM and 10 mM) compared to seawater (~28 mM) provide insights on the effect of sulfate on Mg partitioning in calcite formed in burial marine environments (or for different sea water composition in the past). The

effect of sulfate on the polymorph selection and D_{Mg} of calcite is reduced at lower sulfate concentrations as the formation of sulfate-bearing complexes and consequently the poisoning of crystal growth sites is becoming less important. Overall the incorporation of sulfate in calcite is reduced at lower sulfate concentrations in the reactive solution.

2.5 Conclusions

The experimental results of this study show that mineral growth rate is strongly controlling the incorporation of Mg^{2+} and SO_4^{2-} in calcite. The presence of aqueous sulfate in the growth media can act as an inhibitor of calcite growth and thus promoting aragonite formation. The formation of thermodynamically less stable aragonite instead of the more stable calcite may be explained by adsorption phenomena on the growing crystal surface as calcite growth is inhibited by the adsorption of Mg^{2+} and SO_4^{2-} ions or their aquo-complexes at active growth sites. The formation of aragonite in the present study is strongly dependent on the sulfate concentration of the reactive solution and its degree of supersaturation in respect to aragonite.

An important result of this study is that the presence of dissolved sulfate significantly decreases Mg partitioning between the reactive solution and low-Mg calcite which can be described by two processes. First, the lower D_{Mg} values of calcite formed in the presence of dissolved sulfate are likely caused by the adsorption of sulfate ions or sulfate-bearing complexes on the calcite surface which may be responsible for temporary blocking of active growth sites and are therefore disturbing Mg uptake. Secondly, the uptake of sulfate in the newly growing calcite is causing an anisotropic change of the calcite unit cell parameters. From the obtained results we deduce that an elongation of the c-axis which is linearly correlated with the sulfate content of the solid restricts effectively the presence of Mg in calcite. The incorporation of the tetrahedral sulfate ion results in a significant expansion of the calcite unit cell which makes the presence of Mg in calcite less favorable. As the incorporation of traces like Mg^{2+} and SO_4^{2-} in calcite results in an opposite effect on the crystal lattice dimensions by either shrinking or expanding the unit cell, an anticorrelation of their concentrations in the solid phase can be expected. These observations improve our understanding of the parameters controlling elemental uptake during biomineralisation processes as well as abiotically formed calcium carbonates in the presence of dissolved sulfate.

2.6 Supplementary material

Table A1: Total concentrations of Ca, Mg and alkalinity in the reactive solution at chemical steady-state conditions and distribution of aqueous Ca and Mg species (calculated using PHREEQC with its minteq.v4 database).

Experiment	Conc. at chem. steady–state			Ca(aq) and Mg(aq) species									
	Ca TOTAL	Mg TOTAL	Alkalinity	Ca^{+2}	$CaCO_3^0$	$CaHCO_3^+$	$CaOH^+$	$CaSO_4^0$	Mg^{+2}	$MgCO_3^0$	$MgHCO_3^+$	$MgOH^+$	$MgSO_4^0$
	(mM)	(mM)	(mM)	(mM)	(mM)	(mM)	(mM)	(mM)	(mM)	(mM)	(mM)	(mM)	(mM)
MgS2	23.87	9.55	36.91	16.62	1.8E-02	2.63	3.2E-06	4.60	7.26	4.1E-03	0.69	2.7E-05	1.60
MgS3	23.76	7.93	38.62	16.42	1.8E-02	2.73	3.1E-06	4.59	6.00	3.5E-03	0.59	2.2E-05	1.33
MgS4	23.39	8.62	42.96	15.95	2.3E-02	2.95	3.5E-06	4.47	6.46	4.9E-03	0.71	2.8E-05	1.44
MgS5	24.78	8.97	41.98	16.99	2.2E-02	3.06	3.5E-06	4.71	6.75	4.6E-03	0.73	2.7E-05	1.49
MgS6	29.07	9.66	42.69	20.04	2.6E-02	3.62	4.2E-06	5.38	7.31	5.0E-03	0.79	3.0E-05	1.56
MgS8	26.24	9.19	39.70	18.17	2.3E-02	3.08	3.9E-06	4.97	6.97	4.7E-03	0.70	3.0E-05	1.51
MgS9	18.73	9.96	23.14	17.05	7.2E-03	1.68	2.1E-06	-	9.40	2.1E-03	0.55	2.2E-05	-
MgS10	22.82	8.77	25.25	20.62	9.8E-03	2.19	2.6E-06	-	8.25	2.1E-03	0.52	2.1E-05	-
MgS11	22.02	9.73	34.03	17.82	1.4E-02	2.58	2.8E-06	1.61	8.40	3.5E-03	0.72	2.6E-05	0.60
MgS12	25.74	9.35	42.14	20.31	2.5E-02	3.61	4.0E-06	1.80	7.94	5.1E-03	0.84	3.1E-05	0.56
MgS13	26.84	10.13	36.33	20.88	1.7E-02	3.19	3.2E-06	2.75	8.47	3.7E-03	0.77	2.6E-05	0.89
MgS14	24.80	8.95	46.94	18.55	2.9E-02	3.70	4.2E-06	2.52	7.29	6.1E-03	0.87	3.3E-05	0.79
MgS15	24.54	9.56	40.90	18.09	1.9E-02	3.15	3.2E-06	3.28	7.66	4.3E-03	0.80	2.6E-05	1.10
MgS16	34.58	9.66	46.93	25.30	3.7E-02	4.92	5.5E-06	4.32	7.71	6.0E-03	0.90	3.3E-05	1.05
MgS17	25.56	9.86	37.32	18.45	1.7E-02	2.93	3.1E-06	4.17	7.74	3.8E-03	0.73	2.6E-05	1.39
MgS18	25.55	9.45	54.79	17.43	3.6E-02	4.08	4.3E-06	4.00	7.14	7.7E-03	1.00	3.5E-05	1.30
MgS19	26.66	10.16	40.90	18.43	1.9E-02	3.21	3.0E-06	5.01	7.70	4.1E-03	0.80	2.5E-05	1.66
MgS20	32.05	9.91	51.39	21.61	4.0E-02	4.67	5.3E-06	5.73	7.39	7.1E-03	0.95	3.5E-05	1.56
MgS22	20.97	9.04	25.04	14.74	1.0E-02	2.07	2.0E-06	4.15	6.91	2.5E-03	0.58	1.8E-05	1.55
MgS23	16.47	9.02	40.51	14.87	6.4E-03	1.60	1.7E-06	-	8.48	1.9E-03	0.54	1.9E-05	-
MgS24	21.81	8.88	28.25	14.95	1.5E-02	2.62	2.5E-06	4.22	6.68	3.5E-03	0.70	2.2E-05	1.50
MgS25	18.04	9.36	43.79	16.09	7.9E-03	1.94	1.9E-06	-	8.73	2.3E-03	0.63	2.0E-05	-
MgS26	24.06	9.37	27.56	16.40	2.0E-02	3.09	3.1E-06	4.56	7.02	4.6E-03	0.79	2.6E-05	1.55
MgS27	19.47	9.54	44.13	17.42	8.5E-03	2.04	2.1E-06	-	8.91	2.3E-03	0.62	2.1E-05	-
MgS28	26.37	9.88	27.84	18.03	2.4E-02	3.39	3.6E-06	4.93	7.42	5.1E-03	0.83	2.9E-05	1.61
MgS29	19.05	9.24	44.00	17.02	8.8E-03	2.02	2.1E-06	-	8.63	2.4E-03	0.61	2.1E-05	-
MgS30	26.07	9.48	37.12	18.42	2.3E-02	3.45	3.5E-06	4.18	7.33	4.8E-03	0.82	2.7E-05	1.32

Table A2: Sulfate and magnesium concentrations in mol% of selected biogenic calcites. X_{SO4} and X_{Mg} refer to the calcitic part of the shell.

organism	species	X_{SO4} [mol%]*	X_{Mg} [mol%]	Mineralogy	Ref.
Barnacles	*Balanus sp.*	2.5	1.7	calcite	Busenberg and Plummer, 1985
	Balanus sp.	1.6	<2	calcite	Busenberg and Plummer, 1985
	Balanus balanoidesi	2.3	<2	calcite	Busenberg and Plummer, 1985
Brachiopods	*Magellania fragilis*	0.7	0.8 - 1.4 *	calcite	Kampschulte et al., 2001; Brand et al., 2015
	Liothyrella uva	0.7	0.6 - 1.1*	calcite	Kampschulte et al., 2001; Brand et al., 2015
Bivalves	*Mytilus edulis*	0.2	0.2	calcite, aragonite	Kampschulte et al., 2001; Millimann, 1974
	Mytilus edulis	0.2	0.2	calcite, aragonite	Kampschulte et al., 2001; Millimann, 1974
	Pinna fragilis	0.2	0.2	calcite, aragonite	Kampschulte et al., 2001; Millimann, 1974
	Patella vulgata	0.3	1.2 - 1.8*	calcite, aragonite	Kampschulte et al., 2001; Foster and Chacko, 1995
	Patella vulgata	0.4	1.2 - 1.8*	calcite, aragonite	Kampschulte et al., 2001; Foster and Chacko, 1995
	Patella vulgata	0.4	1.2 - 1.8*	calcite, aragonite	Kampschulte et al., 2001; Foster and Chacko, 1995
	Lyropecten nodasus	0.2	0.2	calcite	Busenberg and Plummer, 1985
	Crassostrea virginica	0.2	0.9	calcite	Busenberg and Plummer, 1985
Foraminifera	*Globigerina sp.* (planktonic)	0.1	<1	calcite	Busenberg and Plummer, 1985
Coccoliths		0.1	0.5	calcite	Busenberg and Plummer, 1985

* converted from ppm assuming ideal calcite composition

References

Arroyo-De Dompablo M. E., Fernández-González M. A. and Fernández-Díaz L. (2015) Computational investigation of the influence of tetrahedral oxoanions (sulphate, selenate and chromate) on the stability of calcium carbonate polymorphs. *RSC Adv.* **5**, 59845–59852.

Balan E., Blanchard M., Pinilla C. and Lazzeri M. (2014) First-principles modeling of sulfate incorporation and $^{34}S/^{32}S$ isotopic fractionation in different calcium carbonates. *Chem. Geol.* **374–375**, 84–91.

Balan E., Noireaux J., Mavromatis V., Saldi G. D., Montouillout V., Blanchard M., Pietrucci F., Gervais C., Rustad J. R., Schott J. and Gaillardet J. (2018) Theoretical isotopic fractionation between structural boron in carbonates and aqueous boric acid and borate ion. *Geochim. Cosmochim. Acta* **222**, 117–129.

Balan E., Pietrucci F., Gervais C., Blanchard M., Schott J. and Gaillardet J. (2016) First-principles study of boron speciation in calcite and aragonite. *Geochim. Cosmochim. Acta* **193**, 119–131.

Berner R. A. (1975) The role of magnesium in the crystal growth of calcite and aragonite from sea water. *Geochim. Cosmochim. Acta* **39**, 489–504.

Berner R. A., Scott M. R. and Thomlinson C. (1970) Carbonate alkalinity in the pore waters of anoxic marine sediments. *Limnol. Oceanogr.* **15**, 544–549.

Bots P., Benning L. G., Rickaby R. E. M. and Shaw S. (2011) The role of SO_4 in the switch from calcite to aragonite seas. *Geology* **39**, 331–334.

Böttcher M. E. and Dietzel M. (2010) Metal-ion partitioning during low-temperature precipitation and dissolution of anhydrous carbonates and sulphates. *EMU notes Mineral.* **10**, 139–187.

Brand U., Azmy K., Griesshaber E., Bitner M. A., Logan A., Zuschin M., Ruggiero E. and Colin P. L. (2015) Carbon isotope composition in modern brachiopod calcite: A case of equilibrium with seawater? *Chem. Geol.* **411**, 81–96.

Burdett, J.W., Arthur, M.A., Richardson, M., 1989. A Neogene seawater sulfur isotope age curve from calcareous pelagic microfossils. *Earth Planet. Sci. Lett.* **94**, 189–198.

Burton E. A. and Walter L. M. (1991) The effects of pCO_2 and temperature on magnesium incorporation in calcite in seawater and $MgCl_2$-$CaCl_2$ solutions. *Geochim. Cosmochim. Acta* **55**, 777–785.

Burton W. K., Cabrera N. and Frank F. C. (1951) The Growth of Crystals and the Equilibrium Structure of their Surfaces. *Phil. Trans. R. Soc. Lond.* **243**, 299–358.

Busenberg E. and Plummer L. N. (1985) Kinetic and thermodynamic factors controlling the distribution of SO_4^{2-} and Na^+ in calcites and selected aragonites. *Geochim. Cosmochim. Acta* **49**, 713–725.

Busenberg E. and Plummer N. L. (1989) Thermodynamics of magnesian calcite solid-solutions at 25°C and 1 atm total pressure. *Geochim. Cosmochim. Acta* **53**, 1189–1208.

Canfield D. E., Kristensen E. and Thamdrup B. (2005) Heterotrophic Carbon Metabolism. *Adv. Mar. Biol.* **48**, 129–162.

Chernov A. A. (1984) Modern Crystallography III., Springer-Verlag.

De Villiers J. P. R. (1971) Crystal structures of aragonite, strontianite, and witherite. *Am. Mineral.* **56**, 758–767.

De Yoreo J. J. and Vekilov P. G. (2003) Principles of Crystal Nucleation and Growth. *Rev. Mineral. Geochemistry* **54**, 57–93.

Dietzel M. (2011) Carbonates. *Encycl. Geobiol.*, 261–266.

Elderfield H. and Ganssen G. (2000) Past temperature and $\delta^{18}O$ of surface ocean waters inferred from foraminiferal Mg/Ca ratios. *Nature* **405**, 442–445.

Fernández-Díaz L., Fernández-González Á. and Prieto M. (2010) The role of sulfate groups in controlling $CaCO_3$ polymorphism. *Geochim. Cosmochim. Acta* **74**, 6064–6076.

Fichtner V., Strauss H., Immenhauser A., Buhl D., Neuser R. D. and Niedermayr A. (2017) Diagenesis of carbonate associated sulfate. *Chem. Geol.* **463**, 61–75.

Foster P. and Chacko J. (1995) Minor and trace elements in the shell of Patella vulgata (L.). *Mar. Environ. Res.* **40**, 55–76.

Füger A., Konrad F., Leis A., Dietzel M. and Mavromatis V. (2019) Effect of growth rate and pH on lithium incorporation in calcite. *Geochim. Cosmochim. Acta* **248**, 14–24.

Gabitov R. I., Sadekov A. and Leinweber A. (2014) Crystal growth rate effect on Mg/Ca and Sr/Ca partitioning between calcite and fluid: An in situ approach. *Chem. Geol.* **367**, 70–82.

Goldsmith J. R. and Graf D. L. (1958) Relation between lattice constants and composition of the Ca-Mg carbonates. *Am. Mineral.* **43**, 84–101.

Gussone N., Böhm; F., Eisenhauer A., Dietzel M., Heuser A., Teichert B. M. A., Reitner J., Wörheide G. and Dullo W. C. (2005) Calcium isotope fractionation in calcite and aragonite. *Geochim. Cosmochim. Acta* **69**, 4485–4494.

Hall J. M. and Chan L. H. (2004) Ba/Ca in benthic foraminifera: Thermocline and mid depth circulation in the North Atlantic during the last glaciation. *Paleoceanography* **19**, 1–13.

Han M., Zhao Y., Zhao H., Han Z., Yan H., Sun B., Meng R., Zhuang D., Li D. and Liu B. (2017) A comparison of amorphous calcium carbonate crystallization in aqueous solutions of $MgCl_2$ and $MgSO_4$: implications for paleo-ocean chemistry. *Mineral. Petrol.* **0**, 1–16.

Hartley G. and Mucci A. (1996) The influence of pCO_2 on the partitioning of magnesium in calcite overgrowths precipitated from artificial seawater at 25° and 1 atm total pressure. *Geochim. Cosmochim. Acta* **60**, 315–324.

Hippler D., Buhl D., Witbaard R., Richter D. K. and Immenhauser A. (2009) Towards a better understanding of magnesium-isotope ratios from marine skeletal carbonates. *Geochim. Cosmochim. Acta* **73**, 6134–6146.

Hippler D., Eisenhauer A. and Nägler T. F. (2006) Tropical Atlantic SST history inferred from Ca isotope thermometry over the last 140ka. *Geochim. Cosmochim. Acta* **70**, 90–100.

Horita J., Zimmermann H. and Holland H. D. (2002) Chemical evolution of seawater during the Phanerozoic: Implications from the record of marine evaporites. *Geochim. Cosmochim. Acta* **66**, 3733–3756.

Howson M. R., Pethybridge A. D. and House W. A. (1987) Synthesis and distribution coefficient of low-magnesium calcites. *Chem. Geol.* **64**, 79–87.

Huang Y. and Fairchild I. J. (2001) Partitioning of Sr^{2+} and Mg^{2+} into calcite under karst-analogue experimental conditions. *Geochim. Cosmochim. Acta* **65**, 47–62.

Immenhauser A., Buhl D., Richter D., Niedermayr A., Riechelmann D., Dietzel M. and Schulte U. (2010) Magnesium-isotope fractionation during low-Mg calcite precipitation in a limestone cave - Field study and experiments. *Geochim. Cosmochim. Acta* **74**, 4346–4364.

Kampschulte A., Bruckschen P. and Strauss H. (2001) The sulphur isotopic composition of trace sulphates in Carboniferous brachiopods: Implications for coeval seawater, correlation with other geochemical cyles and isotope stratigraphy. *Chem. Geol.* **175**, 149–173.

Kampschulte A. and Strauss H. (2004) The sulfur isotopic evolution of Phanerozoic seawater based on the analysis of structurally substituted sulfate in carbonates. *Chem. Geol.* **204**, 255–286.

Kartnaller V., Ribeiro E. M., Venancio F., Rosario F. F. and Cajaiba J. (2018) polymorphs during calcium carbonate. *CrystEngComm* **20**, 2241–2244.

Katsifaras A. and Spanos N. (1999) Effect of inorganic phosphate ions on the spontaneous precipitation of vaterite and on the transformation of vaterite to calcite. *J. Cryst. Growth* **204**, 183–190.

Kawano J., Sakuma H. and Nagai T. (2015) Incorporation of Mg^{2+} in surface Ca^{2+} sites of aragonite: an ab initio study. *Prog. Earth Planet. Sci.* 2:7.

Kitano Y., Okumura M. and Idogaki M. (1975) Incorporation of sodium, chloride and sulfate with calcium carbonate. *Geochem. J.* **9**, 75–84.

Kontrec J., Kralj D., Brečević L., Falini G., Fermani S., Noethig-Laslo V. and Mirosavljević K. (2004) Incorporation of inorganic anions in calcite. *Eur. J. Inorg. Chem.*, 4579–4585.

Lin Y. P. and Singer P. C. (2009) Effect of Mg^{2+} on the kinetics of calcite crystal growth. *J. Cryst. Growth* **312**, 136–140.

Lin Y. P. and Singer P. C. (2005) Effects of seed material and solution composition on calcite precipitation. *Geochim. Cosmochim. Acta* **69**, 4495–4504.

Lippmann F. (1973) Sedimentary Carbonate Minerals., Springer, Berlin.

Lorens R. B. (1981) Sr, Cd, Mn and Co distribution coefficients in calcite as a function of calcite precipitation rate. *Geochim. Cosmochim. Acta* **45**, 553–561.

Lorrain A., Gillikin D. P., Paulet Y. M., Chauvaud L., Le Mercier A., Navez J. and André L. (2005) Strong kinetic effects on Sr/Ca ratios in the calcitic bivalve Pecten maximus. *Geology* **33**, 965–968.

Lowenstein T. K., Hardie L. A., Timofeeff M. N. and Demicco R. V. (2003) Secular variation in seawater chemistry and the origin of calcium chloride basinal brines. *Geology* **31**, 857–860.

Markgraf S. and Reeder R. (1985) High-temperature structure refinements of calcite and magnesite. *Am. Miner.* **70**, 590–600.

Marriott C. S., Henderson G. M., Crompton R., Staubwasser M. and Shaw S. (2004) Effect of mineralogy, salinity, and temperature on Li/Ca and Li isotope composition of calcium carbonate. *Chem. Geol.* **212**, 5–15.

Mavromatis V., Gautier Q., Bosc O. and Schott J. (2013) Kinetics of Mg partition and Mg stable isotope fractionation during its incorporation in calcite. *Geochim. Cosmochim. Acta* **114**, 188–203.

Mavromatis V., Goetschl K. E., Grengg C., Konrad F., Purgstaller B. and Dietzel M. (2018) Barium partitioning in calcite and aragonite as a function of growth rate. *Geochim. Cosmochim. Acta* **237**, 65–78.

Mavromatis V., González A. G., Dietzel M. and Schott J. (2019) Zinc isotope fractionation during the inorganic precipitation of calcite – Towards a new pH proxy. *Geochim. Cosmochim. Acta* **244**, 99–112.

Mavromatis V., Immenhauser A., Buhl D., Purgstaller B., Baldermann A. and Dietzel M. (2017) Effect of organic ligands on Mg partitioning and Mg isotope fractionation during low-temperature precipitation of calcite in the absence of growth rate effects. *Geochim. Cosmochim. Acta* **207**, 139–153.

Mavromatis V., Montouillout V., Noireaux J., Gaillardet J. and Schott J. (2015) Characterization of boron incorporation and speciation in calcite and aragonite from co-precipitation experiments under controlled pH, temperature and precipitation rate. *Geochim. Cosmochim. Acta* **150**, 299–313.

McIntire W. L. (1963) Trace element partition coefficients - a review of theory and applications to geology. *Geochim. Cosmochim. Acta* **27**, 1209–1264.

Meyer H. J. (1984) The influence of impurities on the growth rate of calcite. *J. Cryst. Growth* **66**, 639–646.

Milliman J. D. (1974) *Marine Caronates.*, Springer, Berlin.

Morse J. W., Arvidson R. S. and Lüttge A. (2007) Calcium carbonate formation and dissolution. *Chem. Rev.* **107**, 342–381.

Morse J. W. and Bender M. L. (1990) Partition coefficients in calcite: Examination of factors influencing the validity of experimental results and their application to natural systems. *Chem. Geol.* **82**, 265–277.

Morse J. W. and Mackenzie F. T. (1990) *Geochemistry of sedimentary carbonates.*, Elsevier, Amsterdam, Oxford, New York, Tokyo.

Morse J. W., Wang Q. and Tsio M. Y. (1997) Influences of temperature and Mg:Ca ratio on CaCO$_3$ precipitates from seawater. *Geology* **25**, 85–87.

Mucci A. (1987) Influence of temperature on the composition of magnesian calcite overgrowths precipitated from seawater. *Geochim. Cosmochim. Acta* **51**, 1977–1984.

Mucci A., Canuel R. and Zhong S. (1989) The solubility of calcite and aragonite in sulfate-free seawater and the seeded growth kinetics and composition of the precipitates at 25°C. *Chem. Geol.* **74**, 309–320.

Mucci A. and Morse J. W. (1983) The incorporation of Mg^{2+} and Sr^{2+} into calcite overgrowths: influences of growth rate and solution composition. *Geochim. Cosmochim. Acta* **47**, 217–233.

Nielsen M. R., Sand K. K., Rodriguez-Blanco J. D., Bovet N., Generosi J., Dalby K. N. and Stipp S. L. S. (2016) Inhibition of Calcite Growth: Combined Effects of Mg^{2+} and SO$_4^{2-}$. *Cryst. Growth Des.* **16**, 6199–6207.

Noireaux J., Mavromatis V., Gaillardet J., Schott J., Montouillout V., Louvat P., Rollion-Bard C. and Neuville D. R. (2015) Crystallographic control on the boron isotope paleo-pH proxy. *Earth Planet. Sci. Lett.* **430**, 398–407.

Onuk P., Dietzel M. and Hauzenberger C. A. (2014) Formation of helictite in the cave Dragon Belly (Sardinia, Italy)-Microstructure and incorporation of Mg, Sr, and Ba. *Chemie der Erde* **74**, 443–452.

Oomori T., Kaneshima H., Maezato Y. and Kitano Y. (1987) Distribution coefficient of Mg^{2+} ions between calcite and solution at 10-50°C. *Mar. Chem.* **20**, 327–336.

Paquette J. and Reeder R. J. (1990) Single-crystal X-ray structure refinements of fwo biogenic magnesian calcite crystals. *Am. Mineral.* **75**, 1151–1158.

Paquette J. and Reeder R. J. (1995) Relationship between surface structure, growth mechanism, and trace element incorporation in calcite. *Geochim. Cosmochim. Acta* **59**, 735-749.

Peck L. S., Brockington S. and Brey T. (1997) Growth and Metabolism in the Antarctic Brachiopod Liothyrella uva. *Phil. Trans. R. Soc. Lond. B* **352**, 851–858.

Pingitore N. E., Meitzner G. and Love K. M. (1995) Identification of sulfate in natural carbonates by x-ray absorption spectroscopy. *Geochim. Cosmochim. Acta* **59**, 2477–2483.

Plummer L. N. and Busenberg E. (1982) The solubilities of calcite, aragonite and vaterite in CO$_2$-H$_2$O solutions between 0 and 90°C, and an evaluation of the aqueous model for the system CaCO$_3$-CO$_2$-H$_2$O. *Geochim. Cosmochim. Acta* **46**, 1011–1040.

Purgstaller B., Konrad F., Dietzel M., Immenhauser A. and Mavromatis V. (2017) Control of Mg^{2+}/Ca^{2+} Activity Ratio on the Formation of Crystalline Carbonate Minerals via an Amorphous Precursor. *Cryst. Growth Des.* **17**, 1069–1078.

Purgstaller B., Mavromatis V., Immenhauser A. and Dietzel M. (2016) Transformation of Mg-bearing amorphous calcium carbonate to Mg-calcite - In situ monitoring. *Geochim. Cosmochim. Acta* **174**, 180–195.

Raiswell R. and Fisher Q. J. (2004) Rates of carbonate cementation associated with sulphate reduction in DSDP/ODP sediments: Implications for the formation of concretions. *Chem. Geol.* **211**, 71–85.

Reddy M. M. and Nancollas G. H. (1976) The crystallization of calcium carbonate. IV. The effect of magnesium, strontium and sulfate ions. *J. Cryst. Growth* **35**, 33–38.

Reddy M. M. and Wang K. K. (1980) Crystallization of calcium carbonate in the presence of metal ions. *J. Cryst. Growth* **50**, 470–480.

Rimstidt J. D., Balog A. and Webb J. (1998) Distribution of trace elements between carbonate minerals and aqueous solutions. *Geochim. Cosmochim. Acta* **62**, 1851–1863.

Saldi G. D., Noireaux J., Louvat P., Faure L., Balan E., Schott J. and Gaillardet J. (2018) Boron isotopic fractionation during adsorption by calcite – Implication for the seawater pH proxy. *Geochim. Cosmochim. Acta* **240**, 255–273.

Schlager W. (2005) *Carbonate Sedimentology and Sequence Stratigraphy. 8th ed.*, SEPM (Society for Sedimentary Geology).

Stumm W. and Morgan J. J. (1996) *Aquatic chemistry. 3th edition.*, Wiley-Interscience Publication, New York, Chichester, Brisbane, Toronto, Singapore.

Sunagawa I. (2005) *Crystals: Growth, Morphology and Perfection.*, Cambridge University Press.

Swanson H. E. and Fuyat R. K. (1953) Standard X-ray Diffraction Powder Patterns. *Circ. Natl. Bur. Stand.* 539 II.

Takano B. (1985) Geochemical implications of sulfate in sedimentary carbonates. *Chem. Geol.* **49**, 393–403.

Tang J., Köhler S. J. and Dietzel M. (2008) Sr^{2+}/Ca^{2+} and $^{44}Ca/^{40}Ca$ fractionation during inorganic calcite formation: I. Sr incorporation. *Geochim. Cosmochim. Acta* **72**, 3718–3732.

Tesoriero A. J. and Pankow J. F. (1996) Solid solution partitioning of Sr^{2+}, Ba^{2+}, and Cd^{2+} to calcite. *Geochim. Cosmochim. Acta* **60**, 1053–1063.

Tucker M. E. and Wright V. P. (1990) *Carbonate Sedimentology.*, Blackwell Science Ltd.

Uchikawa J., Harper D. T., Penman D. E., Zachos J. C. and Zeebe R. E. (2017) Influence of solution chemistry on the boron content in inorganic calcite grown in artificial seawater. *Geochim. Cosmochim. Acta* **218**, 291–307.

Uchikawa J., Penman D. E., Zachos J. C. and Zeebe R. E. (2015) Experimental evidence for kinetic effects on B/Ca in synthetic calcite: Implications for potential $B(OH)_4^-$ and $B(OH)_3$ incorporation. *Geochim. Cosmochim. Acta* **150**, 171–191.

Veizer J., Ala D., Azmy K., Bruckschen P., Buhl D., Bruhn F., Carden G. A. F., Diener A., Ebneth S., Godderis Y., Jasper T., Korte C., Pawellek F., Podlaha O. G. and Strauss H. (1999) $^{87}Sr/^{86}Sr$, ^{13}C and ^{18}O evolution of Phanerozoic seawater. *Chem. Geol.* **161**, 59–88.

Voigt M., Mavromatis V. and Oelkers E. H. (2017) The experimental determination of REE partition coefficients in the water-calcite system. *Chem. Geol.* **462**, 30–43.

Walter L. M. (1986) Relative efficiency of carbonate dissolution and precipitation during diagenesis: a progress report on the role of solution chemistry. *Roles Org. Matter Sediment Diagenes.* **38**, 1–12.

Watson E. B. (2004) A conceptual model for near-surface kinetic controls on the trace-element and stable isotope composition of abiogenic calcite crystals. *Geochim. Cosmochim. Acta* **68**, 1473–1488.

Watson E. B. (1996) Surface enrichment and trace-element uptake during crystal growth. *Geochim. Cosmochim. Acta* **60**, 5013–5020.

Watson E. B. and Liang Y. (1995) A simple model for sector zoning in slowly grown crystals: implications for growth rate and lattice diffusion, with emphasis on accessory minerals in crustal rocks. *Am. Mineral.* **80**, 1179–1187.

Wotte T., Shields-Zhou G. A. and Strauss H. (2012) Carbonate-associated sulfate: Experimental comparisons of common extraction methods and recommendations toward a standard analytical protocol. *Chem. Geol.* **326–327**, 132–144.

Yates K. K. and Halley R. B. (2006) Diurnal variation in rates of calcification and carbonate sediment dissolution in Florida Bay. *Estuaries and Coasts* **29**, 24–39.

Zhang Y. and Dawe R. A. (2000) Influence of Mg^{2+} on the kinetics of calcite precipitation and calcite crystal morphology. *Chem. Geol.* **163**, 129–138.

Zhong S. and Mucci A. (1995) Partitioning of rare earth elements (REEs) between calcite and seawater solutions at 25°C and 1 atm, and high dissolved REE concentrations. *Geochim. Cosmochim. Acta* **59**, 443–453.

Chapter 3

Control of $MgSO_4^0(aq)$ on the transformation of amorphous calcium carbonate to high–Mg calcite and long–term reactivity of the crystalline solid

Katja E. Goetschl[1], Martin Dietzel[1], Bettina Purgstaller[1], Cyrill Grengg[1], Vasileios Mavromatis[2]

[1]Institute of Applied Geosciences, Graz University of Technology, Rechbauerstrasse 12, 8010 Graz, Austria
[2]Géosciences Environment Toulouse (GET), CNRS, UMR 5563, Observatoire Midi-Pyrénées, 14 Av. E. Belin, 31400 Toulouse, France

ABSTRACT: The Mg and SO_4 content of naturally occurring calcite are routinely used as paleoenvironmental proxies. Yet little is known about the mechanisms governing the presence of these ions in carbonate minerals when their formation proceeds via an amorphous precursor. To address this, the transformation of Mg-free amorphous calcium carbonate (ACC) into nanocrystalline high-Mg calcite (HMC) was experimentally studied in solutions containing 27 mM of Mg and a range of 10 to 90 mM of SO_4. The obtained results suggest that ACC is stable for several minutes in the experimental solutions and this amorphous phase actively uptakes Mg and SO_4 that are incorporated in its structure. Additionally, the obtained results suggest that the stabilization of ACC is not affected by its Mg content and that the transformation to HMC is effectively controlled by the abundance of the free $Mg^{2+}(aq)$ ion. The transformation of ACC to HMC occurs earlier at elevated SO_4 concentrations because SO_4 limits the availability of $Mg^{2+}(aq)$ due to the formation of the $MgSO_4^0(aq)$ complex. The HMC that is formed from ACC appears as aggregates composed of nanocrystallites and exhibits Mg and SO_4 contents up to 8 and 2 mol% depending on the initial SO_4 concentration in the reactive solution. The precipitated HMC was kept in contact with the reactive solution in order to assess its reactivity for up to 1 year of reaction time. Over time, a continuous exchange of Mg and SO_4 between calcite and reactive solution was observed resulting in enrichment of Mg and depletion of SO_4 affecting the total mass of the aggregates with the distribution of these elements to appear homogeneous in the solid. The high reactivity and the continuous exchange of solutes between the nanocrystalline calcite and the reactive solutions limits the use of Mg and SO_4 content of these HMCs as environmental proxies.

3.1 Introduction

Calcium carbonate ($CaCO_3$) formation in aqueous environments results in minerals containing traces or foreign elements (Morse and Mackenzie, 1990; Reeder, 1990; Dietzel 2011). The chemical and isotopic composition of $CaCO_3$ are routinely used in order to reveal the environmental conditions that occurred at the time of mineral formation. Nowadays it is well accepted that the chemical/isotopic signals recorded in carbonates are affected by a number of parameters including temperature (e.g. Burton and Walter, 1991), pH (e.g. Mavromatis et al., 2015; Uchikawa et al., 2017), growth kinetics (e.g. Lorens, 1981) aqueous complexation (e.g. Mavromatis et al., 2017a) and mineralogy (e.g. Mavromatis et al. 2018). However, less is known about the mechanisms governing the chemical/isotopic composition of carbonate minerals when the formation proceeds via an amorphous precursor (Evans et al., 2020). Amorphous calcium carbonate (ACC) has been identified as precursor phase for crystalline $CaCO_3$ in many calcifying biomineralization strategies (Du and Amstad, 2020; and references therein). Owing to the importance of ACC in biomineralization it has been the subject of research for a large number of studies in the last two decades (e.g. Raz et al., 2000; Addadi et al. 2003; Gower 2008; Long et a., 2011; Gong et al., 2012; Albéric et al., 2018; Jin et al., 2018). Novel non-classical nucleation concepts of amorphous intermediates have been proposed and numerous studies exist that show a wide variety in the hydration level of ACC and the characteristics of its short-range order (Gebauer et al., 2010; Gebauer and Cölfen, 2011; Schmidt et al., 2014; De Yoreo et al., 2015; Sun et al., 2016; Tobler et al., 2016; Du et al., 2018; Mergelsberg et al., 2020).

A large number of experimental studies has explored the mechanisms controlling the transformation of ACC into crystalline $CaCO_3$ polymorphs (e.g. Rodriguez-Blanco et al., 2012; Rodriguez-Navarro et al., 2015; Giuffre at al., 2015; Blue et al., 2017; Purgstaller et al., 2017a; Purgstaller et al., 2017b; Zou et al. 2018). It is for example well known that high-Mg calcite (HMC) with Mg contents exceeding 4 mol% is often formed via the formation and transformation of Mg-bearing ACC by mixing a carbonate-bearing solution with a Ca-Mg-rich solution (e.g. Mavromatis et al., 2012; Long et al., 2014; Purgstaller et al., 2016; Xto et al., 2019). Moreover, the presence of Mg has been shown to temporary stabilize ACC and to retard its transformation in solution (e.g. Loste et al., 2003; Politi et al., 2010; Lin et al., 2015; Konrad et al, 2018). Although the role of Mg in stabilizing ACC has been well studied, significant gaps of knowledge exist with respect to the effect of other ions on the ACC transformation pathway. For example, although SO_4 is the second

most concentrated anion in seawater, only a few studies have examined the effect of SO_4 on the stability and reactivity of the amorphous precursor (Bots et al., 2012; Ihli et al., 2013; Han et al., 2017).

In the presence of aqueous Mg, the transformation of ACC results mostly in the formation of nanocrystalline calcite agglomerations (e.g. Jiang et al., 2011; Long et al., 2011; Blue et al., 2017; Huang et al., 2018; Xto et al., 2019). In this context, an aspect of great importance is the reactivity of the nanocrystalline calcite when in contact with an aqueous solution. The amorphous solid is only present at the initial stages of mineral formation, whereas the nanocrystalline calcite remains in contact with the solution for extended periods of time. In the latter case, the large surface area of the nanocrystalline calcite aggregates can be subject to continuous exchange of solutes (Mavromatis et al., 2017b; Oelkers et al., 2019). Detailed understanding of the distribution of trace elements and isotopes after the transformation of ACC is still largely lacking, but essentially required in order to support geochemical proxies and to unravel information of their (past) formation conditions that is archived in abiotic and biogenic calcite.

The present study explores two features related to calcite formation via ACC: the first is assessing the role of SO_4 in the transformation process and the second is the long-term reactivity of the crystalline product formed from ACC. Thus, ACC transformation experiments were conducted in the presence of aqueous Mg^{2+} and SO_4^{2-} ions and the crystalline solids were kept in contact with the reactive solution for 1 year of reaction time. The experimental set-up allowed to distinguish between (i) the elemental distribution between ACC and reactive solution and (ii) the re-distribution during its transformation to calcite. The molar $Mg/SO_4(aq)$ ratios were varied in order to systematically study the coupled effect of Mg and SO_4 on (i) the elemental exchange between solid ACC and the aqueous phase as well as the stability of ACC, (ii) the transformation kinetics of ACC and (iii) the Mg content of calcite formed via an amorphous precursor. Reactivities of ACC and HMC, elemental distribution and nanostructured features of solid phases are discussed in the scope of (i) their importance for the interpretation of individual proxy data derived from amorphous-to-crystalline carbonate archives and (ii) the limits of Mg and SO_4 distribution in nanocrystalline HMC to reconstruct bulk precipitating water.

3.2 Methods

3.2.1 Synthesis of ACC

Synthetic ACC was prepared following the protocol described earlier in Konrad et al. (2016). Briefly, 80 mL of a 250 mM $CaCl_2$ solution were poured into a glass beaker containing the same volume of a 250 mM Na_2CO_3 solution and mixed vigorously for 2-3 seconds. The solid product of the reaction was separated immediately from the solution by a 0.2 μm cellulose membrane filter using suction filtration. Subsequently, the solid phase was rinsed with ultrapure deionized water to remove Na^+ and Cl^- ions and immediately freeze-dried using a Virtis Benchtop 3L freeze-dryer in order to remove adsorbed water. The synthesis protocol was repeated several times in order to prepare a batch of about 18 g of synthetic ACC as starting material for the transformation experiments. The freeze-dried ACC was stored in a closed vial in a desiccator with silica gel (relative humidity = 3 %) to prevent its transformation to crystalline $CaCO_3$.

3.2.2 Experimental set-up

The transformation of synthetic ACC to calcite was performed in a glass reactor, equipped with a Teflon® coated magnetic stirrer operating at 350 rpm. The reactor initially contained 50 mL of a Mg (and SO_4) -bearing solution (Fig. 1). The experiments were performed at 23 ±1 °C and at pH 8.3 ±0.2 that was adjusted automatically through the titration of a 0.5 M NaOH solution (titrator TitroLine® 7800 from SI Analytics). The initial reactive solution contained ~100 mM $NaHCO_3$ and ~27 mM $MgCl_2$ at pH ~8. The SO_4^{2-} concentrations in the initial solutions ranged between 10 and 90 mM (see Table 1). The experiments were labeled sX, where X refers to the respective concentration of SO_4 (mM) in the initial reactive solution. The experiment with SO_4 concentration of 30 mM was performed in duplicate and was labeled s30_2. A control experiment was conducted in the absence of SO_4 and was labeled s0. The background electrolyte concentration of the initial reactive solutions was adjusted to 330 mM by the addition of NaCl when necessary. All solutions were prepared using ultrapure deionized water and analytical grade chemicals from Roth ($CaCl_2 \cdot 2H_2O$, $MgCl_2 \cdot 6H_2O$, $NaHCO_3$, Na_2CO_3, Na_2SO_4, NaCl).
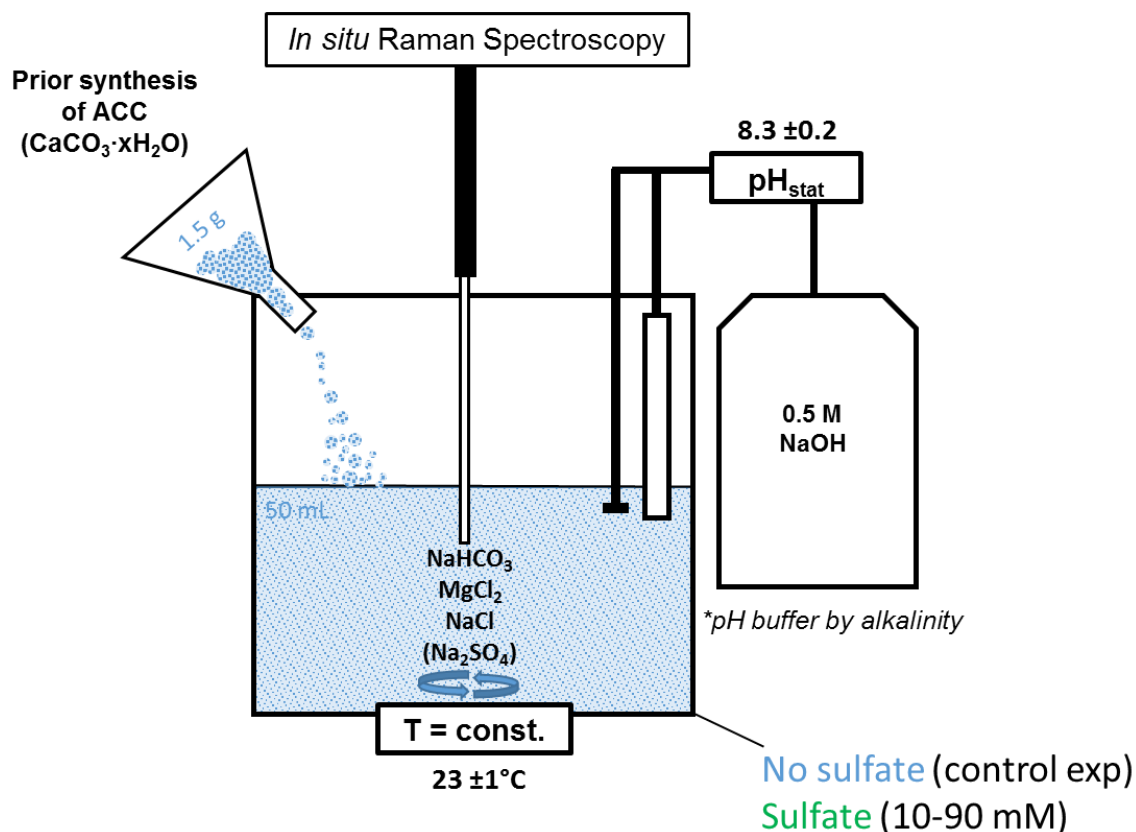
Fig. 1: Experimental set-up of ACC transformation experiments. Synthetic ACC was added to the reactor containing a HCO_3-Mg-(SO_4-)bearing solution. The mineral transformation reaction occurred under controlled physicochemical conditions and was monitored *in situ* by Raman spectroscopy.

At the beginning of the experiment 1.5 g of ACC was introduced into the reactive solution following a similar approach to Konrad et al. (2018) and Purgstaller et al. (2019). The immersion probe of an *in situ* Raman spectrometer was placed into the suspension to monitor the temporal evolution of the solid phase transformation and the vibrational spectra of dissolved species for about 1 hour of reaction time. In order to characterize both, the chemical composition of the solution and the solid phase, homogeneous subsamples (1.5 mL) were collected under stirring with a pipette at certain reaction times (Table 1). The solid material was immediately separated from the reactive solution with the aid of a 0.2 μm cellulose acetate membrane filter using suction filtration, subsequently rinsed extensively with ethanol and dried in the oven at 40 ˚C. After 1 hour of reaction time the suspension was transferred into a polyethylene vial and placed on a

shaker at 23 °C in a constant temperature room. Sub-samples were taken after 1 day, 1 week, 1 month, 9 months and 1 year.

3.2.3 Mineralogical and chemical analyses

3.2.3.1 Solid phases

Time-resolved *in situ* Raman spectra of the reactive suspension were collected every 62 seconds with a Raman RXN2™ analyzer from Kaiser Optical Systems equipped with a quarter-inch immersion optic Kaiser MR probe. The Raman spectra were recorded in the 100-3425 cm^{-1} region with a resolution of 1 cm^{-1} using a 785 nm laser beam with an exposure time of 60 sec. Powder X-ray diffraction (XRD) patterns of the solid phases collected at certain reaction times (see Table 1) were recorded by a PANalytical X'Pert PRO diffractometer using Co-Kα-radiation (40 mA, 40 kV) at a 2θ range from 5° to 85° and a scan speed of 0.03° s^{-1}. For qualitative characterization of the crystalline products the PANalytical HighScore Plus software with the ICSD database was used. Note here, the detection limit of crystalline phases is ~1 wt%. Infrared spectra of the solids in the range of 650 to 4000 cm^{-1} were collected using a Perkin Elmer Spektrum 100 Attenuated Total Reflectance-Fourier Transform Infrared (ATR-FTIR) spectrometer with a resolution of 4 cm^{-1}. Selected precipitates were gold-coated and imaged using a ZEISS DSM 982 Gemini scanning electron microscope (SEM) equipped with a field emission gun operating at 2 kV accelerating voltage.

Additionally, subsamples of selected crystalline solids were embedded in a two-component epoxy resin, polished, carbon coated and analyzed with an electron probe microanalysis (EPMA) using a JEOL JXA8530F Plus Hyper Probe equipped with a field emission gun. Secondary electron (SEI) and back-scattered electron (BSE) images were recorded at an accelerating voltage of 10 kV and 2 nA. Furthermore, (semi)-quantitative high-resolution element distribution images of Ca, Mg and S were recorded using the wave-dispersive analytical mode (WDS), an acceleration voltage of 10 kV and 5 nA and a dwell time of 30 mS. Element quantifications were performed against mineral standards from SPI (Calcite for Ca, Dolomite for Mg and Barite for S). From these images, average Mg and S (given as SO_4) contents in solid samples were calculated using data of 100x100 pixel (Table S2).

3.2.3.2 Reactive solutions

The pH of the reactive solution was measured *in situ* with a SI Analytics Silamid® gel electrode coupled to a SI Analytics TitroLine® 7800. The electrode was calibrated on the activity scale with NIST standard buffer solutions at pH 4.01, 7.00 and 10.00 (analytical uncertainty ±0.03 units). Total alkalinity was determined by a Schott TitroLine alpha plus titrator using a 10 mM HCl solution with an analytical precision of ±2 %. Aqueous Ca, Mg and SO_4 concentrations were measured by Ion Chromatography (IC) using a Dionex IC S 3000 with IonPac® AS19 and CS16 column with an analytical precision of ±3 %. The distribution of aqueous species in the reactive solution and saturation indices (SI) with respect to amorphous and crystalline phases were calculated using the PHREEQC software in combination with its minteq.v4 database modified by the addition of the solubility products for ACC (Brečević and Nielsen, 1989), hydromagnesite (Gautier et al., 2014), nesquehonite, dypingite (Harrison et al., 2019) and bassanite (Shen et al., 2019). In order to calculate SI (SI = IAP/K_{sp}) of the amorphous solids that are enriched in Mg, the ion activity product (IAP) was calculated using the equation

$$IAP = (a_{Ca^{2+}})^{1-x} (a_{Mg^{2+}})^x (a_{CO_3^{2+}}) \tag{1}$$

where a_x denotes the activities of free ions in solution and the solubility product (K_{sp}) of ACC containing 0.6 mol% Mg was calculated using the equation given by Purgstaller et al. (2019). The SO_4 content of ACC accounted for ≤ 0.1 mol% and was therefore not considered in the calculation of the ion activity product.

3.2.3.3 Chemical composition of solid phases

The Mg and SO_4 contents of the solids (in mol%) were calculated by mass balancing the reactive solution sampled at certain time steps (Table 1) and according to the equations

$$[Mg]_{solid} (mol\%) = \frac{n_{Mg}}{n_{Mg}+n_{Ca}} \times 100 \tag{2}$$

$$[SO_4]_{solid} (mol\%) = \frac{n_{SO_4}}{n_{Mg}+n_{Ca}} \times 100 \tag{3}$$

where n_{Mg}, n_{Ca} and n_{SO_4} denote the moles of Mg, Ca and SO_4 in the solid phase. The moles of each element/molecule in the solid phase (n_x) was calculated at each time step by the

subtraction of the actual measured Ca, Mg and SO_4 concentrations from the total available Ca, Mg and SO_4 concentrations in mol/L. The total available concentration of Ca was derived from 1.5 g ACC ($CaCO_3 \cdot 0.4H_2O$; Konrad et al., 2016) with a molecular weight of 107.3 g/mol converted into mol/L whereas total available concentrations of Mg and SO_4 were derived by their initial concentrations (mol/L) in the reactor prior to the introduction of ACC. The sum of the cations $n_{Mg}+n_{Ca}$ represents the sum of the anions $n_{SO_4}+n_{CO_3}$. No correction for the amount of sampled material (solid + solution) in the course of the experimental runs was applied because the suspension was sampled homogeneously. Additionally, the elemental content of digested bulk solids (i.e Ca, Mg and SO_4) was measured by IC following the protocol described in Goetschl et al. (2019). Note here that the elemental contents of the crystalline phase derived from both approaches are in excellent agreement, whereas the elemental composition of the amorphous phase exhibits higher values in the case of the measurement by IC (Table 1).

3.3 Results

3.3.1 Temporal evolution of ACC transformation to HMC

The *in situ* Raman spectra indicate that the transformation of ACC into HMC was initiated within a few minutes after its introduction into the HCO_3-Mg-(SO_4-)bearing solution (e.g. experiment s30 in Fig. S1). Note here that just before introducing ACC, the Raman spectra of the initial reactive solution depicts vibration bands of aqueous HCO_3^- and SO_4^{2-} at 1017 cm^{-1} and 981 cm^{-1}, respectively (Davis and Oliver 1972; Fujita and Kimura, 1981; Wang et al., 2005). The band intensities of aqueous HCO_3^- and SO_4^{2-} are decreasing rapidly in 2 steps during the course of the experiments, correlating with the addition of ACC in the reactor and its transformation to HMC. Immediately after ACC was added to the reactive solution, the recorded Raman spectra exhibit the characteristic broad $v_1(CO_3)$ ACC band at 1080 cm^{-1} (Wang et al., 2012), suggesting that this phase is the only solid present in the reactor within the first 10 min of the experiments. The intensity of the ACC $v_1(CO_3)$ band progressively decreases after ~5 min of reaction time, indicating the dissolution of the amorphous phase. Subsequently, the $v_1(CO_3)$ band at 1087-1088 cm^{-1}, characteristic for HMC (Bischoff et al., 1985), exhibits a strong intensity increase that is accompanied by band sharpening (Fig. S1). The intensity maximum (I_{max}) of the $v_1(CO_3)$ band is observed at 1088 cm^{-1} in experiments conducted in the absence of SO_4 (i.e. s0) and in the presence of 10 mM SO_4 (i.e. s10). In experiments performed at higher SO_4 concentrations of 30, 45,

75 and 90 mM SO_4 (i.e. s30, s45, s75 and s90), the I_{max} of the $\nu_1(CO_3)$ band is observed at 1087 cm^{-1}. After about 20-25 min of reaction time the intensity of the $\nu_1(CO_3)$ band of HMC (1087-1088 cm^{-1}) reaches a plateau (Fig. S2). Thus in all the experimental runs the temporal evolution of the transformation from ACC into HMC follows the same pattern and can be roughly divided into three stages (Fig. 2): (I) $\leq$ about 10 min, ACC occurrs as the only phase; (II) between about 10 to 30 min, ACC co-exists with HMC; (III) $\geq$ about 30 min, HMC is the only solid phase. More details about the exact onset of stage II in each individual experimental run are described in the following paragraph.
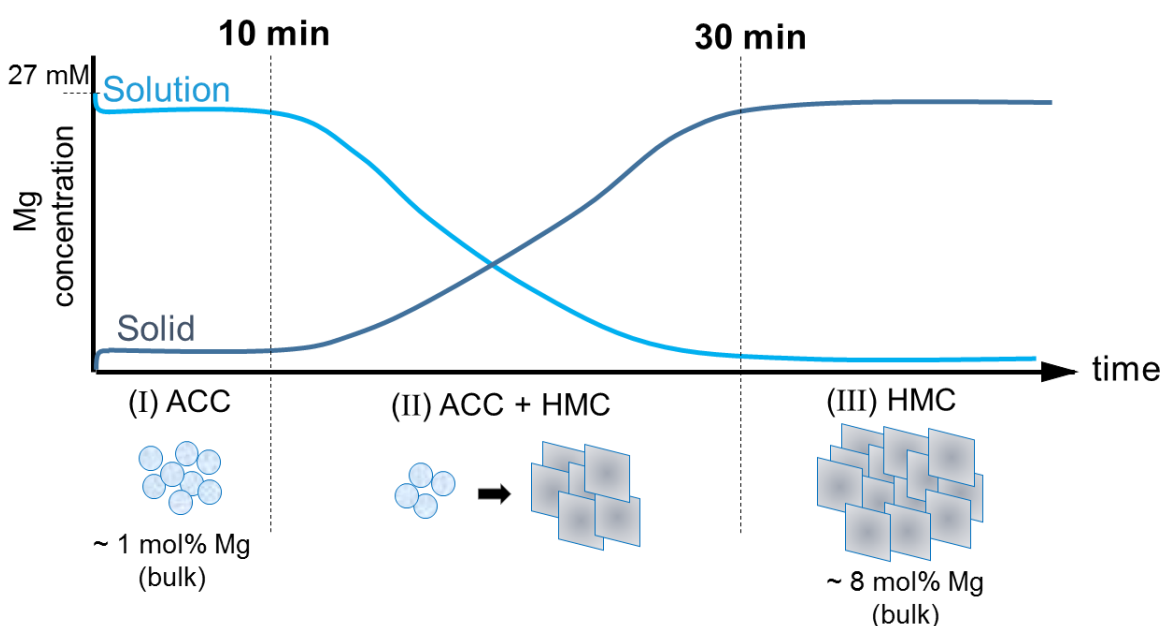
Fig. 2: Simplified illustration of the mineralogical and chemical evolution as a function of reaction time. The light blue line refers to the Mg concentration of the reactive solution and the dark blue line refers to the Mg content of the solid phase. The evolution can be divided in 3 different stages: (I) ACC stable – exchange of solutes between ACC and reactive solution, (II) ACC transformation to HMC via dissolution and re-precipitation, (III) HMC stable – continuous exchange of solutes between HMC and reactive solution.

Actually, the timepoint at which the intensity increase of the $\nu_1(CO_3)$ band occurs - indicative of the onset of HMC formation - appears to be a function of the $MgSO_4^0$ concentration of the reactive solution. Note here that the intensity increase of the $\nu_1(CO_3)$ band is marking the transition from stage I to stage II in the experimental runs. The time of the intensity increase of the intensity maximum (I_{max}) of the $\nu_1(CO_3)$ band for all experiments can be seen in Fig. S2. In the absence of SO_4 the intensity of the $\nu_1(CO_3)$ band

increases after 12.4 min of reaction time, whereas in experiment s90 the intensity of the $\nu_1(CO_3)$ band increases already after 8.3 min of reaction time. Actually, as it can be seen in Fig. 3A, a linear correlation between $MgSO_4^0$ (determined by initial SO_4) concentration and the time of onset of HMC formation exists and can be described by the linear equation

$$time\ (min) = -0.3840(\pm0.0455) \times MgSO_4^0\ (mM) + 12.0430(\pm0.2480);\ R^2 = 0.92 \qquad (4)$$

where reaction *time* is given in minutes and $MgSO_4^0$ denotes total concentration in mM of the reactive solution. The inverse trend is observed when the time of the $\nu_1(CO_3)$ band intensity increase is plotted as a function of free Mg^{2+} concentration (Fig. 3B).
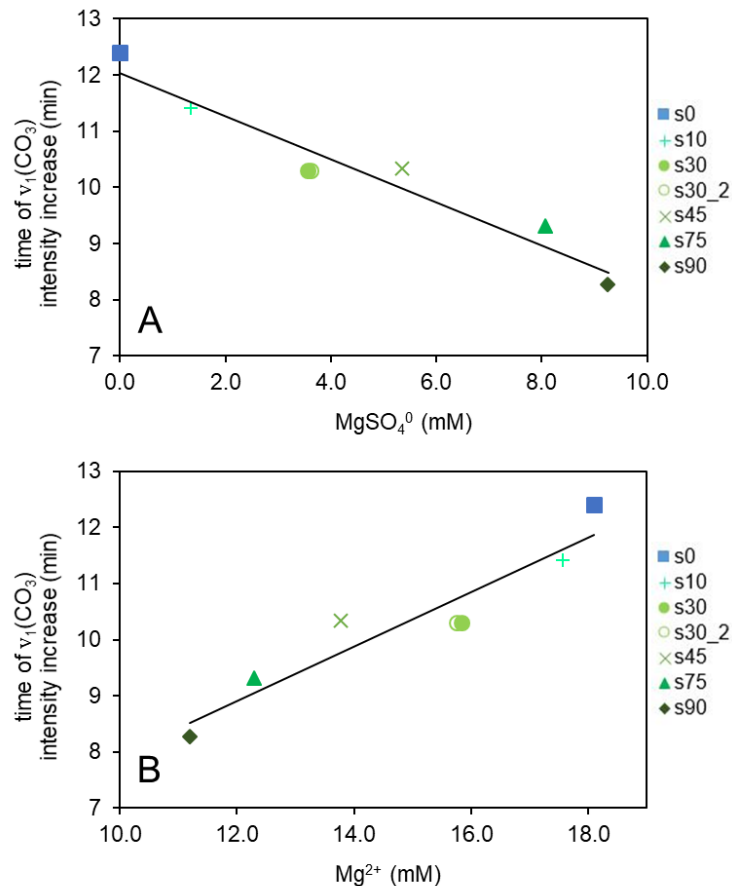
Fig. 3: Time of intensity increase of the intensity maximum (I_{max}) of the $(CO_3)_{solid}\ \nu_1$ band for all experiments obtained using *in situ* Raman spectroscopy. The formation of HMC is indicated by the rapid increase of I_{max} between 8.3 and 12.4 min of reaction time (Fig. S2). A) Elevated $MgSO_4^0$ concentrations of the reactive solution (referring to initial SO_4 concentrations) cause an earlier start of HMC formation B) Elevated Mg^{2+}(aq) concentrations at lower sulfate concentrations induce a longer induction time and therefore prolonged metastability of ACC.

60

The XRD analyses of the solid phases collected during the experimental runs (see Table 1) are in excellent agreement with the observations of the *in situ* Raman measurements. The XRD patterns of samples collected within 7 min of reaction time are consistent with the initial synthetic ACC. The first characteristic HMC peaks are observed in the diffractograms of samples collected at about 10 min of reaction time (e.g. experiment s30 in Fig. S3). Note here that the *in situ* Raman measurements reflect a more precise time of the onset of HMC formation due to the higher temporal resolution of data collection compared to XRD measurements. Comparing the XRD patterns of the HMCs formed via ACC to a pattern of pure calcite reference material ($CaCO_3$ ≥99%, p.a. from Roth), the main calcite peak (104) is significantly lower in intensity, it occurs with an extended full width at half maximum (FWHM) and is shifted to a higher 2θ position by + 0.25° (±0.03°) indicative of its Mg content. Note here that the peak positions of the newly precipitated HMCs analyzed at time steps from 10 to 62 min (Fig. S3) do not differ significantly from each other, indicating similar Mg contents of calcite (Goldsmith et al., 1961; Milliman et al., 1971). No significant peak shifts towards higher 2θ positions of the analyzed HMCs have been observed as a function of experimental reaction time up to 1 year.

The formation of HMC is further confirmed by ATR-FTIR analyses of collected solids. As it can be seen in Fig. 4, the FTIR spectra of ACC are characterized by carbonate vibration bands ν_1 and ν_2 at 1075 and 860 cm^{-1} (Andersen and Brečević, 1991; Loste et al., 2003; Konrad et al., 2018), while the HMC exhibits ν_1, ν_2, and ν_4 bands at 1086, 870/848 and 714 cm^{-1} (White, 1974; Böttcher et al., 1997). Previous studies have shown that the shift of the infrared (CO_3)-bands towards higher or lower wavenumbers is associated with increasing Mg^{2+} substitution (Böttcher et al, 1997; Huang et al., 2018). Moreover, FTIR spectra of the solids that have been collected from experiments performed in the presence of SO_4 - e.g. experiment s75 in Fig. 4 - exhibit additional bands next to the characteristic carbonate bands. In the case of ACC (s75_4 min) an additional broad band at 1134 cm^{-1} appears including a shoulder at ~1160 cm^{-1}, and in the case of HMC (s75_62 min) two additional bands at 1141 and 1161 cm^{-1} are visible (Fig. 4). These additional bands can be ascribed to internal ν_3 vibrations of SO_4 (Takano et al., 1980; Aizenberg et al., 2002; Floquet et al., 2015; Balan et al., 2017).
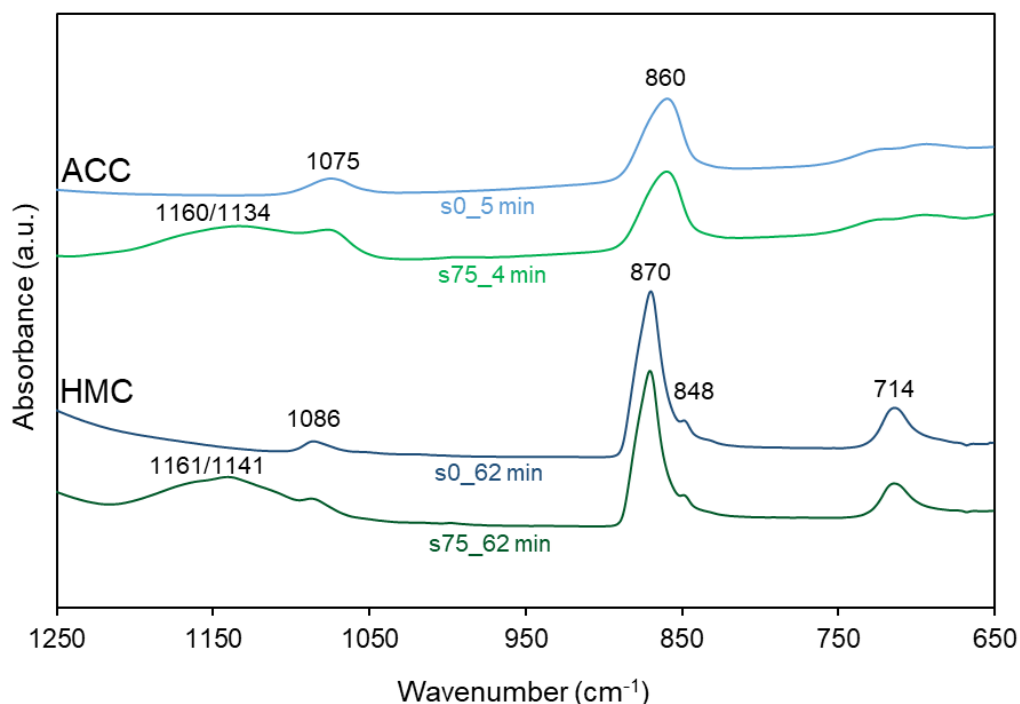
Fig. 4: FTIR spectra from experiments in the absence of sulfate (s0 - blue) and in the presence of 75 mM sulfate (s75 - green) after ~5 min and ~1 hour of reaction time, respectively.

Scanning Electron Microscopy (SEM) observations reveal that synthetic ACC particles that occur as spheres with an average diameter of 90 nm, transformed into HMCs that occur as nanocrystalline aggregates (Fig. 5A). The surface of the HMC aggregates displays numerous idiomorphic, rhombohedral calcite crystals that are interlocked into each other. No significant differences in the crystal morphology of the HMCs, formed in the absence or presence of SO_4, have been observed. Similarly, no changes of the crystal morphology as a function of time, even after 1 year of reaction time, were observed (Fig. S4).

Microphotographs of cross sections of the nanocrystalline HMC aggregates reveal their inner microstructure which appears as radially oriented columns (Fig. 5B). The columns become thicker from the inside out. The rough surface and disrupted centers after thick section polishing indicate a high internal porosity of ACC-derived HMC. Comparing the inner structure of precipitates collected after 1 hour to the ones collected after 1 year the latter exhibit a more dense and solid microstructure (Fig. S5).
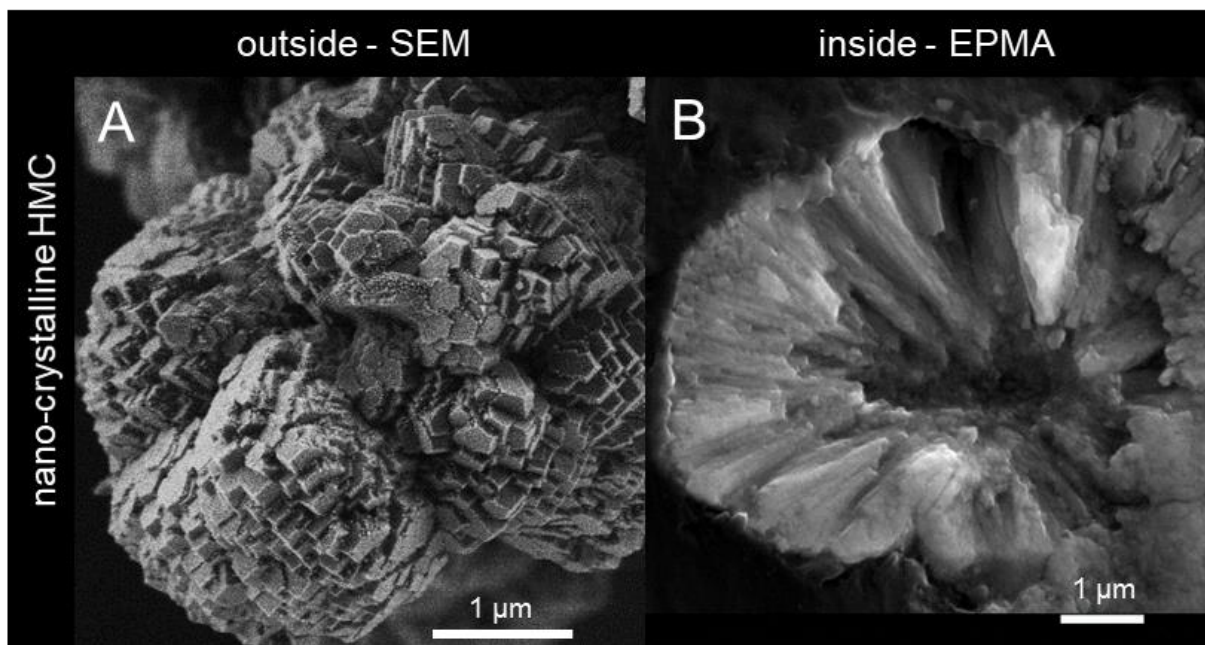
Fig. 5: A) SEM photograph of HMC (experiment s75) shows the outer appearance of the nano-crystalline product after ACC transformation. B) EPMA BSE-image shows the inner microstructure of the nano-crystalline HMC aggregate (experiment s90).

3.3.2 Chemical evolution of the reactive solution

The chemical composition of the reactive solution prior to ACC addition in the reactors, and during the first 30 min of the experimental runs, is illustrated in Fig. 6 (see data in Table 1). The same three stages that are specified by solid characterization, which are described above, can be identified by the temporal evolution of the reactive solution. Note here that the chemical evolution of the reactive solution points towards an ~5 min earlier onset of stage II compared to the solid characterization. The ACC transformation, which is indicated by the pH decrease, occurs in the latter case between 3 and 7 min of reaction time (Table 1; Fig. S6) instead of 8 and 12 min that is observed by *in situ* Raman spectra. It is thus evident that the onset of solid transformation is followed more accurately using the solution composition in contrast to the use of *in situ* Raman spectroscopy which is limited by the detection limit of the method for solid identification. Nevertheless, the kinetics of ACC transformation based on solution chemistry are in accordance with the observations by solid characterization and exhibit the same trend as a function of initial SO_4 concentration.

Table 1: Chemical composition of reactive solutions and solids and mineral composition of the precipitates at certain reaction times. The term "calculated" refers to Mg and SO_4 content of the solid estimated using Eqs. 2 and 3 whereas the term "measured" refers to the bulk solid composition measured after solid digestion.

Sample	Time (min)	pH	Alkalinity (mM)	Solution (mM)			Solid				
				Ca	Mg	SO_4	Mg mol% calculated	Mg mol% measured	SO_4 mol% calculated	SO_4 mol% measured	XRD/Raman
s0_initial		7.98	99	-	26.2	-					
s0_1	0.2	8.34	107	6.2	25.1	-	0.4	1.6	-	-	ACC
s0_2	2.3	8.32	108	6.5	24.5	-	0.6	1.7	-	-	ACC
s0_3	5.2	8.31	106	6.3	24.3	-	0.7	1.9	-	-	ACC
s0_4	7.8	8.30	104	6.2	24.1	-	0.8	2.0	-	-	ACC
s0_5	10.7	8.30	102	5.7	22.1	-	1.5	2.6	-	-	ACC
s0_6	13.1	8.29	92	4.8	16.1	-	3.6	4.2	-	-	ACC, HMC
s0_7	16.0	8.30	78	2.8	8.3	-	6.1	6.5	-	-	ACC, HMC
s0_8	22.1	8.32	68	0.8	3.3	-	7.6	8.0	-	-	ACC, HMC
s0_9	30.8	8.33	65	0.4	2.4	-	7.8	8.2	-	-	ACC, HMC
s0_10	39.9	8.38	65	0.2	2.4	-	7.9	8.2	-	-	HMC
s0_11	62.4	8.51	64	0.2	2.3	-	7.9	8.3	-	-	HMC
s0_12	1434.0	8.52	60	0.1	0.9	-	8.3	8.6	-	-	HMC
s0_13	18960.0	8.67	60	0.1	0.2	-	8.5	8.8	-	-	HMC
s0_14	51900.0	8.72	60	0.1	0.2	-	8.5	9.0	-	-	HMC
s0_15	162720.0	8.88	59	0.1	0.3	-	8.5	9.0	-	-	HMC
s0_16	400320.0	9.05	59	0.3	0.2	-	8.5	9.1	-	-	HMC
s0_17	531360.0	9.16	61	0.1	0.1	-	8.6	9.0	-	-	HMC
s10_initial		7.99	99	-	27.2	9.4					
s10_1	0.2	8.35	109	6.5	25.8	9.3	0.5	1.4	0.0	0.2	ACC
s10_2	2.2	8.33	107	6.8	25.2	9.3	0.7	1.6	0.0	0.2	ACC
s10_3	4.3	8.33	106	6.8	25.0	9.3	0.8	1.7	0.0	0.2	ACC
s10_4	7.3	8.31	106	6.5	24.9	9.4	0.8	2.1	0.0	0.3	ACC
s10_5	9.9	8.30	101	6.3	23.7	9.3	1.3	2.2	0.0	0.3	ACC
s10_6	12.5	8.27	92	5.4	17.5	9.0	3.4	3.8	0.1	0.3	ACC, HMC
s10_7	15.1	8.24	81	3.3	10.8	8.5	5.6	5.5	0.3	0.3	ACC, HMC
s10_8	21.2	8.31	71	1.1	4.9	8.2	7.4	7.5	0.4	0.3	ACC, HMC
s10_9	30.4	8.32	67	0.5	3.7	8.2	7.8	7.8	0.4	0.3	ACC, HMC
s10_10	39.5	8.35	66	0.3	3.6	8.2	7.8	7.8	0.4	0.3	HMC
s10_11	62.3	8.46	66	0.2	3.4	8.2	7.8	7.8	0.4	0.3	HMC
s10_12	1414.0	8.51	66	0.1	1.7	8.4	8.4	8.3	0.3	0.2	HMC
s10_13	17520.0	8.57	60	0.1	0.5	8.4	8.7	8.7	0.3	0.2	HMC
s10_14	50460.0	8.66	60	0.0	0.3	8.5	8.8	8.8	0.3	0.2	HMC
s10_15	-	-	-	-	-	-	-	-	-	-	-
s10_16	398880.0	9.01	59	0.1	0.1	9.0	8.8	9.0	0.1	0.2	HMC
s10_17	529920.0	9.12	61	0.1	0.0	8.6	8.8	8.9	0.2	0.2	HMC
s30_initial		7.99	99	-	26.8	26.8					
s30_1	0.3	8.385	110	6.6	25.9	26.6	0.4	1.7	0.1	1.0	ACC
s30_2	2.2	8.374	109	7.3	25.4	26.6	0.5	1.5	0.0	0.6	ACC
s30_3	4.0	8.371	108	7.1	25.2	26.7	0.6	1.5	0.0	0.7	ACC
s30_4	6.9	8.343	106	7.0	24.8	26.6	0.8	1.7	0.1	0.7	ACC
s30_5	9.9	8.295	100	6.3	21.0	26.4	2.1	2.7	0.1	0.7	ACC, HMC
s30_6	12.0	8.298	90	4.6	14.2	25.5	4.4	4.5	0.4	0.7	ACC, HMC
s30_7	14.9	8.299	77	2.8	8.3	24.6	6.3	6.5	0.7	1.0	ACC, HMC
s30_8	21.1	8.305	71	1.0	4.4	24.0	7.4	7.6	0.9	1.0	ACC, HMC
s30_9	30.2	8.326	69	0.5	3.7	24.0	7.6	7.8	0.9	0.7	ACC, HMC
s30_10	38.7	8.365	70	0.3	3.7	24.0	7.6	7.8	0.9	0.9	HMC
s30_11	62.3	8.483	68	0.2	3.6	24.1	7.7	7.8	0.9	0.9	HMC
s30_12	1420.0	8.5	64	0.1	1.8	24.2	8.2	8.4	0.8	0.5	HMC
s30_13	13200.0	8.56	60	0.2	0.3	24.9	8.7	8.7	0.6	0.5	HMC
s30_14	46140.0	8.58	62	0.1	0.1	25.0	8.7	8.9	0.6	0.5	HMC
s30_15	-	-	-	-	-	-	-	-	-	-	-
s30_16	394560.0	8.98	59	0.0	0.1	25.4	8.7	9.2	0.4	0.5	HMC
s30_17	525600.0	9.11	60	0.0	0.2	25.3	8.7	9.0	0.5	0.5	HMC
s30_2_initial		7.98	99	0.0	27.1	27.3					
s30_2_1	0.2	8.39	108	6.6	25.8	27.1	0.5	1.3	0.1	0.6	ACC

s30_2_2	2.2	8.37	109	6.9	25.4	27.3	0.6	1.7	0.0	0.9	ACC
s30_2_3	4.1	8.37	109	6.8	25.1	27.2	0.8	1.7	0.0	0.9	ACC
s30_2_4	6.9	8.33	107	6.9	24.5	27.2	0.9	2.0	0.1	1.0	ACC
s30_2_5	10.0	8.30	96	5.6	18.9	26.5	2.9	3.4	0.3	1.0	ACC, HMC
s30_2_6	12.5	8.30	85	3.5	10.9	25.5	5.5	5.3	0.6	0.9	ACC, HMC
s30_2_7	15.0	8.30	77	2.3	6.9	24.9	6.8	6.7	0.8	0.9	ACC, HMC
s30_2_8	21.3	8.30	71	1.0	3.9	24.4	7.7	7.7	1.0	1.0	ACC, HMC
s30_2_9	30.3	8.33	69	0.4	3.4	24.5	7.9	7.7	0.9	1.0	ACC, HMC
s30_2_10	39.9	8.37	67	0.3	3.3	24.6	7.9	7.8	0.9	1.0	HMC
s30_2_11	62.4	8.48	68	0.2	3.3	24.6	7.9	7.8	0.9	0.9	HMC
s30_2_12	1415.0	8.53	64	0.2	1.5	24.8	8.4	8.3	0.8	0.5	HMC
s30_2_13	16080.0	8.60	60	0.0	0.5	25.2	8.7	8.7	0.7	0.5	HMC
s30_2_14	49020.0	8.68	62	0.0	0.3	25.5	8.8	8.8	0.6	0.5	HMC
s30_2_15	-	-	-	-	-	-	-	-	-	-	-
s30_2_16	397440.0	9.05	63	0.1	0.1	26.4	8.8	9.0	0.3	0.5	HMC
s30_2_17	528480.0	9.18	64	0.0	0.1	27.0	8.8	8.9	0.1	0.5	HMC
s45_initial		8.07	99	-	27.0	45.9					
s45_1	0.2	8.45	109	-	25.1	41.8	-	1.5	-	1.5	ACC
s45_2	2.2	8.43	109	7.1	25.1	45.7	0.7	1.7	0.1	1.6	ACC
s45_3	4.3	8.43	110	7.2	25.1	45.8	0.7	1.5	0.0	1.3	ACC
s45_4	7.0	8.41	109	7.5	24.7	46.1	0.8	1.6	-0.1	1.2	ACC
s45_5	9.9	8.29	101	6.6	20.5	45.4	2.3	3.0	0.2	1.5	ACC, HMC
s45_6	12.7	8.30	83	3.5	10.1	42.7	5.7	5.5	1.1	1.5	ACC, HMC
s45_7	15.2	8.30	77	2.1	6.8	42.0	6.8	6.8	1.3	1.5	ACC, HMC
s45_8	21.1	8.33	73	0.8	4.8	41.6	7.4	7.4	1.4	1.6	ACC, HMC
s45_9	30.3	8.32	71	0.4	4.6	41.9	7.4	7.4	1.3	1.7	ACC, HMC
s45_10	38.9	8.36	71	0.7	4.6	41.8	7.4	7.4	1.4	1.8	HMC
s45_11	61.1	8.46	70	0.3	4.3	41.9	7.5	7.5	1.3	1.6	HMC
s45_12	1420.0	8.51	68	0.1	2.1	42.2	8.2	8.2	1.2	0.8	HMC
s75_initial		7.98	101	-	26.9	74.3					
s75_1	0.2	8.46	112	7.3	25.9	73.9	0.3	1.5	0.2	2.4	ACC
s75_2	2.1	8.45	112	7.7	25.4	74.1	0.5	1.4	0.1	2.0	ACC
s75_3	4.1	8.45	110	7.7	25.3	74.1	0.6	1.7	0.1	2.6	ACC
s75_4	7.0	8.41	110	7.6	24.4	73.7	0.9	1.9	0.2	2.7	ACC
s75_5	9.9	8.25	96	6.4	16.6	71.6	3.6	3.8	1.0	2.4	ACC, HMC
s75_6	12.0	8.30	88	3.9	11.0	69.9	5.4	5.5	1.5	2.1	ACC, HMC
s75_7	15.0	8.30	79	2.3	7.7	68.7	6.5	6.6	1.9	2.3	ACC, HMC
s75_8	21.1	8.32	76	0.9	6.0	67.8	7.0	7.0	2.2	2.6	ACC, HMC
s75_9	30.2	8.32	75	0.6	5.9	67.8	7.0	7.0	2.2	2.3	ACC, HMC
s75_10	39.3	8.37	74	0.4	5.8	68.1	7.0	7.0	2.1	2.6	HMC
s75_11	62.4	8.48	71	0.2	5.7	68.4	7.0	7.1	2.0	2.5	HMC
s75_12	1405.0	8.48	67	0.1	3.6	68.2	7.7	7.8	2.0	1.3	HMC
s75_13	14640.0	8.52	63	0.1	1.3	69.1	8.4	8.4	1.7	1.4	HMC
s75_14	47580.0	8.57	63	0.1	0.7	69.5	8.6	8.7	1.6	1.2	HMC
s75_15	158400.0	8.77	62	0.4	0.3	69.7	8.7	8.9	1.5	1.1	HMC
s75_16	396000.0	9.02	60	0.0	0.1	70.9	8.7	9.1	1.1	1.2	HMC
s75_17	527040.0	9.14	62	0.0	0.1	71.3	8.7	9.0	1.0	1.1	HMC
s90_initial		8.03	100	-	27.1	92.0					
s90_1	0.2	8.52	110	7.4	25.4	90.1	0.6	1.3	-	2.7	ACC
s90_2	2.2	8.51	111	8.1	25.4	91.9	0.6	1.4	0.0	2.5	ACC
s90_3	4.1	8.49	112	7.9	25.2	92.3	0.7	1.5	-0.1	2.9	ACC
s90_4	6.9	8.40	109	7.9	24.1	91.8	1.1	1.8	0.1	2.7	ACC
s90_5	10.0	8.26	92	5.3	14.1	88.1	4.5	4.5	1.3	3.0	ACC, HMC
s90_6	12.3	8.31	83	3.2	9.1	86.1	6.1	6.1	2.0	2.5	ACC, HMC
s90_7	14.9	8.31	79	1.9	7.1	85.5	6.7	6.7	2.2	3.0	ACC, HMC
s90_8	21.1	8.33	76	0.8	6.1	84.8	7.0	6.9	2.4	3.1	ACC, HMC
s90_9	30.3	8.34	75	0.5	6.0	85.2	7.0	6.9	2.3	2.9	ACC, HMC
s90_10	39.1	8.37	73	0.3	5.8	85.3	7.1	6.9	2.2	3.0	HMC
s90_11	61.4	8.46	74	0.3	5.7	85.6	7.1	7.0	2.1	2.9	HMC
s90_12	1430.0	8.51	70	0.2	3.0	85.2	7.9	7.9	2.2	1.4	HMC
s90_13	13440.0	8.54	63	0.1	1.1	86.9	8.5	8.4	1.7	1.4	HMC
s90_14	46380.0	8.61	62	0.0	0.3	87.5	8.7	8.7	1.5	1.5	HMC
s90_15	-	-	-	-	-	-	-	-	-	-	-
s90_16	394800.0	9.08	60	0.0	0.1	90.8	8.8	9.0	0.4	1.4	HMC
s90_17	525840.0	9.20	63	0.0	0.1	91.1	8.8	8.9	0.3	1.2	HMC

ACC…amorphous calcium carbonate
HMC…high-Mg calcite

The evolution of aqueous Ca concentration (Fig. 6A) and alkalinity (Table 1) of the reactive solution is characterized by a sudden concentration increase caused by ACC addition into the reactor (stage I). The Ca concentrations increase from zero to ~6-8 mM, and remain almost constant during stage I until ACC transformation to HMC was initiated. The alkalinity concentrations increase from ~100 to 107-112 mM and remain almost constant up to 4-7 min of reaction time. This first stage is followed by a substantial and rapid decrease of Ca concentration in the reactive solutions corresponding to HMC formation (stage II). During stage II the Ca concentrations drop to lower values within 30 min of reaction time, in all experiments. The alkalinity concentrations level off achieving steady state concentrations with values between ~65 and 75 mM depending on the SO_4 concentration of each run (see Table 1). The initial increase in Ca and alkalinity concentrations immediately after the addition of ACC into the reactors can be assigned to the rapid dissolution of the amorphous solid. Indeed, the SI_{ACC*} values document that the reactive solution achieves rapidly chemical equilibrium with respect to ACC (SI_{ACC*} about 0; see Fig. 6C and Table S1). The positive correlation between total Ca and SO_4 concentrations of the reactive solution during stage I points towards enhanced ACC dissolution with increasing SO_4 concentration, which is also indicated by the positive correlation between pH and SO_4 concentration during stage I (Fig. S6). The release of Ca into the solution, however, results in increasing oversaturation with respect to other $CaCO_3$ polymorphs, such as calcite and aragonite, as it can be seen in Table 1. Note that although during stage I and up to 10 min of reaction time the reactive solutions are supersaturated with respect to hydromagnesite ($Mg_5(CO_3)_4(OH)_2 \cdot 4H_2O$), this mineral phase is not detected by mineralogical analyses. Other hydrated Mg-carbonate phases such as nesquehonite ($MgCO_3 \cdot 3H_2O$) and dypingite ($Mg_5(CO_3)_4(OH)_2 \cdot 8H_2O$) are undersaturated in all the reactive solutions as well as gypsum ($CaSO_4 \cdot 2H_2O$) and bassanite ($CaSO_4 \cdot 0.5H_2O$) (see Table S1).
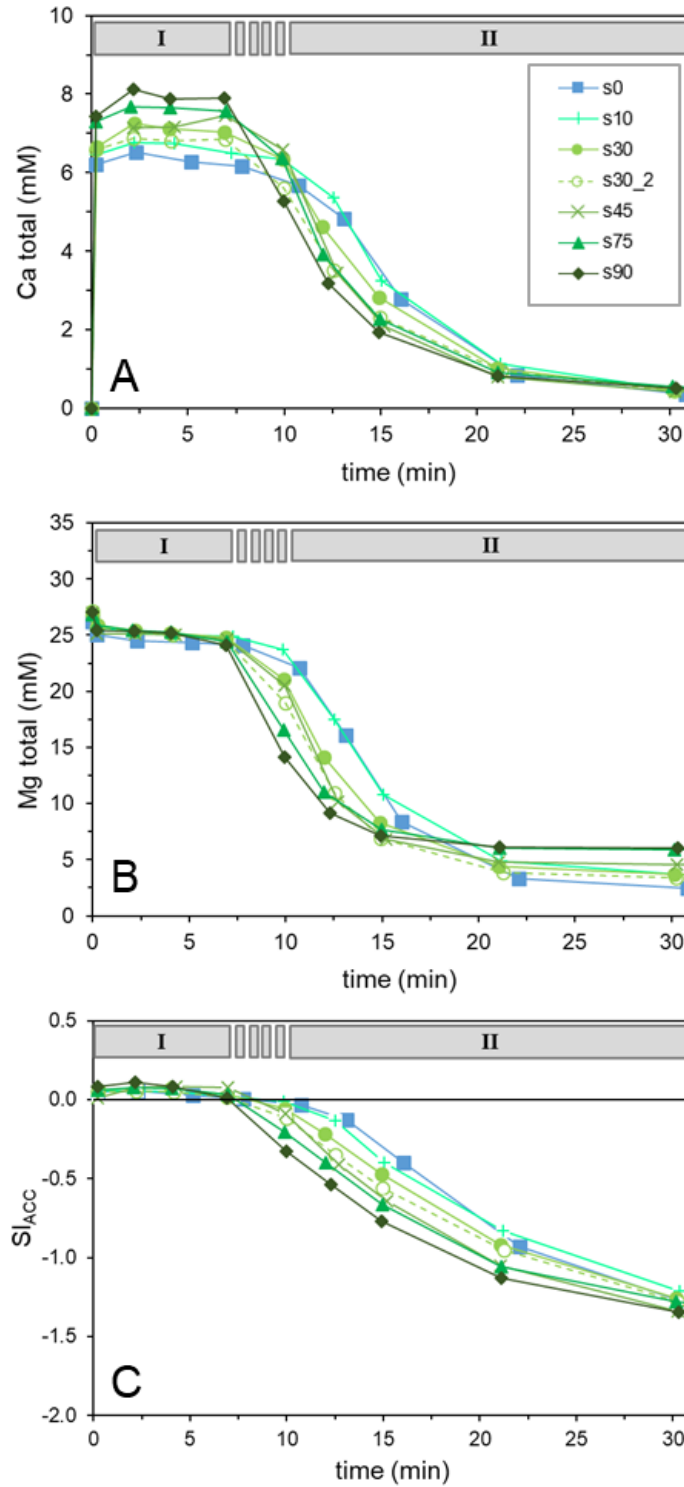
Fig. 6: A, B) Temporal evolution of the Ca and Mg concentration of the reactive solution and C) saturation indices (SI) in respect to ACC containing 0.6 mol% Mg within 30 min of reaction time – stage (I) and (II).

67

In Fig. 6B, it can be seen that in all experimental runs, the initial aqueous Mg concentration (~27 mM) decreases slightly to ~25 mM immediately after the introduction of ACC in the reactors and remains quasi constant during stage I until the onset of the ACC transformation. During the transformation of ACC to HMC (stage II) the temporal evolution of Mg concentration in the reactive solution exhibits a behaviour similar to that of Ca. Up to ~22 min of reaction time the aqueous Mg concentration is reduced rapidly to ~3-6 mM and drops afterwards at a slower rate towards zero values until the end of the experimental runs after 1 year. In experiments containing SO_4, the temporal evolution of SO_4 concentrations follows the same pattern as Mg concentrations in stage I and II (Table 1). After ACC was introduced into the reactors the SO_4 concentrations decrease slightly (stage I) and drop significantly during the transformation (stage II). In contrast to the behaviour of Mg, the SO_4 concentrations increase continuously during stage III until the end of the experiments after 1 year.

Speciation calculations indicate that concentrations of free aqueous Ca^{2+} and Mg^{2+} ions account for 60-35% and 75-45% of their total concentrations respectively, depending on the SO_4 concentration in each experiment (Table S1). The abundance of both Ca^{2+} and Mg^{2+} decreases with increasing SO_4 concentration. In particular, the prevailing Mg^{2+}/Ca^{2+} ratio of the reactive solution (Table S1) follows a clear trend as a function of SO_4 concentration and is decreasing slightly with increasing SO_4 concentrations during stages I and II. However, the Mg^{2+}/Ca^{2+} ratio of the reactive solutions remains almost constant during the ACC transformation and abruptly levels up to higher values towards the end of stage II after 15-20 min of reaction time.

Apparent precipitation rates (r_i) were calculated from the first derivative of the sum of Ca^{2+} and Mg^{2+} concentration of the reactive solution with respect to time, from the onset of ACC transformation to the attainment of quasi constant aqueous concentrations, using the equation

$$r_i = \frac{dc_{(Ca^{2+}+Mg^{2+})}}{dt} \tag{5}$$

where $c_{Ca^{2+}+Mg^{2+}}$ stands for the sum of Ca^{2+} and Mg^{2+} concentrations in the reactive solution and t designates time. In this study, the apparent precipitation rate (r_i) describes the transfer of ions from the reactive solution to the crystalline solid phase during stage II (sub-samples collected within the time interval of 4 to 22 min). Note here that r_i refers to

68

bulk composition of precipitated solid during stage II without considering proportion of amorphous and crystalline material. The calculated precipitation rates are plotted as a function of SO_4 concentration in Fig. 7. The precipitation rate during the ACC transformation (stage II) was lower when the SO_4 concentration was higher. The obtained results suggest that there is a linear correlation between the apparent precipitation rate during stage II and the initial SO_4 concentration of the reactive solution that can be described by the linear equation

$$r_i \ (mM/min) = -0.0055(\pm0.0003) \times SO_4 \ (mM) + 1.2184(\pm0.0157); \ R^2 = 0.98 \qquad (6)$$
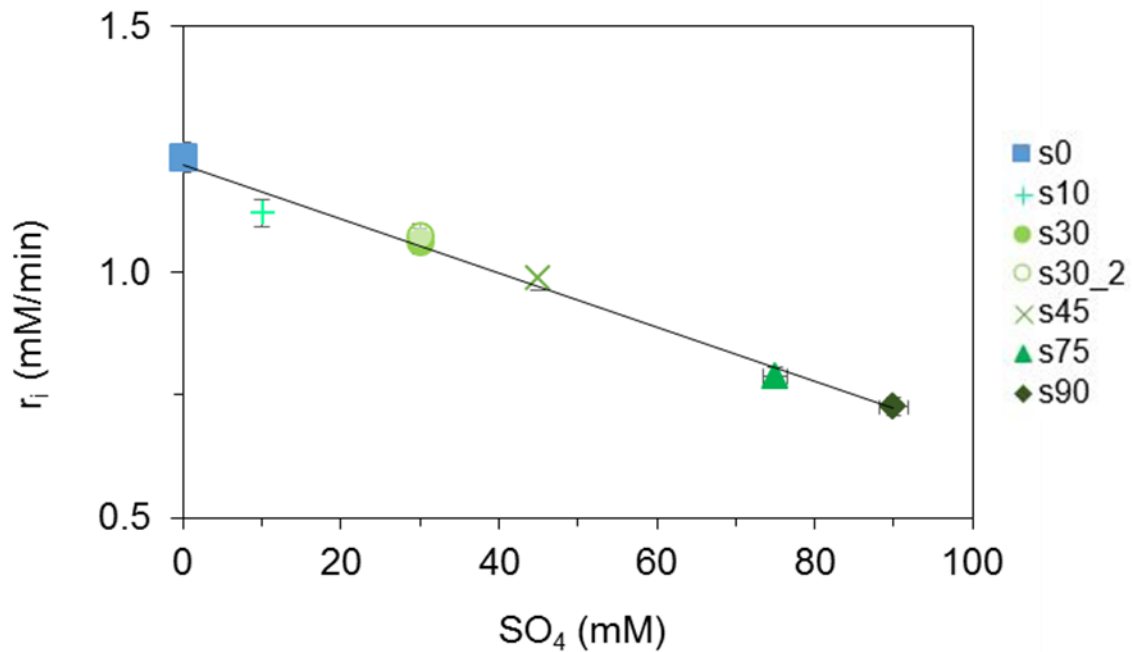
Fig. 7: Apparent precipitation rate (r_i) during stage II plotted as a function of initial sulfate concentration in the reactive solution.

The temporal evolution of Mg and SO_4 in the reactive solutions displayed as cumulative loss (in %) can be seen in Fig. 8. The results show a continuous decrease of Mg concentration and a continuous increase of SO_4 concentration in the reactive solution during stage III where HMC is the only mineral present. Notably, after 1 month of reaction time the Mg concentration of the reactive solution decreases already about 99 % compared to its initial concentration in the reactors.

69
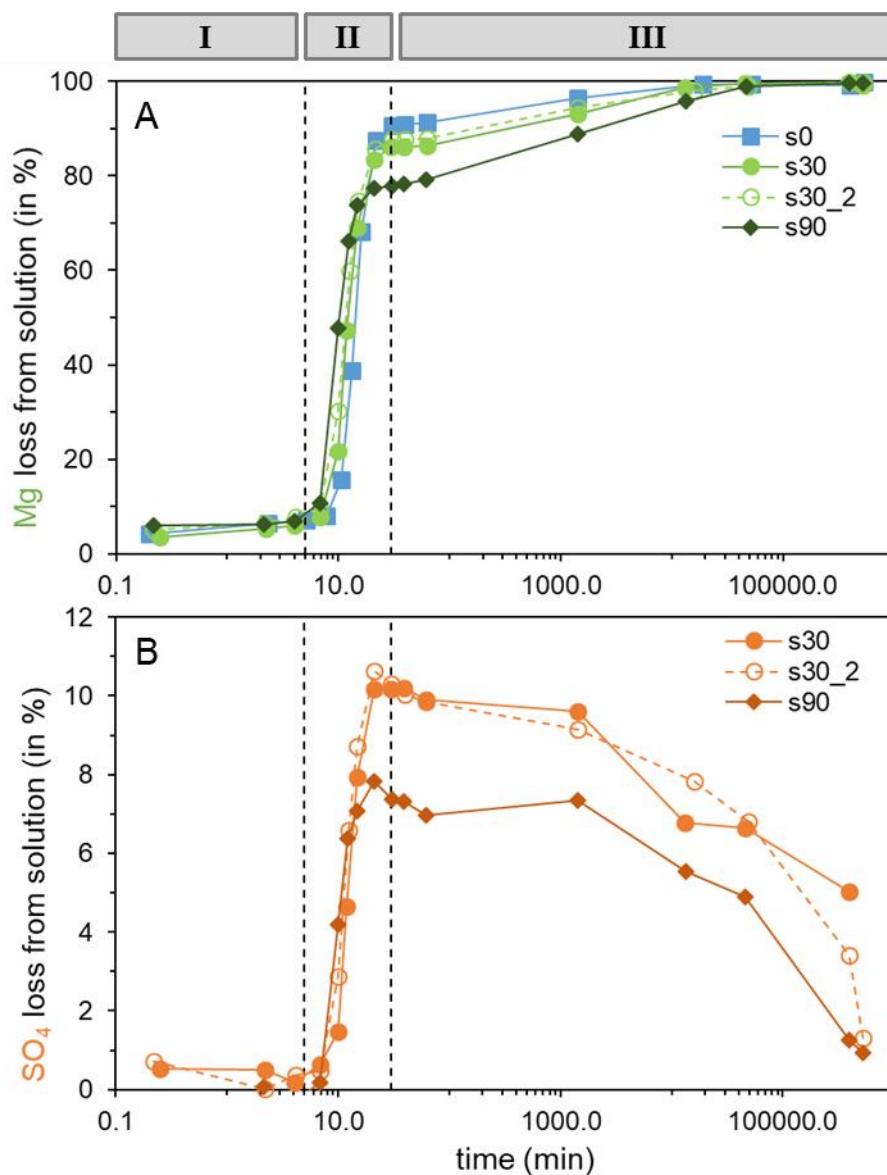
Fig. 8: Long-term chemical evolution up to 1 year of reaction time A) Mg concentration, B) SO_4 concentration.

3.3.3 Chemical evolution of solid phases

After ACC is introduced into the solution, it instantly uptakes Mg and SO_4 (Table 1). Actually, in all the experiments within the first 4 min of reaction time (stage I), the Mg content of ACC is 0.6 ± 0.2 mol%. The SO_4 content of ACC lies within 0 and 0.1 mol% for all amorphous solid samples and does not exhibit a significant trend as a function of SO_4 concentration or reaction time. The Mg content of ACC is independent from the initial SO_4 concentration in the reactive solution, as well as from the SO_4 content of the ACC, which is shown in Fig. 9A.

70
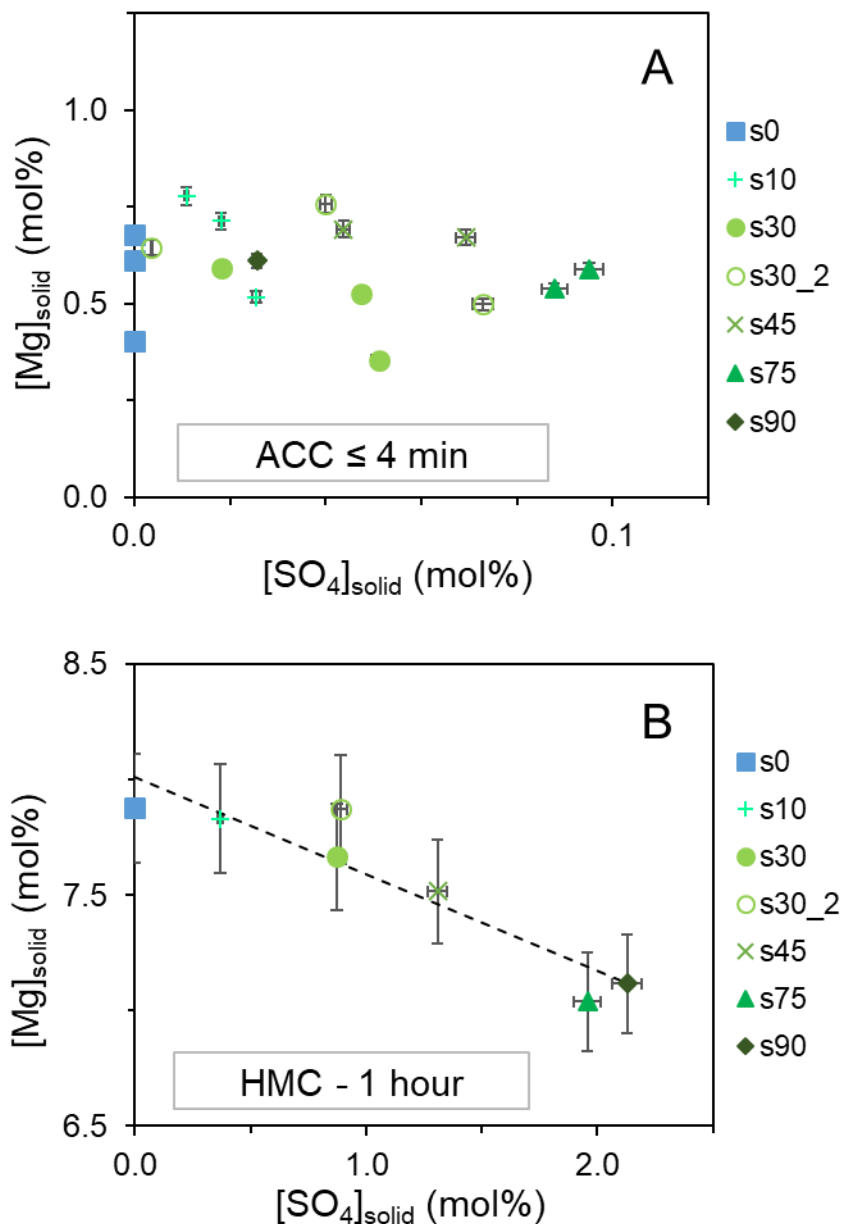
Fig. 9: Chemical composition of the solids during stage I and III. A) Mg and SO_4 contents of ACC within 4 min of reaction time show no correlation. B) Mg and SO_4 contents of HMC collected after 1 hour of reaction time show an anticorrelation.

After the onset of ACC transformation (stage II), a rapid increase of Mg and SO_4 contents of the solids is observed. After 1 hour of reaction time (stage III), HMC is the only solid phase that was identified. The Mg content of this calcite is ranging from 7 to 8 mol% and SO_4 content from 0 to 2 mol%. The Mg content of calcite formed via ACC exhibits a linear anticorrelation with its SO_4 content, whereas the SO_4 content is positively correlated with

the initial SO_4 concentration of the reactive solution (Fig. 9B). During stage III, the Mg content of calcite is continuously increasing whereas its SO_4 content is continuously decreasing (Table 1).

High-resolution element distribution images of cross-sectioned HMC aggregates collected after 1 day and 1 year of reaction time show a homogeneous distribution of Mg and SO_4 (represented by S) within and between the HMC aggregates (Fig. 10 and Fig. S7). The average contents of Ca, Mg and SO_4 are calculated in mol% and listed in Table S2. The extent of Mg and SO_4 contents estimated by WDS analysis of selected HMC samples is in reasonable agreement with the elemental contents estimated by mass balance calculation and bulk measurement after solid digestion.
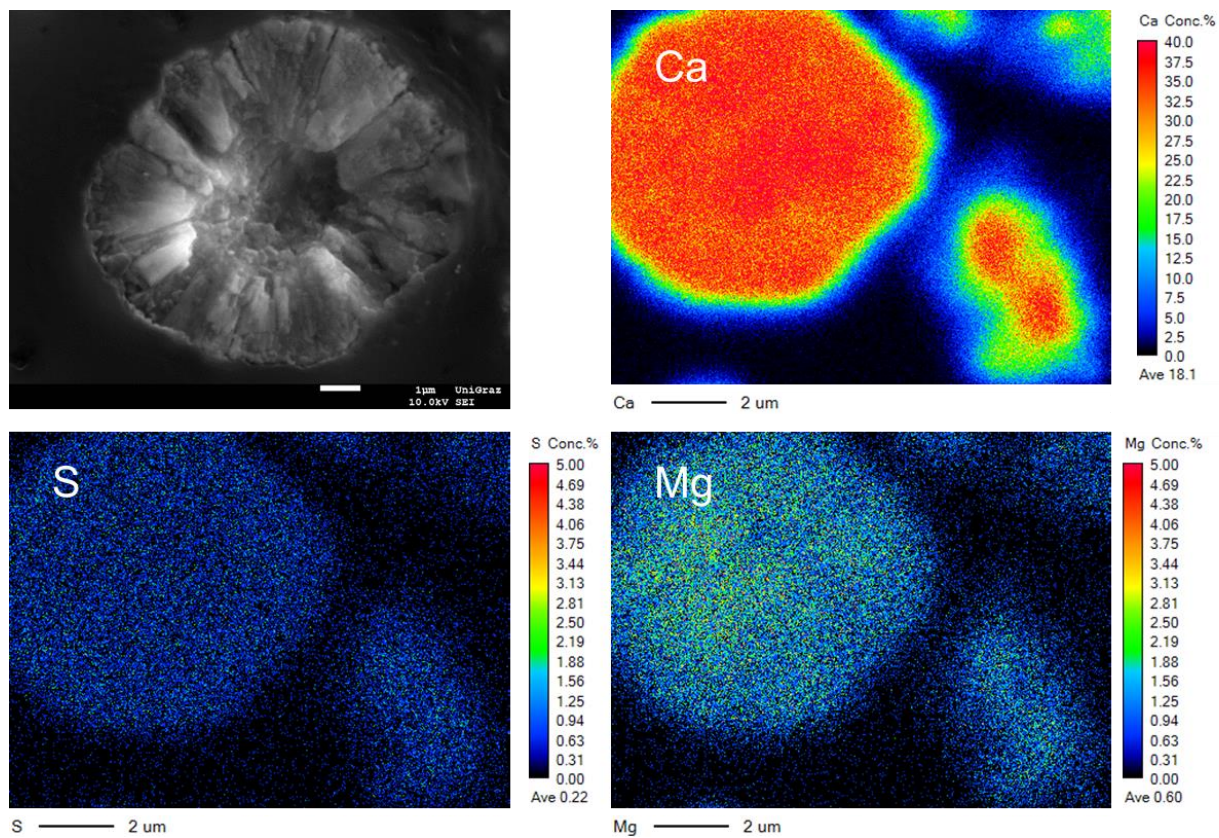
Fig. 10: Element distribution images of HMC collected after 1 day of reaction time (s90_12).

3.4 Discussion

3.4.1 Reactivity of ACC

An interesting feature observed in this study is the change in the chemical composition of the amorphous phase as soon as it comes in contact with the reactive solution, although no transformation to crystalline phase occurs. Indeed, immediately after the addition of synthetic ACC into the reactive solutions, up to 3 wt.% of this solid dissolved until the solution reached saturation with respect to this phase (Fig. 6C). At the same time, the remaining amorphous solid became enriched in Mg and SO_4 (Table 1 and Fig. 9A) owing to a highly dynamic exchange of solutes between the solution and the solid phase ($\leq$ 0.2 min), similar to that observed earlier by Purgstaller et al. (2019). Goodwin et al. (2010) have shown that ACC consists of a nanoporous framework that supports interconnected channels containing water and carbonate molecules. This nanoporous structure of ACC provides large surface areas (Sun et al., 2018; 2019) for fast exchange of solutes between the ACC and the reactive solution. Likely the presence of this network explains the enrichment of the bulk amorphous solid in Mg and SO_4 (Table 1).

The observed enrichment of ACC in Mg and SO_4 however, is not simply due to the presence of these ions in the pore fluid, but actual substitution in the structure of the solid. Evidence to this is provided from the infrared spectra of ACC which was sampled from the experiments performed in the presence of SO_4^{2-}(aq). The incorporation of SO_4 in the solid phase reveals a broad band at 1134/1160 cm^{-1} besides the characteristic vibration bands of CO_3 (Fig. 4). This band can be assigned to internal v_3 vibrations of SO_4, similar to that observed in SO_4-bearing synthetic calcite (Takano et al., 1980). The distinct difference of the position of this band to that of the v_3 vibrational band of SO_4^{2-}(aq) species at 1100 cm^{-1} (Hug, 1997; Wei et al., 2005), suggests that SO_4 in ACC cannot be assigned to SO_4^{2-}(aq) within the nanoporous network of ACC, but is rather incorporated in the bonding environment of the solid phase. The same can be suggested for the presence of Mg in ACC structure. Indeed in agreement with the earlier observations by Huang et al. (2018) a shift of v_1 from 1074 cm^{-1} towards higher frequencies at 1075 cm^{-1} was recorded in the collected FTIR spectra. This distinctive but small shift denotes a distortion of the short-range order of ACC. Note here, vibration bands of other Mg-bearing phases (e.g. brucite, hydromagnesite) were not detected by *in situ* Raman or FTIR at any time during the experimental runs hence the Mg loss in the reactive solution can only be assigned to the transfer of Mg from the solution to the amorphous phase.

3.4.2 Controls of aqueous complexation on ACC transformation to HMC

An interesting finding of this study is that the synthetic ACC, added into the HCO_3-Mg-(SO_4^-)bearing solutions, exhibits a prolonged stability of up to 12 minutes (experiment s0) before it transforms into HMC (Fig. 3). This behavior comes in contrast to earlier observations suggesting instant ACC transformation ($\leq$ 30 sec) into crystalline calcium carbonate polymorphs (e.g. vaterite and calcite) in an additive-free aqueous solution (Bots et al., 2012; Rodriguez-Blanco et al., 2012). Similarly, the stability of ACC in this study cannot be assigned to the presence of Mg in the amorphous solid as it was suggested earlier by Lin et al. (2015). In their study, the structural water bound to Mg ions was suggested to increase considerably the activation energy associated with the dehydration of ACC; a process that has been described to occur before crystallization (Ihli et al., 2014) and is based on the fact that Mg dehydration rate (10^5 s^{-1}) is 4 orders of magnitude slower compared to Ca (10^9 s^{-1}) (Lincoln and Merbach, 1995; Bleuzen et al., 1997).

Within the experimental runs of this study, the initially Mg-free ACC, is becoming enriched in Mg within the first 4 min of reaction time, however, it exhibits the same content of 0.6 ±0.2 mol% Mg (Fig. 9A) in all the experimental runs. Yet as it can be seen in Fig. 3A, the onset of transformation of ACC to crystalline material is varying among the experimental runs and is associated with the concentration of $MgSO_4^0$ in the reactive solution. Note here, that during the transformation when ACC dissolves and HMC is forming, all solutions are undersaturated with respect to calcium sulfate phases such as gypsum and bassanite (Table S1) and the presence of calcium sulfate phases was not confirmed by Raman, FTIR, XRD or SEM. The obtained results suggest that ACC transformation to HMC is controlled by the abundance of Mg^{2+}(aq), which is a function of SO_4^{2-} concentration in experimental runs of this study. Indeed, in the present study, the initial total Mg concentration was the same in all the experiments (~27 mM; Table 1), but the presence of SO_4 strongly reduced the concentration of free Mg ions, Mg^{2+}(aq), due to the formation of the $MgSO_4^0$ aquo complex (Table S1). In the experiment with the highest SO_4 concentration (i.e. s90; 90 mM) Mg^{2+}(aq) represents only 44% of the total Mg concentration, whereas in the SO_4-free experiment (s0) Mg^{2+}(aq) accounts for 73% of the total Mg concentration. Indeed, the obtained linear correlation between the concentration of Mg^{2+}(aq) and the onset of HMC formation (Fig. 3B) indicates that the delay of ACC transformation is strongly controlled by the retarding effect of aqueous Mg^{2+} on calcite

nucleation (Fernández-Díaz et al., 1996; Du and Amstad, 2020). In contrast, SO_4^{2-}(aq) is not retarding the nucleation of calcite, as it is indicated by the reverse trend between SO_4 concentration and the onset of HMC formation (Fig. 3A). Thus, the formation of $MgSO_4^0$ aquo complexes, is the factor controlling the abundance of Mg^{2+}(aq) and subsequently the nucleation of HMC (Fig. 3B).

The obtained results allow the quantification of the effect of dissolved SO_4 on the transformation of ACC to HMC, using the apparent HMC precipitation rate (r_i). As it is illustrated in Fig 6, r_i decreases with increasing SO_4 concentrations in the reactive solutions (Table 2). Considering that crystalline HMC growth proceeds via ion-by-ion addition of dissolved chemical species to advancing steps at the crystal surface (Burton et al., 1951), complexation of SO_4 with aqueous Ca^{2+} and Mg^{2+} is effectively reducing their abundance in the reactive solution (see Table S1) which results in a decreased apparent precipitation rate (Fig. 7). Similar, Han et al. (2017) observed decreased precipitation rates of Mg calcite and aragonite in the presence of $MgSO_4$ and comparable behavior has been seen from results by Nielsen et al. (2016) using a constant composition experimental approach to monitor the individual and combined effects of Mg^{2+} and SO_4^{2-}. Moreover, higher SO_4 concentrations caused lower Mg^{2+}/Ca^{2+} ratios at the time of transformation and resulted in reduced Mg uptake of HMC during transformation (Fig. 9B), an observation that comes in agreement with that of Purgstaller et al. (2021) who found that the prevailing Mg^{2+}/Ca^{2+} ratio of the reactive solution at the time of transformation is the main controlling parameter for enhanced Mg incorporation in HMC.

Previous ACC transformation experiments have shown that the mineralogy of the crystalline product is controlled by the prevailing physicochemical parameters of the experimental solution including pH, temperature and Mg^{2+}/Ca^{2+} ratio (Blue et al., 2017; Purgstaller et al. 2017a; Purgstaller et al., 2017b; Konrad et al., 2018). In the present study, a prevailing Mg^{2+}/Ca^{2+} ratio between 4 and 5 yielded into the formation of HMC, which is in good agreement with results obtained by Blue et al. (2017) and Purgstaller et al. (2017a). Variations in SO_4 concentrations (10-90 mM) had no effect on the pathway of ACC transformation and HMC has been the only resulting crystalline phase. This behaviour comes in contrast to mineral growth experiments where inhibitory effects on low-Mg calcite growth have been observed in the presence of SO_4 ions, promoting aragonite formation instead of calcite (Goetschl et al., 2019), an observation that has important consequences for the interpretation of temporal variations of the primary $CaCO_3$ polymorph in marine environment (Bots et al., 2011). However, the SO_4/CO_3 ratios

of the experimental solutions in which an inhibiting effect on calcite formation was observed have been considerably higher compared to the current experimental conditions.

3.4.3 HMC formed via ACC and implications for natural carbonates

The most interesting feature of this study is that the Mg content of the nanocrystalline HMC is increasing during the whole duration of stage III that lasted until the end of the experimental runs after 1 year of reaction time. The fast precipitation of HMC (10^{-5} mol sec^{-1}) resulted in the formation of aggregates with nanometer sized crystal subunits and a radial-columnar internal structure. The HMC that was initially formed after the transformation of ACC was likely highly porous (Fig. 5B) and its Mg content was affected by both precipitation kinetics (e.g. Mavromatis et al., 2013; Goetschl et al., 2019) and prevailing Mg^{2+}/Ca^{2+} ratio (e.g. Mucci and Morse, 1983; Blue et al. 2017; Purgstaller et al., 2021). In the experimental runs of this study both growth kinetics and Mg^{2+}/Ca^{2+} ratio are affected by the aqueous SO_4 concentration (Fig. 7 and Table S1).

After the complete transformation of ACC into HMC, however, the crystalline solids exhibit changes in their Mg and SO_4 content as a function of time in a process that occurs during the whole duration of the experimental runs up to 1 year of reaction time as it can be seen in Fig. 8. These changes in chemical composition suggest a continuous exchange reaction between solid and solution following a process that is likely controlled by the high reactive surface of the solid as it is evidenced by the high porosity of the nanocrystalline material (Fig. 5B and Fig. S5). Indeed, the measured specific surface area of ACC and nanocrystalline calcite are typically high between 14 and 42 m^2/g (Schultz et al., 2013; Radha and Navrotsky, 2015; Konrad et al., 2016). Interestingly, the continuous enrichment of the solid in Mg during stage III is accompanied by a decrease of its SO_4 content (Table 1; Fig. 8). The Mg-SO_4-anticorrelation of calcite samples observed in this study becomes more pronounced when the reactive solutions achieve chemical compositions that reflect near thermodynamic equilibrium conditions (Table S1). This process is likely related to the contrasting effect caused by the presence of Mg and SO_4 in the crystall lattice of calcite. Indeed, the incorporation of Mg into calcite is causing unit cell contraction (Paquette and Reeder, 1990), whereas the uptake of SO_4 into calcite results in unit cell expansion (Kontrec et al., 2004). As such the enrichment of both ions in nanocrystalline calcite derived from ACC is rather unlikely to occur, a feature which has also been observed during seeded growth of low-Mg calcite (Goetschl et al., 2019).

The continuous exchange of Mg and SO$_4$ between the solid and the reactive solution is affecting the total mass of the nanocrystalline aggregates with a homogeneous distribution of Mg and SO$_4$ and is not limited only to the outer rim of the aggregates. This is evident from the comparison of the elemental distribution maps of calcite collected after 1 day (Fig. 10; Table S2) and after 1 year (Fig. S7; Table S2) in the experiment s90. This observation has major implications for the interpretation of chemical signals in natural carbonates that form via an amorphous precursor, especially if they remain in contact with an aqueous fluid after their initial formation and subsequent transformation. For example, Littlewood et al. (2017) have shown elevated concentrations of Sr in calcite formed from an amorphous precursor. Similar to the behavior of SO$_4$ in our study it is likely that the high Sr content in ACC derived calcite is not retained after longer period of contact with an aqueous phase. Earlier studies have shown that up to 10 unit cells below crystal surface can participate in elemental and isotope exchange between a carbonate mineral phase and the reactive solution (Stipp et al., 1998; Mavromatis et al., 2016; 2017c). In contrast the homogeneous distribution of Mg in calcite that was observed in this study (Fig. 10 and Fig. S7; Table S2) suggest that the chemical composition of the solid would not be preserved, if the composition of the fluid phase is significantly altered. Similar observations have been made for HMC formed from an amorphous precursor using Mg and O isotopes (Mavromatis et al., 2017b; Dietzel et al., 2020). These earlier studies suggest that rapidly after transformation from ACC to calcite isotopic equilibrium is achieved and no information of the isotopic signals of the amorphous precursor is recorded. Considering that ACC precursors commonly occur during the formation of biominerals (Addadi et al., 2003; Du and Amstad, 2020) but also in inorganic environments such as speleothems (Demény et al., 2016), the obtained results suggest that caution is needed for the interpretation of their chemical and likely isotopic signals as environmental proxies.

Additionally the results of this study suggest that nanostructured HMCs with high internal porosity that frequently form in natural environments have a considerable potential for secondary changes of their geochemical signature due to occurring mineral-fluid interactions. Carbonates are subject to variable degrees of post-depositional/post-mortem alteration which may be easily intensified and accelerated if the mineral owns a large reaction surface for ion exchange (Pederson et al., 2020). Hence, determining and quantifying secondary exchange reactions during mineral-fluid interactions of nanocrystalline HMC is urgently required to define the robustness of geochemical

proxies obtained from these solids. On a different view, these nanocrystalline HMCs may indicate distinct reaction pathways and/or environmental conditions of the storage and transformation media.

3.5 Conclusions

In this study we examined the transformation of synthetic ACC in reactive solution containing ~27 mM Mg and variable SO_4 concentrations up to 90 mM. In these experiments, the solid remained in contact with the reactive solution - after the transformation of ACC into HMC - for 1 year and it was characterized for its chemical and mineralogical composition. The obtained results suggest that aqueous complexation of Mg^{2+} with SO_4^{2-} and the formation of $MgSO_4^0(aq)$ is the factor controlling the stability of ACC in the reactive solution. Indeed calcite nucleation is a function of free Mg^{2+} ion concentration in the reactive solution and the formation of $MgSO_4^0$ aquo complexes reduces its availability and subsequently allows for earlier transformation of the amorphous phase to calcite. The nanocrystalline HMC formed from ACC exhibits a homogeneous distribution of Mg and SO_4 as it was revealed by electron microprobe. Interestingly, HMC remained nanocrystalline after 1 year in contact with the reactive solution, but became progressively enriched in Mg and depleted in SO_4. These changes in chemical composition affecting the total mass of the HMC aggregates suggest a continuous exchange process between solid and solution as long as they are in contact. The findings of this study suggest that calcite formed via an amorphous precursor may still be highly reactive in exchanging compounds and as such the chemical and isotopic signals recorded at the time of mineral formation can be reset by interacting with natural fluids of different chemical and/or isotopic composition during and after deposition.

3.6 Supplementary material

Table S1: Concentrations of free and complexed aqueous species and saturation indices (SI) of sampled reactive solutions calculated using PHREEQC.

Sample	Ca^{2+} (mM)	Mg^{2+} (mM)	CO_3^{2-} (mM)	SO_4^{2-} (mM)	$MgSO_4^0$ (mM)	SI_{ACC}*	$SI_{calcite}$	$SI_{aragonite}$	SI_{gypsum}	$SI_{bassanite}$	Mg^{2+}/Ca^{2+}	Ca^{2+} (%)	Mg^{2+} (%)
s0_initial	-	20.1	0.9	-	-						-	-	76.8
s0_1	3.8	18.4	1.9	-	-	0.0	2.2	2.1	-	-	4.80	61.6	73.4
s0_2	4.0	18.0	1.8	-	-	0.1	2.3	2.1	-	-	4.47	61.6	73.3
s0_3	3.9	17.9	1.8	-	-	0.0	2.2	2.0	-	-	4.60	62.1	73.7
s0_4	3.9	17.9	1.7	-	-	0.0	2.2	2.0	-	-	4.61	62.8	74.3
s0_5	3.6	16.5	1.7	-	-	0.0	2.2	2.0	-	-	4.59	63.1	74.5
s0_6	3.1	12.2	1.5	-	-	-0.1	2.1	1.9	-	-	3.88	64.9	76.0
s0_7	1.9	6.5	1.4	-	-	-0.4	1.8	1.6	-	-	3.48	67.6	78.1
s0_8	0.6	2.6	1.3	-	-	-0.9	1.3	1.1	-	-	4.52	69.1	79.7
s0_9	0.3	2.0	1.3	-	-	-1.3	0.9	0.7	-	-	7.53	70.9	80.2
s0_10	0.2	1.9	1.4	-	-	-1.4	0.8	0.6	-	-	11.37	69.5	79.9
s0_11	0.1	1.8	1.8	-	-	-1.5	0.7	0.5	-	-	14.80	69.7	78.7
s0_12	0.1	0.7	1.7	-	-	-1.7	0.5	0.3	-	-	10.72	71.6	79.5
s0_13	0.1	0.1	2.3	-	-	-1.7	0.5	0.3	-	-	2.34	66.9	78.5
s0_14	0.0	0.1	2.5	-	-	-1.8	0.4	0.2	-	-	3.14	65.6	75.4
s0_15	0.0	0.2	3.2	-	-	-2.2	0.0	-0.2	-	-	18.02	12.4	73.9
s0_16	0.2	0.2	4.1	-	-	-1.0	1.2	1.0	-	-	1.04	59.4	71.0
s0_17	0.1	0.0	5.0	-	-	-1.2	1.0	0.8	-	-	0.58	53.7	75.6
s10_initial	-	19.7	0.9	5.4	1.6						-	-	72.4
s10_1	3.7	17.8	2.0	5.2	1.4	0.1	2.3	2.1	-1.2	-1.8	4.78	57.6	68.9
s10_2	3.9	17.5	1.9	5.2	1.3	0.1	2.3	2.1	-1.2	-1.7	4.45	58.2	69.5
s10_3	3.9	17.4	1.9	5.2	1.3	0.0	2.2	2.1	-1.2	-1.7	4.42	58.4	69.6
s10_4	3.8	17.4	1.8	5.3	1.3	0.0	2.2	2.0	-1.2	-1.7	4.55	58.6	69.8
s10_5	3.8	16.7	1.7	5.2	1.3	0.0	2.2	2.0	-1.2	-1.8	4.43	59.6	70.6
s10_6	3.3	12.6	1.5	5.3	1.0	-0.1	2.1	1.9	-1.2	-1.8	3.82	61.4	72.0
s10_7	2.1	7.9	1.3	5.3	0.6	-0.4	1.8	1.6	-1.4	-2.0	3.85	63.4	73.6
s10_8	0.7	3.6	1.3	5.3	0.3	-0.8	1.4	1.2	-1.9	-2.5	4.96	64.6	74.6
s10_9	0.3	2.8	1.3	5.3	0.2	-1.2	1.0	0.8	-2.3	-2.8	9.03	65.6	75.2
s10_10	0.2	2.7	1.3	5.4	0.2	-1.4	0.8	0.6	-2.5	-3.0	14.09	64.7	75.1
s10_11	0.1	2.6	1.7	5.4	0.2	-1.5	0.6	0.5	-2.7	-3.3	23.58	62.2	74.1
s10_12	0.1	1.2	1.8	5.6	0.1	-1.7	0.5	0.3	-2.8	-3.4	16.55	63.6	73.5
s10_13	0.0	0.4	1.9	5.7	0.0	-1.9	0.3	0.1	-3.1	-3.7	10.49	58.8	74.0
s10_14	0.0	0.2	2.2	5.8	0.0	-2.1	0.1	0.0	-3.3	-3.9	9.41	64.8	71.8
s10_15	-	-	-	-	-	-	-	-	-	-	-	-	-
s10_16	0.1	0.1	3.9	6.1	0.0	-1.5	0.7	0.6	-2.9	-3.5	1.10	53.8	65.5
s10_17	0.0	0.0	4.7	5.9	0.0	-1.6	0.6	0.4	-3.2	-3.8	1.04	50.6	69.7
s30_initial	-	17.5	0.9	15.8	4.1						-	-	65.0
s30_1	3.4	16.0	2.2	15.3	3.6	0.1	2.3	2.1	-0.8	-1.3	4.70	51.3	61.9
s30_2	3.7	15.8	2.1	15.3	3.6	0.1	2.3	2.1	-0.7	-1.3	4.23	51.6	62.2
s30_3	3.7	15.7	2.1	15.3	3.5	0.1	2.3	2.1	-0.7	-1.3	4.26	51.7	62.3
s30_4	3.7	15.6	1.9	15.3	3.5	0.0	2.2	2.0	-0.7	-1.3	4.24	52.3	62.8
s30_5	3.4	13.4	1.7	15.4	3.0	-0.1	2.1	2.0	-0.8	-1.3	3.95	53.4	63.7
s30_6	2.5	9.1	1.6	15.6	2.1	-0.2	2.0	1.8	-0.9	-1.5	3.62	54.6	64.6
s30_7	1.6	5.5	1.4	15.7	1.3	-0.5	1.7	1.5	-1.1	-1.6	3.43	56.5	66.0
s30_8	0.6	3.0	1.3	15.8	0.7	-0.9	1.3	1.1	-1.5	-2.1	5.03	56.9	66.7
s30_9	0.3	2.5	1.3	15.9	0.6	-1.3	0.9	0.8	-1.9	-2.4	9.45	56.7	66.7
s30_10	0.2	2.5	1.5	16.0	0.6	-1.4	0.8	0.6	-2.0	-2.6	13.99	55.9	66.3
s30_11	0.1	2.4	1.8	16.1	0.6	-1.5	0.6	0.5	-2.3	-2.8	23.79	55.7	65.8
s30_12	0.1	1.2	1.8	16.3	0.3	-1.9	0.3	0.2	-2.6	-3.1	23.88	55.1	65.8
s30_13	0.1	0.2	1.9	17.1	0.1	-1.6	0.6	0.5	-2.3	-2.8	2.35	55.2	66.4
s30_14	0.1	0.1	2.0	17.2	0.0	-1.7	0.5	0.3	-2.5	-3.0	1.18	54.8	65.1
s30_15	-	-	-	-	-	-	-	-	-	-	-	-	-
s30_16	0.0	0.0	3.8	17.5	0.0	-2.0	0.2	0.0	-3.1	-3.6	2.85	54.4	62.1
s30_17	0.0	0.1	4.6	17.5	0.0	-1.8	0.4	0.3	-2.8	-3.4	5.71	52.1	59.0
s30_2_initial	-	17.6	0.9	16.1	4.2						-	-	64.8
s30_2_1	3.4	16.0	2.1	15.6	3.7	0.0	2.2	2.1	-0.8	-1.3	4.72	51.5	62.1
s30_2_2	3.5	15.7	2.1	15.7	3.6	0.1	2.3	2.1	-0.7	-1.3	4.45	51.4	62.0

s30_2_3	3.5	15.5	2.1	15.7	3.6	0.0	2.2	2.1	-0.7	-1.3	4.44	51.4	62.0
s30_2_4	3.6	15.3	1.9	15.7	3.5	0.0	2.2	2.0	-0.7	-1.3	4.30	52.1	62.6
s30_2_5	3.0	12.1	1.6	15.7	2.8	-0.1	2.1	1.9	-0.8	-1.4	4.01	53.8	63.9
s30_2_6	1.9	7.1	1.5	16.0	1.7	-0.4	1.8	1.7	-1.0	-1.6	3.65	55.2	65.0
s30_2_7	1.3	4.5	1.4	16.1	1.1	-0.6	1.6	1.5	-1.2	-1.7	3.47	56.3	65.9
s30_2_8	0.6	2.6	1.3	16.1	0.6	-1.0	1.2	1.1	-1.5	-2.1	4.67	57.2	66.5
s30_2_9	0.3	2.2	1.3	16.3	0.5	-1.3	0.9	0.7	-1.9	-2.4	8.88	56.6	66.4
s30_2_10	0.2	2.2	1.4	16.4	0.5	-1.4	0.8	0.6	-2.0	-2.6	13.39	57.8	66.4
s30_2_11	0.1	2.1	1.8	16.4	0.5	-1.6	0.6	0.4	-2.3	-2.9	22.58	55.8	65.4
s30_2_12	0.1	1.0	1.9	16.8	0.3	-1.6	0.6	0.4	-2.3	-2.9	12.01	54.1	65.6
s30_2_13	0.0	0.3	2.0	17.3	0.1	-2.2	0.0	-0.1	-2.9	-3.5	15.33	49.1	65.6
s30_2_14	0.0	0.2	2.4	17.5	0.0	-2.2	0.0	-0.2	-3.0	-3.6	11.52	50.9	63.0
s30_2_15	-	-	-	-	-	-	-	-	-	-	-	-	-
s30_2_16	0.0	0.0	4.5	18.0	0.0	-1.7	0.5	0.3	-2.8	-3.3	1.45	48.9	62.7
s30_2_17	0.0	0.0	5.4	18.4	0.0	-1.8	0.4	0.2	-2.9	-3.5	1.57	41.8	56.5
s45_initial	-	15.6	1.1	27.6	6.4						-	-	58.0
s45_1	2.9	13.4	2.3	25.3	5.0	0.0	2.2	2.0	-0.6	-1.2	4.66	-	53.3
s45_2	3.3	14.0	2.4	26.9	5.5	0.1	2.3	2.1	-0.5	-1.1	4.29	45.7	55.7
s45_3	3.3	13.9	2.4	26.9	5.5	0.1	2.3	2.1	-0.5	-1.1	4.26	45.6	55.6
s45_4	3.4	13.8	2.3	27.1	5.5	0.1	2.3	2.1	-0.5	-1.1	4.02	45.9	55.8
s45_5	3.1	11.7	1.7	27.2	4.7	-0.1	2.1	1.9	-0.6	-1.1	3.74	47.7	57.2
s45_6	1.7	5.9	1.5	27.3	2.4	-0.4	1.8	1.6	-0.8	-1.4	3.47	49.5	58.7
s45_7	1.1	4.0	1.4	27.5	1.6	-0.6	1.6	1.4	-1.0	-1.6	3.82	50.0	59.1
s45_8	0.4	2.8	1.4	27.7	1.2	-1.1	1.1	1.0	-1.4	-2.0	7.01	50.4	59.3
s45_9	0.2	2.7	1.4	27.9	1.1	-1.3	0.9	0.7	-1.7	-2.3	12.48	51.0	59.4
s45_10	0.4	2.8	1.5	27.8	1.1	-1.1	1.1	0.9	-1.5	-2.0	7.70	50.6	59.3
s45_11	0.1	2.5	1.8	28.1	1.1	-1.4	0.8	0.6	-1.9	-2.4	16.91	49.0	58.6
s45_12	0.1	1.2	1.9	28.6	0.5	-1.7	0.5	0.3	-2.2	-2.7	17.56	48.8	58.4
s75_initial	-	13.5	0.9	45.9	9.1						-	-	50.2
s75_1	2.9	12.5	2.6	44.7	8.2	0.1	2.3	2.1	-0.4	-0.9	4.36	39.2	48.1
s75_2	3.0	12.2	2.6	44.8	8.0	0.1	2.3	2.1	-0.4	-0.9	4.06	39.2	48.1
s75_3	3.0	12.2	2.5	44.8	8.0	0.1	2.3	2.1	-0.4	-0.9	4.04	39.3	48.2
s75_4	3.0	11.8	2.3	44.7	7.8	0.0	2.2	2.0	-0.4	-0.9	3.94	39.7	48.5
s75_5	2.7	8.3	1.5	44.8	5.5	-0.2	2.0	1.8	-0.4	-1.0	3.13	41.7	50.1
s75_6	1.6	5.5	1.6	45.3	3.7	-0.4	1.8	1.6	-0.6	-1.2	3.36	41.9	50.2
s75_7	1.0	3.9	1.4	45.4	2.6	-0.7	1.5	1.3	-0.8	-1.4	4.03	42.7	50.9
s75_8	0.4	3.1	1.4	45.5	2.1	-1.1	1.1	1.0	-1.2	-1.8	7.89	43.0	51.1
s75_9	0.2	3.0	1.4	45.7	2.0	-1.3	0.9	0.7	-1.4	-2.0	12.73	42.5	51.0
s75_10	0.2	3.0	1.6	45.9	2.0	-1.4	0.8	0.6	-1.6	-2.2	17.90	42.7	50.8
s75_11	0.1	2.9	1.9	46.2	2.0	-1.5	0.6	0.5	-1.8	-2.4	29.79	42.0	50.4
s75_12	0.1	1.8	1.8	46.6	1.3	-1.8	0.4	0.2	-2.1	-2.6	33.07	42.8	50.7
s75_13	0.0	0.7	1.8	48.2	0.5	-2.0	0.2	0.0	-2.2	-2.8	17.91	42.7	50.2
s75_14	0.0	0.3	2.0	48.7	0.2	-2.2	0.0	-0.2	-2.5	-3.0	16.29	39.9	49.7
s75_15	0.2	0.1	2.9	48.7	0.1	-1.2	1.0	0.9	-1.6	-2.2	0.81	40.3	49.3
s75_16	0.0	0.0	4.2	49.6	0.0	-1.9	0.3	0.1	-2.5	-3.1	1.98	41.0	50.1
s75_17	0.0	0.0	5.1	50.1	0.0	-1.9	0.3	0.1	-2.6	-3.2	2.51	36.0	43.4
s90_initial	-	12.5	1.0	57.8	10.6						-	-	46.0
s90_1	2.7	11.3	2.9	55.7	9.2	0.1	2.3	2.1	-0.3	-0.9	4.22	35.9	44.3
s90_2	2.9	11.2	2.9	56.4	9.3	0.1	2.3	2.1	-0.3	-0.8	3.85	35.8	44.2
s90_3	2.8	11.1	2.8	56.8	9.3	0.1	2.3	2.1	-0.3	-0.8	3.95	35.7	44.1
s90_4	2.9	10.8	2.3	56.6	9.0	0.0	2.2	2.0	-0.3	-0.8	3.74	36.5	44.7
s90_5	2.0	6.5	1.5	56.7	5.5	-0.3	1.9	1.7	-0.4	-1.0	3.23	38.4	46.2
s90_6	1.2	4.3	1.5	57.1	3.6	-0.5	1.7	1.5	-0.6	-1.2	3.46	38.6	46.5
s90_7	0.8	3.3	1.5	57.4	2.8	-0.8	1.4	1.2	-0.8	-1.4	4.41	38.9	46.6
s90_8	0.3	2.9	1.5	57.5	2.4	-1.1	1.1	0.9	-1.2	-1.8	8.80	38.9	46.7
s90_9	0.2	2.8	1.5	57.9	2.4	-1.3	0.9	0.7	-1.4	-2.0	14.42	38.6	46.6
s90_10	0.1	2.7	1.5	58.0	2.3	-1.5	0.7	0.5	-1.6	-2.2	20.60	39.5	46.6
s90_11	0.1	2.6	1.9	58.3	2.3	-1.6	0.6	0.5	-1.7	-2.3	27.20	38.1	46.1
s90_12	0.1	1.4	2.0	59.0	1.2	-1.7	0.4	0.3	-1.9	-2.5	24.42	37.6	46.0
s90_13	0.0	0.5	1.9	61.2	0.5	-2.0	0.2	0.0	-2.2	-2.8	16.66	35.9	45.6
s90_14	0.0	0.1	2.2	61.8	0.1	-2.4	-0.2	-0.4	-2.6	-3.2	12.05	38.5	45.3
s90_15	-	-	-	-	-	-	-	-	-	-	-	-	-
s90_16	0.0	0.0	4.5	63.6	0.0	-2.0	0.2	0.0	-2.5	-3.1	2.49	37.0	40.8
s90_17	0.0	0.0	5.6	64.1	0.0	-2.1	0.1	-0.1	-2.7	-3.2	3.78	28.7	40.9

*ACC containing 0.6 mol% Mg

Table S2: Average Ca, Mg and S (given as SO$_4$) contents in HMC samples from experiment s90 collected after 1 day and 1 year of reaction time based on WDS analysis using data of 100x100 pixel.

Sample	Ca (mol%)	DEV	Mg (mol%)	DEV	SO$_4$ (mol%)	DEV
s90_12	91.11	1.50	8.06	0.38	0.91	0.05
s90_12	91.96	1.09	8.47	0.34	0.90	0.05
s90_17	88.50	1.23	10.65	0.71	0.87	0.05
s90_17	87.63	0.98	11.47	0.62	0.87	0.05

DEV...deviation
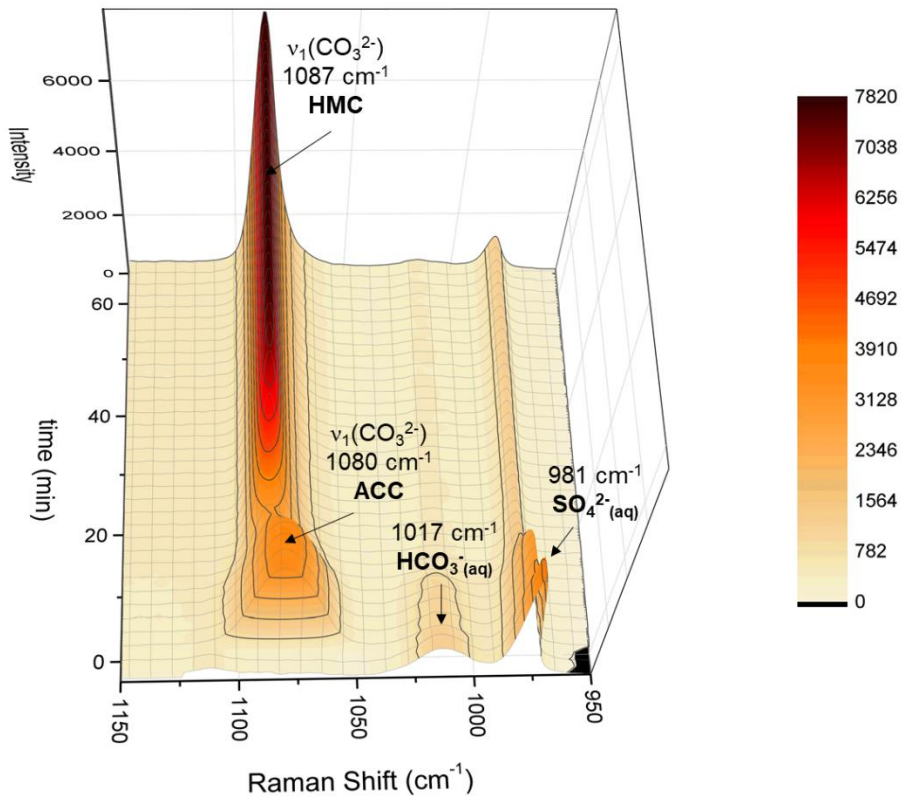
Fig. S1: *In situ* Raman spectra 3-D plot of experiment s30.
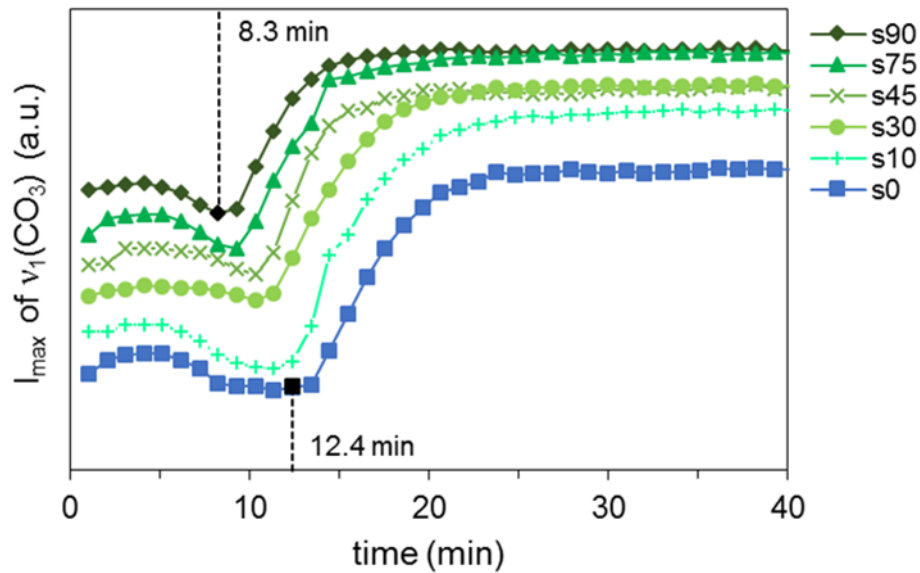
Fig. S2: Temporal evolution of intensity maximum (I_{max}) of the ν_1 vibration band of $(CO_3)_{solid}$ for all experiments obtained using *in situ* Raman spectroscopy. The formation of HMC is indicated by the rapid increase of I_{max} between 8.3 and 12.4 min of reaction time.
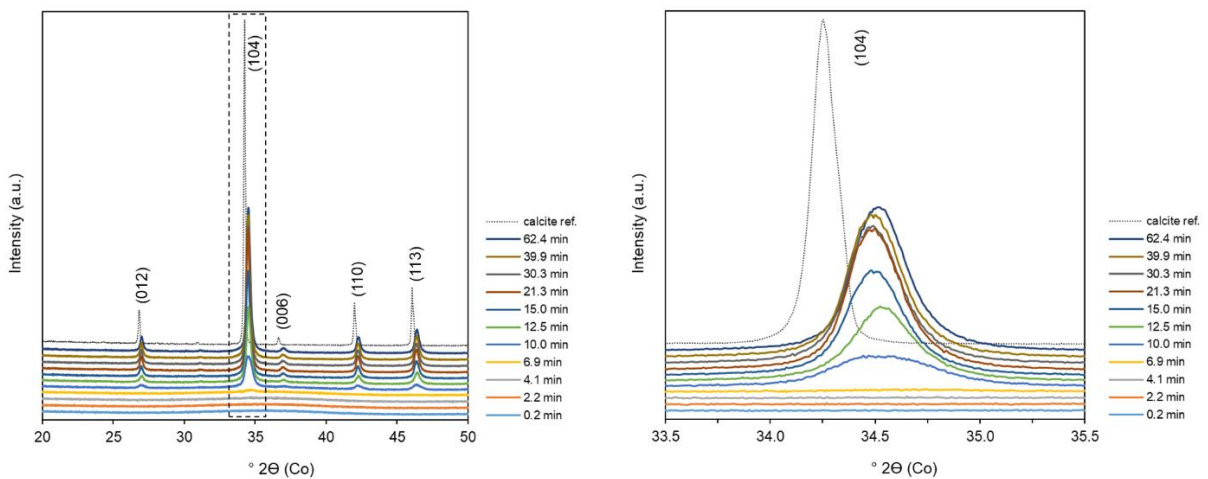
Fig. S3: Stacked XRD diffractograms of experiment s30 within 1 hour of reaction time in comparison to calcite reference material (dotted line). The main calcite peak (d_{104}) is displayed in an enlarged view.
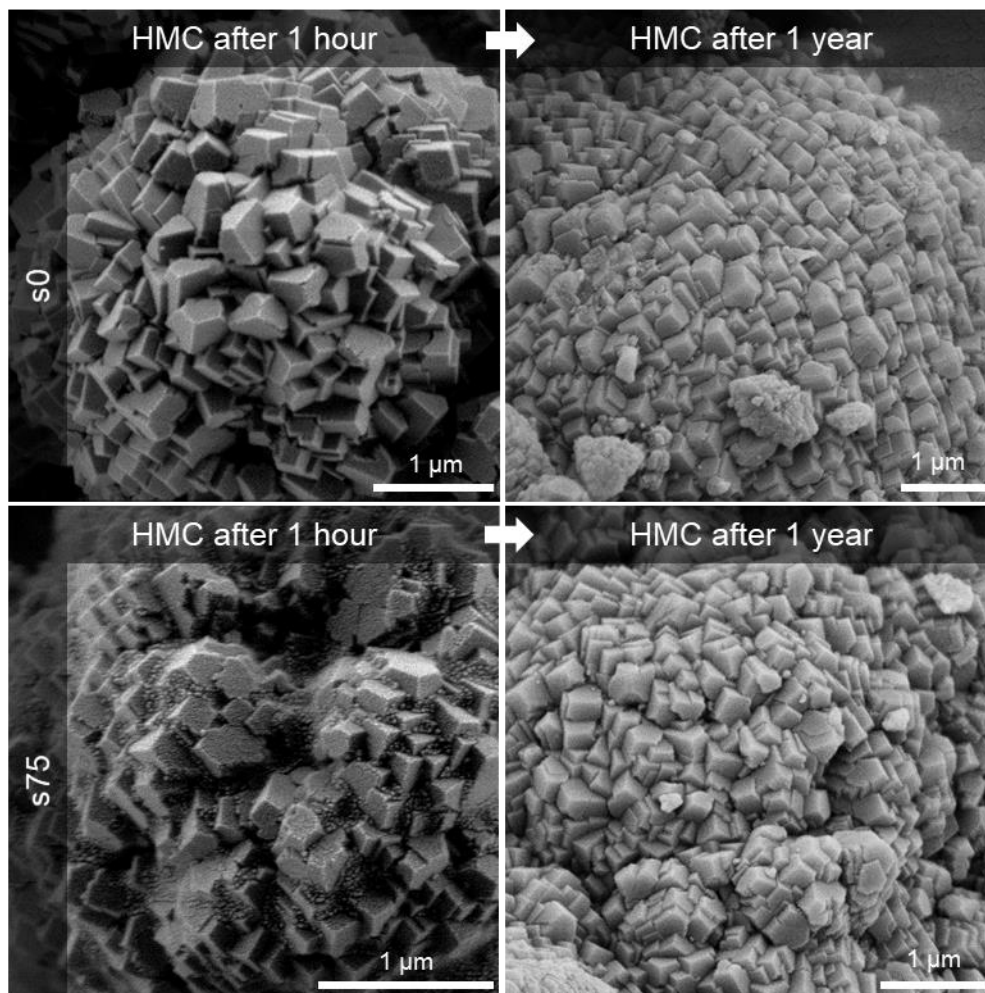
Fig. S4: SEM photographs of HMC from experiments in the absence of sulfate and in the presence of 75 mM sulfate after 1 hour and 1 year of reaction time, respectively.
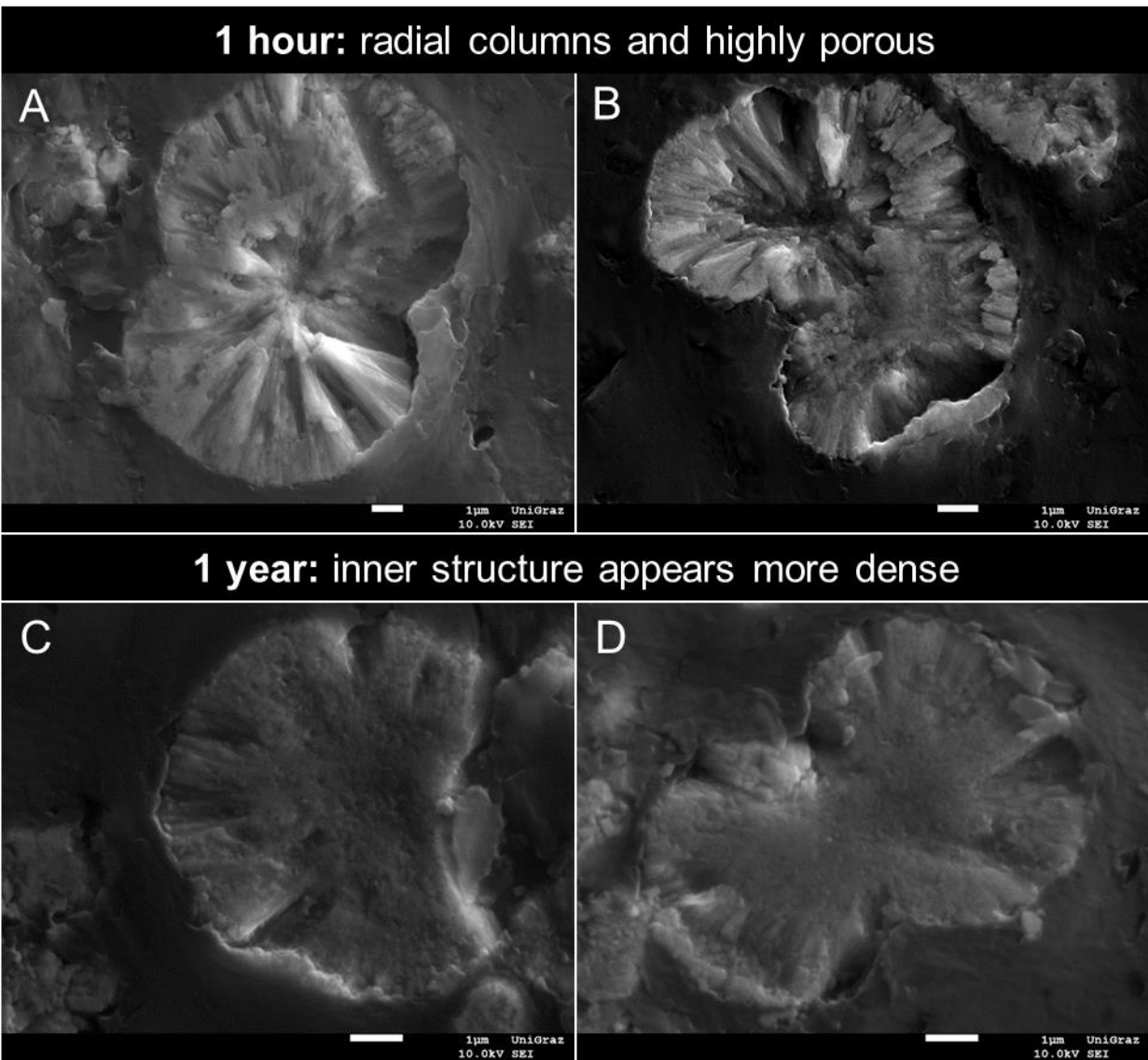
Fig. S5: EPMA BSE-images of cross sectioned HMC aggregates. A and B show the microstructure of HMC collected after 1 hour of reaction time. C and D show the microstructure of HMC collected after 1 year of reaction time.
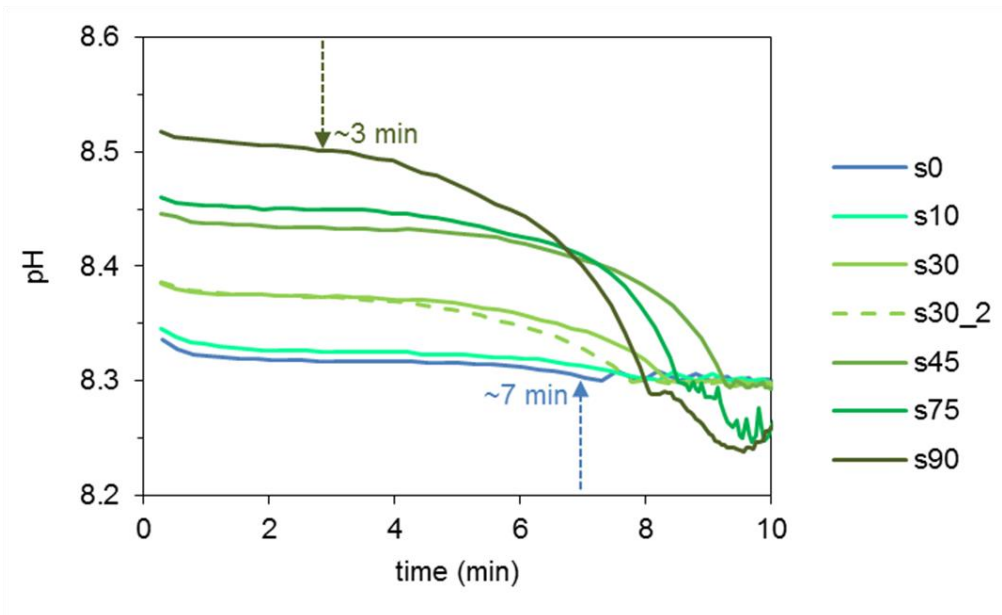
Fig. S6: Evolution of pH as a function of reaction time.
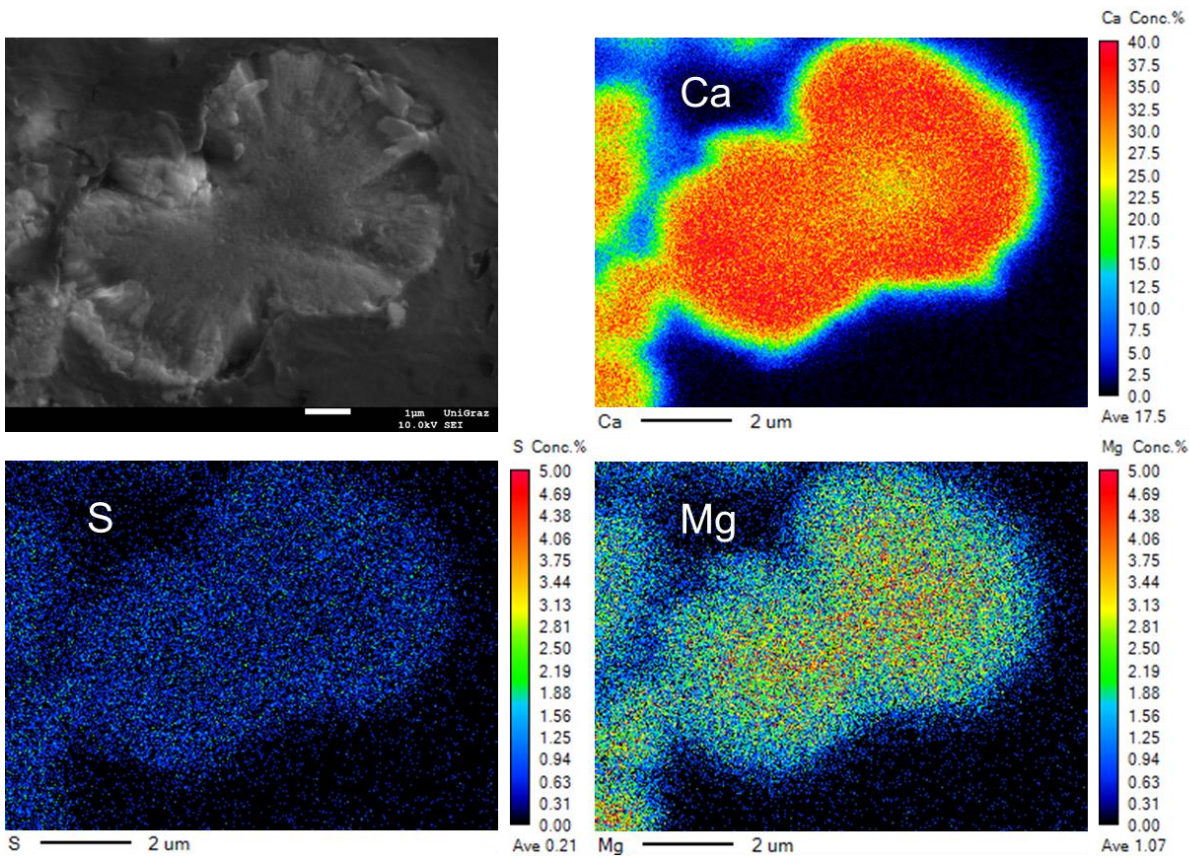
Fig. S7: Element distribution images of HMC collected after 1 year of reaction time (s90_17).

References

Addadi L., Raz S. and Weiner S. (2003) Taking advantage of disorder: Amorphous calcium carbonate and its roles in biomineralization. *Adv. Mater.* **15**, 959–970.

Aizenberg J., Lambert G., Weiner S. and Addadi L. (2002) Factors involved in the formation of amorphous and crystalline calcium carbonate: A study of an ascidian skeleton. *J. Am. Chem. Soc.* **124**, 32–39.

Albéric M., Bertinetti L., Zou Z., Fratzl P., Habraken W. and Politi Y. (2018) The Crystallization of Amorphous Calcium Carbonate is Kinetically Governed by Ion Impurities and Water. *Adv. Sci.* **5**.

Andersen F. A. and Brečević L. (1991) Infrared spectra of amorphous and crystalline calcium carbonate. *Acta Chem. Scand.* **45**, 1018–1024.

Balan E., Aufort J., Pouillé S., Dabos M., Blanchard M., Lazzeri M., Rollion-Bard C. and Blamart D. (2017) Infrared spectroscopic study of sulfate-bearing calcite from deep-sea bamboo coral. *Eur. J. Mineral.* **29**, 397–408.

Bischoff W. D., Sharma S. K. and MacKenzie F. T. (1985) Carbonate ion disorder in synthetic and biogenic magnesian calcites: a Raman spectral study. *Am. Mineral.* **70**, 581–589.

Bleuzen A., Pittet P. A., Helm L. and Merbach A. E. (1997) Water exchange on magnesium(II) in aqueous solution: A variable temperature and pressure ^{17}O NMR study. *Magn. Reson. Chem.* **35**, 765–773.

Blue C.R., Giuffre A., Mergelsberg S., Han N., De Yoreo J.J. and Dove P.M. (2017) Chemical and physical controls on the transformation of amorphous calcium carbonate into crystalline CaCO3 polymorphs. *Geochim. Cosmochim. Acta* **196**, 179–196.

Bots P., Benning L. G., Rickaby R. E. M. and Shaw S. (2011) The role of SO_4 in the switch from calcite to aragonite seas. *Geology* **39**, 331–334.

Bots P., Benning L. G., Rodriguez-Blanco J.-D., Roncal-Herrero T. and Shaw S. (2012) Mechanistic Insights into the Crystallization of Amorphous Calcium Carbonate (ACC). *Cryst. Growth Des.* **12**, 3806–3814.

Böttcher M. E., Gehlken P. L. and Steele D. F. (1997) Characterization of inorganic and biogenic magnesian calcites by fourier transform infrared spectroscopy. *Solid State Ionics* **101–103**, 1379–1385.

Brečević L. and Nielsen A. E. (1989) Solubility of amorphous calcium carbonate. *J. Cryst. Growth* **98**, 504–510.

Burton E. A. and Walter L. M. (1991) The effects of P_{CO_2} and temperature on magnesium incorporation in calcite in seawater and $MgCl_2$-$CaCl_2$ solutions. *Geochim. Cosmochim. Acta* **55**, 777–785.

Burton W. K., Cabrera N. and Frank F. C. (1951) The Growth of Crystals and the Equilibrium Structure of their Surfaces. *Phil. Trans. R. Soc. Lond.* **243**, 299–358.

Davis A. R. and Oliver B. G. (1972) A vibrational-spectroscopic study of the species present in the CO_2-H_2O system. *J. Solution Chem.* **1**, 329–339.

Demény A., Németh P., Czuppon G., Leél-Őssy S., Szabó M., Judik K., Németh T. and Stieber J. (2016) Formation of amorphous calcium carbonate in caves and its implications for speleothem research. *Sci. Rep.* **6**, 39602.

Dietzel M. (2011) Carbonates. *Encycl. Geobiol.*, 261–266.

Dietzel M., Purgstaller B., Kluge T., Leis A. and Mavromatis V. (2020) Oxygen and clumped isotope fractionation during the formation of Mg calcite via an amorphous precursor. *Geochim. Cosmochim. Acta* **276**, 258–273.

Du H. and Amstad E. (2020) Water: How Does It Influence the $CaCO_3$ Formation? *Angew. Chemie – Int. Ed.* **59**, 1798–1816.

Du H., Steinacher M., Borca C., Huthwelker T., Murello A., Stellacci F. and Amstad E. (2018) Amorphous $CaCO_3$: Influence of the Formation Time on Its Degree of Hydration and Stability. *J. Am. Chem. Soc.* **140, 14289–14299.**

Evans D., Gray W. R., Rae J. W. B., Greenop R., Webb P. B., Penkman K., Kröger R. and Allison N. (2020) Trace and major element incorporation into amorphous calcium carbonate (ACC) precipitated from seawater. *Geochim. Cosmochim. Acta* **290**, 293–311.

Fernández-Díaz L., Putnis A., Prieto M. and Putnis C. V (1996) The role of magnesium in the crystallization of calcite and aragonite in a porous medium. *J. Sediment. Res.* **66**, 482–491.

Floquet N., Vielzeuf D., Ferry D., Ricolleau A., Heresanu V., Perrin J., Laporte D. and Fitch A. N. (2015) Thermally Induced Modifications and Phase Transformations of Red Coral Mg-Calcite Skeletons from Infrared Spectroscopy and High Resolution Synchrotron Powder Diffraction Analyses. *Cryst. Growth Des.* **15**, 3690–3706.

Fujita K. and Kimura M. (1981) The Raman Band Shape and Vibrational Relaxation of the v_1 Mode of SO_4^{2-} in Na_2SO_4 and $(NH_4)_2SO_4$ Aqueous Solutions. *J. Raman Spectrosc.* **11**, 108–111.

Gautier Q., Bénézeth P., Mavromatis V. and Schott J. (2014) Hydromagnesite solubility product and growth kinetics in aqueous solution from 25 to 75°C. *Geochim. Cosmochim. Acta* **138**, 1–20.

Gebauer D. and Cölfen H. (2011) Prenucleation clusters and non-classical nucleation. *Nano Today* **6**, 564–584.

Gebauer D., Gunawidjaja P. N., Ko J. Y. P., Bacsik Z., Aziz B., Liu L., Hu Y., Bergström L., Tai C. W., Sham T. K., Edén M. and Hedin N. (2010) Proto-calcite and proto-vaterite in amorphous calcium carbonates. *Angew. Chemie – Int. Ed.* **49**, 8889–8891.

Giuffre A. J., Gagnon A. C., De Yoreo J. J. and Dove P. M. (2015) Isotopic tracer evidence for the amorphous calcium carbonate to calcite transformation by dissolution–reprecipitation. *Geochim. Cosmochim. Acta* **165**, 407–417.

Goetschl K. E., Purgstaller B., Dietzel M. and Mavromatis V. (2019) Effect of sulfate on magnesium incorporation in low-magnesium calcite. *Geochim. Cosmochim. Acta* **265**, 505–519.

Goldsmith J. R., Graf D. L. and Heard H. C. (1961) Lattice constants of the calcium-magnesium carbonates. *Am. Mineral.* **46**, 453–459.

Gong Y., Killian C., Olson I., Appathurai N. P., Amasino A., Martin M., Holt L., Wilt F. and Gilbert P. (2012) Phase transitions in biogenic amorphous calcium carbonate. *Proc. Natl. Acad. Sci. U. S. A.* **109**, 6088–6093.

Goodwin A. L., Michel F. M., Phillips B. L., Keen D. A., Dove M. T. and Reeder R. J. (2010) Nanoporous structure and medium-range order in synthetic amorphous calcium carbonate. *Chem. Mater.* **22**, 3197–3205.

Gower L. B. (2008) Biomimetic model systems for investigating the amorphous precursor pathway and its role in biomineralization. *Chem. Rev.* **108**, 4551–4627.

Han M., Zhao Y., Zhao H., Han Z., Yan H., Sun B., Meng R., Zhuang D., Li D. and Liu B. (2017) A comparison of amorphous calcium carbonate crystallization in aqueous solutions of $MgCl_2$ and $MgSO_4$: implications for paleo-ocean chemistry. *Mineral. Petrol.* **0**, 1–16.

Harrison A. L., Mavromatis V., Oelkers E. H. and Bénézeth P. (2019) Solubility of the hydrated Mg-carbonates nesquehonite and dypingite from 5 to 35 °C: Implications for CO_2 storage and the relative stability of Mg-carbonates. *Chem. Geol.* **504**, 123–135.

Huang Y. C., Gindele M. B., Knaus J., Rao A. and Gebauer D. (2018) On mechanisms of mesocrystal formation: Magnesium ions and water environments regulate the crystallization of amorphous minerals. *CrystEngComm* **20**, 4395–4405.

Hug S. J. (1997) In situ fourier transform infrared measurements of sulfate adsorption on hematite in aqueous solutions. *J. Colloid Interface Sci.* **188**, 415–422.

Ihli J., Kim Y. Y., Noel E. H. and Meldrum F. C. (2013) The effect of additives on amorphous calcium carbonate (ACC): Janus behavior in solution and the solid state. *Adv. Funct. Mater.* **23**, 1575–1585.

Ihli J., Wong W. C., Noel E. H., Kim Y. Y., Kulak A. N., Christenson H. K., Duer M. J. and Meldrum F. C. (2014) Dehydration and crystallization of amorphous calcium carbonate in solution and in air. *Nat. Commun.* **5**, 1–10.

Jiang J., Gao M. R., Qiu Y. H., Wang G. S., Liu L., Cai G. Bin and Yu S. H. (2011) Confined crystallization of polycrystalline high-magnesium calcite from compact Mg-ACC precursor tablets and its biological implications. *CrystEngComm* **13**, 952–956.

Jin W., Jiang S., Pan H. and Tang R. (2018) Amorphous phase mediated crystallization: Fundamentals of biomineralization. *Crystals* **8**, 23–26.

Konrad F., Gallien F., Gerard D. E. and Dietzel M. (2016) Transformation of Amorphous Calcium Carbonate in Air. *Cryst. Growth Des.* **16**, 6310–6317.

Konrad F., Purgstaller B., Gallien F., Mavromatis V., Gane P. and Dietzel M. (2018) Influence of aqueous Mg concentration on the transformation of amorphous calcium carbonate. *J. Cryst. Growth* **498**, 381–390.

Kontrec J., Kralj D., Brečević L., Falini G., Fermani S., Noethig-Laslo V. and Mirosavljević K. (2004) Incorporation of inorganic anions in calcite. *Eur. J. Inorg. Chem.*, 4579–4585.

Lin C.-J., Yang S.-Y., Huang S.-J. and Chan J. C. C. (2015) Structural Characterization of Mg-Stabilized Amorphous Calcium Carbonate by Mg-25 Solid-State NMR Spectroscopy. *J. Phys. Chem. C* **119**, 7225–7233.

Lincoln S. F. and Merbach A. E. (1995) Substitution reactions of solvated metal ions. *Adv. Inorg. Chem.* **42**, 1–88.

Littlewood J. L., Shaw S., Peacock C. L., Bots P., Trivedi D. and Burke I. T. (2017) Mechanism of Enhanced Strontium Uptake into Calcite via an Amorphous Calcium Carbonate Crystallization Pathway. *Cryst. Growth Des.* **17**, 1214–1223.

Long X., Ma Y. and Qi L. (2014) Biogenic and synthetic high magnesium calcite - A review. *J. Struct. Biol.* **185**, 1–14.

Long X., Ma Y. and Qi L. (2011) In vitro synthesis of high Mg calcite under ambient conditions and its implication for biomineralization process. *Cryst. Growth Des.* **11**, 2866–2873.

Lorens R. B. (1981) Sr, Cd, Mn and Co distribution coefficients in calcite as a function of calcite precipitation rate. *Geochim. Cosmochim. Acta* **45**, 553–561.

Loste E., Wilson R. M., Seshadri R. and Meldrum F. C. (2003) The role of magnesium in stabilising amorphous calcium carbonate and controlling calcite morphologies. *J. Cryst. Growth* **254**, 206–218.

Mavromatis V., Gautier Q., Bosc O. and Schott J. (2013) Kinetics of Mg partition and Mg stable isotope fractionation during its incorporation in calcite. *Geochim. Cosmochim. Acta* **114**, 188–203.

Mavromatis V., Goetschl K. E., Grengg C., Konrad F., Purgstaller B. and Dietzel M. (2018) Barium partitioning in calcite and aragonite as a function of growth rate. *Geochim. Cosmochim. Acta* **237**, 65–78.

Mavromatis V., Harrison A. L., Eisenhauer A. and Dietzel M. (2017c) Strontium isotope fractionation during strontianite ($SrCO_3$) dissolution, precipitation and at equilibrium. *Geochim. Cosmochim. Acta*.

Mavromatis V., Immenhauser A., Buhl D., Purgstaller B., Baldermann A. and Dietzel M. (2017a) Effect of organic ligands on Mg partitioning and Mg isotope fractionation during low-temperature precipitation of calcite in the absence of growth rate effects. *Geochim. Cosmochim. Acta* **207**, 139–153.

Mavromatis V., Montouillout V., Noireaux J., Gaillardet J. and Schott J. (2015) Characterization of boron incorporation and speciation in calcite and aragonite from co-precipitation experiments under controlled pH, temperature and precipitation rate. *Geochim. Cosmochim. Acta* **150**, 299–313.

Mavromatis V., Purgstaller B., Dietzel M., Buhl D., Immenhauser A. and Schott J. (2017b) Impact of amorphous precursor phases on magnesium isotope signatures of Mg-calcite. *Earth Planet. Sci. Lett.* **464**, 227–236.

Mavromatis V., Schmidt M., Botz R., Comas-Bru L. and Oelkers E. H. (2012) Experimental quantification of the effect of Mg on calcite-aqueous fluid oxygen isotope fractionation. *Chem. Geol.* **310–311**, 97–105.

Mavromatis V., van Zuilen K., Purgstaller B., Baldermann A., Nägler T. F. and Dietzel M. (2016) Barium isotope fractionation during witherite ($BaCO_3$) dissolution, precipitation and at equilibrium. *Geochim. Cosmochim. Acta* **190**, 72–84.

Mergelsberg S. T., De Yoreo J. J., Miller Q. R. S., Marc Michel F., Ulrich R. N. and Dove P. M. (2020) Metastable solubility and local structure of amorphous calcium carbonate (ACC). *Geochim. Cosmochim. Acta* **289**, 196–206.

Milliman J. D., Gastner M. and Müller J. (1971) Utilization of Magnesium in Coralline Algae Utilization of Magnesium in Coralline Algae. *Geol. Soc. Am. Bull.* **82**, 573–580.

Morse J. W. and Mackenzie F. T. (1990) *Geochemistry of sedimentary carbonates.*, Elsevier, Amsterdam, Oxford, New York, Tokyo.

Mucci A. and Morse J. W. (1983) The incorporation of Mg^{2+} and Sr^{2+} into calcite overgrowths: influences of growth rate and solution composition. *Geochim. Cosmochim. Acta* **47**, 217–233.

Nielsen M. R., Sand K. K., Rodriguez-Blanco J. D., Bovet N., Generosi J., Dalby K. N. and Stipp S. L. S. (2016) Inhibition of Calcite Growth: Combined Effects of Mg^{2+} and SO_4^{2-}. *Cryst. Growth Des.* **16**, 6199–6207.

Oelkers E. H., Pogge von Strandmann P. A. E. and Mavromatis V. (2019) The rapid resetting of the Ca isotopic signatures of calcite at ambient temperature during its congruent dissolution, precipitation, and at equilibrium. *Chem. Geol.* **512**, 1–10.

Paquette J. and Reeder R. J. (1990) Single-crystal X-ray structure refinements of two biogenic magnesian calcite crystals. *Am. Mineral.* **75**, 1151–1158.

Pederson C. L., Mavromatis V., Dietzel M., Rollion-Bard C., Breitenbach S. F. M., Yu D., Nehrke G. and Immenhauser A. (2020) Variation in the diagenetic response of aragonite archives to hydrothermal alteration. *Sediment. Geol.* **406**, 105716.

Politi Y., Batchelor D. R., Zaslansky P., Chmelka B. F., Weaver J. C., Sagi I., Weiner S. and Addadi L. (2010) Role of magnesium ion in the stabilization of biogenic amorphous calcium carbonate: A structure-function investigation. *Chem. Mater.* **22**, 161–166.

Purgstaller B., Dietzel M., Baldermann A. and Mavromatis V. (2017b) Control of temperature and aqueous Mg^{2+}/Ca^{2+} ratio on the (trans-)formation of ikaite. *Geochim. Cosmochim. Acta* **217**, 128–143.

Purgstaller B., Goetschl K. E., Mavromatis V. and Dietzel M. (2019) Solubility investigations in the amorphous calcium magnesium carbonate system. *CrystEngComm* **21**, 155–164.

Purgstaller Bettina, Konrad F., Dietzel M., Immenhauser A. and Mavromatis V. (2017a) Control of Mg^{2+}/Ca^{2+} Activity Ratio on the Formation of Crystalline Carbonate Minerals via an Amorphous Precursor. *Cryst. Growth Des.* **17**, 1069–1078.

Purgstaller B., Mavromatis V., Goetschl K. E., Steindl F. R. and Dietzel M. (2021) Effect of temperature on the transformation of amorphous calcium magnesium carbonate with near-dolomite stoichiometry into high Mg-calcite. *CrystEngComm* **23**, 1969–1981.

Purgstaller B., Mavromatis V., Immenhauser A. and Dietzel M. (2016) Transformation of Mg-bearing amorphous calcium carbonate to Mg-calcite - In situ monitoring. *Geochim. Cosmochim. Acta* **174**, 180–195.

Radha A. V. and Navrotsky A. (2015) Direct experimental measurement of water interaction energetics in amorphous carbonates MCO_3 (M = Ca, Mn, and Mg) and implications for carbonate crystal growth. *Cryst. Growth Des.* **15**, 70–78.

Raz S., Weiner S. and Addadi L. (2000) Formation of high-magnesian calcites via an amorphous precursor phase: Possible biological implications. *Adv. Mater.* **12**, 38–42.

Reeder R. J. (1990) Carbonates: Mineralogy and Chemistry. *Rev. Mineral. Geochemistry* **11**.

Rodriguez-Blanco J. D., Shaw S., Bots P., Roncal-Herrero T. and Benning L. G. (2012) The role of pH and Mg on the stability and crystallization of amorphous calcium carbonate. In *Journal of Alloys and Compounds* pp. S477–S479.

Rodriguez-Navarro C., Kudłacz K., Cizer Ö. and Ruiz-Agudo E. (2015) Formation of amorphous calcium carbonate and its transformation into mesostructured calcite. *CrystEngComm* **17**, 58–72.

Schmidt M. P., Ilott A. J., Phillips B. L. and Reeder R. J. (2014) Structural changes upon dehydration of amorphous calcium carbonate. *Cryst. Growth Des.* **14**, 938–951.

Schultz L. N., Andersson M. P., Dalby K. N., Müter D., Okhrimenko D. V., Fordsmand H. and Stipp S. L. S. (2013) High surface area calcite. *J. Cryst. Growth* **371**, 34–38.

Shen L., Sippola H., Li X., Lindberg D. and Taskinen P. (2019) Thermodynamic Modeling of Calcium Sulfate Hydrates in the $CaSO_4$-H_2O System from 273.15 to 473.15 K with Extension to 548.15 K. *J. Chem. Eng. Data* **64**, 2697–2709.

Stipp S. L. S., Konnerup-Madsen J., Franzreb K., Kulik A. and Mathieu H. J. (1998) Spontaneous movement of ions through calcite at standard temperature and pressure. *Nature* **396**, 356–359.

Sun R., Willhammar T., Svensson Grape E., Strømme M. and Cheung O. (2019) Mesoscale Transformation of Amorphous Calcium Carbonate to Porous Vaterite Microparticles with Morphology Control. *Cryst. Growth Des.* **19**, 5075–5087.

Sun R., Zhang P., Bajnóczi É. G., Neagu A., Tai C. W., Persson I., Strømme M. and Cheung O. (2018) Amorphous Calcium Carbonate Constructed from Nanoparticle Aggregates with Unprecedented Surface Area and Mesoporosity. *ACS Appl. Mater. Interfaces* **10**, 21556–21564.

Sun S., Chevrier D. M., Zhang P., Gebauer D. and Cölfen H. (2016) Distinct Short-Range Order Is Inherent to Small Amorphous Calcium Carbonate Clusters (<2 nm). *Angew. Chemie – Int. Ed.* **55**, 12206–12209.

Takano B., Asano Y. and Watanuki K. (1980) Characterization of sulfate ion in travertine. *Contrib. to Mineral. Petrol.* **72**, 197–203.

Tobler D. J., Rodriguez Blanco J. D., Sørensen H. O., Stipp S. L. S. and Dideriksen K. (2016) Effect of pH on Amorphous Calcium Carbonate Structure and Transformation. *Cryst. Growth Des.* **16**, 4500–4508.

Uchikawa J., Harper D. T., Penman D. E., Zachos J. C. and Zeebe R. E. (2017) Influence of solution chemistry on the boron content in inorganic calcite grown in artificial seawater. *Geochim. Cosmochim. Acta* **218**, 291–307.

Wang D., Hamm L. M., Bodnar R. J. and Dove P. M. (2012) Raman spectroscopic characterization of the magnesium content in amorphous calcium carbonates. *J. Raman Spectrosc.* **43**, 543–548.

Wang F., Zhang Y. H., Li S. H., Wang L. Y. and Zhao L. J. (2005) A strategy for single supersaturated droplet analysis: Confocal Raman investigations on the complicated hygroscopic properties of individual $MgSO_4$ droplets on the quartz substrate. *Anal. Chem.* **77**, 7148–7155.

Wei Z. F., Zhang Y. H., Zhao L. J., Liu J. H. and Li X. H. (2005) Observation of the first hydration layer of isolated cations and anions through the FTIR-ATR difference spectra. *J. Phys. Chem. A* **109**, 1337–1342.

White W. B. (1974) The carbonate minerals. In *The Infrared Spectra of Minerals* pp. 227–284.

Xto J. M., Du H., Borca C. N., Amstad E., Van Bokhoven J. A. and Huthwelker T. (2019) Tuning the Incorporation of Magnesium into Calcite during Its Crystallization from Additive-Free Aqueous Solution. *Cryst. Growth Des.* **19**, 4385–4394.

De Yoreo J. J., Gilbert P. U. P. A., Sommerdijk N. A. J. M., Penn R. L., Whitelam S., Joester D., Zhang H., Rimer J. D., Navrotsky A., Banfield J. F., Wallace A. F., Michel F. M., Meldrum F. C., Colfen H. and Dove P. M. (2015) Crystallization by particle attachment in synthetic, biogenic, and geologic environments. *Science* **349**, aaa6760.

Zou Z., Polishchuk I., Bertinetti L., Pokroy B., Politi Y., Fratzl P. and Habraken W. J. E. M. (2018) Additives influence the phase behavior of calcium carbonate solution by a cooperative ion-association process. *J. Mater. Chem. B* **6**, 449–457.

Chapter 4

Solubility Investigations in the Amorphous Calcium Magnesium Carbonate System

Bettina Purgstaller[1], Katja E. Goetschl[1], Vasileios Mavromatis[1,2], Martin Dietzel[1]

[1]Institute of Applied Geosciences, Graz University of Technology, Rechbauerstrasse 12, 8010 Graz, Austria
[2]Géosciences Environment Toulouse (GET), CNRS, UMR 5563, Observatoire Midi-Pyrénées, 14 Av. E. Belin, 31400 Toulouse, France

GRAPHICAL ABSTRACT
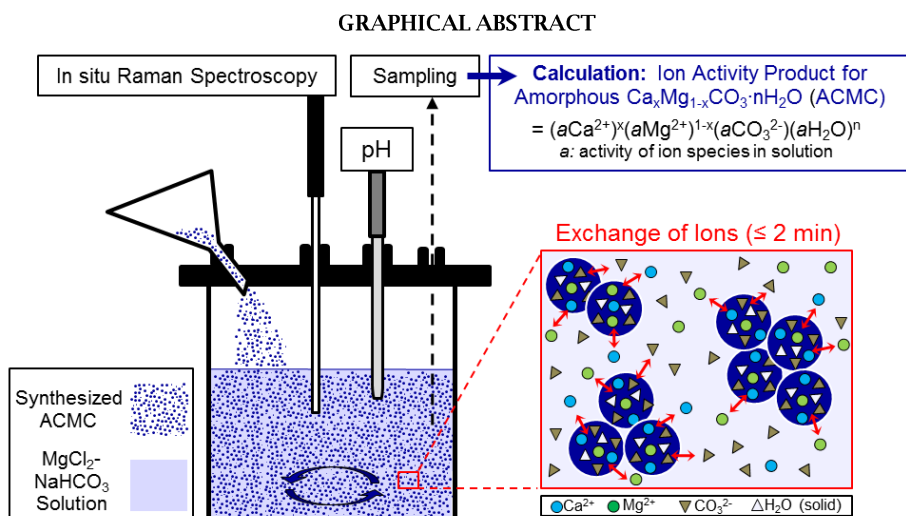
ABSTRACT: Amorphous precursors are known to occur in the early stages of carbonate mineral formation in both biotic and abiotic environments. Although the Mg content of amorphous calcium magnesium carbonate (ACMC) is a crucial factor for its temporal stabilization, to date less is known about its control on ACMC solubility. Therefore, amorphous $Ca_xMg_{1-x}CO_3 \cdot nH_2O$ solids with $0 \leq x \leq 1$ and $0.4 \leq n \leq 0.8$ were synthesized and dispersed in $MgCl_2$-$NaHCO_3$ buffered solutions at 24.5 ±0.5 °C. The chemical evolution of the solution and the precipitate clearly shows an instantaneous exchange of ions between ACMC and aqueous solution. The obtained ion activity product for ACMC (IAP_{ACMC} = "solubility product") increases as a function of its Mg content ($[Mg]_{ACMC} = (1-x) * 100$ in mol %) according to the expression: $\log(IAP_{ACMC}) = 0.0174$ (±0.0013) * $[Mg]_{ACMC} - 6.278$ (±0.046) ($R^2 = 0.98$), where the $\log(IAP_{ACMC})$ shift from Ca (-6.28 ±0.05) to Mg (-4.54 ±0.16) ACMC endmember, can be explained by the increasing water content and changes in short-range order, as Ca is substituted by Mg in the ACMC structure. The results of this study shed light on the factors controlling ACMC solubility and its temporal stability in aqueous solutions.

4.1 Introduction

Amorphous calcium carbonate (ACC) is a highly soluble solid phase that commonly occurs as a precursor of crystalline $CaCO_3$ (e.g. calcite, aragonite) in modern biotic and abiotic precipitation environments. Its (trans)formation has been observed in calcifying organisms (Aizenberg et al., 2002; Khairoun et al., 2002; Weiner and Dove, 2003; Politi et al., 2004; 2010; Sethmann et al., 2006; Jacob et al., 2008; Tao et al., 2009), microbialites from alkaline lakes (Benzerara et al., 2006; Couradeau et al., 2012), biofilms from hot springs (Jones and Peng, 2012) and speleothems (Demény et al., 2016). ACC can include significant amounts of $MgCO_3$, which is known to play a significant role in its temporal stabilization (Politi et al., 2010; Couradeau et al., 2012). In this context, the transformation of amorphous calcium magnesium carbonates (ACMC) into crystalline Ca-Mg carbonate minerals is of particular interest as it represents an energetically favorable pathway for high magnesian calcite (Mg calcite) and disordered dolomite formation (Schmidt et al., 2005; Mavromatis et al., 2012; Rodriuguez-Blanco et al., 2015; Purgstaller et al., 2016; Yu et al., 2017). However, the impact of Mg on the temporal stability and transformation behavior of ACMC is not fully elucidated and a systematic study on the solubility of the ACMC system is still missing.

The earlier experimental work of Brečević and Nielsen (1989) showed that Mg-free ACC is significantly more soluble than calcite. These authors also documented an ion activity product of ACC ($log(IAP_{ACC})$; "solubility" of ACC) of -6.39 ±0.02 at 25 °C. More recently, Gebauer et al. (2008) found the solubility of ACC to be lower and reported $log(IAP_{ACC})$ values of -7.51 and -7.42 for ACC phases with a "calcite-like" and a "vaterite-like" short range order, respectively. To our knowledge the only published values so far for ACMC are those obtained in our previous study (Purgstaller et al., 2016), where we documented $log(IAP_{ACMC})$ values ranging from -6.14 to -7.01 for ACMC with ≤ 10 mol% Mg.

In the scope of an energetic study on synthetic ACMCs, Radha et al. (2012) observed that ACMC with low Mg content transforms faster into crystalline carbonates than ACMC with high Mg content under atmospheric conditions. The longer stability of ACMC with elevated Mg content has been attributed to the strong bond between structural water and Mg ions which retards the process of dehydration and subsequent phase transformation (Radha et al., 2012; Lin et al., 2015). However, inconsistent data are available for the water contents of ACMC at distinct Mg concentrations (Radha et al., 2012; Blue and Dove, 2015; Lin et al., 2015). For example, the moles of water per unit formula $Ca_xMg_{1-x}CO_3$ are

reported to vary from 0.81 to 1.75 for ACMC with 45 ±2 mol% Mg (Radha et al, 2012; Lin et al., 2015). New findings indicate that the stability of Mg-free ACC under atmospheric conditions is significantly controlled by the availability of H_2O in the transformation environment. In this regard, Konrad et al. (2016) proposed that H_2O molecules are adsorbed by ACC promoting its transformation into calcite/vaterite via a dissolution and reprecipitation mechanism. More recently, experimental studies on ACMC (trans)formation in an aqueous solution suggested that the chemical composition of the reactive solution (e.g. Mg/Ca ratio) significantly affects the temporal stability of ACMC and its subsequent transformation into the final product (Mg calcite, monohydrocalcite etc.; Blue et al., 2017; Mavromatis et al., 2017a; Purgstaller et al., 2017; Konrad et al., 2018). However, the exact mechanisms controlling ACMC stability and transformation behavior is still under debate and further experimental work is needed to describe the interaction between solutions and ACMC phases.

The aim of the present work is to provide an advanced understanding about the "solubility product" of ACMC as a function of its Mg content in terms of an ion activity product at chemical steady-state conditions. Therefore, distinct ACMCs ($Ca_xMg_{1-x}CO_3$ nH_2O; $0 \leq x \leq 1$ and $0.4 \leq n \leq 0.8$) were synthesized and subsequently dispersed in $MgCl_2$-$NaHCO_3$ buffered solutions in order to assess (i) the elemental exchange of ACMC with the aqueous phase and (ii) the factors controlling ACMC solubility and its temporal stability in aqueous solutions.

4.2 Experimental section

4.2.1 Synthesis of Amorphous Calcium Magnesium Carbonates

Amorphous calcium magnesium carbonates with Mg contents ranging from 0 to 100 mol% Mg (hereafter referred to as ACMCs) were synthesized by a previously described method (Konrad et al., 2016). Briefly, 80 mL of a 250 mM $(Ca,Mg)Cl_2$ solution was poured into a beaker containing 80 mL of a 250 mM Na_2CO_3 solution. The reaction products were immediately separated from solution by a 0.2 μm cellulose filter using a suction filtration unit. Subsequently, the separated precipitate was washed with ultrapure water (Millipore Integral 3: 18.2 MΩcm⁻¹) and transferred into a freeze dryer (Virtis Benchtop 3L). The freeze-dried ACMCs were stored in closed vials in a desiccator with silica gel (relative humidity = 3%). In total, 9 synthesis experiments were carried out, where the Mg content of the $(Ca,Mg)Cl_2$ stock solution, $[Mg]_{stock} = \{[Mg]/([Ca]+[Mg])\} * 100$, was systematically

varied between 0 and 100 mol% (see Table 1). All solutions were prepared by analytical grade chemicals (CaCl$_2 \cdot$ 2H$_2$O, MgCl$_2 \cdot$ 6H$_2$O and Na$_2$CO$_3$ from Roth) mixed with ultrapure water.

4.2.2 Experimental Setup for Solubility Study

The chemical composition of the synthesized ACMC solids used for solubility investigations is shown in Table 1. Experiments were performed at 24.5 ±0.5 °C in a 100 mL glass reactor containing 50 mL of a 100 mM NaHCO$_3$ and 30 mM MgCl$_2$ solution, stirred at 350 rpm. The pH of the solution was adjusted to 8.33 ±0.03 by the addition of a 500 mM NaOH solution. At the onset of the experiment, 1.5 g of the synthetic ACMC sample was introduced into the reactor. The temporal evolution of the mineralogy was monitored using an *in situ* Raman probe immersed in the suspension. In order to follow the chemical composition of the solution and the solid phase, homogeneous sub-samples of the experimental solution/suspension (1.5 mL) were collected with a pipette at certain reaction times (Table S1). The solids were separated from the solution by a 0.2 μm cellulose acetate filter using a suction filtration unit, washed with ethanol and dried in an oven at 40 °C.

4.2.3 Solid Phase Characterization

X-ray diffraction (XRD) patterns of the synthesized ACMCs (Fig. S1) and of the ACMCs separated from the experimental solutions during the solubility study (not shown) were acquired using a PANalytical X´Pert Pro diffractometer (Co-Kα radiation) at a 2θ range from 4 to 85° and a scan speed of 0.03° s^{-1}. Thermogravimetric analyses (TGA) of freeze-dried ACMCs (Fig. S2) were realized using a PerkinElmer STA8000. The samples were heated from 25 °C to 800 °C at 10 °C/min in the presence of 99.999% N$_2$ atmosphere. Selected synthesized ACMCs were gold coated and imaged (Fig. S3) using a scanning electron microscope (SEM, ZEISS DSM 982 Gemini). Time-resolved *in situ* Raman spectroscopy of the experimental solution/suspension was realized using a Raman RXN2™ analyzer from Kaiser Optical Systems with a Kaiser MR Probe head (quarter-inch immersion optic) and a 785 nm laser beam. *In situ* Raman spectra were collected every 60 sec in the 100–1890 cm^{-1} region with a resolution of 1 cm^{-1}.

4.2.4 Chemical Composition of the Experimental Solutions and Solids

During the experimental run, the pH of the experimental solution was measured with a SI Analytics Silamid® gel electrode, which was calibrated against NIST buffer standard solutions at pH 4.01 and 7.00. The total alkalinity of the experimental solutions was measured by a Schott TitroLine alpha plus titrator using a 10 mM HCl solution with a precision of ±2%. The aqueous Ca, Mg and Na concentrations of the $(Ca,Mg)Cl_2$ stock solutions, of the experimental solutions and of the solids (digested in 6% HNO_3) were determined using inductively coupled plasma optical emission spectrometry (Perkin Elmer Optima 8300 DV). The analytical error was <±3% for Ca and Mg analyses and <±5% for Na analyses.

4.2.5 Aqueous Speciation and Ion Activity Product Calculation

The aqueous speciation of the experimental solutions was calculated at 25 °C using the PHREEQC software together with its minteq.v4 database. For the ionic strength of our experiments (i.e. 0.17 ±0.02 M; Table S2), the calculation of individual ion activity coefficients for the solute species is based on the Davis equation (Allison et al., 1991; Appelo and Postma, 2005). The activities (a) of Ca^{2+}, Mg^{2+} and CO_3^{2-} ions in solution and the stoichiometry of the digested $Ca_xMg_{1-x}CO_3 \cdot nH_2O$ solids (where $(1-x) = [Mg]_{ACMC}/100$) were used to calculate ion activity products for the amorphous calcium magnesium carbonates (IAP_{ACMC}) as a function of experimental time according to equation

$$IAP_{ACMC} = (aCa^{2+})^{x}(aMg^{2+})^{1-x}(aCO_3^{2-})(aH_2O)^{n} \qquad (1)$$

In the present solubility experiments, the aH$_2$O values of the experimental solutions remained constant at 0.955 ±0.004. Thus, for the calculation of the IAP_{ACMC}, the aH$_2$O was assumed to be unity.

4.3 Results and discussion

4.3.1 Characterization of synthesized ACMC material

The measured Mg contents of the stock solutions, $[Mg]_{stock}$, and of the synthesized ACMC samples, $[Mg]_{ACMC}$, are reported in Table 1 and displayed in Fig. 1. The results reveal a preferential enrichment of the amorphous solid in Ca and are in good agreement with those of Radha et al. (2012), who synthesized a set of amorphous $Ca_xMg_{1-x}CO_3 \cdot nH_2O$ solids by batch method using $(Ca,Mg)Cl_2$ and Na_2CO_3 solutions (Fig. 1). The preferential enrichment of the amorphous phase in Ca likely stems from the strong free energy of hydration of the Mg^{2+} ion compared to Ca^{2+} (Radha et al., 2012; Mavromatis et al., 2013). The strongly hydrated aqueous Mg^{2+} is a well-known limitation in the formation of anhydrous crystalline Ca-Mg-carbonates, such as Mg calcite, dolomite and magnesite, at ambient temperatures (Tommaso and Leeuw, 2010). Instead, hydrous crystalline Mg-carbonates (e.g. hydromagnesite; Konrad et al., 2018) and hydrous ACMC phases (Raz et al., 2000; Loste et al., 2003) tend to precipitate.

Table 1: Chemical Composition of Synthesized ACMCs.

Sample	$[Mg]_{stock}$[a] (mol%)	$[Mg]_{ACMC}$[b] (mol%)	$nH_2O_{p.f.}$[c] (mol%)	Sample Composition
ACC	0	0	0.44	$CaCO_3 \cdot 0.44H_2O$
ACMC_9	20.1	9.0	0.49	$Ca_{0.91}Mg_{0.09}CO_3 \cdot 0.49H_2O$
ACMC_15	30.3	14.9	0.51	$Ca_{0.85}Mg_{0.15}CO_3 \cdot 0.51H_2O$
ACMC_22	40.1	21.9	0.53	$Ca_{0.78}Mg_{0.22}CO_3 \cdot 0.53H_2O$
ACMC_31	50.1	30.8	0.56	$Ca_{0.69}Mg_{0.31}CO_3 \cdot 0.56H_2O$
ACMC_39	60.7	39.4	0.59	$Ca_{0.61}Mg_{0.39}CO_3 \cdot 0.59H_2O$
ACMC_53	72.1	53.4	0.66	$Ca_{0.47}Mg_{0.53}CO_3 \cdot 0.66H_2O$
ACMC_80	89.1	80.0	0.71	$Ca_{0.20}Mg_{0.80}CO_3 \cdot 0.71H_2O$
AMC	100	100	0.79	$MgCO_3 \cdot 0.79H_2O$

[a]Mg content of the stock solution in mol%. [b]Mg content of the ACMC solid in mol%. [c]moles of water per formula unit $Ca_xMg_{1-x}CO_3$, where $(1-x) = [Mg]_{ACMC} / 100$.
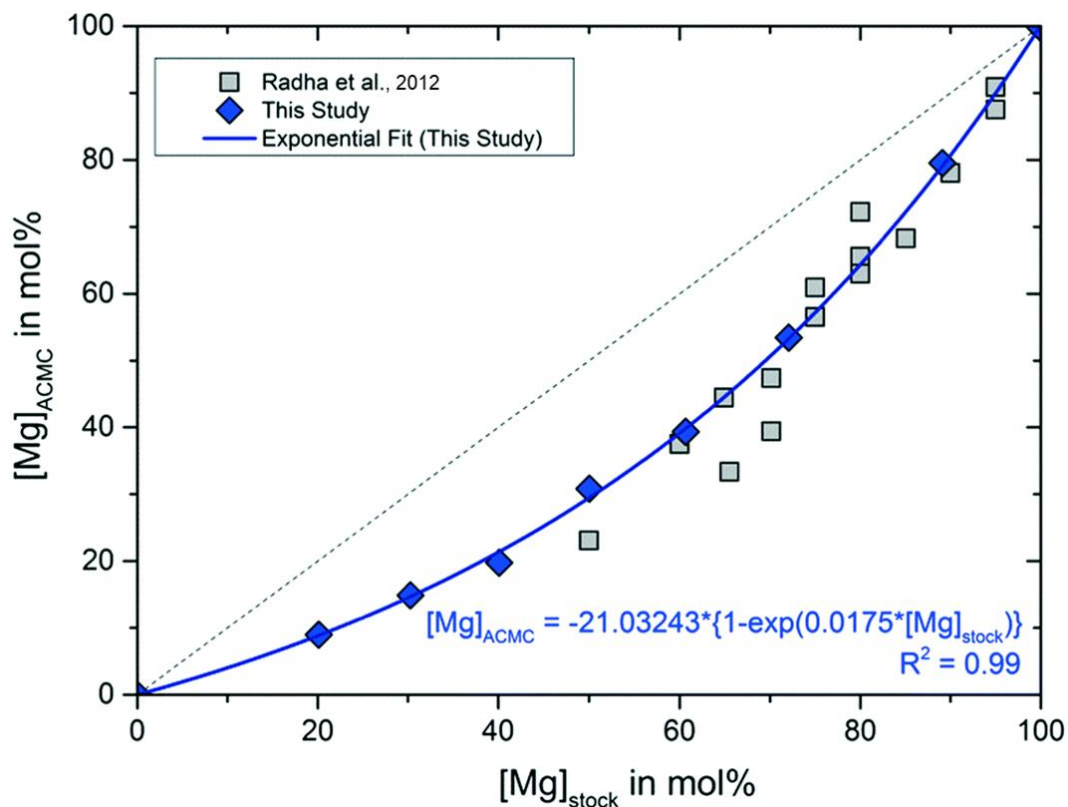
Fig. 1: Mg content of the stock solutions, $[Mg]_{stock}$, versus Mg content of the ACMC precipitates, $[Mg]_{ACMC}$, and respective values reported by Radha et al. (2012). The increase of $[Mg]_{ACMC}$ as a function of $[Mg]_{stock}$ of this study can be described by the equation $[Mg]_{ACMC} = -21.03243 \pm 2.1968*\{1-exp(0.0175 \pm 0.0009 *[Mg]_{stock})\}$ (R^2=0.99; solid line). Analytical uncertainties are included in the symbol size.

Representative Thermogravimetric Analysis (TGA) and Differential Scanning Calorimetry (DSC) curves of the synthesized ACMCs are presented in Fig. S2 (supplementary material). The DSC curve of ACC (Ca endmember of ACMC) shows an endothermic peak at 120 °C, a sharp exothermic peak at 340 °C and a second endothermic peak at 731 °C (Fig. S2A). These DSC features have been earlier shown to be associated with the enthalpies of dehydration, crystallization and decomposition of ACC (Radha et al., 2012; Schmidt et al., 2014). In contrast to ACC, AMC (Mg endmember of ACMC) decomposes without crystallization, as it is indicated by the absence of the sharp exothermic peak in the DSC curve (Fig. S2F). The weight loss curves of ACC and AMC show two weight loss steps (Fig. S2A, F), where the first step is due to the loss of structural water and the second step due to the decomposition of $CaCO_3$ and $MgCO_3$ to CaO, MgO and CO_2 (Radha et al., 2012; Schmidt et al., 2014). After ACC dehydration, the TGA curve achieves a plateau in heating before $CaCO_3$ decomposes to CaO and CO_2 at near 600 °C (Fig. S2A). In

contrast, AMC shows a continuous drop of the TGA curve (without a plateau) for the same temperature range, which indicates that AMC dehydration and decomposition may overlap (Fig. S2F). Based on our TGA data we suggest that AMC decomposition occurs at around 275 °C, as it is indicated by the inflection point of the weight loss curve (Fig. S2F). In contrast to the pure endmembers, the ACMCs show multistep weight loss curves (Fig. S2B-E). These trends are in accordance with the findings of Radha et al. (2012), who associated these features with multistep carbonate decomposition caused by (i) an initial heterogeneous amorphous material or (ii) thermally induced phase segregation during the heating process.

The water contents of the synthetic ACMCs were calculated from the weight losses between 25 and 275 °C. Above this temperature, mass loss might occur due to the decomposition of $MgCO_3$ to MgO, as it is suggested by the TGA curve of AMC (Fig. S2F). The moles of water per unit formula $Ca_xMg_{1-x}CO_3(nH_2O_{p.f.})$ determined by thermal analyses vary between 0.4 for ACC and 0.8 for AMC (Table 1, Fig. 2). As it can be seen in Fig. 2, the water content determined for ACC is in excellent agreement with those reported by Schmidt et al. (2014) and Konrad et al. (2016). Overall, thermal analyses revealed a linear correlation between the $nH_2O_{p.f.}$ and the $[Mg]_{ACMC}$ according to the equation

$$nH_2O_{p.f.} = 0.0034 \pm 0.0002 \, [Mg]_{ACMC} + 0.4574 \pm 0.0124 \qquad (2)$$

where $R^2 = 0.99$. Previous experimental work documented significantly higher $nH_2O_{p.f.}$ values for ACMCs (Fig. 2; Radha et al., 2012). These differences probably originate from different drying methods (freeze-dryer versus vacuum oven). In the study of Radha et al. (2012), the loosely bound physisorbed H_2O on the ACMC particles were probably not completely removed by the vacuum oven prior to thermogravimetric analyses. However, our findings are in good agreement with the results of Lin et al. (2015), who reported $nH_2O_{p.f.}$ values of 0.6, 0.8 and 0.9 for ACMC with 17, 44 and 100 mol% Mg (Fig. 2). In the latter case, the synthesized ACMC samples were washed with ethanol and lyophilized prior to TGA-analysis.

Earlier models on the structure of Mg-free ACC suggested the presence of partially mobile water in the amorphous phase (Nebel et al., 2008; Ihli et al., 2014). In this context, ACC has been described to consist of a porous Ca-framework with interconnected channels formed by water molecules and carbonate ions, allowing water mobility to a certain extent (Goodwin et al., 2010). More recently, Jensen et al. (2018) has shown that

water molecules are mainly coordinated to Ca and carbonate ions and less frequently to other water molecules, ruling out the scenario of hydrogen-bonded networks. This is consistent with the NMR-results of Lin et al. (2015) who concluded that the coordination shell of Mg in ACMC contains at least one water molecule. Indeed, in the present study, the $nH_2O_{p.f.}$ increases as a function of the Mg content (Fig. 2), indicating that partially hydrated Mg is incorporated into the amorphous solid. Our obtained results however suggest that the $nH_2O_{p.f.}$ values for ACMC are significantly lower than previously reported (Radha et al., 2012; Blue and Dove, 2015).
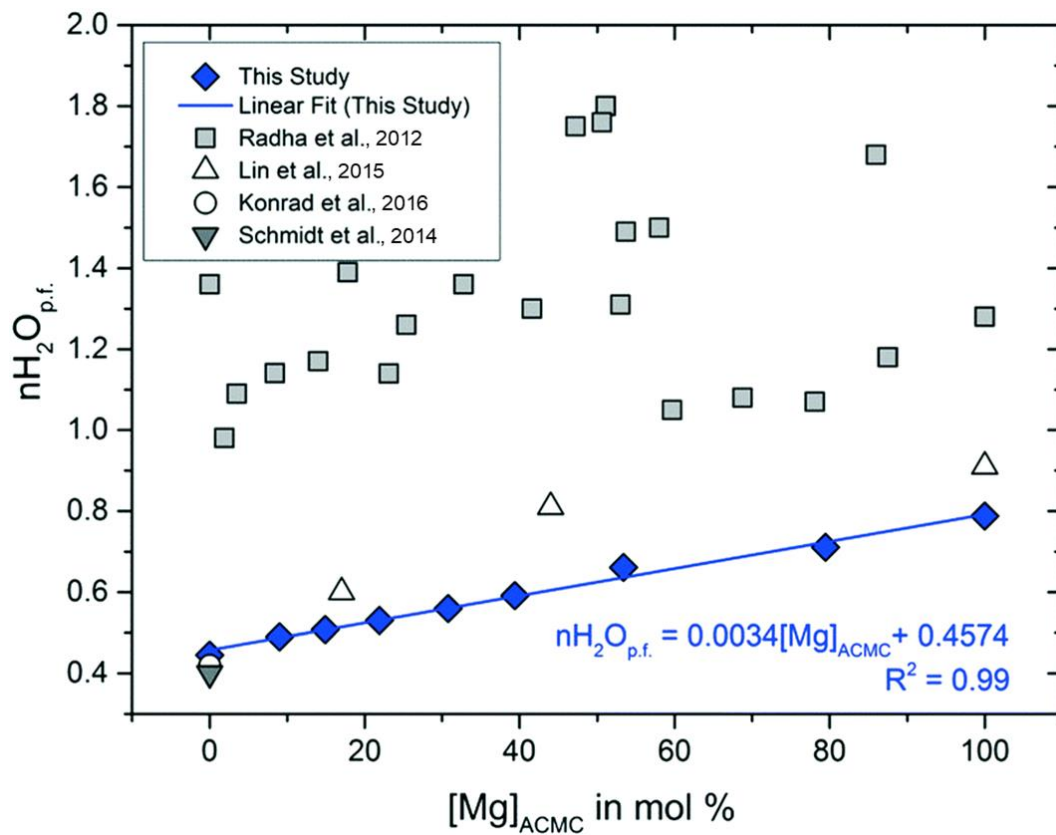
Fig. 2: Mg content of ACMC, $[Mg]_{ACMC}$, versus the moles of water per unit formula $Ca_xMg_{1-x}CO_3$, $nH_2O_{p.f.}$, from synthesis experiments conducted in the present study and from literature. Analytical uncertainties are included in the symbol size.

4.3.2 Exchange of ions between ACMC and aqueous solution

After the synthesized ACMCs were dispersed in the $MgCl_2$-$NaHCO_3$ buffered solutions, the collected *in situ* Raman spectra of the suspensions revealed the presence of a broad CO_3^{2-} symmetric stretch (v_1 band) of ACMC at $1080 - 1098$ cm^{-1} (e.g. experiments ACMC_9 and ACMC_53 in Fig. 3). The v_1 band shows systematic shifts in peak position (Table 2) and peak broadening due to different Mg contents of the ACMCs. These features arise from changes in the metal–oxygen bond length due to the presence of shorter Mg-O bonds compared to those of Ca-O in the amorphous solid (Wang et al., 2012; Purgstaller et al., 2016). The intensities of the v_1 bands of the ACMC phases remained constant for experimental times ranging from 5 to 85 min (referred to as Time$_{ACMC}$ in Table 2). After this time interval, the v_1 bands of the ACMCs decreased in intensity, while the v_1 bands of crystalline hydrous and/or anhydrous Ca-Mg carbonates (Mg calcite, monohydrocalcite and/or nesquehonite) evolved (not shown here). Thus, Time$_{ACMC}$ denotes the time interval in which the ACMC was stable in the experimental solution (Table 2). Note that, the *in situ* Raman observations were confirmed by ex situ XRD analyses of the collected solid samples.

Although, Time$_{ACMC}$ increased as a function of the Mg content in experiments conducted with ACMCs containing ≤ 22 mol% Mg, a reverse trend was obtained in experiments with ACMCs containing > 22 mol% (Table 2). These observations imply that the temporal stability of ACMC in a solution is not strictly controlled by its primary Mg content. In contrast, the obtained data revealed changes in the chemical composition of the reacting ACMC and the experimental solution which might play a crucial role in the temporal stabilization of the precursor phase and its subsequent transformation into distinct crystalline calcium magnesium carbonates.
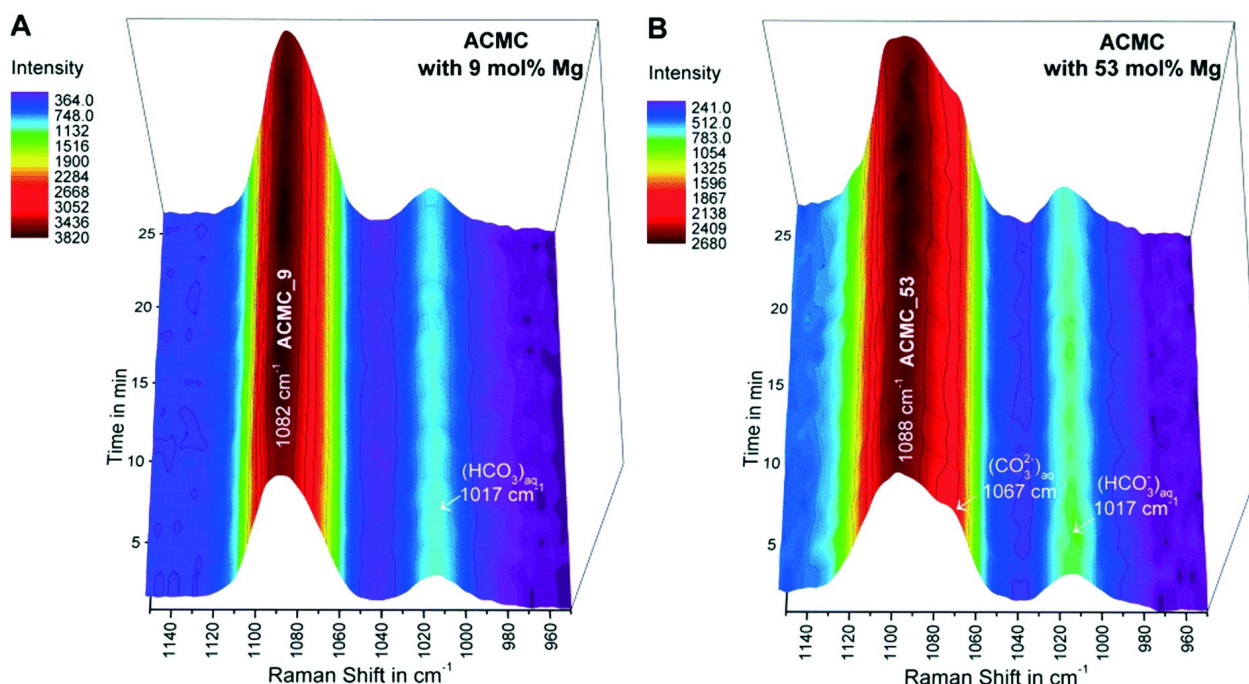
Fig. 3: 3D plots of *in situ* Raman spectra showing the temporal evolution of the ν_1 band of ACMC for the experiments conducted with ACMC_9 (A) and ACMC_53 (B). The Raman bands at 1067 cm^{-1} and 1017 cm^{-1} correspond to aqueous CO_3^{2-} and HCO_3^-, respectively.

The chemical composition of the experimental solutions and solids collected during Time$_{ACMC}$ can be found in Table S1. Exemplarily, the temporal evolution of the chemical composition of the solutions and solids in experiments conducted with ACMC_53 (53 mol% Mg) and with ACMC_9 (9 mol% Mg) is illustrated in Fig. 4A-C. The obtained results documented a significant change in the chemical composition of the solids and experimental solutions within about 10 sec after the ACMCs were dispersed into the MgCl$_2$-NaHCO$_3$ solutions. In each experiment, chemical steady state conditions were attained at a reaction time of about 2 min (Fig. 4A-C; Table S1). The fast reaction between the amorphous solid and the solution can be explained by the nano-porous structured ACMC material consisting of large and highly reactive surface areas (Fig. S3). The shifts in pH and alkalinity of the MgCl$_2$-NaHCO$_3$ buffered solution increase with increasing Mg content of the synthesized ACMCs (Fig. 4D). For example, dispersion of ACMC with 9 mol% Mg (ACMC_9) yields a slight shift in pH and alkalinity from 8.3 to 8.5 and 104 to 107 mM, respectively, whereas for ACMC with 53 mol% Mg (ACMC_53) a significant shift in pH to 9.1 and alkalinity to 143 mM was observed (Fig. 4A-B). This indicates that for attainment of chemical equilibrium between solid and solution, larger amounts of ACMC

are required to dissolve in the experiment with ACMC_53 (53 mol% Mg) compared to the experiment conducted with ACMC_9 (9 mol% Mg).

The results revealed two distinctive trends of Mg and Ca exchange between ACMCs and the solution, depending on the Mg concentrations of synthesized ACMCs: (i) in experiments conducted with ACMCs containing ≤ 15 mol% Mg a net release of Ca into the solution together with an uptake of Mg from the solution into the solid is observed, which results in ACMCs with slightly higher Mg contents compared to the synthesized ACMC (e.g. ACMC_9 in Fig. 4B-C; Table S1). (ii) In contrast, in experiments conducted with ACMCs containing ≥ 20 mol% Mg a net release of Mg into the experimental solution and lower $[Mg]_{ACMC}$ values compared to the synthesized ACMCs were observed (e.g. ACMC_53 in Fig. 4B-C; Table S1). These observations suggest a dynamic exchange of Me^{2+} (Ca^{2+} and Mg^{2+}) ions between the amorphous solid and the experimental solution. It is likely that the total availability of Me^{2+} (Ca^{2+} and Mg^{2+}) and CO_3^{2-} ions in the prevailing solution affects the formation of distinct crystalline calcium magnesium carbonates and the temporal stability of the ACMC precursor in solution. Evidence for that also comes from a recent study on ACC transformation, showing prolonged stability of Mg-free ACC of up to ~11 hours in high concentrated $MgCl_2$ solutions (up to 1000 mM; Konrad et al., 2018). It was concluded that strong aquocomplex formation of the dissolved carbonate molecule with Mg^{2+} ions retarded mineral formation and increased the stability of ACC in solution (Konrad et al., 2018).
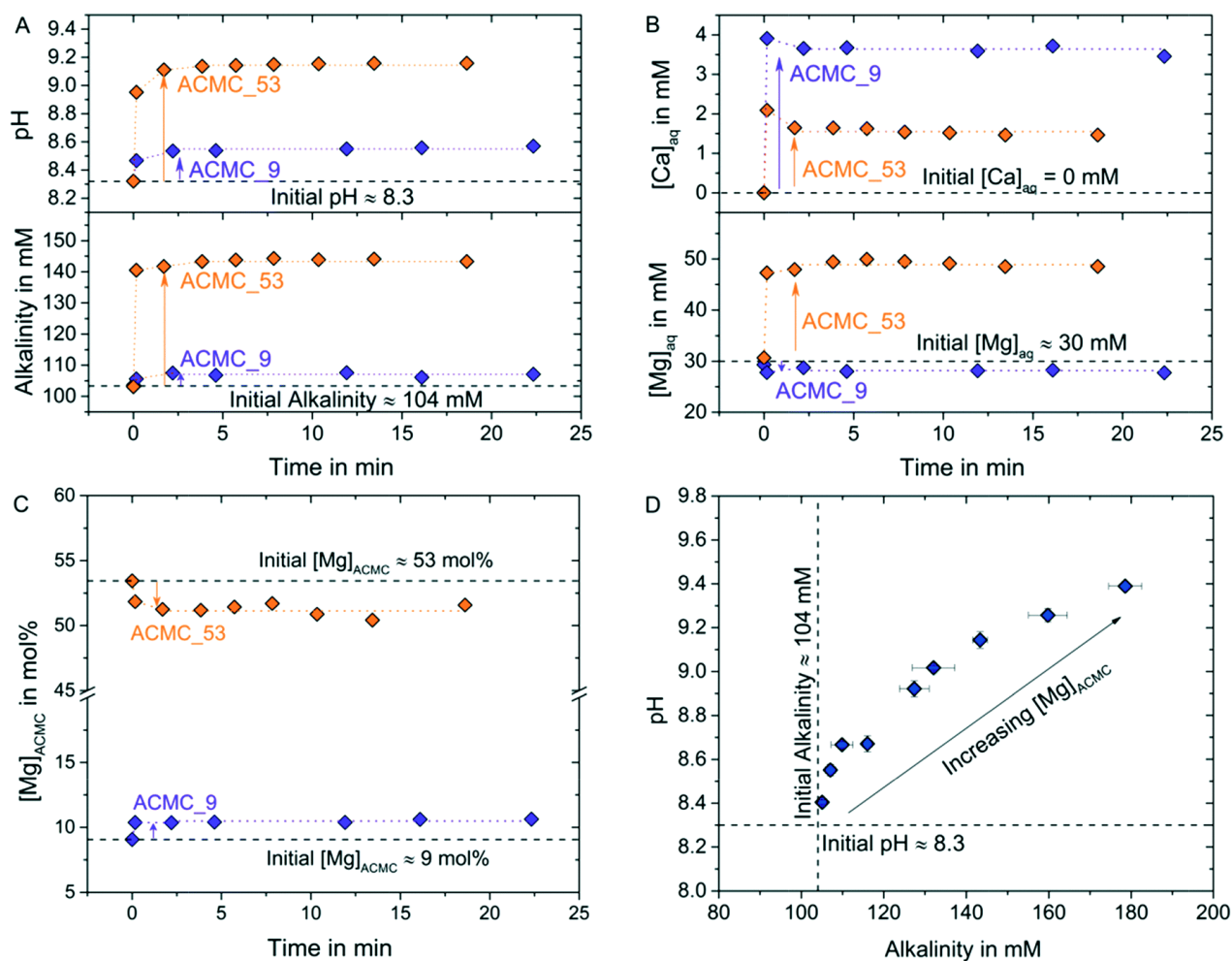
Fig. 4: Temporal evolution of (A) pH and alkalinity concentration, (B) aqueous Ca and Mg concentration of the experimental solution, $[Ca]_{aq}$ and $[Mg]_{aq}$, and (C) Mg content of ACMC solid, $[Mg]_{ACMC}$, after synthesized ACMC solids were dispersed into the $MgCl_2$-$NaHCO_3$ solutions. Exemplarily the data for ACMC_53 and ACMC_9 are shown, where the experimental solution achieves constant chemical composition after 2 min of reaction time. Note that chemical data obtained at > 2 min were used for estimating the ion activity products of the distinct ACMCs according to eq. 1 (Table 2). (D) Average alkalinity concentration versus pH values of the experimental solution at chemical steady state conditions (> 2 min, see Table S2). The shifts in pH and alkalinity increase with increasing $[Mg]_{ACMC}$.

4.3.3 Solubility Approach

The experimental solution in all experimental runs achieved chemical steady state conditions after 2 min of reaction time. These conditions remained steady during the time interval in which solid analyses (Raman spectra and XRD pattern) documented the stability of ACMC in the aqueous phase (Time$_{ACMC}$ in Table 2). Thus, speciation calculations were performed at reaction times $\geq$ 2 min and $\leq$ Time$_{ACMC}$. The input data for speciation calculations using PHREEQC modeling and selected output data are summarized in Table S2. The results showed that the experimental solutions exhibit internal partial pressures of CO_2 ranging from $10^{-1.8}$ to $10^{-2.9}$ atmospheres (see p$_{CO2(g)}$ in Table S2). As such, the p$_{CO2}$ pressure of the experimental solutions is higher compared to the atmosphere and thus CO_2 is likely degassing from the experimental solutions. However, in context of the present study, samples of the suspensions were collected during a short time interval (< 45 min) in which p$_{CO2(g)}$, pH and alkalinity values were monitored to be constant within the analytical precision (Table S2). Thus, the obtained activities of Ca^{2+}, Mg^{2+} and CO_3^{2-} ions of the solution and the ACMC stoichiometry at the given reaction time were used to calculate individual IAP$_{ACMC}$ (solubility) values according to eq. 1 (Table S2). The average log(IAP$_{ACMC}$) values are listed in Table 2 and plotted in Fig. 5 as a function of the Mg content of the ACMC. Note here that the average Mg content of the ACMC solid at chemical steady state conditions (after Ca and Mg ion exchange) was used for IAP$_{ACMC}$ calculations (Table 2) and was plotted in Fig. 5. The results clearly show that the solubility of ACMC increases as a function of the Mg content (Fig. 5). The linear fit of the log(IAP$_{ACMC}$) values obtained in the context of the present study is in good agreement with the log(IAP) value for ACC documented by Brečević and Nielsen (1989), while the solubility products for ACCs reported by Gebauer et al. (2008) are significantly smaller. The obtained log(IAP$_{ACMC}$) values of -6.19 ±0.02 and -6.13 ±0.02 for ACMCs with 2 and 10 mol% Mg, respectively, lay within the range of -6.14 ±0.04 for the low-Mg ACMC reported by Purgstaller et al. (2016). In this respect, it has to be noted that the solids collected in the present experiments were filtered through 0.2 μm membranes. Although the separation yields aggregated spherical nano-particles (see Fig. S4) and the solutions were visibly clear after filtration, the presence of ACMC individuals in the filtered solutions cannot be completely ruled out at this stage. Partially remaining ACMC in the solution would slightly increase the measured ion concentrations. However, the linear fit of the herein obtained log(IAP$_{ACMC}$) values is in good agreement with the log(IAP$_{ACC}$) value from Brečević and Nielsen (1989), who determined the solubility of ACC by titration of

water into the suspension without physical separation of the solid phase, indicating the effect of ACMC individuals in the filtered solutions to be negligibly small. The positive correlation between the $\log(IAP_{ACMC})$ and $[Mg]_{ACMC}$ values obtained from this study, from Brečević and Nielsen (1989) and Purgstaller et al. (2016) can be described by the expression:

$$\log(IAP_{ACMC}) = 0.0174 \pm 0.0013 * [Mg]_{ACMC} - 6.278 \pm 0.046 \tag{3}$$

where $R^2 = 0.98$. Note here that the calculation of the IAP_{ACMC} values is based on the assumption that the ACMCs are amorphous Ca-Mg carbonate solid-solutions. However, a previous study on synthetic ACMCs by Radha et al. (2012) points towards a phase separation of ACMC solids with ≥ 47 mol% Mg. It has been suggested that ACMC with ≥ 47 mol% are composed by a mixture of a material nearly pure AMC with a material nearly 50 mol% Mg. However, such heterogeneity may also be induced during the heating of the ACMC solids during thermogravimetric analyses (thermally driven $MgCO_3$ segregation; Radha et al., 2012). More recently, the ^{13}C-NMR measurements on ACMCs by Yang et al. (2016) showed two types of carbonate ions in synthetic ACMC solids, whose short-range orders are identical to those of ACC and AMC. Based on these observations, Yang et al. (2016) suggested that the ACMC solids comprise a homogeneous mixture of the nano-clusters of ACC and AMC. In order to test the validity of the Ca-Mg carbonate solid-solution system, we calculated the IAP values of the experimental solutions at chemical steady state conditions with respect to the endmembers ACC and AMC according to the equations $IAP_{ACC} = (aCa^{2+}) \cdot (aCO_3^{2-})$ and $IAP_{AMC} = (aMg^{2+}) \cdot (aCO_3^{2-})$, respectively. As the Mg content of the solid increases from 2 to 78 mol% Mg, the $\log(IAP_{AMC})$ and $\log(IAP_{ACC})$ values change from -5.4 to -4.5 and -6.2 to -6.5, respectively. If the ACMCs consist of an ideal two phase mixture of ACC and AMC, we would expect constant $\log(IAP_{ACC})$ and $\log(IAP_{AMC})$ in all experiments, irrespective of the Mg content of the solid initially introduced into the reactor. As such, the presence of discrete AMC and ACC phases in the ACMC solid can be excluded. In contrast, the obtained linear correlation between the average $\log(IAP_{ACMC})$ and $[Mg]_{ACMC}$ values (see Fig. 5) points toward the presence of an homogeneous single phase in each experimental run.

Table 2: Summary of *in situ* Raman results and calculated ion activity product values of solubility experiments

Sample	Raman v_1 Band[a] (cm^{-1})	Time$_{ACMC}$[b] (min)	[Mg]$_{ACMC\_av}$[c] (mol%)	log(aCO$_3^{2-}$)$_{av}$[d]	log(aCa^{2+})$_{av}$[d]	log(aMg^{2+})$_{av}$[d]	log(IAP$_{ACMC}$)$_{av}$[e]
ACC	1080 ±1	15	2.2 ±0.2	-3.14 ±0.01	-3.08 ±0.03	-2.25 ±0.02	-6.20 ±0.02
ACMC_9	1082 ±1	24	10.5 ±0.2	-3.01 ±0.02	-3.22 ±0.03	-2.23 ±0.01	-6.13 ±0.02
ACMC_15	1083 ±1	54	15.8 ±0.3	-2.91 ±0.01	-3.31 ±0.04	-2.21 ±0.01	-6.04 ±0.03
ACMC_22	1084 ±1	85	21.2 ±0.7	-2.87 ±0.03	-3.38 ±0.05	-2.20 ±0.03	-6.00 ±0.03
ACMC_31	1085 ±1	64	29.3 ±1.6	-2.67 ±0.02	-3.54 ±0.08	-2.18 ±0.05	-5.81 ±0.07
ACMC_39	1086 ±1	51	37.4 ±0.5	-2.58 ±0.02	-3.68 ±0.06	-2.21 ±0.06	-5.71 ±0.03
ACMC_53	1088 ±1	20	51.3 ±0.6	-2.51 ±0.02	-3.78 ±0.05	-2.12 ±0.01	-5.43 ±0.02
ACMC_80	1095 ±1	9	78.5 ±0.4	-2.39 ±0.03	-4.10 ±0.10	-2.14 ±0.01	-4.96 ±0.01
AMC	1098 ±1	5	100	-2.30 ±0.01	-	-2.12 ±0.01	-4.42 ±0.01

[a]Raman v_1 peak positions of ACMC solids dispersed in the MgCl$_2$-NaHCO$_3$ buffered solutions. [b]Time interval in which ACMC was stable in the experimental solution. [c]Average Mg content of the ACMC solid at chemical steady state conditions (used for IAP$_{ACMC}$ calculation). [d]Average activities of CO$_3^{2-}$, Ca^{2+} and Mg^{2+} ions in the experimental solution at chemical steady state conditions (used for IAP$_{ACMC}$ calculation). [e]Average ion activity product for ACMC calculated according to eq. 1. Note that the input data for speciation calculations and selected output data are listed in Table S2.

It is also worth pointing out that the ^{13}C-NMR measurements on ACMCs by Yang et al. (2016) indicated the existence of bicarbonate species embedded in the matrix formed by ACC and AMC. Moreover, based on the Mg isotope composition of Mg-ACCs, Mavromatis et al. (2017b) suggested that during the very fast precipitation of the amorphous phase from a highly supersaturated solution, MgHCO$_3^+$ and MgCO$_3^0$ species might be directly incorporated into the precipitating solid together with Mg(H$_2$O)$_6^{2+}$. If this holds true, the activities of Ca and Mg carbonate species have to be considered in the calculation of the IAP$_{ACMC}$ values. For this purpose, however, a more detailed characterization of the structure of ACMC is required, which should be in the focus of future studies.

Although the solubility of ACC is about two orders of magnitude higher than that of calcite, the dependence of IAP$_{ACMC}$ on the Mg content of the solid (Fig. 5) is somehow similar to that observed for the Mg calcite system (Busenberg and Plummer, 1989). Indeed, experimental work conducted during the last 3 decades documents an overall increase in solubility of Mg-bearing calcites with increasing Mg content (Bischoff et al., 1987; 1993; Busenberg and Plummer, 1989). Note, that significant discrepancies exist

between reported solubility values of Mg calcites, which were attributed to differences in mineral source and structure (biogenic or synthetic solids) as well as different experimental setups (Bischoff et al., 1987; 1993; Busenberg and Plummer, 1989). The change in calcite solubility as Mg is incorporated in its structure can likely be attributed to the distortion of the octahedral site in calcite. The substitution of Ca by Mg in the calcite structure results in a decrease of interatomic metal-O distances and shortening of the c-axis (Althoff, 1977; Bischoff et al., 1985). Consequently, Ca, C and O atoms exhibit large thermal motions which cause periodic stretching and weakening of the bonds in the structure (Althoff, 1977).

In contrast to the crystalline Ca-Mg carbonate system, amorphous carbonates exhibit no order beyond 1.5 nm (Michel et al., 2008; Wang et al., 2012). *In situ* Raman results from the present work and from previous studies (Wang et al., 2012; Demény et al., 2016) however showed that the substitution of Ca^{2+} by Mg^{2+} changes the average metal-oxygen bond lengths in the amorphous phase, which might change its short-range order and solubility. Moreover, the linear relationship between the IAP_{ACMC} and $[Mg]_{ACMC}$ values (Fig. 1) as well as of the $[Mg]_{ACMC}$ and $nH_2O_{p.f.}$ values (Fig. 2) suggests that the increase in solubility of ACMC as a function of the Mg content is attributed to the increasing water content in the structure of ACMC. A similar behavior has been observed for the hydrated crystalline Mg-carbonate system, where the more hydrated lansfordite ($MgCO_3 \cdot 5H_2O$) exhibits a higher solubility than the less hydrated nesquehonite ($MgCO_3 \cdot 3H_2O$) at 25 °C (Marion, 2001).
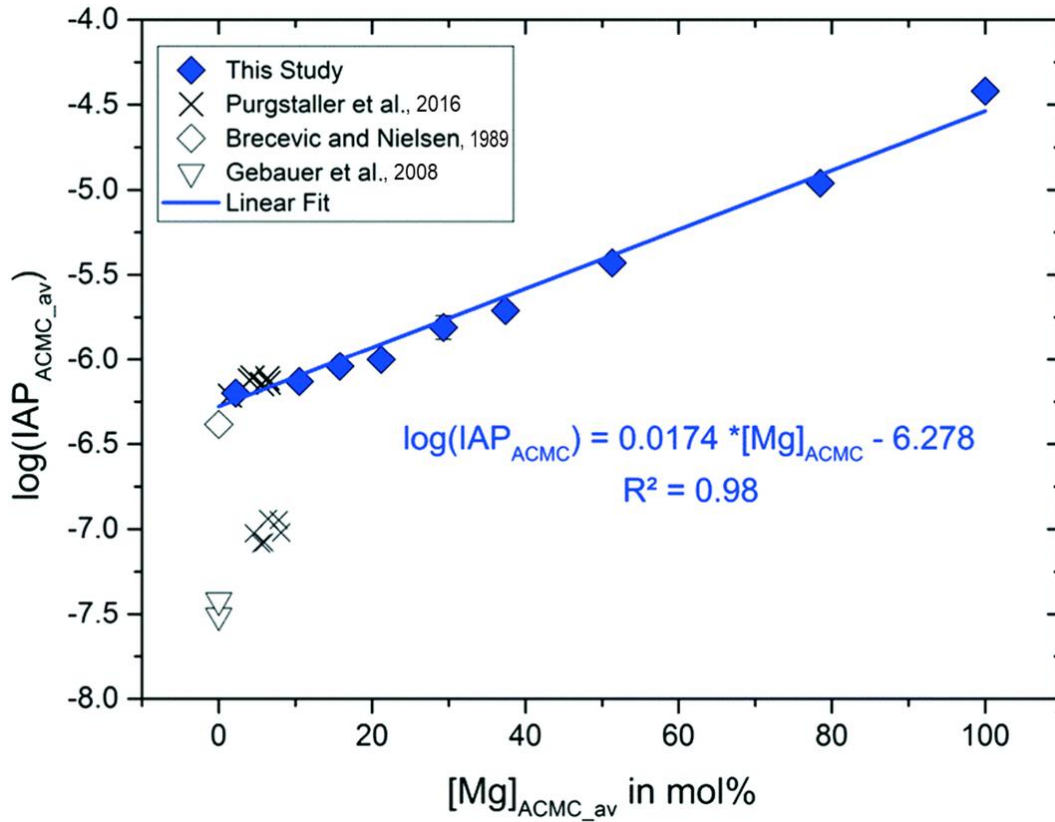
Fig. 5: Average Mg content of ACMC, $[Mg]_{ACMC\_av}$, versus the average ion activity product of ACMC, $\log(IAP_{ACMC})_{av}$ (resembling the solubility product of the ACMC phase), calculated according to eq. 1 at chemical steady state conditions (see values in Table 2). The $\log(IAP_{ACMC})$ values for Mg-free ACC are taken from Brečević and Nielsen (1989) and Gebauer et al. (2008), while those for ACMC with ≤ 10 mol% Mg are taken from Purgstaller et al. (2016). The analytical uncertainties are included in the symbol size.

4.4 Conclusions

The experimental results indicated a fast exchange of ions between the synthesized amorphous ACMC solids and the aqueous solutions, which is likely stimulated by the large surface area of the nano-porous ACMC solid. Chemical steady state conditions between ACMC and corresponding solution were reached within 2 min of reaction time. The calculated ion activity products documented that the solubility of ACMC increases as a function of the Mg content. This feature is probably linked to the increasing water content and changes in short-range order, as Ca is substituted by Mg in the ACMC structure. Overall, the results reveal a high sensitivity of the ACMC phase in respect to the chemical composition (e.g. magnesium concentration) of the aqueous environment.

The exchange of ions between the amorphous solid and the solution causes changes in the chemical composition of the solution (e.g. pH and alkalinity) and that of the solid (e.g. Mg content). This ion exchange probably affects the temporal stability of the amorphous precursor in solution and its subsequent transformation into distinct crystalline calcium magnesium carbonates. Essentially, our findings suggest that the Mg content of ACMC is not the governing parameter for its temporal stability in solution. In contrast, the chemical composition of both the solution and the amorphous solid, have to be taken into account as a potential parameter controlling ACMC stability and transformation behavior. For example, in a closed system the chemistry of the fluid (e.g. calcifying fluid in the biomineralization space) would influence the temporal stability of the amorphous precursor and its transformation pathway to the final crystalline carbonate mineral.

4.5 Supplementary material

Table S1: Chemical composition of experimental solutions and solids of solubility experiments. Sample: synthetic ACMC sample used for solubility experiments (see Table 1); Time: reaction time during the experimental run; pH: pH of the experimental solution; Alkalinity: alkalinity concentration of the experimental solution; $[Ca]_{aq}$, $[Mg]_{aq}$, $[Na]_{aq}$: measured Ca, Mg and Na concentration of the experimental solution; $[Mg]_{ACMC}$: Mg content of the ACMC solid; IAP_{ACMC}: ion activity product of the experimental solution calculated according to eq. 1.

Sample	Time min	pH	Alkalinity mM	$[Ca]_{aq}$ mM	$[Mg]_{aq}$ mM	$[Na]_{aq}$ mM	$[Mg]_{ACMC}$ mol%
ACC	0	8.30	104.2	0	28.6	99.3	0
	0.2	8.37	106.1	4.6	24.9	96.8	1.8
	2.3	8.41	105.0	4.9	26.4	105.1	2.1
	4.4	8.40	105.7	4.8	25.9	103.8	2.1
	6.4	8.40	104.6	4.9	25.8	103.4	2.2
	8.7	8.40	105.4	4.6	25.0	99.4	2.3
	12.5	8.41	104.4	4.5	25.1	102.7	2.3
ACMC_9	0	8.32	103.6	0	29.3	101.4	9.1
	0.2	8.47	105.6	3.9	27.8	100.7	10.4
	2.2	8.54	107.5	3.7	28.7	104.3	10.4
	4.6	8.54	106.8	3.7	28.0	103.3	10.4
	11.9	8.55	107.6	3.6	28.1	103.9	10.4
	16.1	8.56	106.1	3.7	28.3	103.8	10.6
	22.3	8.57	107.1	3.5	27.7	104.1	10.6
ACMC_15	0	8.40	103.5	0	30.2	103.6	14.9
	0.2	8.64	112.3	4.0	30.6	102.0	15.7
	1.7	8.66	111.2	3.5	30.7	101.6	15.7
	4.1	8.66	111.7	3.3	30.3	102.3	15.8
	6.3	8.66	110.8	3.3	30.9	104.2	15.5
	9.8	8.67	108.9	3.2	30.7	104.2	15.7
	14.0	8.67	108.8	3.1	30.3	101.4	15.8
	21.2	8.67	108.8	3.0	29.8	101.9	16.0
	28.4	8.68	108.8	3.0	30.1	102.7	16.0
	35.7	8.69	109.8	3.1	30.4	103.6	15.9
ACMC_22	0	8.33	103.3	0.0	25.6	99.0	21.9
	0.2	8.60	140.9	2.5	31.0	-	21.5
	4.6	8.66	115.9	2.9	32.0	98.4	21.2
	7.8	8.67	115.9	2.9	30.8	97.8	20.8
	12.1	8.68	116.5	2.7	31.1	98.5	21.0
	17.9	8.69	115.0	2.9	32.7	98.1	21.9
	27.5	8.70	116.3	2.6	30.4	97.4	21.3
	44.7	8.71	115.3	2.7	32.3	103.7	21.2
ACMC_31	0.0	8.32	104.8	0	27.0	106.7	30.8
	0.2	8.43	124.5	2.5	35.9	106.5	29.4
	2.0	8.89	126.9	2.5	36.0	103.0	30.4
	4.0	8.91	128.1	2.0	34.2	101.3	29.0
	6.1	8.92	124.9	2.1	36.2	104.9	28.2
	8.8	8.92	128.4	2.2	37.3	105.6	29.2
	11.9	8.93	128.4	2.3	40.1	102.1	30.6
	14.2	8.94	129.8	2.5	39.4	103.8	29.3
	18.6	8.94	125.3	2.5	40.4	106.6	28.9
	35.7	8.95	124.5	2.1	38.7	102.5	28.9

ACMC_39	0	8.32	104.7	0	28.8	101.5	39.4
	0.2	8.87	125.1	2.3	39.1	101.9	38.2
	5.2	9.01	133.6	2.0	40.8	102.2	37.2
	8.2	9.02	133.7	1.8	39.9	102.2	37.4
	11.3	9.02	132.8	1.8	35.5	102.7	37.7
	14.9	9.02	132.9	1.7	35.2	102.7	37.2
	19.1	9.02	131.8	1.7	36.4	101.7	37.7
	39.1	9.02	133.2	1.8	37.6	102.0	37.1
ACMC_53	0	8.32	103.1	0	30.7	102.9	53.4
	0.2	8.95	140.5	2.1	47.3	104.7	51.8
	1.7	9.11	141.7	1.6	47.9	101.5	51.2
	3.9	9.14	143.3	1.6	49.4	103.7	51.2
	5.7	9.14	143.8	1.6	49.9	104.6	51.4
	10.4	9.15	143.9	1.5	49.1	103.7	50.9
	13.5	9.16	144.1	1.5	48.5	101.8	50.4
	18.6	9.16	143.3	1.5	48.5	103.5	51.6
ACMC_80	0.0	8.33	104.0	0.0	28.3	100.9	79.5
	0.2	9.01	154.7	1.4	48.6	98.4	78.6
	1.8	9.23	159.4	1.0	51.5	99.8	78.3
	3.9	9.25	162.0	0.9	52.2	100.5	78.5
	5.7	9.26	160.6	0.8	52.1	100.2	78.4
	7.8	9.27	161.4	0.8	51.8	100.1	78.8
AMC	0	8.33	103.1	0	28.5	102.7	100
	0.2	9.31	189.4	0	67.78	102.3	100
	1.9	9.39	181.4	0	61.6	100.1	100
	3.8	9.39	175.7	0	59.8	102.4	100

Table S2: Input data for PhreeqC calculations and selected output data of experimental solutions at chemical steady state conditions (> 2 min). Sample: synthetic ACMC sample used for solubility experiments (see Table 1); Time: reaction time during the experimental run; Alkalinity: alkalinity concentration; $[Ca]_{aq}$, $[Mg]_{aq}$, $[Na]_{aq}$: measured Ca, Mg and Na concentration; $[Cl]_{aq}$: Cl concentration given by the $MgCl_2$ added in the initial experimental solution ($[Cl]_{aq} = 2*$ initial $[Mg]_{aq}$; see Table 1); I: ionic strength; charge: electrical charge balance; %Err: percentage error based on the charge imbalance ($100*(Cat-An)/(Cat+An)$); $p_{CO2(g)}$: logarithm of internal CO_2 partial pressure; $\log(aCO_3^{2-})$, $\log(aCa^{2+})$, $\log(aCa^{2+})$: activities of Ca^{2+}, Mg^{2+} and CO_3^{2-} ions; $[Mg]_{ACMC}$: Mg content of the sampled ACMC solid; IAP_{ACMC}: ion activity product of the experimental solution calculated according to eq. 1.

Sample	Time min	pH	Alk. mM	$[Ca]_{aq}$ mM	$[Mg]_{aq}$ mM	$[Na]_{aq}$ mM	$[Cl]_{aq}$ mM	I	charge	%Err	$p_{CO2(g)}$	$\log(aCO_3^{2-})$	$\log(aCa^{2+})$	$\log(aMg^{2+})$	$[Mg]_{ACMC}$ mol%	$\log(IAP_{ACMC})$
ACC	2.3	8.41	105.0	4.9	26.4	105.1	57.1	0.17	5.6E-03	1.9	-1.81	-3.14	-3.07	-2.24	2.1	-6.19
	4.4	8.40	105.7	4.8	25.9	103.8	57.1	0.17	2.4E-03	0.8	-1.79	-3.14	-3.08	-2.24	2.1	-6.20
	6.4	8.40	104.6	4.9	25.8	103.4	57.1	0.17	3.1E-03	1.1	-1.80	-3.15	-3.07	-2.24	2.2	-6.20
	8.7	8.40	105.4	4.6	25.0	99.4	57.1	0.16	-3.9E-03	-1.4	-1.79	-3.14	-3.09	-2.26	2.3	-6.21
	12.5	8.41	104.4	4.5	25.1	102.7	57.1	0.17	4.0E-04	0.1	-1.81	-3.14	-3.10	-2.26	2.3	-6.22
Average	-	*8.40*	*105.0*	*4.7*	*25.6*	*102.9*	*57.1*	*0.17*	-	-	*-1.80*	*-3.14*	*-3.08*	*-2.25*	*2.2*	*-6.20*
±2δ	-	*±0.01*	*±1.1*	*±0.04*	*±1.2*	*±4.3*	-	*±0.01*	-	-	*±0.02*	*±0.01*	*±0.03*	*±0.02*	*±0.2*	*±0.02*
ACMC_9	2.2	8.54	107.5	3.7	28.7	104.3	58.6	0.17	3.0E-03	1.0	-1.95	-3.02	-3.21	-2.22	10.4	-6.13
	4.6	8.54	106.8	3.7	28.0	103.3	58.6	0.17	1.3E-03	0.4	-1.95	-3.02	-3.21	-2.23	10.4	-6.13
	11.9	8.55	107.6	3.6	28.1	103.9	58.6	0.17	1.1E-03	0.4	-1.96	-3.01	-3.23	-2.23	10.4	-6.14
	16.1	8.56	106.1	3.7	28.3	103.8	58.6	0.17	3.1E-03	1.1	-1.98	-3.01	-3.21	-2.22	10.6	-6.11
	22.3	8.57	107.1	3.5	27.7	104.1	58.6	0.17	8.0E-04	0.3	-1.99	-2.99	-3.24	-2.23	10.6	-6.12
Average	-	*8.55*	*107.0*	*3.6*	*28.2*	*103.9*	*58.6*	*0.17*	-	-	*-1.97*	*-3.01*	*-3.22*	*-2.23*	*10.5*	*-6.13*
±2δ	-	*±0.03*	*±1.2*	*±0.2*	*±0.7*	*±0.8*	-	-	-	-	*±0.04*	*±0.02*	*±0.03*	*±0.01*	*±0.2*	*±0.02*
ACMC_15	1.7	8.66	111.2	3.5	30.7	101.6	60.3	0.17	-1.5E-03	-0.5	-2.08	-2.91	-3.27	-2.21	15.7	-6.01
	4.1	8.66	111.7	3.3	30.3	102.3	60.3	0.17	-2.5E-03	-0.9	-2.08	-2.91	-3.29	-2.21	15.8	-6.03
	6.3	8.66	110.8	3.3	30.9	104.2	60.3	0.17	1.5E-03	0.5	-2.08	-2.91	-3.29	-2.20	15.5	-6.03
	9.8	8.67	108.9	3.2	30.7	104.2	60.3	0.17	2.8E-03	1.0	-2.10	-2.91	-3.30	-2.20	15.7	-6.04
	14.0	8.67	108.8	3.1	30.3	101.4	60.3	0.17	-9.0E-04	-0.3	-2.10	-2.91	-3.32	-2.21	15.8	-6.06
	21.2	8.67	108.8	3.0	29.8	101.9	60.3	0.17	-1.6E-03	-0.6	-2.10	-2.91	-3.33	-2.22	16.0	-6.06
	28.4	8.68	108.8	3.0	30.1	102.7	60.3	0.17	-2.0E-04	-0.1	-2.11	-2.90	-3.33	-2.21	16.0	-6.05
	35.7	8.69	109.8	3.1	30.4	102.4	60.3	0.17	-7.0E-04	-0.2	-2.12	-2.89	-3.32	-2.21	15.9	-6.03
Average	-	*8.67*	*109.9*	*3.2*	*30.4*	*102.6*	*60.3*	*0.17*	-	-	*-2.10*	*-2.91*	*-3.31*	*-2.21*	*15.8*	*-6.04*
±2δ	-	*±0.02*	*±2.4*	*±0.3*	*±0.7*	*±2.2*	-	-	-	-	*±0.03*	*±0.01*	*±0.04*	*±0.01*	*±0.3*	*±0.03*
ACMC_22	4.6	8.66	115.9	2.9	32.0	98.4	51.2	0.17	1.1E-03	0.4	-2.06	-2.89	-3.36	-2.19	21.2	-6.00
	7.8	8.67	115.9	2.9	30.8	97.8	51.2	0.16	-1.9E-03	-0.7	-2.07	-2.88	-3.36	-2.21	20.8	-6.00
	12.1	8.68	116.5	2.7	31.1	98.5	51.2	0.17	-1.6E-03	-0.6	-2.08	-2.87	-3.39	-2.21	21.0	-6.01
	17.9	8.69	115.0	2.9	32.7	98.1	51.2	0.17	3.1E-03	1.1	-2.10	-2.87	-3.36	-2.19	21.9	-5.97
	27.5	8.70	116.3	2.6	30.4	97.4	51.2	0.16	-4.1E-03	-1.5	-2.10	-2.85	-3.42	-2.22	21.3	-6.01
	44.7	8.71	115.3	2.7	32.3	103.7	51.2	0.17	7.2E-03	2.5	-2.13	-2.85	-3.40	-2.20	21.2	-6.00
Average	–	*8.69*	*115.8*	*2.8*	*31.6*	*99.0*	*51.2*	*0.17*	-	-	*-2.09*	*-2.87*	*-3.38*	*-2.20*	*21.2*	*-6.00*
±2δ	–	*±0.04*	*±1.1*	*±0.3*	*±1.8*	*±4.7*	-	*±0.01*	-	-	*±0.05*	*±0.03*	*±0.05*	*±0.02*	*±0.7*	*±0.03*

ACMC_31	2.0	8.89	126.9	2.5	36.0	103.0	54.0	0.17	1.0E-03	0.3	-2.32	-2.69	-3.49	-2.19	30.4	-5.79
	4.0	8.91	128.1	2.0	34.2	101.3	54.0	0.17	-4.1E-03	-1.4	-2.33	-2.66	-3.60	-2.22	29.0	-5.86
	6.1	8.92	124.9	2.1	36.2	104.9	54.0	0.17	-2.2E-04	-0.1	-2.36	-2.67	-3.57	-2.19	28.2	-5.85
	8.8	8.92	128.4	2.2	37.3	105.6	54.0	0.17	3.8E-04	0.1	-2.35	-2.66	-3.56	-2.18	29.2	-5.82
	11.9	8.93	128.4	2.3	40.1	102.1	54.0	0.18	9.1E-03	3.1	-2.38	-2.67	-3.53	-2.15	30.6	-5.78
	14.2	8.94	129.8	2.5	39.4	103.8	54.0	0.17	2.5E-03	0.9	-2.38	-2.65	-3.50	-2.16	29.3	-5.76
	18.6	8.94	125.3	2.5	40.4	106.6	54.0	0.17	9.6E-03	3.3	-2.40	-2.67	-3.49	-2.14	28.9	-5.77
	35.7	8.96	124.5	2.1	38.7	102.5	54.0	0.17	2.2E-03	0.8	-2.42	-2.65	-3.57	-2.17	28.9	-5.82
Average	–	*8.93*	*127.0*	*2.3*	*37.8*	*103.7*	*54*	*0.17*	–	–	*-2.37*	*-2.67*	*-3.54*	*-2.18*	*29.3*	*-5.81*
±2δ	–	*±0.04*	*±3.9*	*±0.4*	*±4.4*	*±3.7*	–	*±0.01*	–	–	*±0.07*	*±0.03*	*±0.08*	*±0.05*	*±1.6*	*±0.07*
ACMC_39	5.2	9.01	133.6	2.0	40.8	102.2	57.6	0.18	-3.4E-03	-1.2	-2.47	-2.59	-3.63	-2.17	37.2	-5.68
	8.2	9.02	133.7	1.8	39.9	102.2	57.6	0.18	-5.7E-03	-2.0	-2.47	-2.58	-3.68	-2.18	37.4	-5.70
	11.3	9.02	132.8	1.8	35.5	102.7	57.6	0.17	-1.3E-02	-4.5	-2.46	-2.57	-3.68	-2.24	37.7	-5.71
	14.9	9.02	132.9	1.7	35.2	102.7	57.6	0.17	-1.4E-02	-4.8	-2.46	-2.57	-3.71	-2.24	37.2	-5.73
	19.1	9.02	131.8	1.7	36.4	101.7	57.6	0.17	-1.2E-02	-4.0	-2.47	-2.58	-3.70	-2.22	37.7	-5.72
	39.1	9.02	133.2	1.8	37.6	102.0	57.6	0.17	-1.0E-02	-3.4	-2.47	-2.58	-3.68	-2.21	37.1	-5.72
Average	-	*9.02*	*133.0*	*1.8*	*37.6*	*102.3*	*57.6*	*0.17*	-	–	*-2.47*	*-2.58*	*-3.68*	*-2.21*	*37.4*	*-5.71*
±2δ	-	*±0.01*	*±1.4*	*±0.2*	*±4.7*	*±0.8*	-	*±0.01*	-	–	*0.01*	*0.02*	*0.06*	*0.06*	*±0.5*	*±0.04*
ACMC_53	1.7	9.11	141.7	1.6	47.9	101.5	61.3	0.18	-2.5E-03	-0.8	-2.60	-2.53	-3.75	-2.12	51.2	-5.44
	3.9	9.14	143.3	1.6	49.4	103.7	61.3	0.19	1.1E-03	0.4	-2.64	-2.51	-3.76	-2.11	51.2	-5.43
	5.7	9.14	143.8	1.6	49.9	104.6	61.3	0.19	2.5E-03	0.8	-2.64	-2.51	-3.76	-2.11	51.4	-5.42
	10.4	9.15	144.3	1.5	49.5	103.7	61.3	0.19	1.0E-04	0.0	-2.65	-2.50	-3.80	-2.12	51.7	-5.43
	13.5	9.15	143.9	1.5	49.1	101.8	61.3	0.18	-2.2E-03	-0.7	-2.65	-2.50	-3.80	-2.12	50.9	-5.45
	18.6	9.16	143.3	1.5	48.5	103.5	61.3	0.18	-1.1E-03	-0.4	-2.66	-2.49	-3.80	-2.13	51.6	-5.43
Average	-	*9.14*	*143.4*	*1.6*	*49.1*	*103.1*	*61.3*	*0.19*	-	–	*-2.64*	*-2.51*	*-3.78*	*-2.12*	*51.3*	*-5.43*
±2δ	-	*±0.03*	*±1.8*	*±0.1*	*±1.5*	*±2.4*	-	*±0.01*	-	–	*±0.04*	*±0.03*	*±0.05*	*±0.01*	*±0.6*	*±0.02*
ACMC_80	1.8	9.23	159.4	1.0	51.5	99.8	56.5	0.18	-1.1E-02	-3.7	-2.72	-2.41	-4.03	-2.14	78.3	-4.96
	3.9	9.25	162.0	0.9	52.2	100.5	56.5	0.18	-1.2E-02	-4.1	-2.74	-2.39	-4.08	-2.14	78.5	-4.95
	5.7	9.26	160.6	0.8	52.1	100.2	56.5	0.18	-1.1E-02	-3.8	-2.76	-2.39	-4.13	-2.14	78.4	-4.96
	7.8	9.27	161.4	0.8	51.8	100.1	56.5	0.18	-1.3E-02	-4.3	-2.77	-2.38	-4.14	-2.15	78.8	-4.95
Average	-	*9.25*	*160.9*	*0.9*	*51.9*	*100.2*	*56.5*	*0.18*	-	-	*-2.75*	*-2.39*	*-4.10*	*-2.14*	*78.5*	*-4.96*
±2δ	-	*±0.03*	*±2.3*	*±0.2*	*±0.6*	*±0.6*	-	-	-	-	*±0.04*	*±0.03*	*±0.10*	*±0.01*	*±0.4*	*±0.01*
AMC	1.9	9.39	181.4	0	61.6	100.1	57.0	0.19	-1.5E-02	-5.0	-2.92	-2.29	-	-2.12	100	-4.41
	3.8	9.39	175.7	0	59.8	102.4	57.0	0.19	-1.1E-02	-3.6	-2.93	-2.30		-2.12	100	-4.42
Average	-	*9.39*	*178.6*	*-*	*60.7*	*101.3*	*57.0*	*0.19*	-	-	*-2.93*	*-2.30*	*-*	*-2.12*	*100*	*-4.42*
±2δ	-	*-*	*±8.1*	*-*	*±2.6*	*±3.3*	-	-	-	-	*±0.01*	*±0.01*	*-*	*-*	–	*±0.01*
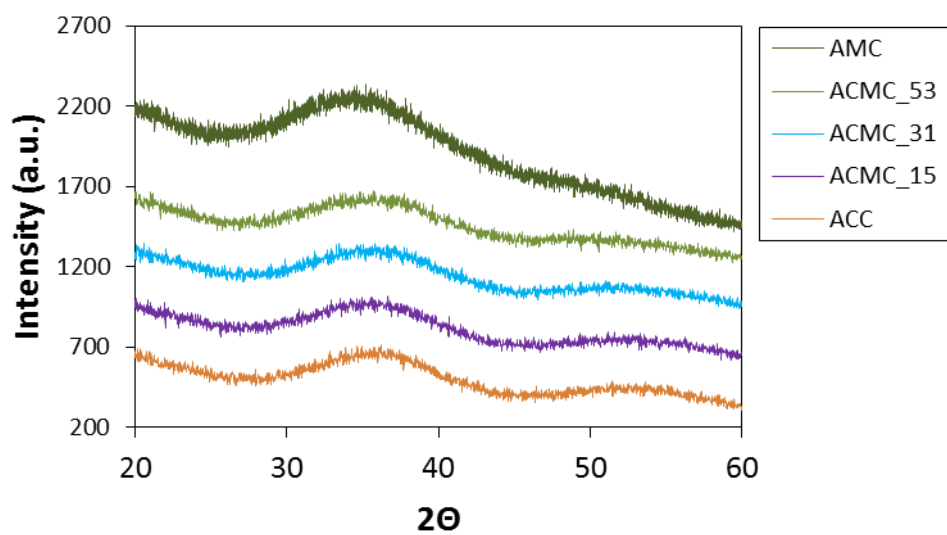
Fig. S1: X-ray diffraction patterns of representative synthetic ACMC samples (see Table 1).
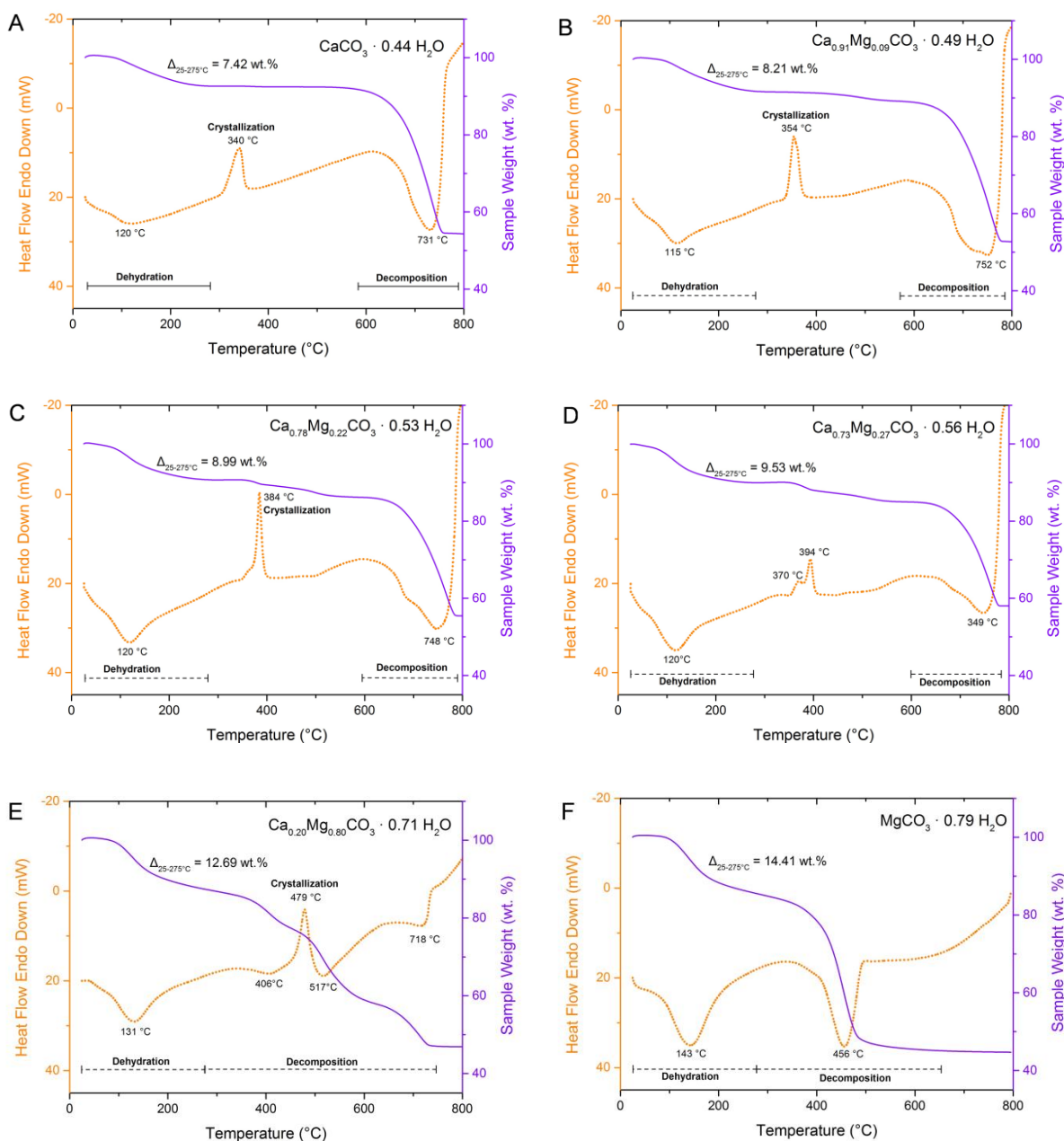
Fig. S2: Thermogravimetric analysis (TGA – organge solid lines) and differential scanning calorimetry (DSC – violet dashed lines) curves of ACC (A), ACMC_9 (B), ACMC_22 (C), ACMC_53(D), ACMC_80 (E) and AMC (H) synthesized in the context of the present study (see Table 1).
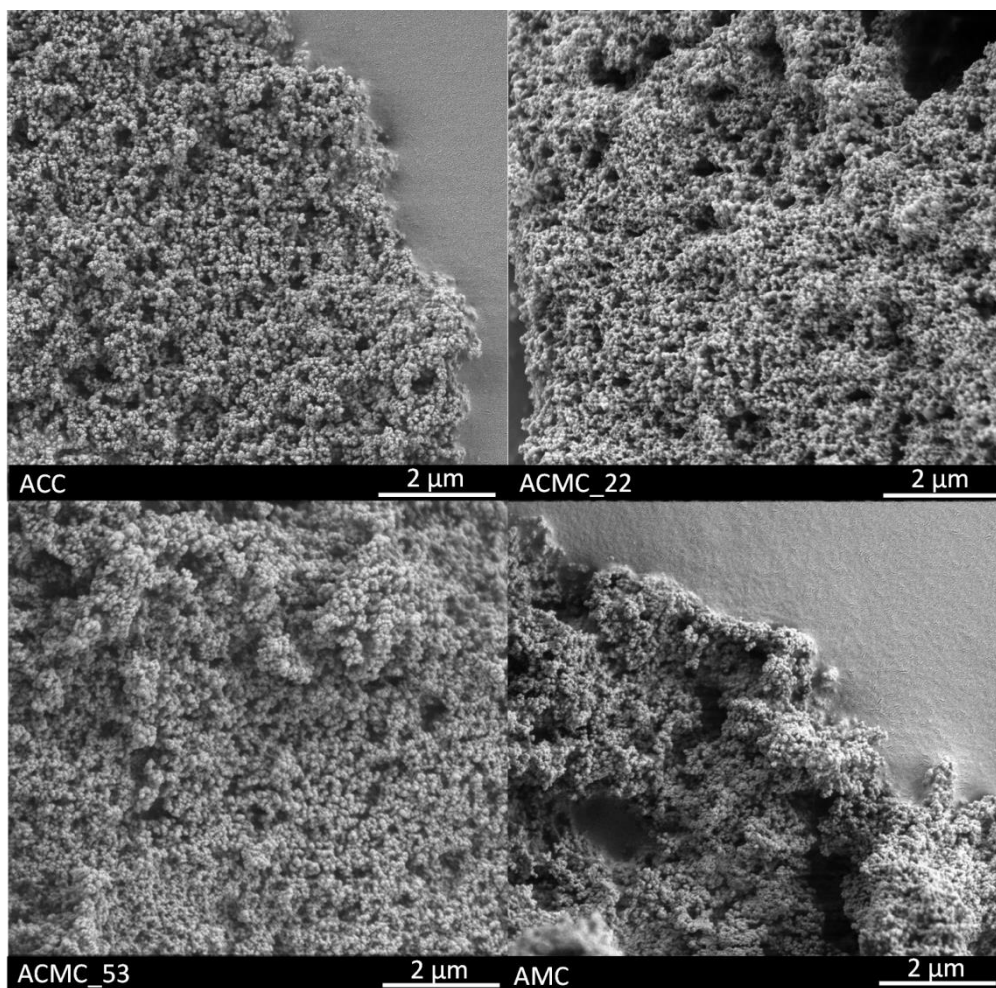
Fig. S3: Scanning Electron Microscopy (SEM) images of representative ACMC samples (Table 1).
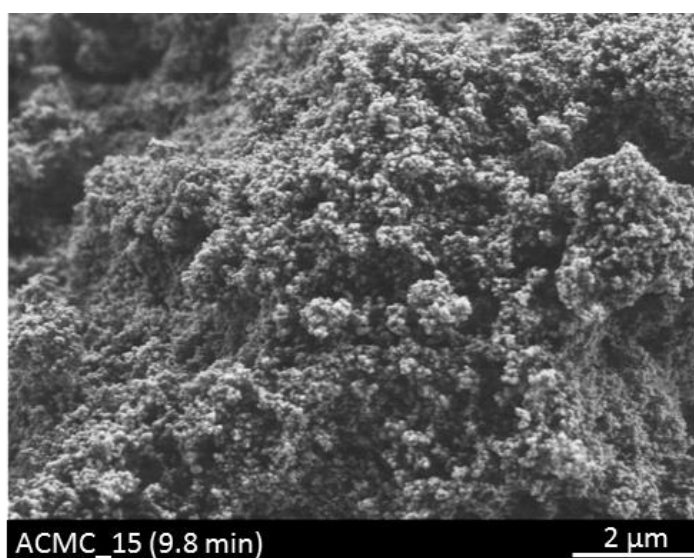
Fig. S4: Scanning Electron Microscopy (SEM) image of ACMC collected after 9.8 min of reaction time in the experiment conducted with 15 mol% Mg (ACMC_15).

References

Aizenberg J., Lambert G., Weiner S. and Addadi L. (2002) Factors involved in the formation of amorphous and crystalline calcium carbonate: A study of an ascidian skeleton. *J. Am. Chem. Soc.* **124**, 32–39.

Allison J. D., Brown D. S. and Novo-Gradac K. J. (1991) MINTEQA2/PRODEFA2, A Geochemical Assessment Model for Environmental Systems: Version 3.0 User's Manual. *U.S. Environ. Prot. Agency*, 107.

Althoff P. L. (1977) Structural refinements of dolomite and a magnesian calcite and implications for dolomite formation in the marine environment. *Am. Mineral.* **62**, 772–783.

Appelo C. A. J. and Postma D. (2005) *Geochemistry, groundwater and pollution.* 2nd ed., A.A. Balkema Publishers, Amsterdam, the Netherlands.

Benzerara K., Menguy N., Lopez-Garcia P., Yoon T.-H., Kazmierczak J., Tyliszczak T., Guyot F. and Brown G. E. (2006) Nanoscale detection of organic signatures in carbonate microbialites. *Proc. Natl. Acad. Sci.* **103**, 9440–9445.

Bischoff W. D., Bertram M. A., Mackenzie F. T. and Bishop F. C. (1993) Diagenetic stabilization pathways of magnesian calcites. *Carbonates and Evaporites* **8**, 82–89.

Bischoff W. D., Mackenzie F. T. and Bishop F. C. (1987) Stabilities of synthetic magnesian calcites in aqueous solution: Comparison with biogenic materials. *Geochim. Cosmochim. Acta* **51**, 1413–1423.

Bischoff W. D., Sharma S. K. and MacKenzie F. T. (1985) Carbonate ion disorder in synthetic and biogenic magnesian calcites: a Raman spectral study. *Am. Mineral.* **70**, 581–589.

Blue C. R. and Dove P. M. (2015) Chemical controls on the magnesium content of amorphous calcium carbonate. *Geochim. Cosmochim. Acta* **148**, 23–33.

Blue C. R., Giuffre A., Mergelsberg S., Han N., De Yoreo J. J. and Dove P. M. (2017) Chemical and physical controls on the transformation of amorphous calcium carbonate into crystalline $CaCO_3$ polymorphs. *Geochim. Cosmochim. Acta* **196**, 179–196.

Brečević L. and Nielsen A. E. (1989) Solubility of amorphous calcium carbonate. *J. Cryst. Growth* **98**, 504–510.

Busenberg E. and Plummer N. L. (1989) Thermodynamics of magnesian calcite solid-solutions at 25°C and 1 atm total pressure. *Geochim. Cosmochim. Acta* **53**, 1189–1208.

Couradeau E., Benzerara K., Gerard E., Moreira D., Bernard S., Brown G. E. and Lopez-Garcia P. (2012) An Early-Branching Microbialite Cyanobacterium Forms Intracellular Carbonates. *Science (80-.).* **336**, 459–462.

Demény A., Németh P., Czuppon G., Leél-Őssy S., Szabó M., Judik K., Németh T. and Stieber J. (2016) Formation of amorphous calcium carbonate in caves and its implications for speleothem research. *Sci. Rep.* **6**, 39602.

Gautier Q., Bénézeth P., Mavromatis V. and Schott J. (2014) Hydromagnesite solubility product and growth kinetics in aqueous solution from 25 to 75°C. *Geochim. Cosmochim. Acta* **138**, 1–20.

Gebauer D., Völkel A. and Cölfen H. (2008) Stable prenucleation calcium carbonate clusters. *Science (80-.).* **322**, 1819–1822.

Goodwin A. L., Michel F. M., Phillips B. L., Keen D. A., Dove M. T. and Reeder R. J. (2010) Nanoporous structure and medium-range order in synthetic amorphous calcium carbonate. *Chem. Mater.* **22**, 3197–3205.

Ihli J., Wong W. C., Noel E. H., Kim Y. Y., Kulak A. N., Christenson H. K., Duer M. J. and Meldrum F. C. (2014) Dehydration and crystallization of amorphous calcium carbonate in solution and in air. *Nat. Commun.* **5**, 1–10.

Jacob D. E., Soldati A. L., Wirth R., Huth J., Wehrmeister U. and Hofmeister W. (2008) Nanostructure, composition and mechanisms of bivalve shell growth. *Geochim. Cosmochim. Acta* **72**, 5401–5415.

Jensen A. C. S., Imberti S., Parker S. F., Schneck E., Politi Y., Fratzl P., Bertinetti L. and Habraken W. J. E. M. (2018) Hydrogen Bonding in Amorphous Calcium Carbonate and Molecular Reorientation Induced by Dehydration. *J. Phys. Chem. C* **122**, 3591–3598.

Jones B. and Peng X. (2012) Amorphous calcium carbonate associated with biofilms in hot spring deposits. *Sediment. Geol.* **269-270**, 58–68.

Khairoun I., Magne D., Gauthier O., Bouler J. M., Aguado E., Daculsi G. and Weiss P. (2002) In vitro characterization and in vivo properties of a carbonated apatite bone cement. *J. Biomed. Mater. Res.* **60**, 633–642.

Konrad F., Gallien F., Gerard D. E. and Dietzel M. (2016) Transformation of Amorphous Calcium Carbonate in Air. *Cryst. Growth Des.* **16**, 6310–6317.

Konrad F., Purgstaller B., Gallien F., Mavromatis V., Gane P. and Dietzel M. (2018) Influence of aqueous Mg concentration on the transformation of amorphous calcium carbonate. *J. Cryst. Growth* **498**, 381–390.

Lin C.-J., Yang S.-Y., Huang S.-J. and Chan J. C. C. (2015) Structural Characterization of Mg-Stabilized Amorphous Calcium Carbonate by Mg-25 Solid-State NMR Spectroscopy. *J. Phys. Chem. C* **119**, 7225–7233.

Loste E., Wilson R. M., Seshadri R. and Meldrum F. C. (2003) The role of magnesium in stabilising amorphous calcium carbonate and controlling calcite morphologies. *J. Cryst. Growth* **254**, 206–218.

Marion G. M. (2001) Carbonate mineral solubility at low temperatures in the. *Geochim. Cosmochim. Acta* **65**, 1883–1896.

Mavromatis V., Gautier Q., Bosc O. and Schott J. (2013) Kinetics of Mg partition and Mg stable isotope fractionation during its incorporation in calcite. *Geochim. Cosmochim. Acta* **114**, 188–203.

Mavromatis V., Immenhauser A., Buhl D., Purgstaller B., Baldermann A. and Dietzel M. (2017a) Effect of organic ligands on Mg partitioning and Mg isotope fractionation during low-temperature precipitation of calcite in the absence of growth rate effects. *Geochim. Cosmochim. Acta* **207**, 139–153.

Mavromatis V., Purgstaller B., Dietzel M., Buhl D., Immenhauser A. and Schott J. (2017b) Impact of amorphous precursor phases on magnesium isotope signatures of Mg-calcite. *Earth Planet. Sci. Lett.* **464**, 227–236.

Mavromatis V., Schmidt M., Botz R., Comas-Bru L. and Oelkers E. H. (2012) Experimental quantification of the effect of Mg on calcite-aqueous fluid oxygen isotope fractionation. *Chem. Geol.* **310-311**, 97–105.

Michel F. M., MacDonald J., Feng J., Phillips B. L., Ehm L., Tarabrella C., Parise J. B. and Reeder R. J. (2008) Structural characteristics of synthetic amorphous calcium carbonate. *Chem. Mater.* **20**, 4720–4728.

Nebel H., Neumann M., Mayer C. and Epple M. (2008) On the structure of amorphous calcium carbonate - A detailed study by solid-state NMR spectroscopy. *Inorg. Chem.* **47**, 7874–7879.

Politi Y., Arad T., Klein E., Weiner S. and Addadi L. (2004) Sea urchin spine calcite forms via a transient amorphous calcium carbonate phase. *Science (80-.).* **306**, 1161–1164.

Politi Y., Batchelor D. R., Zaslansky P., Chmelka B. F., Weaver J. C., Sagi I., Weiner S. and Addadi L. (2010) Role of magnesium ion in the stabilization of biogenic amorphous calcium carbonate: A structure-function investigation. *Chem. Mater.* **22**, 161–166.

Purgstaller B., Konrad F., Dietzel M., Immenhauser A. and Mavromatis V. (2017) Control of Mg^{2+}/Ca^{2+} Activity Ratio on the Formation of Crystalline Carbonate Minerals via an Amorphous Precursor. *Cryst. Growth Des.* **17**, 1069–1078.

Purgstaller B., Mavromatis V., Immenhauser A. and Dietzel M. (2016) Transformation of Mg-bearing amorphous calcium carbonate to Mg-calcite - In situ monitoring. *Geochim. Cosmochim. Acta* **174**, 180–195.

Radha A. V., Fernandez-Martinez A., Hu Y., Jun Y. S., Waychunas G. A. and Navrotsky A. (2012) Energetic and structural studies of amorphous $Ca_{1-x}Mg_xCO_3 \cdot nH_2O$ ($0 \leq x \leq 1$). *Geochim. Cosmochim. Acta* **90**, 83–95.

Raz S., Weiner S. and Addadi L. (2000) Formation of high-magnesian calcites via an amorphous precursor phase: Possible biological implications. *Adv. Mater.* **12**, 38–42.

Rodriguez-Blanco J. D., Shaw S. and Benning L. G. (2015) A route for the direct crystallization of dolomite. *Am. Mineral.* **100**, 1172–1181.

Schmidt M. P., Ilott A. J., Phillips B. L. and Reeder R. J. (2014) Structural changes upon dehydration of amorphous calcium carbonate. *Cryst. Growth Des.* **14**, 938–951.

Schmidt M., Xeflide S., Botz R. and Mann S. (2005) Oxygen isotope fractionation during synthesis of CaMg-carbonate and implications for sedimentary dolomite formation. *Geochim. Cosmochim. Acta* **69**, 4665–4674.

Sethmann I., Hinrichs R., Wörheide G. and Putnis A. (2006) Nano-cluster composite structure of calcitic sponge spicules - A case study of basic characteristics of biominerals. *J. Inorg. Biochem.* **100**, 88–96.

Tao J., Zhou D., Zhang Z., Xu R. and Tang R. (2009) Magnesium-aspartate-based crystallization switch inspired from shell molt of crustacean. *Proc. Natl. Acad. Sci. U. S. A.* **106**, 22096–22101.

Tommaso D. Di and De Leeuw N. H. (2010) Structure and dynamics of the hydrated magnesium ion and of the solvated magnesium carbonates: Insights from first principles simulations. *Phys. Chem. Chem. Phys.* **12**, 894–901.

Wang D., Hamm L. M., Bodnar R. J. and Dove P. M. (2012) Raman spectroscopic characterization of the magnesium content in amorphous calcium carbonates. *J. Raman Spectrosc.* **43**, 543–548.

Weiner S. and Dove P. M. (2003) An Overview of Biomineralization Processes and the Problem of the Vital Effect. *Rev. Mineral. Geochemistry* **54**, 1–29.

Yang S.-Y., Chang H.-H., Lin C.-J., Huang S.-J. and Chan J. C. C. (2016) Is Mg-stabilized amorphous calcium carbonate a homogeneous mixture of amorphous magnesium carbonate and amorphous calcium carbonate? *Chem. Commun.* **52**, 11527–11530.

Yu P. T., Tsao C., Wang C. C., Chang C. Y., Wang C. H. and Chan J. C. C. (2017) High-Magnesium Calcite Mesocrystals: Formation in Aqueous Solution under Ambient Conditions. *Angew. Chemie – Int. Ed.* **56**, 16202–16206.

Chapter 5

Effect of temperature on the transformation of amorphous calcium magnesium carbonate with near–dolomite stoichiometry into high–Mg calcite

Bettina Purgstaller[1], Vasileios Mavromatis[2], Katja E. Goetschl[1], Florian R. Steindl[1], Martin Dietzel[1]

[1]Institute of Applied Geosciences, Graz University of Technology, Rechbauerstrasse 12, 8010 Graz, Austria

[2]Géosciences Environment Toulouse (GET), CNRS, UMR 5563, Observatoire Midi-Pyrénées, 14 Av. E. Belin, 31400 Toulouse, France

GRAPHICAL ABSTRACT
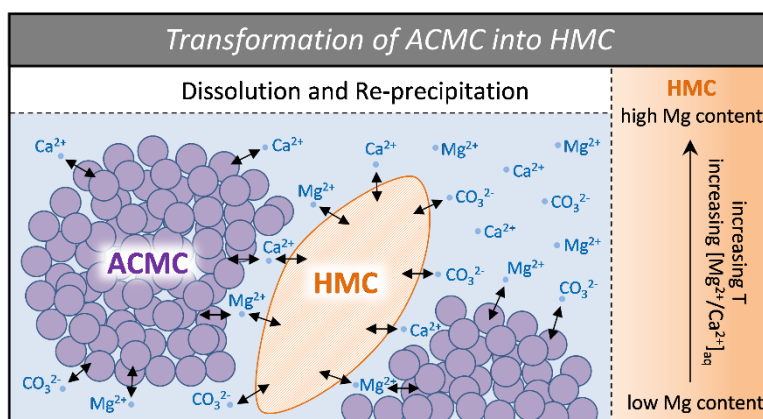
ABSTRACT: High-Mg calcite (HMC) is thermodynamically unstable under ambient conditions, yet it has been found in many biogenic and abiotic depositional settings with Mg contents up to 50 mol%. The elevated Mg content of HMC was frequently attributed to an amorphous calcium magnesium carbonate (ACMC) precursor, but the effects of transformation conditions on the Mg content of HMC are still debated and far from being quantified. Therefore, the transformation of ACMC with near-dolomite stoichiometry (~48 mol% Mg) into HMC has been studied in a $MgCl_2$–$NaHCO_3$ buffered solution at moderate pH (7.6) and temperatures from 10 to 80 °C. The obtained chemical data show that the apparent solubility of ACMC (K_{ACMC}) is lower at higher temperature and the relative increase of K_{ACMC} as a function of the Mg content is similar between 10 and 80 °C which can be assessed by the equation: $\log(K_{ACMC}) = 0.01629 * [Mg]_{ACMC} - 0.0001096 \, T^2 + 0.0545 \, T - 12.919$, where T is reported in Kelvin and $[Mg]_{ACMC}$ refers to the amount of Mg in ACMC in mol%. The Mg content of the final HMC increases from 5 to 40 mol% with increasing temperature, thus is significantly lower compared to the Mg content of the ACMC precursor. Our findings argue for a

dissolution and re-precipitation process during ACMC transformation, where at higher temperatures the Mg incorporation into HMC is enhanced due to (i) the reduced solvation energy barrier of aqueous Mg^{2+} and (ii) the high prevailing molar Mg^{2+}/Ca^{2+} ratio of the solution after its reaction with the ACMC. Notably, the Mg^{2+}/Ca^{2+} ratio of the latter solution is controlled by the temperature-dependent solubility of ACMC. Finally, the findings indicate that the nanocrystalline HMCs formed *via* transformation of ACMC are physically defective from rapid crystal growth and have higher solubilities compared to well-crystallized Mg-bearing calcites.

5.1 Introduction

Calcite is the most abundant calcium carbonate ($CaCO_3$) mineral in marine and terrestrial environments (Morse and Mackenzie, 1990; Reeder, 1990). In the crystal structure of calcite, Ca^{2+} can be substituted by other divalent cations present in natural waters. Predominant in these replacement reactions is the substitution of Ca^{2+} by Mg^{2+} (Mackenzie et al., 1983; Bischoff et al., 1985; Gregg et al., 2015). In the literature, calcite containing > 4 mol% Mg is usually referred to as high-Mg calcite (HMC; $Ca_{1-x}Mg_xCO_3$, x > 0.04), whereas calcite with lower Mg content is referred to as low-Mg calcite (LMC; $Ca_{1-x}Mg_xCO_3$, x < 0.04; Tucker and Wright, 1990; Gregg et al., 2015). Abiogenic HMCs with < 20 mol% Mg form marine cements consolidating sedimentary materials, e.g. in shallow tropical carbonate factories (Mackenzie et al., 1983), in zones affected by anaerobic oxidation of methane (Mavromatis et al., 2014) and in coastal sabkha settings (Paul and Lokier, 2017). Biogenic HMCs with up to 25 mol% Mg are a common building material of e.g. skeletons of coralline algae, foraminifers and echinoderms (Mackenzie et al., 1983; Raz et al., 2000; Bentov and Erez, 2006; Gayathri et al., 2007; Nash et al., 2011). The Mg content can be even higher (40-45 mol%) in structural elements of sea urchin teeth (Schroeder et al., 1969; Ma et al., 2009). A few examples of HMC with up to nearly 50 mol% Mg have been reported in natural depositional settings which are usually rich in microbial activity such as in algal sediments from a hypersaline lake (Salt Pond) of San Salvador Island, Bahamas (Furman et al., 1993), in microbial mats of the Lagoa Vermelha, Brazil (Vasconcelos and McKenzie, 1997), in microbial films of the Seroe Domi Formation of Curacao, Netherland Antilles (Sumrall et al., 2017) and in sediments of the shallow, alkaline Lake Neusiedl, Austria (Fussmann et al., 2020). Note here that HMC phases with near-dolomite stoichiometry, but lacking cation ordering, are also referred to as very high-Mg calcite (VHMC) or protodolomite (Gregg et al., 2015).

Despite several decades of research, the formation of HMC and VHMC in natural systems is a poorly understood process because (i) the (V)HMC structure is destabilized by the uptake of Mg^{2+} (Busenberg and Plummer, 1989) and (ii) the inorganic precipitation of HMC with > 20 mol% Mg in the laboratory under ambient conditions remains an enigma as high aqueous Mg^{2+}/Ca^{2+} ratios inhibit the nucleation and growth of HMC from solution and favor the precipitation of aragonite ($CaCO_3$; Lippmann, 1973; Berner, 1975; Fernández-Díaz et al., 1996; Goetschl et al., 2019). The inhibiting effect of aqueous Mg^{2+} on the formation of calcite originates from the strong affinity of the Mg^{2+} ion for the aqueous solution which is reflected by its high hydration Gibbs free energy (Markham et al., 1996) and low rate of exchange of water molecules in its hydration sphere (Bleuzen et al., 1997; Schott et al., 2009). The dehydration of the hydrophilic Mg^{2+} ion at the lattice growth site is therefore one of the most rate-limiting steps during the formation of (V)HMC.

Experimental studies on mineral formation, however, have shown that besides direct precipitation from solution (classical formation pathway), carbonate minerals can be formed via the transformation of amorphous precursor phases (Brečević and Nielsen, 1989; Ogino et al., 1990). Evidence for this alternative formation pathway also comes from calcifying organisms, where calcite formation often proceeds through an amorphous calcium carbonate (ACC) precursor phase (Addadi et al., 2003; Politi et al., 2010). In this context, it has been suggested that Mg-containing ACC is a necessary prerequisite for the formation of HMC (Raz et al., 2000) and VHMC (Rodriguez-Blanco et al., 2015). In most studies, the formation of amorphous calcium magnesium carbonate (ACMC) was induced by mixing a Na_2CO_3 solution (pH > 11) with $(Ca,Mg)Cl_2$ solutions (pH = 6 - 7) at room temperature (Raz et al., 2000; Radha et al., 2012; Rodriguez-Blanco et al., 2012; 2015; Lin et al., 2015; Purgstaller et al., 2019). The chemical composition of the initial solution for ACMC synthesis (e.g Mg/Ca ratio, pH) has been suggested to control the amount of Mg incorporated into the ACMC and the final HMC (Long et al., 2011; Yang et al., 2015; Xto et al., 2019). Specifically, the formation of VHMC via ACMC has been achieved from synthesis in aqueous solutions with high Mg/Ca ratios at high pH (~ 10), high carbonate-to-calcium ratios (> 2:1) or by thermal treatment (> 40 °C; Kelleher and Redfern, 2002; Schmidt et al., 2005; Rodriguez-Blanco et al, 2015; Yang et al., 2015; Xto et al., 2019). However, in most studies, the chemical compositions of the reactive solutions and solids during the formation of ACMC and its transformation into Mg calcite were not concerned or even not documented. In particular, the effect of temperature on the Mg content of HMC formed via the amorphous pathway in aqueous solution has not been investigated in

earlier studies. In order to better understand the fate of Mg during the transformation of ACMC into HMC, we investigated the transformation behavior of synthetic ACMC with near-dolomite stoichiometry (48 mol % Mg) in solution at moderate pH (7.6) and reaction temperatures ranging from 10 to 80 ±1 °C. The aim of the present study is to provide a more detailed understanding of the interplay between the chemical composition of (i) ACMC, (ii) the corresponding reactive solution and (iii) (V)HMC formed via ACMC in the apparent aqueous environment. Moreover, the obtained chemical data were used to assess the solubility of ACMC and HMC.

5.2 Methods

5.2.1 Synthesis of Amorphous Calcium Magnesium Carbonate

The synthesis of ACMC material with 47.9 ±1.5 mol% Mg was carried out by a previously developed protocol (Konrad et al., 2016; Purgstaller et al., 2019). Briefly, a 0.25 M (Ca,Mg)Cl_2 solution (Mg/Ca ratio = 2.1) and a 0.25 M Na_2CO_3 solution were prepared using $CaCl_2 \cdot 2H_2O$, $MgCl_2 \cdot 6H_2O$, and Na_2CO_3 chemicals (p.a. Roth) and ultrapure water (Millipore Integral 3; 18.2 MΩcm^{-1}). The two stock solutions were cooled in a fridge for 4 hours (T = 10 ±2 °C). The precipitation of ACMC was induced by pouring 100 mL of the (Ca,Mg)Cl_2 solution into a beaker containing 100 mL of the Na_2CO_3 solution. The ACMC was separated from solution by a 0.2 μm cellulose filter using a suction filtration unit and was subsequently freeze-dried for 12 hours (Virtis Benchtop 3L). The synthesis protocol was repeated several times until about 20 g of ACMC were produced. The obtained ACMC material was analysed by X-ray diffraction (Fig. S1A) and was stored in a desiccator with silica gel.

5.2.2 Experimental Setup for ACMC transformation into HMC

Transformation of ACMC in solution was performed at 10, 20, 40, 60 and 80 °C (see Table 1). Initially, 50 mM $NaHCO_3$ solutions were prepared in 150 mL gas-tight glass bottles which were placed either in a cooling chamber (10 ±2 °C), a temperature-controlled room (20 ±2 °C) or in ovens (40 ±2 °C, 60 ±2 °C and 80 ±2 °C) over a period of 24 to 60 h. 52 mL of the pre-cooled/heated $NaHCO_3$ solution was added into a 150 mL borosilicate glass reactor containing 6.099 g $MgCl_2 \cdot 6H_2O$ to obtain a Mg concentration of 30 mM. 2 mL of the $NaHCO_3$-$MgCl_2$ solution was collected with a pipette to measure its initial Mg and alkalinity concentration (Table 2). The $MgCl_2$-$NaHCO_3$ solutions exhibit an initial pH value of 8.02 ±0.15 (Table 2). The reactor was placed in an Easy Max System (Max™ 102; Mettler Toledo) in order to control the stirring of the solution at 200 rpm and its temperature at 10.0, 20.0, 40.0, 60.0 or 80.0

±0.1 °C (Fig. 1). Subsequently, 1.5 g of the synthesized ACMC was introduced into the buffered NaHCO$_3$-MgCl$_2$ solution (Fig. 1). After a short homogenization period between the ACMC material and the solution, a homogeneous sub-sample of the suspension (2 mL) was collected with a pipette (t = 0.3 min). Subsequently, the pH of the experimental solution was adjusted to 7.58 ±0.04 (within ≤ 3 min) by computer-controlled titration of a 2 M HCl solution (Schott; TitroLine alpha plus) (Fig. S2). Note here that the pH of the solution was adjusted to 7.6 to prevent the precipitation of hydrous Ca- or Mg- carbonate phases, such as monohydrocalcite and nesquehonite (Purgstaller et al., 2017a; Konrad et al., 2018; Xto et al., 2019). Further homogeneous sub-samples of the experimental suspension (2 mL) were collected with a pipette at 5 min, 11 min, 21 min, 32 min and 61 min. After 61 min of reaction time, the experimental solutions were transferred into 100 mL gastight bottles which were again placed in the fridge (10 ±2 °C), temperature-controlled room (20 ±2 °C) and ovens (40 ±2 °C, 60 ±2 °C and 80 ±2 °C) over a period of 2 months. Additional homogeneous sub-samples were collected after 1 day, 1 week and 2 months of reaction time. The solids were separated from the solutions by a 0.2 μm cellulose acetate filter using a suction filtration unit and washed with ethanol. Subsequently, the solids were dried overnight in an oven at 40 °C and stored in a desiccator with silica gel.
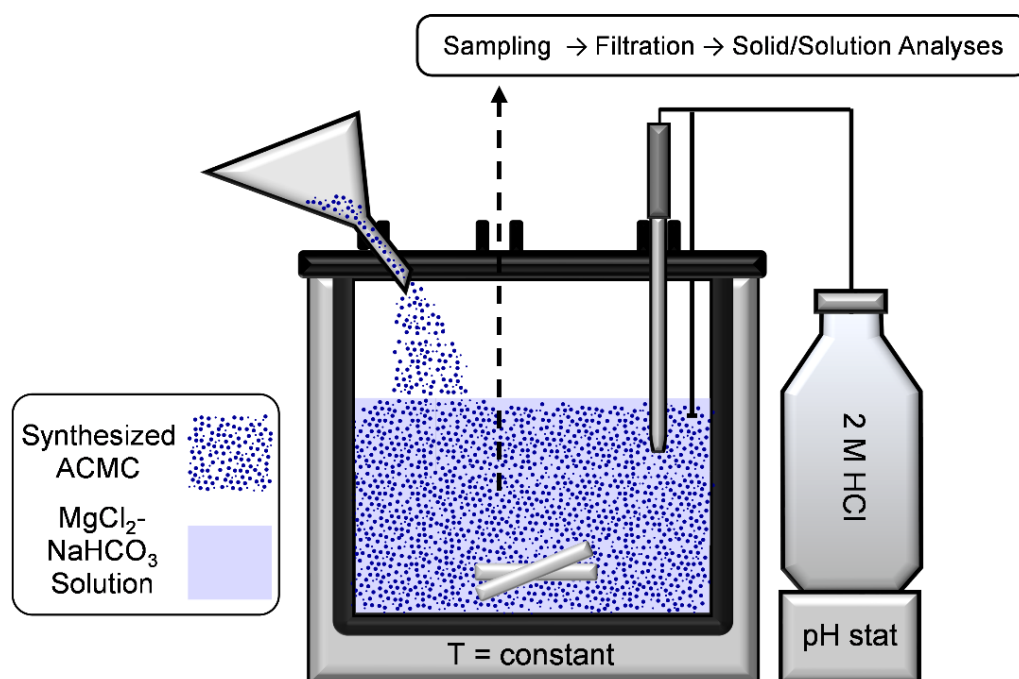
Fig. 1: Experimental setup used for transformation of amorphous calcium magnesium carbonate (ACMC). Synthesized ACMC standard material (Ca$_{0.52}$Mg$_{0.48}$CO$_3$ · 0.67H$_2$O) was introduced in a MgCl$_2$–NaHCO$_3$ buffered solution at 10, 20, 40, 60 or 80 °C. Subsequently, the pH of the experimental solution was adjusted to 7.58 ±0.04 by automatic titration of a 2 M HCl solution.

5.2.3 Analytical Procedures

Thermogravimetric analyses (TGA) of the freeze-dried ACMC was realized using a PerkinElmer STA8000. The ACMC was heated from 25 °C to 800 °C at 10 °C min^{-1} in the presence of 99.999% N_2 atmosphere. The mineralogy of the precipitates collected during the ACMC transformation experiments was determined by a PANalytical X'Pert PRO diffractometer using Co-Kα Radiation (40 mA, 40 kV) at a 2θ range from 4 to 85° with a step size of 0.008°2θ and 40 sec count time per step. The mineral phases of the reaction products were quantified using Rietveld refinement (software HighScore Plus, PANalytical) using the crystal structure data given in Table S1. The estimated analytical uncertainty of the quantification lies within 1 wt.%. The refinement values consisted of the specimen displacement, a 7-term polynomial background function and scale factors and lattice parameters for all phases. For major phases, the peak shape was refined using a pseudo-Voigt profile function and peak asymmetry. The preferred orientation of calcite was refined for the (104) plane with the March-Dollase function. If two separate calcite phases were present, all their refined values, except of the scale factor and lattice parameters, were constrained with each other to ensure a stable refinement. The d-value and the left full-width at half-maximum (left FWHM, for asymmetric peaks) of the (104) reflection (hereafter referred to as d_{104} and $FWHM_{d_{104}}$, respectively) was obtained from the refinement results. The d_{104} value of the calcite phases was used to calculate their Mg content ($[Mg]_{XRD}$) according to Goldsmith et al. (1961) and this content was then used to adapt the occupancy of Ca and Mg in the structure data used for the refinement. Note that the accuracy of the determination of the d_{104} value and the $FWHM_{d_{104}}$ is limited by the step size of the XRD measurement (0.008°2θ).

Selected precipitates were gold-coated and imaged using a scanning electron microscope (SEM, ZEISS DSM 982 Gemini). The total alkalinity of the experimental solutions was measured by a Schott TitroLine alpha plus titrator using a 10 mM HCl solution with a precision of ±2%. The aqueous Ca and Mg concentrations of experimental solutions and solids (digested in 6% HNO$_3$) were determined using inductively coupled plasma optical emission spectrometry (ICP-OES, Perkin Elmer Optima 8300 DV) with an analytical precision of ±3% for Ca and Mg analyses. The Mg content of the bulk solid ([Mg]$_{solid}$ in mol%, Table 2) was calculated according to the equation:

$$[Mg]_{solid} = \frac{[Mg]_s}{[Mg]_s + [Ca]_s} \cdot 100 \tag{1}$$

where [Mg]$_s$ and [Ca]$_s$ are the measured concentrations of Ca and Mg of the solid (mol/kg) determined by chemical digestion and ICP-OES analysis.

5.2.4 Geochemical Modeling

The aqueous speciation and ion activities of the reactive solutions were calculated using the PHREEQC computer code with the minteq.v4 database. The apparent solubility product (K) for amorphous calcium magnesium carbonate (ACMC, Ca$_{1-x}$Mg$_x$CO$_3 \cdot$ nH$_2$O) and high-Mg calcite (HMC, Ca$_{1-x}$Mg$_x$CO$_3$) was calculated using the equation

$$K = (aCa^{2+})^{1-x}(aMg^{2+})^x(aCO_3^{2-}) \tag{2}$$

where aCa^{2+}, aMg^{2+} and aCO$_3^{2-}$ are the activities of Ca^{2+}, Mg^{2+} and CO$_3^{2-}$ ions in solution, respectively and x is the mole fraction of Mg in the precipitated solid (for HMC: [Mg]$_{XRD}$ in Table 1; for ACMC: [Mg]$_{solid}$ in Table 2). In the latter case the Mg and Ca content of the solid was measured by acid digestion and subsequent ICP-OES analysis, thus representing bulk composition ion-balanced by cation ions. Although water molecules are present in ACMC, the activity of water (aH$_2$O) was not included in eq. 2 (see also Purgstaller et al., 2019). The activity of water (aH$_2$O) was assumed to be equal to unity, in agreement with the estimated aH$_2$O values of 0.995 ±0.002 of all experimental solutions. It is also worth pointing out that the term solubility product (K) is used herein to be comparable to K values of crystalline phases, although this term is not necessarily valid for amorphous solids (Brečević and Nielsen, 1989).

Table 1: Mineralogical composition of the solids obtained at certain reaction times during experiments performed from 10 to 80 °C. The quantification of high-Mg calcite (HMC), aragonite (ARG) and hydromagnesite (HMG) at >1 day of reaction time was realized by Rietveld refinement. $[Mg]_{XRD}$ of HMC: Mg content of HMC calculated from the d_{104} reflection according to Goldsmith et al. (1961); d_{104}: position of the $d_{(104)}$ reflection of HMC; $FWHM_{d_{104}}$: left full-width at half-maximum of the d_{104} reflection of HMC.

Experiment	Time	Composition	HMC	ARG	HMG	$[Mg]_{XRD}$ of HMC	d_{104}	$FWHM_{d_{104}}$
	min/day		wt.%	wt.%	wt.%	mol%		°2θ
T_10°C	0.3 min	ACMC	-	-	-	-	-	-
	5 min	ACMC	-	-	-	-	-	-
	11 min	ACMC	-	-	-	-	-	-
	21 min	ACMC, HMC_I	-	-	-	I: 4.8	I: 3.0204	-
	32 min	HMC_I, ACMC	-	-	-	I: 5.1	I: 3.0194	-
	61 min	HMC_I, HMC_II	-	-	-	I: 6.2, II: 14.5	I: 3.0163, II: 2.9921	-
	1 day	**HMC_I, HMC_II**, ARG	I: 56, II: 42	2	0	I: 6.6, II: 15.4	I: 3.0153, II: 2.9896	0.375*
	1 week	**HMC_I, HMC_II**, ARG	I: 57, II: 41	2	0	I: 7.1, II: 16.3	I: 3.0136, II: 2.9869	0.373*
	2 months	**HMC_I, HMC_II**, ARG	I: 56, II: 41	3	0	I: 6.4, II: 15.8	I: 3.0157, II: 2.9882	0.380*
T_20°C	0.3 min	ACMC	-	-	-	-	-	-
	5 min	ACMC	-	-	-	-	-	-
	11 min	ACMC, HMC	-	-	-	11.9	2.9996	-
	21 min	ACMC, HMC	-	-	-	12.8	2.9970	-
	32 min	HMC, ACMC	-	-	-	15.2	2.9902	-
	61 min	HMC, ARG	-	-	-	17.0	2.9848	-
	1 day	**HMC**, ARG	99	1	0	18.0	2.9820	0.459
	1 week	**HMC**, ARG	99	1	0	18.3	2.9810	0.475
	2 months	**HMC**, ARG	98	2	0	18.8	2.9795	0.489
T_40°C	0.3 min	ACMC	-	-	-	-	-	-
	5 min	ACMC	-	-	-	-	-	-
	11 min	ACMC, HMC	-	-	-	23.0	2.9675	-
	21 min	HMC, ACMC	-	-	-	28.4	2.9516	-
	32 min	HMC	-	-	-	29.9	2.9471	-
	61 min	HMC	-	-	-	29.7	2.9477	-
	1 day	**HMC**	100	0	0	30.3	2.9460	0.644
	1 week	**HMC**, HMG	94	0	6	29.7	2.9479	0.596

130

	2 months	**HMC**, HMG	91	0	9	30.9	2.9443	0.544
T_60°C	0.3 min	ACMC	-	-	-	-	-	-
	5 min	ACMC	-	-	-	-	-	-
	11 min	ACMC, HMC	-	-	-	34.2	2.9346	-
	21 min	HMC, ACMC	-	-	-	39.4	2.9197	-
	32 min	HMC	-	-	-	39.9	2.9181	-
	61 min	HMC	-	-	-	39.8	2.9183	-
	1 day	**HMC**	100	0	0	40.7	2.9159	0.659
	1 week	**HMC**	100	0	0	40.5	2.9163	0.550
	2 months	**HMC**	100	0	0	40.6	2.9159	0.530
T_80°C	0.3 min	ACMC	-	-	-	-	-	-
	5 min	ACMC	-	-	-	-	-	-
	11 min	HMC, HMG, ACMC	-	-	-	39.6	2.9189	-
	21 min	HMC, HMG, ARG	-	-	-	39.2	2.9201	-
	32 min	HMC, HMG, ARG	-	-	-	39.5	2.9193	-
	61 min	HMC, HMG, ARG	-	-	-	39.7	2.9187	-
	1 day	**HMC**, HMG, ARG	78	7	15	39.7	2.9187	0.351
	1 week	**HMC**, HMG, ARG	80	7	13	40.4	2.9167	0.354
	2 months	**HMC**, ARG, **	-	-	-	41.6	2.9132	0.362

*average FWHM of HMC_I and HMC_II

**additional phase that could correspond to magnesite

Table 2: Chemical composition of experimental solutions and solids obtained during experiments performed from 10 to 80 °C. $[Ca]_{aq}$ and $[Mg]_{aq}$: Ca and Mg concentration of the experimental solution; $[Mg]_{solid}$: Mg content of the bulk solid determined by chemical digestion (see eq. 1).

Experiment	Time min/day	pH	Alkalinity mM	$[Ca]_{aq}$ mM	$[Mg]_{aq}$ mM	$[Mg]_{solid}$ mol%
T_10°C	0 min	8.15	49.7	0.0	29.0	47.9 ±1.5
	0.3 min	9.15	80.6	2.5	41.7	46.0 ±1.5
	5 min	7.52	126.1	35.1	84.3	38.0 ±1.4
	11 min	7.55	138.8	41.3	94.3	35.4 ±1.4
	21 min	7.31	134.3	24.5	110.1	25.5 ±1.1
	32 min	7.59	137.8	20.1	118.1	22.3 ±1.0
	61 min	7.53	133.8	12.9	125.2	11.4 ±0.6
	1 day	7.31	109.1	2.3	122.0	13.0 ±0.7
	1 week	7.52	97.3	0.6	120.3	14.4 ±0.7
	2 months	7.77	89.9	0.3	120.7	15.5 ±0.8
T_20°C	0 min	8.17	48.4	0.0	29.1	47.9 ±1.5
	0.3 min	9.21	77.5	2.1	41.4	45.6 ±1.5
	5 min	7.62	119.4	25.1	81.8	38.0 ±1.4
	11 min	7.53	126.1	20.8	92.8	34.7 ±1.4
	21 min	7.59	129.5	16.7	105.6	29.5 ±1.2
	32 min	7.59	134.2	15.7	115.1	21.9 ±1.0
	61 min	7.53	118.3	6.9	117.7	16.6 ±0.8
	1 day	7.49	96.2	0.9	114.2	19.0 ±0.9
	1 week	7.80	88.2	0.3	111.6	20.8 ±1.0
	2 months	7.92	79.7	0.2	110.4	22.2 ±1.0
T_40°C	0 min	8.01	49.7	0.0	29.0	47.9 ±1.5
	0.3 min	8.85	70.2	1.7	38.3	47.0 ±1.5
	5 min	7.59	102.1	14.2	75.3	39.3 ±1.4
	11 min	7.60	108.3	10.5	85.5	35.5 ±1.4
	21 min	7.59	110.4	7.8	97.1	30.4 ±1.3
	32 min	7.55	99.5	3.1	99.0	28.8 ±1.2
	61 min	7.58	86.4	1.1	97.0	29.6 ±1.2
	1 day	7.57	60.9	0.4	85.1	33.0 ±1.3
	1 week	8.52	12.0	0.3	65.2	40.1 ±1.4
	2 months	8.39	8.1	0.3	64.8	41.2 ±1.5
T_60°C	0 min	8.00	49.6	0.0	29.2	47.9 ±1.5
	0.3 min	8.35	60.4	1.7	32.9	47.5 ±1.5
	5 min	7.60	80.2	6.6	58.9	43.0 ±1.5
	11 min	7.59	83.3	5.5	65.6	41.1 ±1.5
	21 min	7.59	73.9	3.9	67.1	40.5 ±1.4
	32 min	7.55	57.7	1.1	64.2	40.4 ±1.4
	61 min	7.57	45.5	0.6	61.3	41.2 ±1.5
	1 day	7.46	20.1	0.6	48.9	43.8 ±1.5
	1 week	7.46	7.5	0.5	43.3	45.2 ±1.5
	2 months	7.64	3.1	0.8	42.2	45.3 ±1.5
T_80°C	0 min	7.79	48.5	0.0	29.4	47.9 ±1.5
	0.3 min	7.82	51.3	1.6	28.1	48.3 ±1.5
	5 min	7.59	53.7	3.2	33.1	47.6 ±1.5
	11 min	7.49	39.7	1.4	25.0	48.8 ±1.5
	21 min	7.41	20.7	0.3	21.8	49.0 ±1.5
	32 min	7.42	16.7	0.3	20.4	49.3 ±1.5
	61 min	7.57	10.7	0.3	17.3	49.5 ±1.5
	1 day	7.87	5.6	0.3	15.7	49.8 ±1.5
	1 week	7.87	6.3	0.3	16.0	49.6 ±1.5
	2 months	7.54	6.7	0.9	15.3	49.8 ±1.5

5.3 Results

5.3.1 Solid Phase Characterization

Scanning electron microscope observations of the synthesised ACMC (47.9 ±1.5 mol% Mg) solid reveal spherical particles with < 100 nm in size (Fig. S1B) similar to synthetic amorphous calcium (magnesium) carbonate reported by other authors (Long et al., 2011; Blue and Dove, 2015; Konrad et al., 2016). The water content of the ACMC determined by thermal analysis is 0.67 ±0.01 moles per unit formula (Fig. S1C), thus, its stoichiometric formula can be written as $Ca_{0.52}Mg_{0.48}CO_3 \cdot 0.67H_2O$. This water content is in good agreement with that of the ACMC ($Ca_{0.47}Mg_{0.53}CO_3 \cdot 0.66H_2O$) precipitated by Purgstaller et al. (2019).

X-ray diffraction (XRD) patterns of the solids collected during the ACMC transformation experiments are shown in Fig. 2 at a 2θ range from 33° to 37°, while overview XRD patterns (2θ range = 4° - 65°) are displayed in Fig. S3. The XRD patterns indicate the sole occurrence of ACMC for 11 min in experiment T_10°C (Fig. 2A, Fig. S3A) and for 5 min in experiments performed at ≥ 20 °C (Fig. 2B-E, Fig. S3B-E). Subsequently, XRD peaks appear due to the transformation of ACMC into high-Mg calcite (HMC) and partly into aragonite (ARG) and hydromagnesite (HMG). XRD analyses reveal that for all experiments at ≤ 60 °C, the reaction products consist mainly of HMC (≥ 98 wt.%) and traces of ARG (< 2 wt.%) (Table 1). In experiment T_10°C two peaks were detected in the XRD pattern corresponding to high-Mg calcites with distinct Mg contents, hereafter mentioned as HMC_I and HMC_II (Table 1 and Fig. 2A). The reflection peaks of HMC_I appear in the XRD pattern at ≥ 21 min (during ACMC transformation), while those of HMC_II can be detected at ≥ 61 min of reaction time (Fig. 2A and Fig. S3A). Note that in experiment T_40°C, minor amounts of HMG (9 wt.%) were detected beside HMC and ARG after 2 weeks of reaction time (Table 1, Fig. S3C). At 80 °C, XRD patterns show the transformation of ACMC into HMC, HMG and ARG which account for 78, 15 and 7 wt.%, respectively, after 1 day of reaction time (Fig. S3E; Table 1). After 2 months of reaction time, the presence of HMG was no longer detected (Fig. S3E). Instead, a reflection peak at 2.77 Å indicates the presence of new phase (labeled as * in Fig. S3E), which could correspond to magnesite ($MgCO_3$; Reeder, 1990). Indeed, earlier studies reported the formation of magnesite by the transformation of pre-existing hydrated Mg-carbonate phases such as hydrogmagnesite and dypingite at elevated temperatures (e.g. Montes-Hernandez et al., 2012).
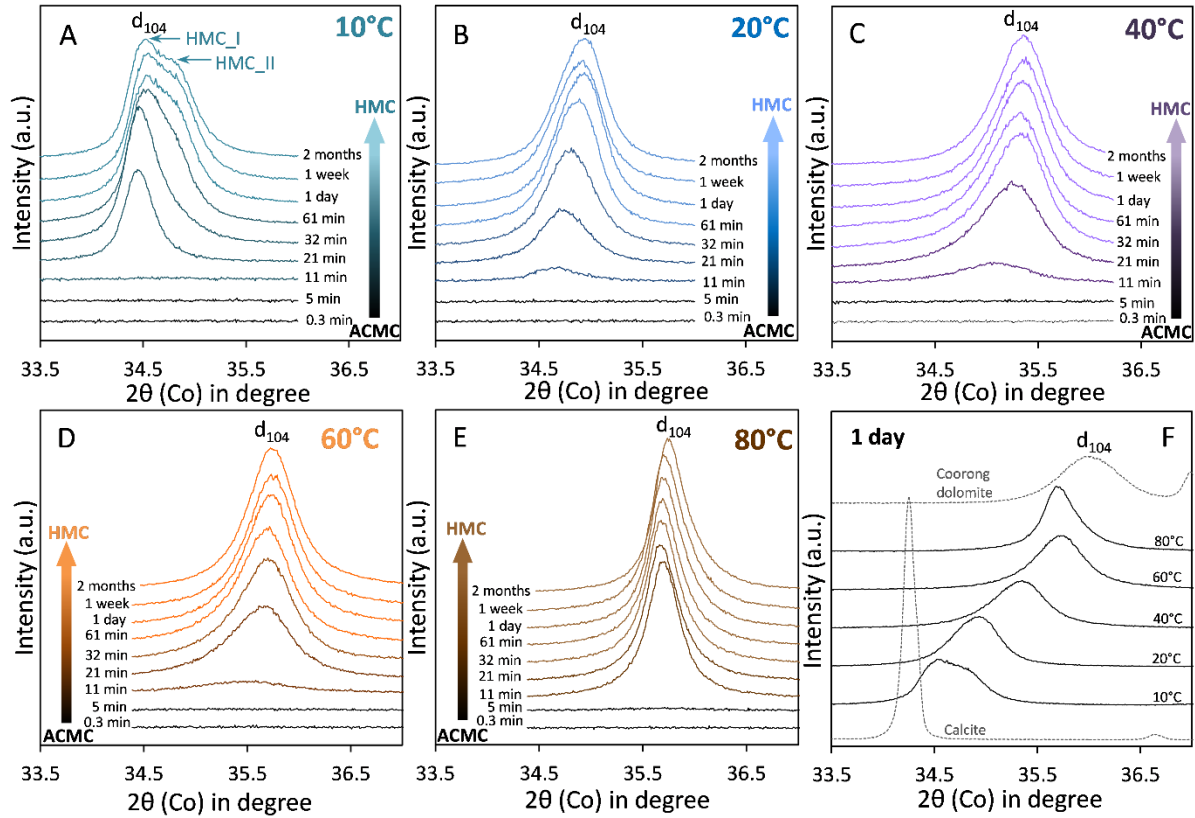
Fig. 2: X-ray diffraction pattern showing the evolution of the d_{104} peak reflection of high-Mg calcite (HMC) formed via transformation of amorphous calcium magnesium carbonate (ACMC) at (A) 10 °C, (B) 20 °C, (C) 40 °C, (D) 60 °C and (E) 80 °C. XRD pattern from 4° to 65° 2θ are shown in Fig. S3. Note that the d_{104}-value of the final HMC (F) is generally decreasing at higher temperature (increasing 2θ values) due to elevated Mg content (Goldsmith et al., 1961). The X-ray diffraction peaks of the HMCs are broader in comparison to the reference calcite (Merck), but are similar to the reference Coorong dolomite (South Australia).

Figure 2F shows that the XRD reflection peaks of the final HMCs are broader in comparison to the reference calcite (Merck). This observation is confirmed by comparing the $FWHM_{d104}$ values, which shows that the $FWHM_{d104}$ is higher for the HMCs (0.351 – 0.644; Table 1) than for the reference calcite (0.094). The obtained $FWHM_{d104}$ values of the HMCs however are similar to that determined for the reference Coorong dolomite ($FWHM_{d104}$ = 0.649; Fig. S4A). Broad XRD reflection peaks are referred to non-ideal crystal structure phenomena which can be caused by small (nanocrystalline) particle sizes (Bischoff et al., 1983; Kelleher and Redfern, 2002; Schmidt et al., 2005) and inhomogeneities in the Ca and Mg composition (Zhang et al., 2010) of the crystalline solid. Indeed, the broad XRD peaks obtained for the HMCs and the reference Coorong dolomite (Fig. 2F) can result from their small crystal sizes: SEM

images reveal aggregates composed of nanocrystals with < 100 and < 300 nm in size for the HMCs (Fig. 3D) and the Coorong dolomite (Fig. S4B), respectively.

To get insights into the evolution of the Mg content of the forming HMC via ACMC, the characteristic d_{104}-peak value of HMC was used to calculate its Mg content ($[Mg]_{XRD}$) according to Goldsmith et al. (1961) (Table 1). The Mg content of the HMCs obtained after 1 day of reaction time is higher at elevated temperature as indicated by lower d_{104}-values (corresponds to higher 2θ values in Fig. 2F). Note that a maximum concentration of 40 ±1 mol% Mg in HMC was obtained in experiments T_60°C and T_80°C (Table 1). In experiment T_10°C, the HMC_I that was detected in the samples collected at ≥ 21 min exhibits 6 ±1 mol% Mg, which is ~9 mol% lower than the Mg content of HMC_II (15 ±1 mol%) that was detected in the samples obtained at ≥ 61 min of reaction time (Fig.2A, Table 1). Rietveld refinement of the reaction products after 1 day shows that the amount of HMC_I (7 mol% Mg) and HMC_II (15 mol% Mg) is 56 and 42 wt.%, respectively (Table 1). In experiments performed between 20 °C and 60 °C, the initial HMC phase that was detected beside ACMC (at 11 min in Fig. 2B-E; Table 1) shows a significant lower Mg content than the HMC that was obtained during ACMC transformation (Table 1). This indicates that the Mg uptake in HMC is not uniform throughout the transformation process but ends up in HMC with distinct Mg content. In contrast, in experiment T_80°C, the HMCs show no significant change in the $[Mg]_{XRD}$ values during the experimental run (Table 1).

Scanning electron microscope images show that in experiments performed at ≤ 20 °C, the precipitates obtained at 5 min of reaction time consist of amorphous spherical particles (Fig. 3A), similar to the synthesized ACMC standard material (Fig. S1B). In experiments performed ≥ 40 °C, traces of HMC or HMG nanocrystals were observed beside the ACMC particles at 5 min of reaction time (Fig. 3A), although XRD results show that the solids obtained at 5 min are solely amorphous (Fig. 2C-E). The HMC (T_40°C and T_60°C) consists of spindle-shaped aggregates composed of nanocrystals, whereas the HMG crystals (T_80°C) show a plate-like morphology. These morphologies are similar to those observed for HMC and HMG obtained at a later stage in the experimental runs (Fig. 3B-D). At a reaction time of 21 min (Fig. 3B), large amounts of spherical ACMC particles were observed in the precipitates obtained in experiments performed at ≤ 20 °C, whereas at ≥ 40 °C ACMC was rarely observed in the collected solids. Note here that no ACMC particles were observed in the collected solids at ≥ 21 min in experiment T_80°C (Fig. 3B), at ≥ 32 min in experiments T_40°C and T_60°C (not shown) and at ≥ 61 min in experiments T_10°C and T_20°C (Fig. 3C).

SEM images of the final HMC show aggregates composed of spindle-shaped assemblages of nanocrystals at lower temperatures ($\leq$ 20 ˚C), whereas at higher temperatures ($\geq$ 40 ˚C) the HMC-nanocrystals coalesced into spheroidal aggregates (Fig. 3C-D). These spindle-shaped and spherical morphologies are consistent with those of high-Mg calcites formed via amorphous precursors from previous studies (Schmidt et al., 2005; Zhang et al., 2010; Purgstaller et al., 2016; 2017b; Blue et al., 2017). In experiment T_10˚C, large amounts of star-shaped aggregates composed of linearly arranged nanoparticles were detected beside the spindle-shaped HMC aggregates (Fig. 3D). These star-shaped aggregates most likely correspond to HMC_II that was detected beside HMC_I in the XRD-pattern at $\geq$61 min in experiment T_10˚C (Fig. 2A). Trace amounts of those aggregates could also be observed in the final solids of experiments T_20˚C and T_40˚C (Fig. 3D). Note here that the aragonite detected in experiments T_10˚C, T_20˚C and T_40˚C (2 – 7 wt. %, Table 1) could not be found in SEM images.
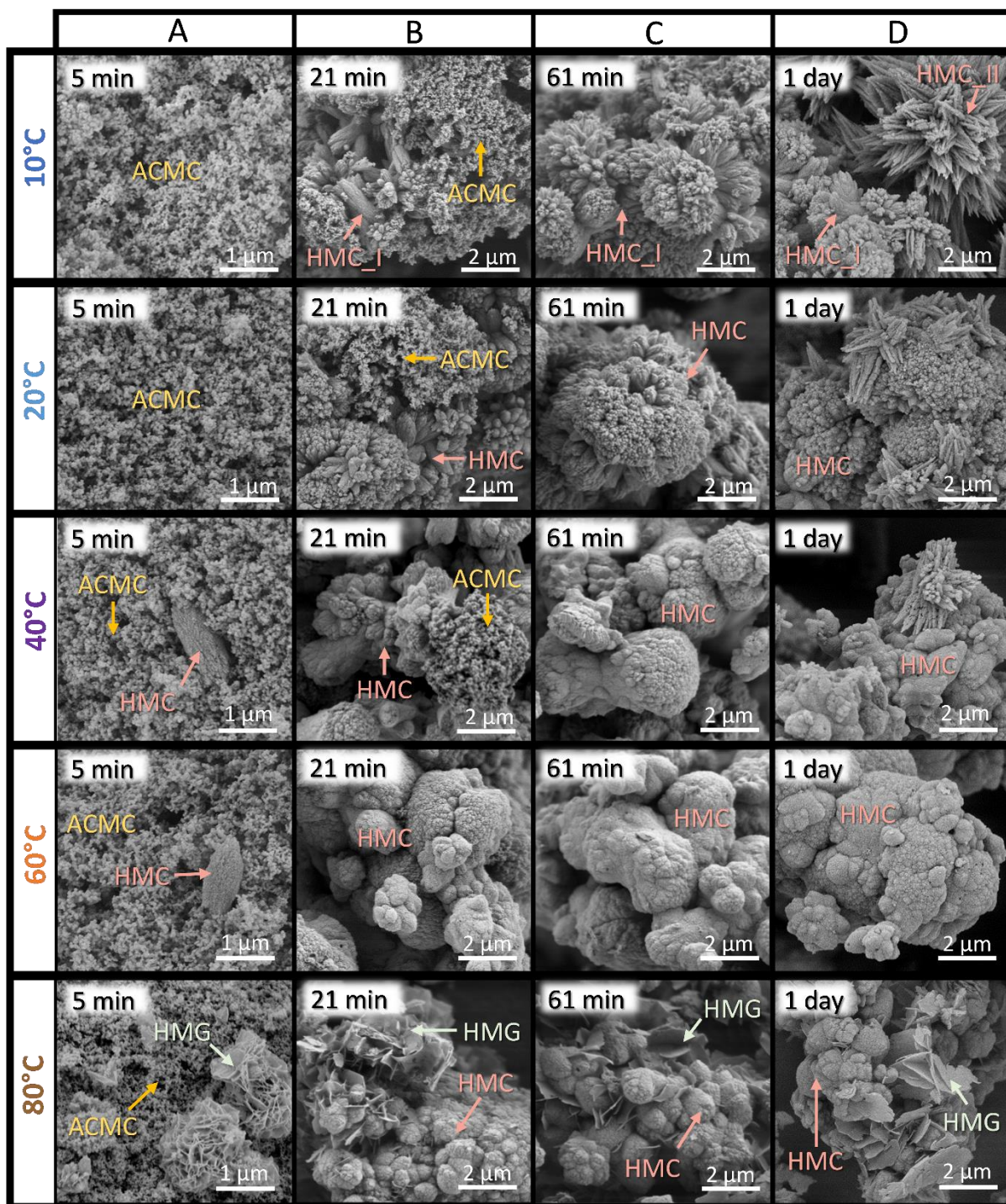
Fig. 3: SEM images of solids collected at 5 min (A), 21 min (B), 61 min (C) and 1 day (D) of reaction time in experiments performed from 10 to 80 °C, showing the transformation of amorphous calcium magnesium carbonate (ACMC) into high-Mg calcite (HMC) at ≤ 60 °C and into HMC and hydromagnesite (HMG) at 80 °C (see Table 1).

5.3.2 Chemical Evolution of the Reactive Solutions and Solids

The addition of ACMC into the MgCl$_2$-NaHCO$_3$ solutions induced an increase of pH as well as of Ca, Mg and alkalinity concentrations (at 0.3 min in Fig. 4A-C, Table 2) which is attributed to the dissolution of ACMC. At lower temperatures, higher amounts of ACMC likely dissolved as it is indicated by higher Ca, Mg and alkalinity concentrations at 0.3 min of reaction time compared to higher temperature experiments (Fig. 4A-C, Table 2). Moreover, the obtained data from experiments performed at lower temperatures show a preferential release of Mg ions into the solution, resulting in ACMCs with slightly lower Mg contents (e.g. 46 mol% Mg in T_10°C) compared to original composition of the synthetic ACMC material introduced in the reactors (48 mol% Mg; Fig. 4D).

After a short initial homogenization period between the ACMC material and the solution, the pH of the experimental solutions was adjusted to 7.58 ±0.04 by automatic titration of HCl solution (Fig. S2). The adjustment of the pH resulted in the further dissolution of ACMC, which causes an increase in alkalinity, Ca and Mg concentrations of the experimental solutions between 0.3 and 5 min (Fig. 4A-C). After about 5 min, the Ca and alkalinity concentrations of the experimental solutions decrease (Fig. 4A and C) due to the transformation of ACMC into crystalline Ca-Mg carbonate phases (Fig. 2). With the exception of experiment T_80°C, the aqueous Mg concentrations of the solutions increase in the same time frame (Fig. 4B). The net release of Mg into the solution with an uptake of Ca into the solid during the ACMC transformation step results in HMCs with lower Mg contents compared to that of the initial ACMC precursor in experiments performed at ≤ 60 °C (Fig. 4D). In contrast, in experiment T_80°C, the Mg content of the bulk solid increases slightly during the ACMC transformation step (Fig. 4D), due to the formation of HMG (Mg$_5$(CO$_3$)$_4$(OH)$_2$·4H$_2$O) beside HMC and ARG (Table 1, Fig. S3). Note that in experiment T_40°C, the Mg content of the bulk solid increased between 1 week and 2 months of reaction time, owing to the additional formation of HMG at this stage of the experiment (Fig. 4D).
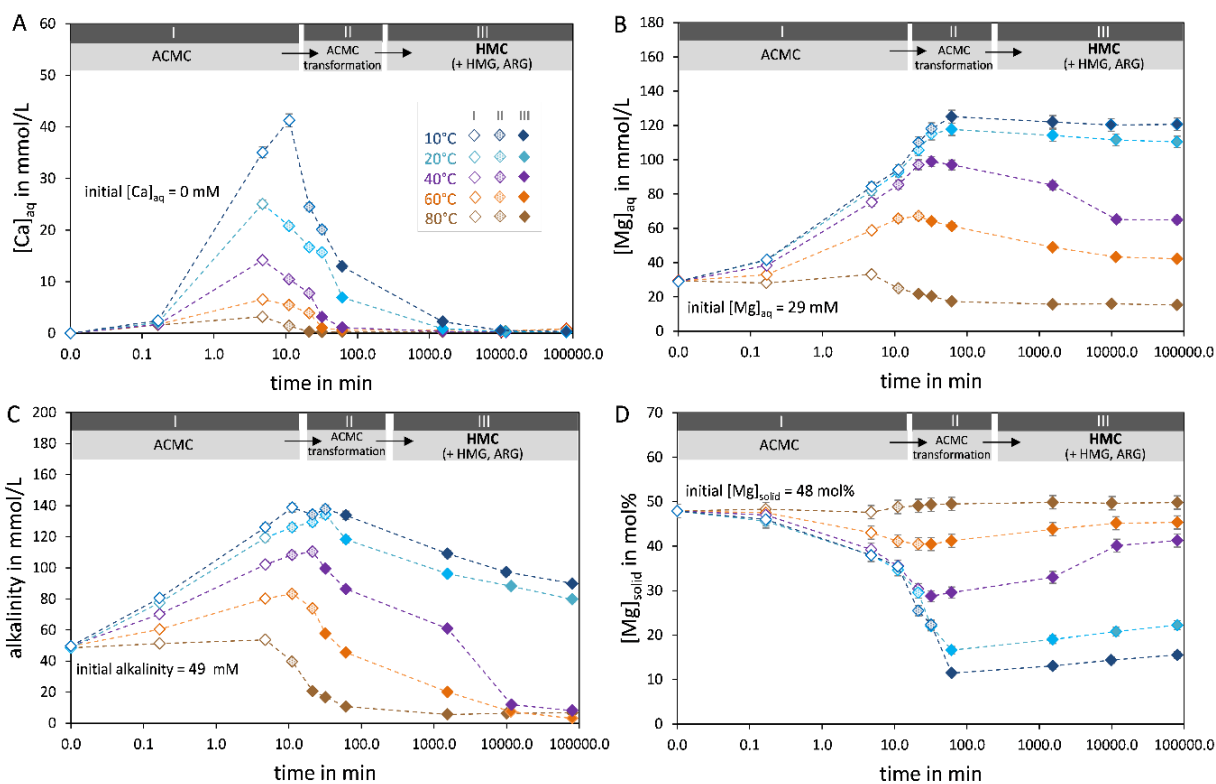
Fig. 4: Concentration of calcium (A), magnesium (B), alkalinity (C) of the solution and Mg content of the bulk solid (D) (see eq. 1) during amorphous calcium magnesium carbonate (ACMC) transformation into high-Mg calcite (HMC) and in case partly into hydromagnesite (HMG) and aragonite (ARG) (see Table 1) at 10, 20, 40, 60 and 80 °C. Stage I: ACMC is the sole solid phase (open diamonds); Stage II: ACMC transforms to the crystalline phases (shaded diamonds); Stage III: solid phase is crystalline (solid diamonds). Note that the pH of the solution was adjusted to 7.58 ±0.04 within ≤ 3 min by computer-controlled titration of a 2 M HCl solution (Fig. S2).

At higher temperatures, the transformation of ACMC into HMC occurs faster as revealed by XRD and SEM observations (Fig 2-3). This is further supported by the temporal evolution of pH and HCl solution addition derived from titration data (Fig. S2). In experiments performed at ≤ 60 °C, our data reveal that additional amounts of HCl solution were automatically added into the experimental solution to keep the pH constant at 7.58 ±0.04 during the transformation of ACMC into HMC (Fig. S2A-D). The rise in pH and consequent titration of HCl may be explained by a fast dissolution of ACMC and slow precipitation of HMC during the ACMC transformation step. At higher temperatures, the HCl solution was added into the experimental solution in shorter periods of time (e.g. 17 min in T_60°C) than at lower temperatures (e.g. 34 min in T_20°C), indicating that the transformation of ACMC into HMC occurs faster at elevated temperatures. Note that in experiment T_80°C, where ACMC transformed into HMC, HMG and ARG (Fig. 2E, Table 1), no additional HCl was added into the

solution (Fig. S2E). In the latter case, the pH decreased slightly from 7.59 to 7.41 during the ACMC transformation step.

5.4 Discussion

5.4.1 Effect of Temperature on the Mg content of HMC formed via ACMC with near-dolomite stoichiometry

Earlier studies showed a strong correlation between the physicochemical parameters of the initial solution used for ACMC synthesis and the amount of Mg incorporated into ACMC and the final HMC (Long et al., 2011; Rodriguez-Blanco et al., 2015; Purgstaller et al., 2016; Blue et al., 2017). In this context, it has been suggested that tuning the amount of Mg in ACMC controls the amount of Mg incorporated into HMC. In contrast, the results of this study show that the Mg content of the HMC is by far not pre-determined by the Mg content of the initial ACMC (48 mol% Mg) that was introduced into the solution (Fig. 5A). In experiments performed at temperatures $\leq$ 40 $°$C, the Mg content of the final HMC is significantly lower (e.g. 18 mol% Mg in experiment T_20$°$C) than of the initial ACMC, whereas at higher temperatures ($\geq$ 60 $°$C), the final HMCs reach Mg contents comparable to those of VHMC (40 mol%; Fig. 5A). These findings clearly document that the Mg content of the forming calcite is strongly regulated by the reaction temperature prevailing during ACMC transformation. It is generally acknowledged that the transformation mechanism of ACMC into (V)HMC involves (i) dissolution of ACMC and (ii) nucleation and crystal growth of (V)HMC (Kelleher and Redfern, 2002; Rodriguez-Blanco et al., 2015; Blue et al., 2017; Xto et al., 2019). The relationship in Fig. 5A suggests that the Mg content of calcite forming at the ACMC-solution interface is significantly controlled by the temperature-dependent dehydration kinetic of aqueous Mg^{2+}. The incorporation of Mg into anhydrous carbonates is generally postulated to be kinetically limited under low-temperature conditions, due to the strong hydration of Mg^{2+} compared to Ca^{2+} (Lippmann, 1973; Mavromatis et al., 2013). In contrast, higher temperatures reduce the Mg-solvation energy barrier and favor anhydrous Ca-Mg-carbonate formation (Lorenzo et el., 2014). Thus, the amount of Mg incorporated into calcite formed via ACMC is enhanced at higher reaction temperatures (Fig. 5A).

The obtained results further support previous observations (Blue et al., 2017) that the incorporation of Mg into calcite formed via ACMC is controlled by the Mg^{2+}/Ca^{2+} ratio of the reactive solution at the time of transformation. Blue et al. (2017) synthesized ACMCs with different Mg contents under constant pH conditions (pH 8.3 - 9.1) using a mixed flow reactor and investigated their crystallization pathway in aqueous

solution under stirred and unstirred conditions. Their results document a positive correlation between the Mg content of calcite and the Mg^{2+}/Ca^{2+} ratio of the solution from which the mineral formed. In the experimental setup used in the present study, Mg^{2+} and CO_3^{2-} ions were present in the initial solution, whereas Ca^{2+} ions exclusively originated from the dissolution of the ACMC. At higher temperatures, lower amounts of ACMC dissolved in the $NaHCO_3$-$MgCl_2$ solution as indicated by less Ca^{2+} ions released into the reactive solution (Fig. 4A). This can be explained by the anticorrelation between amorphous carbonate mineral solubility and temperature (for ACC: Brečević and Nielsen, 1989). Thus, at 5 min of reaction time, the reactive solutions exhibit higher aqueous Mg^{2+}/Ca^{2+} ratios as a function of increasing temperature (Fig. 5B; Table S2). Indeed, by comparing the Mg content of the initial HMC with the Mg^{2+}/Ca^{2+} ratio of the solution after its reaction with the ACMC, we find a good agreement of the results obtained at 25 °C and those reported by Blue et al. (2017) (Fig. 5C).
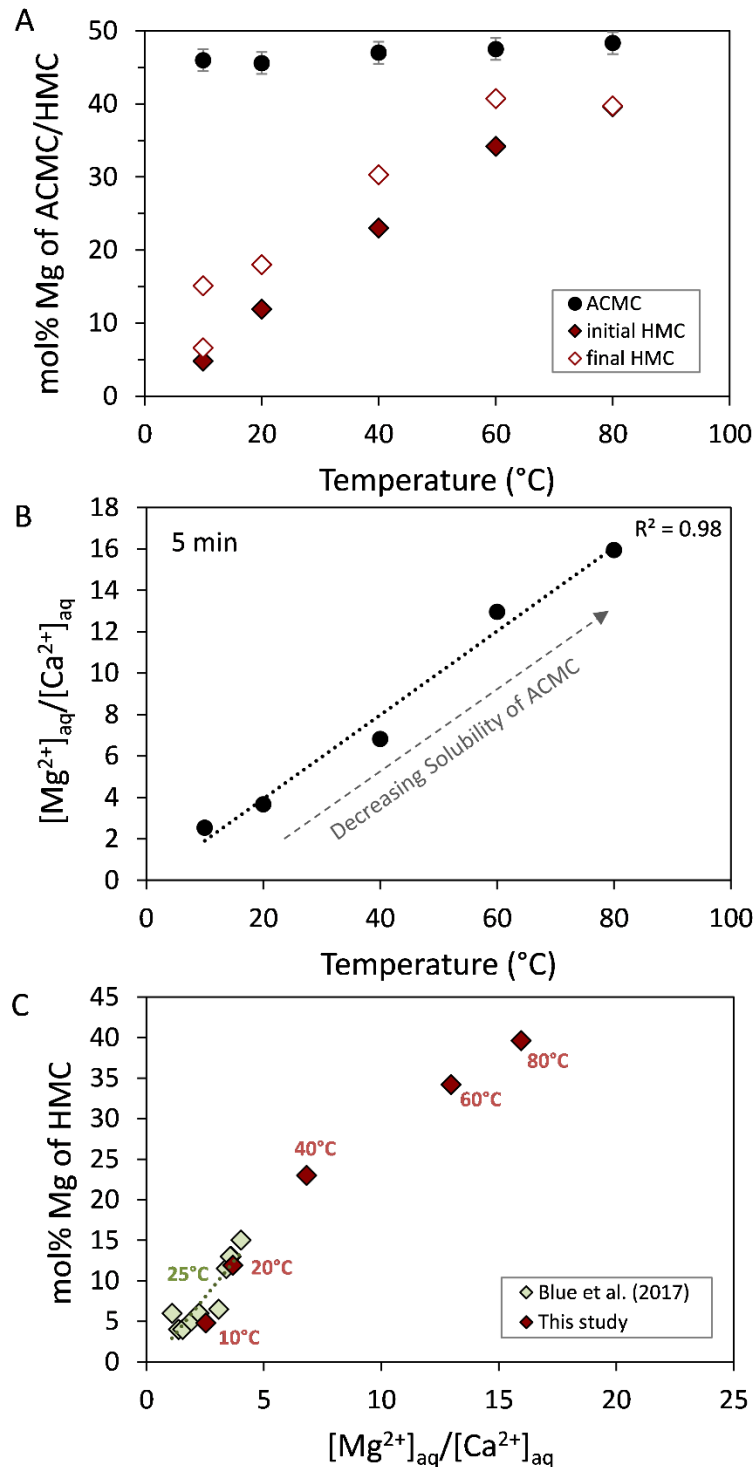
Fig. 5: (A) Temperature of the solution versus the Mg content of (i) ACMC obtained at 0.3 min of reaction time ([Mg]$_{solid}$ values in Table 2), (ii) initial HMC obtained at 21 min in experiment T_10°C and 11 min in experiments performed at ≥ 20 °C and (iii) final HMC obtained at 1 day of reaction time. Note here that the Mg contents of HMCs were calculated from the d$_{104}$ values of calcite XRD peaks ([Mg]$_{XRD}$ values in Table 1), whereas the Mg content of ACMC was calculated from solid digestion ([Mg]$_{solid}$ values in Table 2). (B) Temperature of the solution versus the Mg^{2+}/Ca^{2+} ratio of the solution at 5 min of reaction time (Table S2). (C) Mg^{2+}/Ca^{2+} ratio of the solution at 5 min versus the Mg content of (i) initial HMC from this study, of initial HMC from experiments conducted at stirred conditions reported by Blue et al. (2017).

142

During the ongoing transformation of ACMC into HMC, the Mg^{2+}/Ca^{2+} ratio of the solution increases (Table S2) due to stronger uptake of Ca^{2+} compared to Mg^{2+} from the solution into the solid. This increasing Mg^{2+}/Ca^{2+} ratio likely results in the formation of HMC with higher Mg contents as a function of reaction time ($[Mg]_{XRD}$ values in Table 1). Hence, the final HMCs exhibit higher Mg contents compared to the initial HMCs (Fig. 5A). This effect is temporally better resolved at low temperatures, due to slower transformation kinetics of ACMC into HMC (Table 1). For example, at 20 °C the Mg content of HMC increases slowly from 12 to 17 mol% between 11 and 61 min of reaction time (Table 1). In contrast, at higher temperatures, the transformation of ACMC into HMC occurs faster and the transition from lower to higher Mg contents for HMCs occurs in shorter time intervals (Table 1).

The positive relationship between aqueous Mg^{2+}/Ca^{2+} ratios and Mg content of the forming HMC from ACMC transformation (Fig. 5C) indicates that the Mg content into calcite might be enhanced to higher levels by increasing the Mg^{2+}/Ca^{2+} ratio of the reactive transformation solution. However, experimental studies at 25 °C and moderate pH conditions (8.3 - 9.1) documented that at higher prevailing Mg^{2+}/Ca^{2+} ratios (> 4: Blue et al., 2017; ≥ 8: Purgstaller et al., 2017a), ACMC transforms into hydrous Ca- or Mg-carbonate phases, i.e. monohydrocalcite and nesquehonite, rather than into calcite, due to the inhibition of the latter (Blue et al., 2017; Purgstaller et al., 2017b). These observations suggest a maximum limit of about 20 mol% Mg in calcite formed via the amorphous pathway (Purgstaller et al., 2016; 2017b; Blue et al., 2017). It should be emphasized that when ACMC transforms under unstirred conditions, Mg contents of up to 30 mol% Mg for HMC were reported in experimental studies conducted at moderate pH conditions and ambient temperatures (Han et al., 2013; Blue et al., 2017). However, the process by which physical mixing influences the formation of distinct crystalline Ca-Mg-carbonates and the Mg content of calcite is still poorly understood and needs further investigations.

5.4.2 Solubility considerations of ACMC and HMC

At higher reaction temperatures, less ACMC dissolved in the $NaHCO_3$-$MgCl_2$ solutions as it is indicated by the lower concentrations of Ca, Mg and CO_3 ions in the reactive solutions at 0.3 min of reaction time (Fig. 4A). In order to assess the effect of temperature on the solubility (K) of ACMC, the activities of Ca^{2+}, Mg^{2+} and CO_3^{2-} ions in the reactive solution (Table S3) and the ACMC stoichiometry (at 0.3 min) were used to calculate K_{ACMC} values according to eq. 2 (see also Purgstaller et al., 2019). The obtained K_{ACMC} values for ACMC with 47.0 ±1.5 mol% Mg (t = 0.3 min) indicate that the solubility

of ACMC is lower at higher temperature (Fig. 6A), analogous to the temperature-dependent solubility of ACC determined by Brečević and Nielsen (1989). A similar behaviour is also well known for anhydrous carbonate minerals such as calcite (Plummer and Busenberg, 1982) and magnesite (Bénézeth et al., 2011) which exhibit lower K values at higher temperatures (Fig. 6A). The relationship between the solubility of ACMC (with 47.0 ±1.5 mol% Mg) and temperature (T in Kelvin) can be described by the polynomial function:

$$\log(K_{ACMC}) = -0.0001434 \pm 0.0000137 \ T^2 + 0.0760 \pm 0.0087 \ T - 15.537 \pm 1.375 \qquad (3)$$
($R^2 = 0.99$)

It is strongly emphasized that in the present study the experimental data for calculating K_{ACMC} values are limited (Table S3) and further experimental work is needed to verify the obtained relationship between K_{ACMC} and temperature (Fig. 6A).

As it can be seen in Fig. 6A the solubility products of ACMC are higher compared to Mg-free ACC at any temperature suggesting that ACMC is more soluble than ACC. This feature can be attributed to the increasing water content and changes in short-range order, as Ca is substituted by Mg in the amorphous structure (Purgstaller et al., 2019). The relationship between the solubility of ACMC and its Mg content is displayed in Fig. 6B. Note that the slopes of the regression lines between the K_{ACC} value of Brečević and Nielsen (1989) and the K_{ACMC} value of this study are similar at 10, 20, 40, 60 and 80 °C (slope = 0.01634 ±0.00066; Fig. 6B and Table S4) and are in good agreement with the slope value of the linear relationship between K_{ACMC} and the Mg content of ACMC at 25 °C (slope = 0.01602; Mg content of ACMC = 2 to 51 mol%, Table S4) presented by Purgstaller et al. (2019). Considering the close agreement between K values obtained in this study and those of Brečević and Nielsen (1989) and Purgstaller et al. (2019) a quantitative description of the variations of K_{ACMC} with temperature and Mg content of ACMC can be obtained starting from the relationship between ACC solubility (K_{ACC}) and temperature (T in Kelvin) determined by Brečević and Nielsen (1989):

$$\log(K_{ACC}) = -0.0001096 \ T^2 + 0.0545 \ T - 12.919 \qquad (4)$$

Based on the assumption that the relative increase of K_{ACMC} values as a function of the Mg content is independent of temperature and can be described by the same linear function with an average slope of 0.01629 ±0.00060 (see Table S4), the variation of

the solubility of ACMC with temperature and Mg content can be obtained from the equation:

$$\log(K_{ACMC}) = 0.01629 * [Mg]_{ACMC} - 0.0001096\,T^2 + 0.0545\,T - 12.919 \qquad (5)$$

where $[Mg]_{ACMC}$ refers to the Mg content of ACMC in mol% (eq. 1) and T is the temperature reported in Kelvin. Note that the obtained relationship between K_{ACMC}, $[Mg]_{ACMC}$ and temperature is only valid for the studied ranges of $[Mg]_{ACMC} = 0 - 51$ mol% and T = 10 – 80 °C of the present study, Brečević and Nielsen (1989) and Purgstaller et al. (2019).
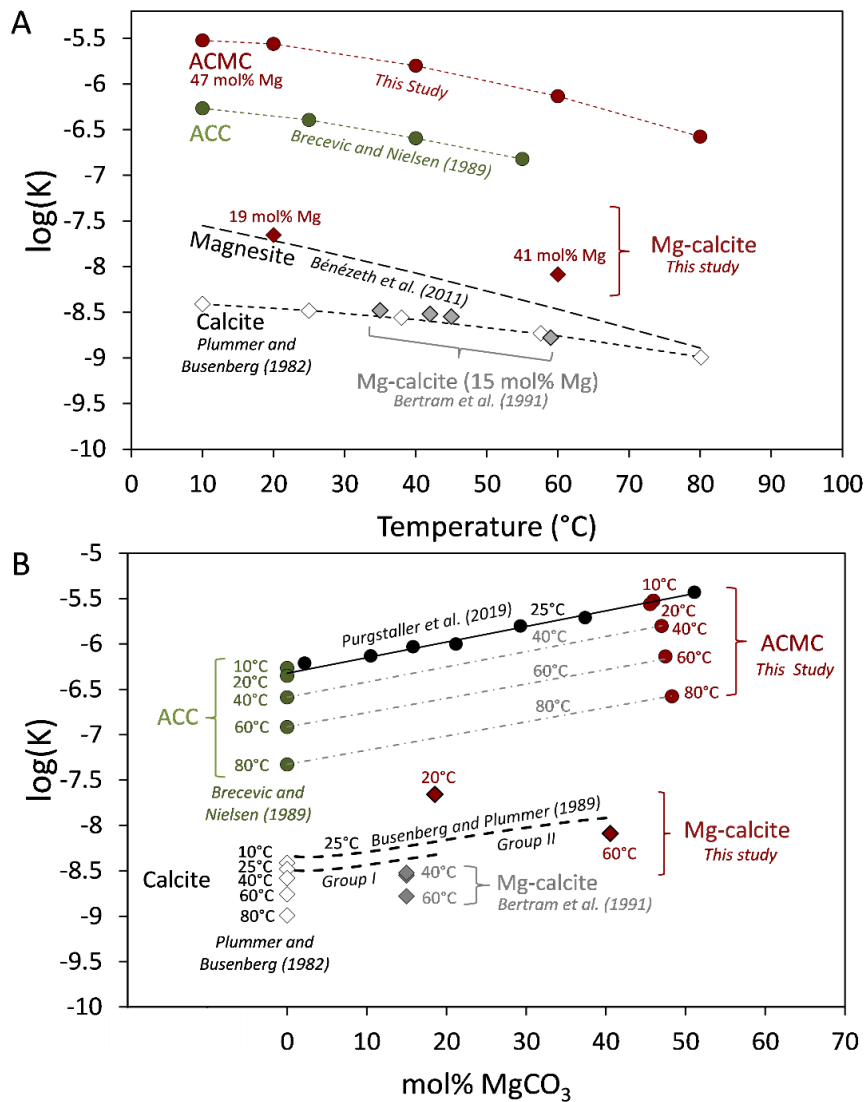
Fig. 6: Solublity product (K) of ACC (Brecevic and Nielsen, 1989), ACMC (present study and Purgstaller et al., 2019), calcite (Plummer and Busenberg, 1982), Mg calcite (present study, Busenberg and Plummer, 1989 and Bertram et al., 1991) and magnesite (Bénézeth et al., 2011) as a function of (A) temperature and (B) Mg mole fraction. The K of ACMC and Mg calcite was calculated according to eq. 2.

145

The dependence of ACMC solubility on the Mg content is similar to that of Mg calcite (above 4 mol% Mg), where high Mg contents in calcite result in higher solubilities (for 25 °C: Busenberg and Plummer, 1989; Fig. 6B). However, the impact of temperature on the solubility of HMC is not fully elucidated and to our knowledge only Bertram et al. (1991) studied the solubility of synthetic Mg calcites with 1.9 to 15 mol% Mg between 25 to 64 °C and showed that the decrease in solubility of Mg calcite with increasing temperature parallels that of calcite (see K data of Mg calcite with 15 mol% Mg in Fig. 6A). No experimental data, however, exist for the solubility dependence of HMC with > 15 mol% Mg at elevated temperatures. Figure 6A-B shows the calculated K values of the final HMC (K_{HMC}) from experiment T_20°C and T_60°C. The K-values were calculated using the chemical data and the HMC stoichiometry (based on $[Mg]_{XRD}$, Table 1) at 1 week and 2 months of reaction time (Table S3). At this time the system achieved near-equilibrium conditions (Table 2). Note that K_{HMC} values were not calculated in experiments T_10°C, T_40°C and T_80°C because the final solids of T_10°C consist of two Mg calcites with different Mg contents (Fig. 2A) and those of T_40°C and T_80°C include HMG (6 - 15 wt.%, Table 1). As it can be seen in Fig. 6B, the HMC formed via ACMC at 20 °C (with 18 mol% Mg) is significantly more soluble (log(K_{HMC})= -7.83) than the biogenic and synthetic Mg calcites of Group II reported by Busenberg and Plummer (1989), which exhibit similar Mg contents (e.g. log(K_{HMC})= -8.16 for biogenic Mg calcite with 19 mol% Mg at 25 °C). Note that Busenberg and Plummer (1989) distinguished two groups of Mg calcites with distinct solubilities, reflecting crystal structure defects (Fig. 6B). Group I consists of metamorphic and hydrothermal Mg calcites and synthetic Mg calcites prepared at high temperatures and pressures or low temperatures and low supersaturations (saturation index ≤ 0.2). Group II Mg calcites are of either biogenic origin or synthetic Mg calcites prepared at high supersaturations (saturation index ≥ 0.5). The Mg calcites of Group I are thought to be relatively free of structural defects, whereas Group II Mg calcites were described as more defective Mg calcites which exhibit higher solubilities. The discrepancy between the reported solubility value of Busenberg and Plummer (1989) and of the present study might be explained by different physical defects originating from rapid crystal growth during HMC formation. Considering an ACMC transformation step, the solution in equilibrium with ACMC is highly supersaturated with respect to calcite (saturation index > 2; Rodriguez-Blanco et al., 2015; Purgstaller et al., 2016). Such high calcite supersaturation degrees probably promote rapid precipitation of HMC at the ACMC-solution interface. Indeed, in the present study, ACMC transformed into nanocrystalline HMC at relatively short time intervals (< 60 min, Fig. 2-3). These solids

146

are likely more defective and thus exhibit higher solubilities compared to well-crystallized HMC (Fig. 6B). The elevated solubilities of nanocrystalline HMC appears to be consist with recent results of Davis et al. (2000) who demonstrated, based on microscopic observations, enhanced solubilities of Mg calcites at the nanometric scale.

5.5 Conclusions

In the present study, the transformation of ACMC with near-dolomite stoichiometry (47.9 ±1.5 mol% Mg) into HMC was investigated in a $MgCl_2$–$NaHCO_3$ buffered solution at pH 7.6 and in the temperature range from 10 to 80 ±1 °C. The results provide an advanced understanding of the complex interplay between the chemical composition of ACMC, the corresponding solution and the finally formed Mg calcite. At first, the experimental data indicate that the apparent solubility of ACMC is lower at higher temperature and the relative increase of solubility as a function of the Mg content of ACMC is similar from 10 to 80 °C which can be assessed by eq.5. At ambient temperatures, the Mg content of HMC formed via the transformation of ACMC is as low as 18 mol%, whereas at 60 and 80 °C, the final HMCs reach Mg levels comparable with those of VHMC (40 mol%). Hence, the Mg content of the HMC is not pre-determined by the Mg content of the amorphous precursor, but strongly influenced by the reaction temperature during ACMC transformation. The transformation of ACMC to HMC proceeds via a dissolution and re-precipitation mechanism where at higher temperatures the amount of Mg incorporated into calcite is enhanced due to (i) the reduced solvation energy barrier of aqueous Mg^{2+} and (ii) the high Mg^{2+}/Ca^{2+} ratio of the reactive solution after its reaction with the ACMC. The high Mg^{2+}/Ca^{2+} ratio of the latter solution can be explained by low solubility of ACMC at elevated temperatures. The obtained solubilities of the final HMC are higher compared to those of well-crystalline Mg-bearing calcites, which is most likely caused by nanometric-sized HMC crystals with structural defects originated from fast crystal growth.

5.6 Supplementary material

Abbreviations

ACC: amorphous calcium carbonate; **ACMC:** amorphous calcium magnesium carbonate; **ARG:** aragonite; **FWHM:** full-width at half-maximum; **ICP–OES:** inductively coupled plasma optical emission spectrometry; **LMC:** low-Mg calcite; **HMC:** high-Mg calcite; **HMG:** hydromagnesite; **SEM:** scanning electron microscope; **TGA:** thermogravimetric analyses; **XRD:** X-ray diffraction

Table S1: ICSD Database Code and Reference used for mineral phase quantification.

Mineral phase	ICSD Database Code	Reference
Mg Calcite	-	Paquette and Reeder (1990) Single-crystal X-ray structure refinements of two biogenic magnesian calcite crystals. *American Mineralogists* 75, 1151-1158
Aragonite	170225	Caspi et al. (2005) On the structure of aragonite. *Acta Crystallographica B* 61, 129-132
Hydromagnesite	920	Akao and Iwai (1977) The hydrogen Bonding of Hydromagnesite, *Acta Crystallographica B* 33, 1273-1275

Table S2: Concentrations of free Ca^{2+} and Mg^{2+} ions and calculated Mg^{2+}/Ca^{2+} ratios of the experimental solutions

Experiment	Time min/day	$[Ca^{2+}]_{aq}$ mM	$[Mg^{2+}]_{aq}$ mM	$[Mg^{2+}]_{aq}/[Ca^{2+}]_{aq}$
T_10°C	0.3 min	1.4	28.0	20.1
	5 min	25.8	65.4	2.5
	11 min	29.9	72.1	2.4
	21 min	18.0	84.8	4.7
	32 min	14.5	90.3	6.2
	61 min	9.5	96.4	10.2
	1 day	1.7	97.9	56.6
	1 week	0.5	98.5	216.2
	2 months	0.3	99.9	370.4
T_20°C	0.3 min	1.0	26.0	25.5
	5 min	17.2	63.2	3.7
	11 min	14.1	71.1	5.0
	21 min	11.3	80.6	7.1
	32 min	10.6	87.5	8.3
	61 min	4.8	91.9	19.1
	1 day	0.7	92.8	139.8
	1 week	0.2	91.5	409.6
	2 months	0.2	91.9	605.2
T_40°C	0.3 min	0.8	24.5	31.6
	5 min	8.6	58.6	6.8
	11 min	6.2	65.8	10.6
	21 min	4.6	74.8	16.1
	32 min	1.9	78.0	40.6
	61 min	0.7	78.4	109.8
	1 day	0.3	72.6	252.9
	1 week	0.3	62.0	228.7
	2 months	0.3	62.8	191.5
T_60°C	0.3 min	0.8	22.9	28.6
	5 min	3.6	46.2	13.0
	11 min	3.0	51.4	17.4
	21 min	2.2	53.9	24.3
	32 min	0.7	53.7	78.4
	61 min	0.4	53.0	131.0
	1 day	0.5	45.6	92.9
	1 week	0.5	42.1	91.3
	2 months	0.8	41.6	53.8
T_80°C	0.3 min	0.8	20.7	27.0
	5 min	1.6	25.9	15.9
	11 min	0.8	20.6	26.1
	21 min	0.2	19.6	92.2
	32 min	0.2	18.1	80.6
	61 min	0.2	15.6	63.6
	1 day	0.3	14.5	53.8
	1 week	0.3	14.4	54.4
	2 months	0.8	13.9	17.9

Table S3: Activities (a) of Ca^{2+}, Mg^{2+} and CO_3^{2-} ions in the experimental solutions and apparent solubility product values (K) for ACMC and HMC calculated according to eq. 2.

Experiment	Time min/day	ionic strength M	$\log(aCa^{2+})$	$\log(aMg^{2+})$	$\log(aCO_3^{2-})$	K
T_10°C	0.3 min	0.14	-3.32	-2.01	-2.81	-5.52
	5 min	0.35	-2.12	-1.72	-4.11	-
	11 min	0.38	-2.06	-1.67	-4.06	-
	21 min	0.38	-2.28	-1.60	-4.31	-
	32 min	0.39	-2.37	-1.58	-4.03	-
	61 min	0.39	-2.56	-1.55	-4.09	-
	1 day	0.37	-3.29	-1.54	-4.39	-
	1 week	0.36	-3.87	-1.54	-4.23	-
	2 months	0.36	-4.10	-1.53	-4.03	-
T_20°C	0.3 min	0.14	-3.45	-2.05	-2.75	-5.56
	5 min	0.31	-2.30	-1.73	-3.95	-
	11 min	0.33	-2.39	-1.69	-4.02	-
	21 min	0.35	-2.49	-1.63	-3.95	-
	32 min	0.37	-2.52	-1.60	-3.95	-
	61 min	0.36	-2.86	-1.58	-4.05	-
	1 day	0.35	-3.72	-1.57	-4.18	-
	1 week	0.34	-4.19	-1.58	-3.92	-7.63
	2 months	0.34	-4.36	-1.58	-3.85	-7.68
T_40°C	0.3 min	0.13	-3.59	-2.09	-2.92	-5.80
	5 min	0.27	-2.61	-1.78	-3.88	-
	11 min	0.29	-2.76	-1.73	-3.85	-
	21 min	0.31	-2.89	-1.68	-3.86	-
	32 min	0.31	-3.27	-1.66	-3.94	-
	61 min	0.30	-3.70	-1.66	-3.97	-
	1 day	0.28	-4.09	-1.69	-4.12	-
	1 week	0.24	-4.10	-1.75	-4.03	-
	2 months	0.24	-4.02	-1.74	-4.29	-
T_60°C	0.3 min	0.13	-3.59	-2.13	-3.24	-6.13
	5 min	0.21	-3.00	-1.89	-3.82	-
	11 min	0.23	-3.09	-1.85	-3.82	-
	21 min	0.23	-3.21	-1.83	-3.87	-
	32 min	0.22	-3.72	-1.82	-4.01	-
	61 min	0.22	-3.95	-1.83	-4.09	-
	1 day	0.19	-3.85	-1.88	-4.54	-
	1 week	0.18	-3.87	-1.91	-4.96	-8.04
	2 months	0.18	-3.64	-1.91	-5.20	-8.14
T_80°C	0.3 min	0.12	-3.62	-2.19	-3.65	-6.58
	5 min	0.14	-3.32	-2.12	-3.85	-
	11 min	0.12	-3.61	-2.20	-4.05	-
	21 min	0.12	-4.17	-2.21	-4.41	-
	32 min	0.11	-4.14	-2.24	-4.49	-
	61 min	0.10	-4.10	-2.29	-4.54	-
	1 day	0.10	-4.05	-2.32	-4.62	-
	1 week	0.10	-4.06	-2.32	-4.55	-
	2 months	0.06	-3.52	-2.27	-4.78	-

Table S4: Summary of solubility data of amorphous Ca-(Mg-) carbonate of this study, Brečević and Nielsen (1989) and Purgstaller et al. (2019). The solubility (K) values of ACC ($[Mg]_{solid}$ = 0 mol% Mg) were calculated using the equation K = -0.00010960 T^2 + 0.05453848 T - 12.91852871, where T is given in Kelvin (Brečević and Nielsen, 1989). At a given temperature, the linear increase of the solubility (K) of ACMC as a function of the Mg content $[Mg]_{solid}$ (in mol%) is expressed as K = m $[Mg]_{solid}$ + y_0 (m = slope; y_0 = intercept). Note that the average m value of 0.01629 ± 0.00060 is given in eq. 5.

Temperature	Reference	$[Mg]_{solid}$ mol%	K	slope m	intercept y_0
10 °C	Brečević and Nielsen, 1989	0	-6.26	0.01603	-6.260
	This study	46.0	-5.52		
20 °C	Brečević and Nielsen, 1989	0	-6.35	0.01723	-6.346
	This study	45.6	-5.56		
40 °C	Brečević and Nielsen, 1989	0	-6.58	0.01665	-6.584
	This study	47.0	-5.80		
60 °C	Brečević and Nielsen, 1989	0	-6.91	0.01632	-6.910
	This study	47.5	-6.13		
80 °C	Brečević and Nielsen, 1989	0	-7.32	0.01548	-7.323
	This study	48.3	-6.58		
10, 20, 40, 60 and 80 °C	Brečević and Nielsen, 1989 This study			Average = 0.01634 ± 0.00066	
25 °C	Purgstaller et al., 2019	2.2	-6.20	0.01602	-6.286
	Purgstaller et al., 2019	10.5	-6.13		
	Purgstaller et al., 2019	15.8	-6.04		
	Purgstaller et al., 2019	21.2	-6.00		
	Purgstaller et al., 2019	29.3	-5.81		
	Purgstaller et al., 2019	37.4	-5.71		
	Purgstaller et al., 2019	51.1	-5.43		
10, 20, 25, 40, 60 and 80 °C	Brečević and Nielsen, 1989 This study Purgstaller et al., 2019			Average = 0.01629 ± 0.00060	
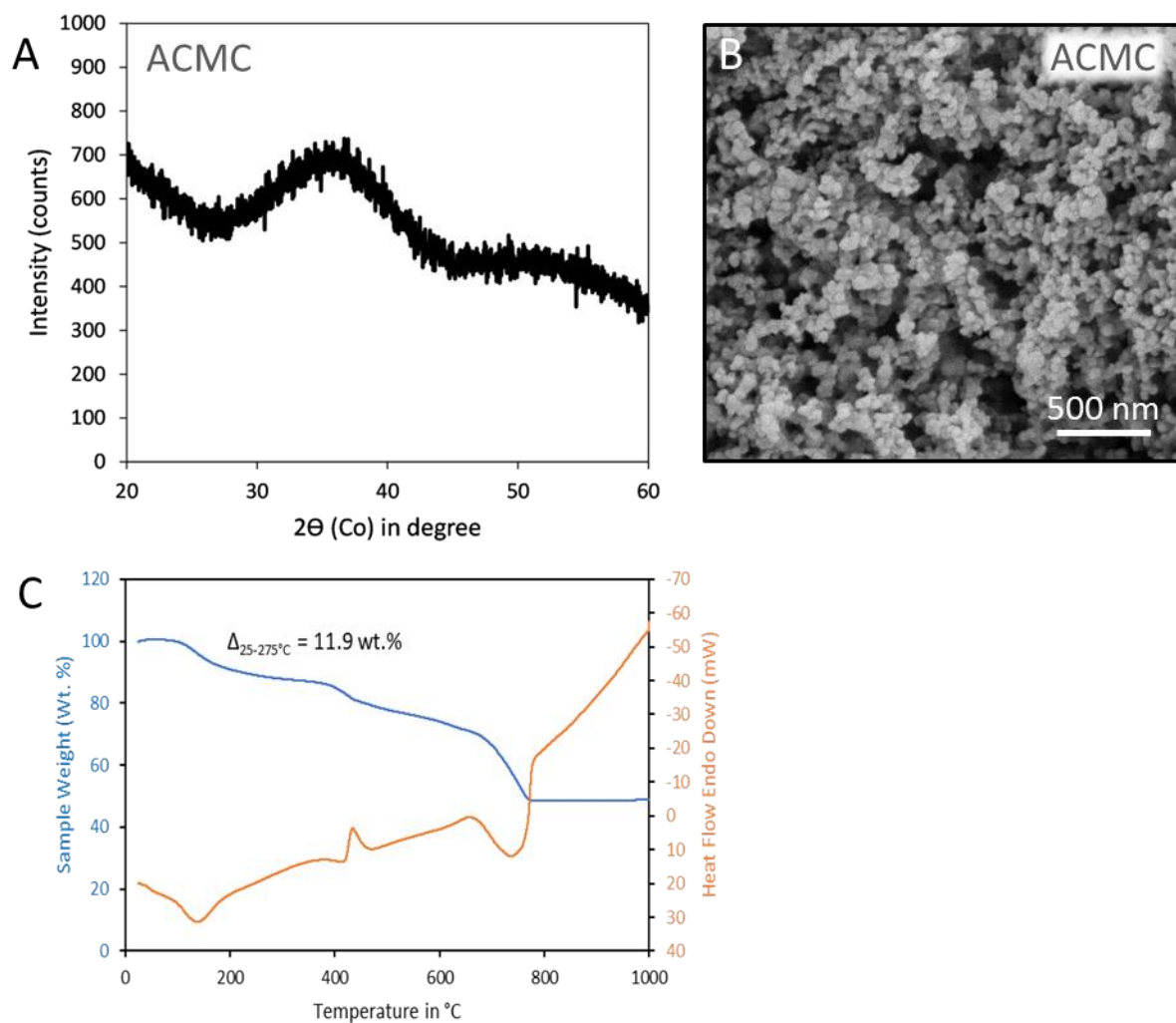
Fig. S1: (A) X-ray diffraction pattern, (B) SEM image and (C) thermal analysis (TGA: blue line, DSC: orange line) of synthesized ACMC with 47.9 ±0.2 mol% $MgCO_3$. The water content of ACMC was calculated from the weight loss between 25 and 275 °C ($\Delta_{25-275°C}$) to be 0.67 moles per unit formula $Ca_{0.52}Mg_{0.48}CO_3$ (see also Purgstaller et al., 2019).
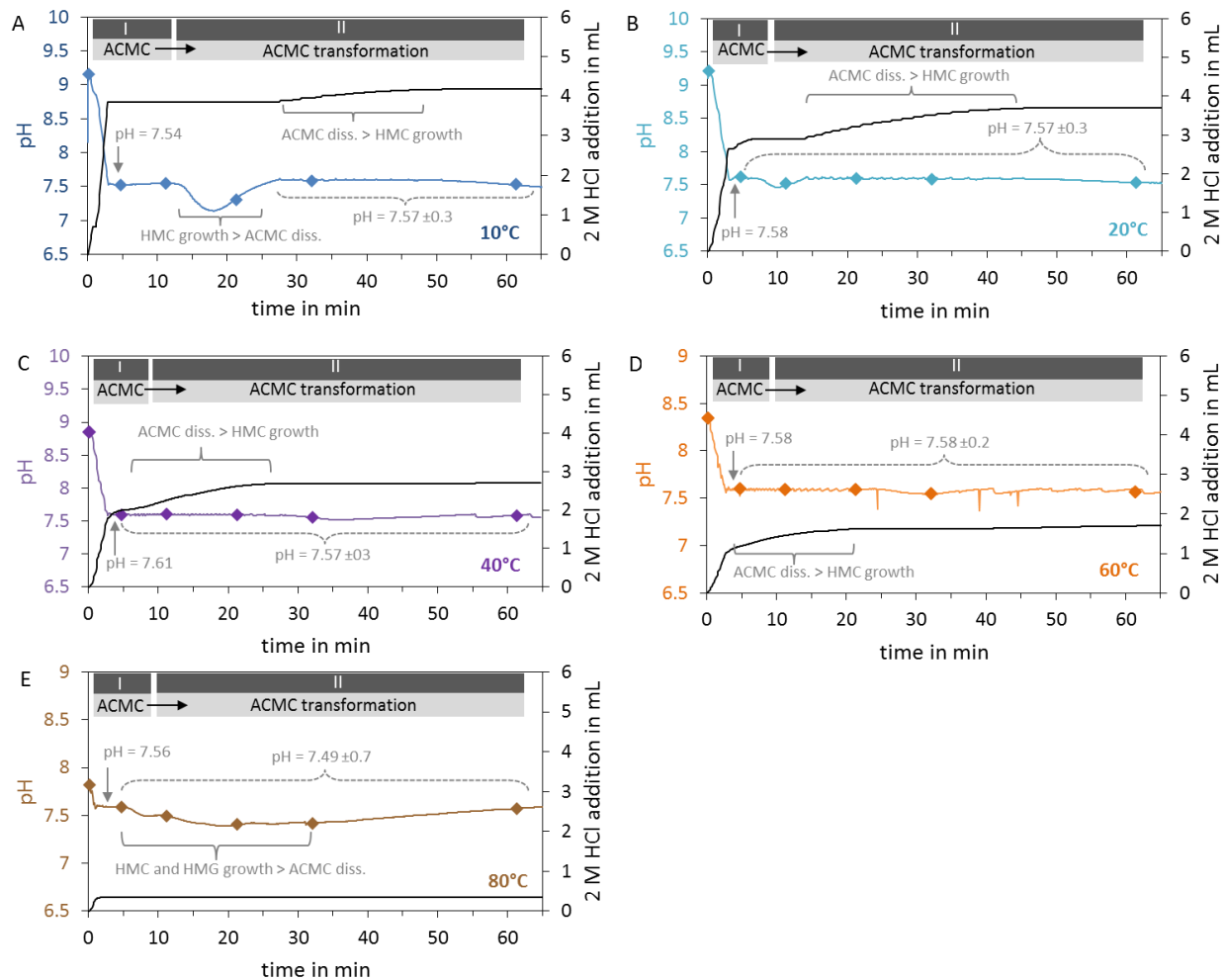
Fig. S2: Temporal evolution of pH of the experimental solution and of the mL HCl (2 M) added to the experimental solution by titration to keep the pH constant for experiments performed at (A) 10 ˚C, (B) 20 ˚C, (C) 40 ˚C, (D) 60 ˚C and (E) 80 ˚C.
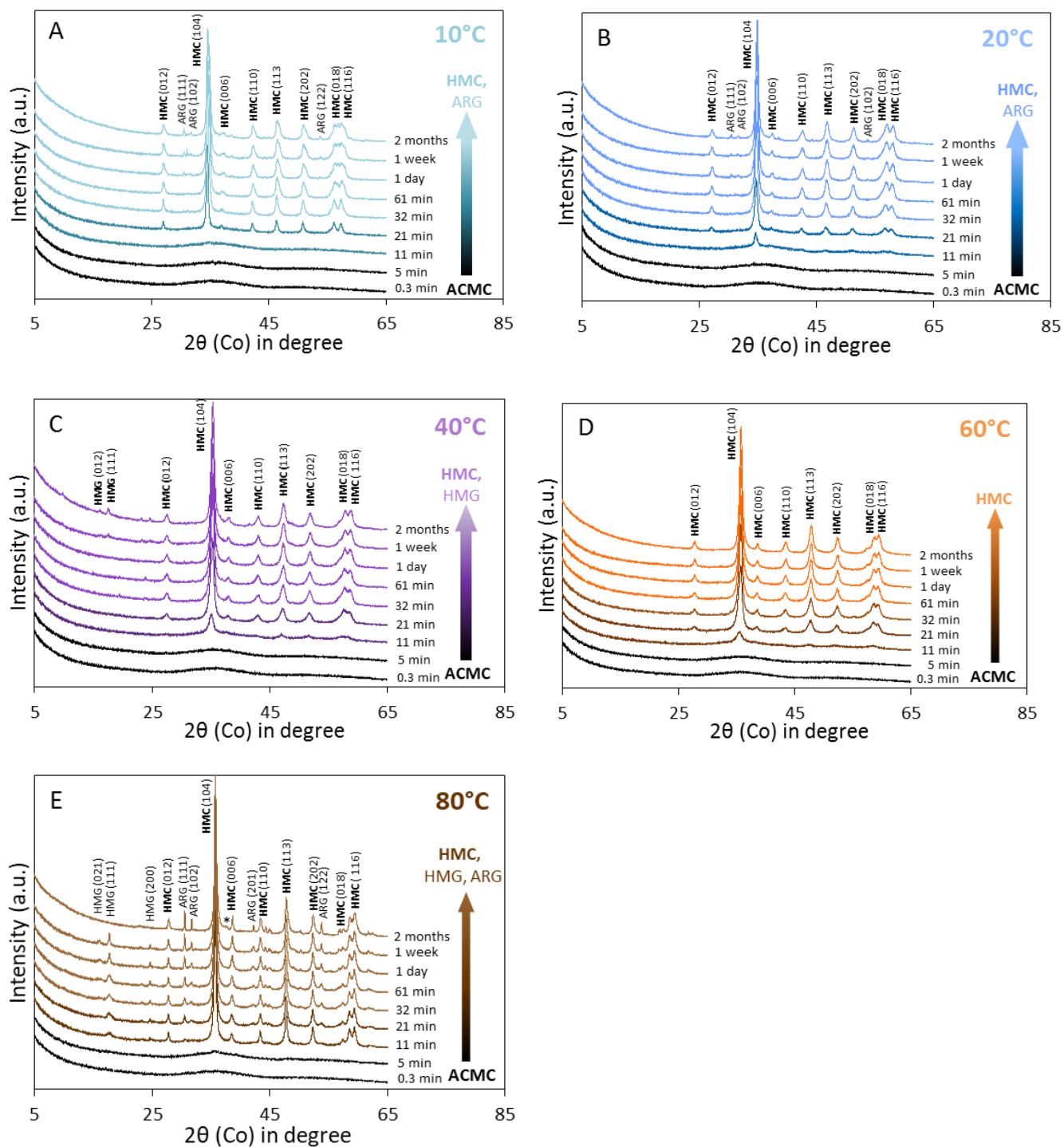
Fig. S3: Overview XRD patterns (2θ range = 4–65°) of precipitates obtained between 0.3 min and 2 months of reaction time in experiments performed at (A) 10 °C, (B) 20 °C, (C) 40 °C, (D) 60 °C and (E) 80 °C (see Table 1). ACMC: Amorphous calcium magnesium carbonate; HMC: High-Mg calcite; ARG: Aragonite; HMG: Hydromagnesite; *: Additional phase that could correspond to magnesite.
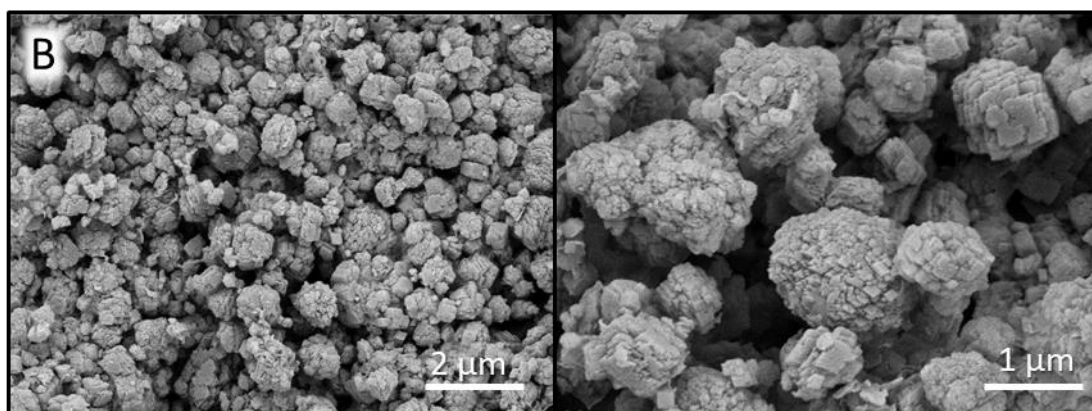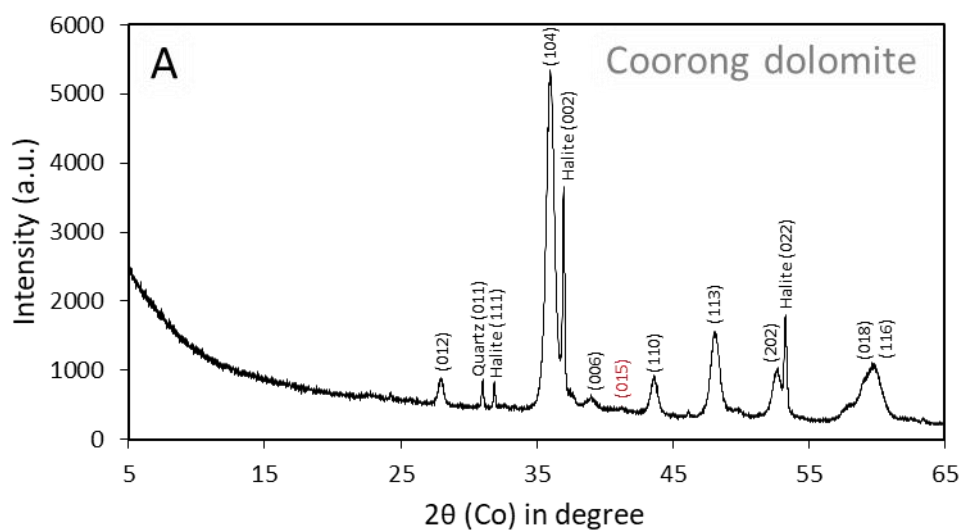
Fig. S4: (A) XRD pattern and (B) SEM images of the reference Coorong dolomite (48 mol% $MgCO_3$). Note that the 015 peak of the Coorong dolomite is very weak, indicating a low cation ordering degree.

References

Addadi L., Raz S. and Weiner S. (2003) Taking advantage of disorder: Amorphous calcium carbonate and its roles in biomineralization. *Adv. Mater.* **15**, 959–970.

Bénézeth P., Saldi G. D., Dandurand J. L. and Schott J. (2011) Experimental determination of the solubility product of magnesite at 50 to 200°C. *Chem. Geol.* **286**, 21–31.

Bentov S. and Erez J. (2006) Impact of biomineralization processes on the Mg content of foraminiferal shells: A biological perspective. *Geochemistry, Geophys. Geosystems* **7**.

Berner R. A. (1975) The role of magnesium in the crystal growth of calcite and aragonite from sea water. *Geochim. Cosmochim. Acta* **39**, 489–504.

Bertram M. A., Mackenzie F. T., Bishop F. C. and Bischoff W. D. (1991) Influence of temperature on the stability of magnesian calcite. *Am. Mineral.* **76**, 1889–1896.

Bischoff W. D., Bishop F. C. and Mackenzie F. T. (1983) Biogenically produced magnesian calcite: inhomogeneities in chemical and physical properties: comparison with synthetic phases. *Am. Mineral.* **68**, 1183–1188.

Bischoff W. D., Sharma S. K. and MacKenzie F. T. (1985) Carbonate ion disorder in synthetic and biogenic magnesian calcites: a Raman spectral study. *Am. Mineral.* **70**, 581–589.

Bleuzen A., Pittet P. A., Helm L. and Merbach A. E. (1997) Water exchange on magnesium(II) in aqueous solution: A variable temperature and pressure ^{17}O NMR study. *Magn. Reson. Chem.* **35**, 765–773.

Blue C. R. and Dove P. M. (2015) Chemical controls on the magnesium content of amorphous calcium carbonate. *Geochim. Cosmochim. Acta* **148**, 23–33.

Blue C. R., Giuffre A., Mergelsberg S., Han N., De Yoreo J. J. and Dove P. M. (2017) Chemical and physical controls on the transformation of amorphous calcium carbonate into crystalline $CaCO_3$ polymorphs. *Geochim. Cosmochim. Acta* **196**, 179–196.

Brečević L. and Nielsen A. E. (1989) Solubility of amorphous calcium carbonate. *J. Cryst. Growth* **98**, 504–510.

Busenberg E. and Plummer N. L. (1989) Thermodynamics of magnesian calcite solid-solutions at 25°C and 1 atm total pressure. *Geochim. Cosmochim. Acta* **53**, 1189–1208.

Davis K. J. (2000) The Role of Mg^{2+} as an Impurity in Calcite Growth. *Science (80-.).* **290**, 1134–1137.

Fernández-Díaz L., Putnis A., Prieto M. and Putnis C. V. (1996) The role of magnesium in the crystallization of calcite and aragonite in a porous medium. *J. Sediment. Res.* **66**, 482–491.

Furman F. C., Woody R. E., Rasberry M. A., Keller D. J. and Gregg J. M. (1993) Carbonate and Evaporite Mineralogy of Holocene (<1900 RCYBP) Sediments at Salt Pond, San Salvador Island, Bahamas: Preliminary Study. *Proc. Sixth Symp. Geol. Bahamas*, 47–54.

Fussmann D., Jean Elisabeth Von Hoyningen-Huene A., Reimer A., Schneider D., Babková H., Peticzka R., Maier A., Arp G., Daniel R. and Meister P. (2020) Authigenic formation of Ca-Mg carbonates in the shallow alkaline Lake Neusiedl, Austria. *Biogeosciences* **17**, 2085–2106.

Gayathri S., Lakshminarayanan R., Weaver J. C., Morse D. E., Manjunatha Kini R. and Valiyaveettil S. (2007) In vitro study of magnesium-calcite biomineralization in the skeletal materials of the seastar Pisaster giganteus. *Chem. – A Eur. J.* **13**, 3262–3268.

Goetschl K. E., Purgstaller B., Dietzel M. and Mavromatis V. (2019) Effect of sulfate on magnesium incorporation in low-magnesium calcite. *Geochim. Cosmochim. Acta* **265**, 505–519.

Goldsmith J. R., Graf D. L. and Heard H. C. (1961) Lattice constants of the calcium-magnesium carbonates. *Am. Mineral.* **46**, 453–459.

Gregg J. M., Bish D. L., Kaczmarek S. E. and Machel H. G. (2015) Mineralogy, nucleation and growth of dolomite in the laboratory and sedimentary environment: A review. *Sedimentology* **62**, 1749–1769.

Han N., Blue C. R., De Yoreo J. J. and Dove P. M. (2013) The Effect of Carboxylates on the Mg Content of Calcites that Transform from ACC. *Procedia Earth Planet. Sci.* **7**, 223–227.

Kelleher I. J. and Redfern S. A. T. (2002) Hydrous calcium magnesium carbonate, A possible precursor to the formation of sedimentary dolomite. *Mol. Simul.* **28**, 557–572.

Konrad F., Gallien F., Gerard D. E. and Dietzel M. (2016) Transformation of Amorphous Calcium Carbonate in Air. *Cryst. Growth Des.* **16**, 6310–6317.

Konrad F., Purgstaller B., Gallien F., Mavromatis V., Gane P. and Dietzel M. (2018) Influence of aqueous Mg concentration on the transformation of amorphous calcium carbonate. *J. Cryst. Growth* **498**, 381–390.

Lin C. J., Yang S. Y., Huang S. J. and Chan J. C. C. (2015) Structural characterization of Mg stabilized amorphous calcium carbonate by Mg-25 solid-state NMR spectroscopy. *J. Phys. Chem. C* **119**, 7225–7233.

Lippmann F. (1973) *Sedimentary Carbonate Minerals.*, Springer, Berlin.

Long X., Ma Y. and Qi L. (2011) In vitro synthesis of high Mg calcite under ambient conditions and its implication for biomineralization process. *Cryst. Growth Des.* **11**, 2866–2873.

Di Lorenzo F., Rodríguez-Galán R. M. and Prieto M. (2014) Kinetics of the solvent-mediated transformation of hydromagnesite into magnesite at different temperatures. *Mineral. Mag.* **78**, 1363–1372.

Ma Y., Aichmayer B., Paris O., Fratzl P., Meibom A., Metzler R. A., Politi Y., Addadi L., Gilbert P. U. P. A. and Weiner S. (2009) The grinding tip of the sea urchin tooth exhibits exquisite control over calcite crystal orientation and Mg distribution. *Proc. Natl. Acad. Sci. U. S. A.* **106**, 6048–6053.

Mackenzie F. T., Bischoff W. D., Bishop F. C., Loijens M., Schoonmaker J. and Wollast R. (1983) Magnesian calcites: low-temperature occurrence, solubility and solid-solution behavior. *Carbonates Mineral. Chem.*, 97–144.

Markham G. D., Glusker J. P., Bock C. L., Trachtman M. and Bock C. W. (1996) Hydration energies of divalent beryllium and magnesium ions: An ab initio molecular orbital study. *J. Phys. Chem.* **100**, 3488–3497.

Mavromatis V., Botz R., Schmidt M., Liebetrau V. and Hensen C. (2014) Formation of carbonate concretions in surface sediments of two mud mounds, offshore Costa Rica: a stable isotope study. *Int. J. Earth Sci.* **103**, 1831–1844.

Mavromatis V., Gautier Q., Bosc O. and Schott J. (2013) Kinetics of Mg partition and Mg stable isotope fractionation during its incorporation in calcite. *Geochim. Cosmochim. Acta* **114**, 188–203.

Montes-Hernandez G., Renard F., Chiriac R., Findling N. and Toche F. (2012) Rapid precipitation of magnesite microcrystals from $Mg(OH)_2$-H_2O-CO_2 slurry enhanced by NaOH and a heat-aging step (from ~20 to 90 °c). *Cryst. Growth Des.* **12**, 5233–5240.

Morse J. W. and Mackenzie F. T. (1990) *Geochemistry of sedimentary carbonates*, Elsevier, Amsterdam, Oxford, New York, Tokyo.

Nash M. C., Troitzsch U., Opdyke B. N., Trafford J. M., Russell B. D. and Kline D. I. (2011) First discovery of dolomite and magnesite in living coralline algae and its geobiological implications. *Biogeosciences* **8**, 3331–3340.

Ogino T., Suzuki T. and Sawada K. (1990) The rate and mechanism of polymorphic transformation of calcium carbonate in water. *J. Cryst. Growth* **100**, 159–167.

Paul A. and Lokier S. W. (2017) Holocene marine hardground formation in the Arabian Gulf: Shoreline stabilisation, sea level and early diagenesis in the coastal sabkha of Abu Dhabi. *Sediment. Geol.* **352**, 1–13.

Plummer L. N. and Busenberg E. (1982) The solubilities of calcite, aragonite and vaterite in CO2-H2O solutions between 0 and 90°C, and an evaluation of the aqueous model for the system $CaCO_3$-CO_2-H_2O. *Geochim. Cosmochim. Acta* **46**, 1011–1040.

Politi Y., Batchelor D. R., Zaslansky P., Chmelka B. F., Weaver J. C., Sagi I., Weiner S. and Addadi L. (2010) Role of magnesium ion in the stabilization of biogenic amorphous calcium carbonate: A structure-function investigation. *Chem. Mater.* **22**, 161–166.

Purgstaller B., Dietzel M., Baldermann A. and Mavromatis V. (2017a) Control of temperature and aqueous Mg^{2+}/Ca^{2+} ratio on the (trans-)formation of ikaite. *Geochim. Cosmochim. Acta* **217**, 128–143.

Purgstaller B., Goetschl K. E., Mavromatis V. and Dietzel M. (2019) Solubility investigations in the amorphous calcium magnesium carbonate system. *CrystEngComm* **21**, 155–164.

Purgstaller Bettina, Konrad F., Dietzel M., Immenhauser A. and Mavromatis V. (2017b) Control of Mg^{2+}/Ca^{2+} Activity Ratio on the Formation of Crystalline Carbonate Minerals via an Amorphous Precursor. *Cryst. Growth Des.* **17**, 1069–1078.

Purgstaller B., Mavromatis V., Immenhauser A. and Dietzel M. (2016) Transformation of Mg-bearing amorphous calcium carbonate to Mg-calcite - In situ monitoring. *Geochim. Cosmochim. Acta* **174**, 180–195.

Radha A. V., Fernandez-Martinez A., Hu Y., Jun Y. S., Waychunas G. A. and Navrotsky A. (2012) Energetic and structural studies of amorphous $Ca_{1-x}Mg_xCO_3 \cdot nH_2O$ (0≤x≤1). *Geochim. Cosmochim. Acta* **90**, 83–95.

Raz S., Weiner S. and Addadi L. (2000) Formation of high-magnesian calcites via an amorphous precursor phase: Possible biological implications. *Adv. Mater.* **12**, 38–42.

Reeder R. J. (1990) Carbonates: Mineralogy and Chemistry. *Rev. Mineral. Geochemistry* **11**.

Rodriguez-Blanco J. D., Shaw S. and Benning L. G. (2015) A route for the direct crystallization of dolomite. *Am. Mineral.* **100**, 1172–1181.

Rodriguez-Blanco J. D., Shaw S., Bots P., Roncal-Herrero T. and Benning L. G. (2012) The role of pH and Mg on the stability and crystallization of amorphous calcium carbonate. In *Journal of Alloys and Compounds* pp. S477–S479.

Schmidt M., Xeflide S., Botz R. and Mann S. (2005) Oxygen isotope fractionation during synthesis of CaMg-carbonate and implications for sedimentary dolomite formation. *Geochim. Cosmochim. Acta* **69**, 4665–4674.

Schott J., Pokrovsky O. S. and Oelkers E. H. (2009) The link between mineral dissolution/precipitation kinetics and solution chemistry. *Rev. Mineral. Geochemistry* **70**, 207–258.

Schroeder J. H., Dwornik E. J. and Papike J. J. (1969) Primary Protodolomite in Echinoid Skeletons. *Geol. Soc. Am. Bull.* **80**, 1613–1616.

Sumrall J. B., Larson E. B. and Mylroie J. E. (2017) Very high magnesium calcite formation and microbial communities found in porosity of the Seroe Domi Formation of Curacao, Netherland Antilles. *Carbonates and Evaporites* **32**, 123–133.

Tucker M. E. and Wright V. P. (1990) *Carbonate Sedimentology.*, Blackwell Science Ltd.

Vasconcelos C. and McKenzie J. A. (1997) Microbial mediation of modern dolomite precipitation and diagenesis under anoxic conditions (Lagoa Vermelha, Rio de Janeiro, Brazil). *J. Sediment. Petrol.* **67**, 378–390.

Xto J. M., Du H., Borca C. N., Amstad E., Van Bokhoven J. A. and Huthwelker T. (2019) Tuning the Incorporation of Magnesium into Calcite during Its Crystallization from Additive-Free Aqueous Solution. *Cryst. Growth Des.* **19**, 4385–4394.

Yang H., Chai S., Zhang Y. and Ma Y. (2015) A study on the influence of sodium carbonate concentration on the synthesis of high Mg calcites. *CrystEngComm* **18**, 157–163.

Zhang F., Xu H., Konishi H. and Roden E. E. (2010) A relationship between d_{104} value and composition in the calcite-disordered dolomite solid-solution series. *Am. Mineral.* **95**, 1650–1656.

Chapter 6 – **PERSPECTIVES**

The results of the experimental studies performed in this thesis reveal that the presence of $SO_4(aq)$ is affecting the Mg incorporation in calcite during its formation. The mechanisms that control limited Mg incorporation in calcite are (i) the aqueous complexation between Mg^{2+} and SO_4^{2-} to form $MgSO_4^0(aq)$ and the consequently decreased activity of Mg^{2+} in the reactive solutions, and (ii) the simultaneous incorporation of SO_4 into the calcite crystal lattice which is causing a unit cell expansion. However, up to now the exact structural position of the SO_4 ion in calcite which is substituting for carbonate ions is still a matter of debate. To gain insights on the structural orientation of CAS in calcite, high resolution structural analysis has been performed on precipitates that resulted from the experimental studies described in chapter 2 and 3 by using X-ray emission spectroscopy (XES) at the Paul Scherrer Institute (PSI) synchrotron facility. Yet, the collected data require in-depth treatment which will be part of future tasks. A detailed molecular picture of the exact position and orientation of the sulfate ion within the calcite crystal lattice including distances and angles between the different ions is suggested to reveal reasons for kinetically preferences of SO_4 incorporation in calcite. The sulfur isotopy of CAS is commonly used as a proxy for reconstructing the marine sulfur cycle. It is still unclear if or to what extent the final S isotope fractionation of calcite or aragonite is affected by metastable precursor phases. As such, knowledge of the S isotope fractionation of ACC and how the amorphous-to-crystalline mineral formation pathway might affect the isotopic signal of the finally formed crystalline polymorph is of great relevance for the interpretation of $\delta^{34}S_{CAS}$. In the current literature, a study quantifying this issue does not exist. Further experimental investigations including a multi-proxy approach ($\delta^{34}S$, $\delta^{18}O$, $\delta^{26}Mg$, …) are highly requested in order to better understand the complex reaction mechanisms and controlling environmental parameters during $CaCO_3$ mineral formation considering that the (trans)formation of amorphous carbonate phases is of tremendous relevance in many natural surroundings. Evaluating the fate of the primary chemical and isotopic composition of the amorphous precursor is of key relevance for the accurate interpretation of environmental proxies in carbonate archives that were formed via an amorphous precursor.

APPENDIX

A.1 Peer–reviewed publications

A.1.1 Publications as first author

Goetschl K.E., Purgstaller B., Dietzel M. and Mavromatis V. (2019) Effect of sulfate on magnesium incorporation in low-magnesium calcite. *Geochim. Cosmochim. Acta* 265, 505–519.

Goetschl K.E., Dietzel M., Purgstaller B., Grengg C. and Mavromatis V. (2021) Control of $MgSO_4^0$(aq) on the transformation of amorphous calcium carbonate to high-Mg calcite and long-term reactivity of the crystalline solid. *Geochim. Cosmochim. Acta*, in Press.

A.1.2 Publications as co-author

Mavromatis V., **Goetschl K.E.**, Grengg C., Konrad F., Purgstaller B. and Dietzel M. (2018) Barium partitioning in calcite and aragonite as a function of growth rate. *Geochim. Cosmochim. Acta* 237, 65–78.

Novoselov A.A., Konstantinov A.O., Lim A.G., **Goetschl K.E.**, Loiko S.V., Mavromatis V. and Pokrovsky O.S. (2019) Mg-rich authigenic carbonates in coastal facies of the vtoroe zasechnoe lake (Southwest siberia): First assessment and possible mechanisms of formation. *Minerals* 9, 1–19.

Purgstaller B., **Goetschl K.E.**, Mavromatis V. and Dietzel M. (2019) Solubility investigations in the amorphous calcium magnesium carbonate system. *CrystEngComm* 21, 155–164.

Ge Y., Pederson C.L., Lokier S.W., Traas J.P., Nehrke G., Neuser R.D., **Goetschl K.E.** and Immenhauser A. (2020) Late Holocene to Recent aragonite-cemented transgressive lag deposits in the Abu Dhabi lagoon and intertidal sabkha. *Sedimentology* 67, 2426–2454.

Purgstaller B., Mavromatis V., **Goetschl K.E.**, Steindl F.R. and Dietzel M. (2021) Effect of temperature on the transformation of amorphous calcium magnesium carbonate with near-dolomite stoichiometry into high Mg-calcite. *CrystEngComm* 23, 1969–1981.

Mavromatis V., Brazier J-M., **Goetschl K.E.** (submitted) The role of temperature and mineral growth rate on Mg incorporation in aragonite.

A.2 Conference contributions

EGU General Assembly 2018, Vienna, Austria

Goetschl K.E., Purgstaller B., Mavromatis V., and Dietzel M.: *In situ* monitoring of calcium carbonate formation via an amorphous precursor in the presence of aqueous magnesium and sulfate. (Poster)

Goldschmidt Conference 2018, Boston, USA

Goetschl K.E., Purgstaller B., Dietzel M., and Mavromatis V.: How do Ligands Affect Mg Partitioning in Calcite Formed via an Amorphous Precursor? (Talk)

Goldschmidt Conference 2019, Barcelona, Spain

Goetschl K.E., Dietzel M., and Mavromatis V.: The control of mineral growth rate on sulfate partitioning in calcite and aragonite - An experimental study. (Talk)

MinPet 2019, Graz, Austria

Goetschl K.E., Mavromatis V., Purgstaller B., and Dietzel M.: Experimental determination of sulfate incorporation in calcite, Mg-calcite and aragonite. (Poster)

EGU General Assembly 2020, virtual

Goetschl K.E., Spirk T., Purgstaller B., and Dietzel M.: Transformation of Amorphous Calcium Carbonate in Air - The Role of Additives and Humidity. (Display)